Additive manufacturing of 3D architectured metallic biomaterials by robocasting

Marion Coffigniez

N°d'ordre NNT : 2021LYSEI007

THESE de DOCTORAT DE L'UNIVERSITE DE LYON
opérée au sein de
L'Institut National des Sciences Appliquées de Lyon

Ecole Doctorale N° ED 34
Matériaux de Lyon

Spécialité/ discipline de doctorat : Science des Matériaux

Soutenue publiquement le 15/01/2021, par :
Marion Coffigniez

Additive manufacturing of 3D architectured metallic biomaterials by robocasting

---

Devant le jury composé de :

Poquillon, Dominique	Professeur	INP – ENSIACET	Rapporteure
Missiaen, Jean-Michel	Professeur	INP – Phelma	Rapporteur
Gloriant, Thierry	Professeur	INSA Rennes	Président
Gremillard, Laurent	Directeur de recherche	INSA Lyon	Directeur de thèse
Boulnat, Xavier	Maître de conférences	INSA Lyon	Directeur de thèse
Rigollet, Claire	Maître de conférences	ECAM	Invitée
Andrieux, Jérôme	Maître de conférences	UCBL	Invité

Département FEDORA – INSA Lyon - Ecoles Doctorales – Quinquennal 2016-2020

SIGLE	ECOLE DOCTORALE	NOM ET COORDONNEES DU RESPONSABLE
CHIMIE	**CHIMIE DE LYON** **http://www.edchimie-lyon.fr** Sec. : Renée EL MELHEM Bât. Blaise PASCAL, 3e étage **secretariat@edchimie-lyon.fr** INSA : R. GOURDON	**M. Stéphane DANIELE** Institut de recherches sur la catalyse et l'environnement de Lyon IRCELYON-UMR 5256 Équipe CDFA 2 Avenue Albert EINSTEIN 69 626 Villeurbanne CEDEX **directeur@edchimie-lyon.fr**
E.E.A.	**ÉLECTRONIQUE, ÉLECTROTECHNIQUE, AUTOMATIQUE** **http://edeea.ec-lyon.fr** Sec. : M.C. HAVGOUDOUKIAN **ecole-doctorale.eea@ec-lyon.fr**	**M. Gérard SCORLETTI** École Centrale de Lyon 36 Avenue Guy DE COLLONGUE 69 134 Écully Tél : 04.72.18.60.97 Fax 04.78.43.37.17 **gerard.scorletti@ec-lyon.fr**
E2M2	**ÉVOLUTION, ÉCOSYSTÈME, MICROBIOLOGIE, MODÉLISATION** **http://e2m2.universite-lyon.fr** Sec. : Sylvie ROBERJOT Bât. Atrium, UCB Lyon 1 Tél : 04.72.44.83.62 INSA : H. CHARLES **secretariat.e2m2@univ-lyon1.fr**	**M. Philippe NORMAND** UMR 5557 Lab. d'Ecologie Microbienne Université Claude Bernard Lyon 1 Bâtiment Mendel 43, boulevard du 11 Novembre 1918 69 622 Villeurbanne CEDEX **philippe.normand@univ-lyon1.fr**
EDISS	**INTERDISCIPLINAIRE SCIENCES-SANTÉ** **http://www.ediss-lyon.fr** Sec. : Sylvie ROBERJOT Bât. Atrium, UCB Lyon 1 Tél : 04.72.44.83.62 INSA : M. LAGARDE **secretariat.ediss@univ-lyon1.fr**	**Mme Sylvie RICARD-BLUM** Institut de Chimie et Biochimie Moléculaires et Supramoléculaires (ICBMS) - UMR 5246 CNRS - Université Lyon 1 Bâtiment Curien - 3ème étage Nord 43 Boulevard du 11 novembre 1918 69622 Villeurbanne Cedex Tel : +33(0)4 72 44 82 32 **sylvie.ricard-blum@univ-lyon1.fr**
INFOMATHS	**INFORMATIQUE ET MATHÉMATIQUES** **http://edinfomaths.universite-lyon.fr** Sec. : Renée EL MELHEM Bât. Blaise PASCAL, 3e étage Tél : 04.72.43.80.46 **infomaths@univ-lyon1.fr**	**M. Hamamache KHEDDOUCI** Bât. Nautibus 43, Boulevard du 11 novembre 1918 69 622 Villeurbanne Cedex France Tel : 04.72.44.83.69 **hamamache.kheddouci@univ-lyon1.fr**
Matériaux	**MATÉRIAUX DE LYON** **http://ed34.universite-lyon.fr** Sec. : Stéphanie CAUVIN Tél : 04.72.43.71.70 Bât. Direction **ed.materiaux@insa-lyon.fr**	**M. Jean-Yves BUFFIÈRE** INSA de Lyon MATEIS - Bât. Saint-Exupéry 7 Avenue Jean CAPELLE 69 621 Villeurbanne CEDEX Tél : 04.72.43.71.70 Fax : 04.72.43.85.28 **jean-yves.buffiere@insa-lyon.fr**
MEGA	**MÉCANIQUE, ÉNERGÉTIQUE, GÉNIE CIVIL, ACOUSTIQUE** **http://edmega.universite-lyon.fr** Sec. : Stéphanie CAUVIN Tél : 04.72.43.71.70 Bât. Direction **mega@insa-lyon.fr**	**M. Jocelyn BONJOUR** INSA de Lyon Laboratoire CETHIL Bâtiment Sadi-Carnot 9, rue de la Physique 69 621 Villeurbanne CEDEX **jocelyn.bonjour@insa-lyon.fr**
ScSo	**ScSo*** **http://ed483.univ-lyon2.fr** Sec. : Véronique GUICHARD INSA : J.Y. TOUSSAINT Tél : 04.78.69.72.76 **veronique.cervantes@univ-lyon2.fr**	**M. Christian MONTES** Université Lyon 2 86 Rue Pasteur 69 365 Lyon CEDEX 07 **christian.montes@univ-lyon2.fr**

*ScSo : Histoire, Géographie, Aménagement, Urbanisme, Archéologie, Science politique, Sociologie, Anthropologie

Acknowledgements

Il semblerait que le moment soit venu de passer à l'écriture de ces quelques pages de remerciements... A la fois redouté et attendu, il s'agit avant tout pour moi d'un moment précieux, ouvert à l'expression d'une gratitude profonde. Pourtant son ambivalence est palpable. Ces quelques pages sont la touche finale à apporter à ce manuscrit, synonyme d'un bel accomplissement, mais elles signent aussi malheureusement la fin de ces trois et quelques très belles années, qui n'auraient pu avoir la même saveur sans vos contributions à vous tous.

Je souhaiterais commencer par remercier mes deux rapporteurs, Dominique Poquillon et Jean-Michel Missiaen, d'avoir accepté de se pencher sur l'intégralité de ses travaux de thèse pour en permettre la finalisation. En particulier, merci Dominique pour ton enthousiasme et ta passion pour la science, qui ont créé une atmosphère engageante malgré les barrières de la visio, et merci Jean-Michel pour ta gentillesse et ton soutien jusque dans la recherche des coquilles ! J'aimerais également remercier Thierry Gloriant d'avoir accepté de faire partie de ce jury. Après t'avoir croisé un certain nombre de fois en conférences, ce fût un plaisir de t'avoir comme président de jury toujours aussi bienveillant et curieux.

Mais pour en arriver à cette belle discussion scientifique finale que l'on appelle soutenance de thèse, il m'a été donné la chance de passer ces trois années de navigation dans les méandres scientifiques aux côtés de Xavier Boulnat et Laurent Gremillard. Xavier, Laurent, vous m'avez offert l'équilibre dont j'avais besoin pour avancer sur ce chemin. Tous les deux débordants d'idées, vous êtes également extrêmement attentifs à la personne que vous avez en face de vous, ce qui vous a permis de me témoigner votre confiance par l'autonomie que vous m'avez laissé prendre, tout en m'apportant votre soutien dans les moments de doute. Je ne vous remercierai probablement jamais assez pour ça, et j'espère, pour le bonheur de futurs doctorants, que vous continuerez à co-encadrer des thèses ensemble car vos deux caractères se marient vraiment bien pour cette réalisation-là.

Merci Xavier pour ton énergie débordante, ton énorme capacité de synthèse, ton optimisme sans faille, ta volonté de toujours voir les choses avancer, qui sont autant de forces motrices pour aller chercher un peu plus au fond des choses. Ton petit côté très ancré dans le professionnalisme est ponctué par tes petites pointes d'humour toujours bien placées, et se double d'un profond mélange d'attention et de gentillesse à notre égard (au point de nous prêter ta maison en plein mois d'août pour une semaine de rédaction plus au vert et

à la fraîche !). Merci infiniment pour tout ce que tu es, et surtout ne change rien (hormis peut-être de prendre un peu plus de temps pour toi histoire de te ménager un peu quand même !).

Laurent, au-delà du brillant scientifique aux apparences timides, tu es aussi une personne chaleureuse, doté d'une grande capacité d'écoute, d'une véritable empathie et de ce précieux don de rassurer, qui sont autant de qualités pour lesquelles je souhaite profondément te remercier. Merci aussi pour ton côté plus raisonnable que nous, qui nous a permis de garder un peu plus les pieds sur terre quand on avait envie de croire que le temps était infini ! Et à défaut d'avoir pu transformer cette croyance (ou aspiration) en vérité, j'espère ne jamais perdre contact avec vous deux !

J'aimerais également chaleureusement remercier toutes les personnes des laboratoires voisins qui ont bien voulu m'accueillir et m'aider à enrichir cette étude à travers de nouvelles expériences. Merci à Claire Rigollet et Sandra Simon, du Labecam, pour les discussions intéressantes que l'on a pu avoir autour des problématiques liées aux traitements de déliantage et frittage, mais aussi pour votre accueil toujours bienveillant lorsque je suis venue réaliser certains essais avec vous (ATG, tentative de frittage). Merci aussi à Erik Bonjour et Patrick Jame d'avoir été toujours promptes à m'accueillir à l'ISA et en particulier Erik pour ta disponibilité et ton côté toujours prêt à m'aider pour ces mesures de taux d'interstitiels. Egalement un grand merci à Guillaume Deffrennes, pour m'avoir transmis ton expérience sur les traitements thermiques du magnésium avec ton côté toujours enjoué, pour avoir pris ce temps-là alors que tu étais en fin de thèse et pour m'avoir mis en contact avec ton équipe encadrante au LMI. J'en profite de ce fait pour remercier Jérôme Andrieux, pour toutes ces discussions intéressantes qui en ont découlé et pour ton accueil chaleureux au LMI. Merci également à Bruno Gardiola pour ta gentillesse et ton savoir-faire lors de la réalisation de ces quelques encapsulations sous vide avec toi. Enfin merci également à Christophe Reynaud du CETIM, pour ton accueil bienveillant et la réalisation de cet essai de frittage avec votre équipement d'une autre échelle.

Au-delà de ces collaborations ponctuelles, cette thèse s'étant avant tout déroulée au laboratoire MATEIS, c'est principalement l'atmosphère qui y règne qui a pu donner cette saveur particulière à ces trois années. L'entraide et le partage y sont de mise, et ce même au-delà des problématiques scientifiques, ce qui en fait un laboratoire où il fait "bon vivre". C'est la raison pour laquelle je souhaiterais vivement remercier l'ensemble des membres de MATEIS qui contribuent à cet état d'esprit et à ce fonctionnement.

Maintenant, avant de rentrer plus en détail dans les faits marquants de cette aventure humaine vécue à MATEIS, je souhaiterais commencer par remercier Damien Fabrègue, sans qui tout ceci n'aurait probablement jamais commencé. Damien, merci infiniment pour ta passion pour la science que tu as l'art de transmettre, merci d'avoir semé une petite graine dans ma tête pendant mon projet de fin d'étude puis de lui avoir gentillement laissé le temps de germer et de grandir, merci d'avoir ensuite respecté mon entêtement à vouloir travailler sur les biomatériaux et de m'avoir envoyée dans les pattes de Xavier et Laurent,

c'était un excellent conseil ! Et de manière plus globale, merci pour ta confiance, pour les moments sportifs que tu partages avec nous, mais aussi pour ton écoute et la sensibilité que tu caches sous ta carapace.

Le début d'une thèse est souvent marqué par une phase de prise en main, aussi bien du point de vue technique vis-à-vis des équipements expérimentaux que du point de vue du fonctionnement global. Il y a, heureusement, tout un tas de personnes bienveillantes qui participent à cette prise en main et que je souhaite remercier fortement. Tout d'abord merci Florian pour tous les renseignements que tu peux nous procurer sur à peu près tout ce qu'il y a au labo, pour ta bienveillance permanente, pour ta gestion efficace des salles céramiques et pour ton aide sur tout ce qui touche à la gleeble ou au SPS. Merci aussi à Benjamin de l'INL pour ta gentillesse et ta gestion du MEB SGM en main de maître. Pour continuer sur cette lancée de microscopistes, merci infiniment Sophie, à la fois pour ta patience pour nous former à l'EBSD, mais aussi pour tes conseils toujours pertinents, pour ta franchise, pour ta pédagogie et le temps que tu prends pour nous former sur les TP des 4SGM. Je souhaite également remercier Sylvain Meille, pour ton aide dans la mise en place des essais de flexion avec la Bose mais aussi pour ton attention à l'égard de l'ensemble des doctorants de l'équipe. Et pour passer de Blaise Pascal à Jules Verne, merci à Jérôme pour ton aide sur la tomographie, pour ton coté toujours prêt à dépanner et ton suivi des projets de chacun d'entre nous. Enfin, parce qu'acquérir de belles données est une chose, mais que savoir les exploiter en est une autre, je souhaite dire un énorme merci à Joël L. ! Merci pour la patience dont tu as fait preuve pour m'expliquer comment fonctionnait ton protocole pour effectuer cette fameuse comparaison CAO / tomo et merci d'avoir pris le temps de mettre au point ce dit protocole d'exploitation de données. Ce projet de comparaison n'aurait tout simplement pas pu voir le jour sans ton aide. Merci également pour la mise au point du suivi par DIC de mes essais de compression et pour l'exploitation des données DIC et DVC de relativement dernière minute... Et plus généralement, merci pour ton calme olympien, pour ta prise de recul et pour ces discussions qui finissent toujours par prendre un beau côté philosophique.

Toujours en lien avec la mise en place de manips, j'aimerais remercier José, Christophe et Lucas, de l'atelier électronique, pour leur aide précieuse et soigneuse lorsque l'on a besoin de mettre en place de nouveaux systèmes d'acquisitions ou de modifier les possibilités offertes par certains équipements.

Les thématiques un peu plus biologiques sont arrivées tardivement dans ce projet et ce sont vu abrégées par la crise sanitaire, mais je souhaiterais néanmoins remercier l'ensemble des membres de l'équipe I2B, et en particulier Sandra, pour la réalisation de ces premiers essais, et Jérôme, pour t'être penché avec moi sur la problématique du "comment caractériser ces échantillons", à travers ces discussions à la fois fort sympathiques mais aussi très enrichissantes pour la novice que je suis en terme de biologie.

Durant cette thèse j'ai également eu l'occasion, très formatrice et enrichissante, de co-encadrer deux projets de fin d'étdues. Aussi je souhaites profondément remercier Sara, pour

ta constante bonne humeur et pour m'avoir fait découvrir à quel point c'était agréable et motivant d'encadrer quelqu'un aussi intéressé et impliqué que ce que tu l'étais. J'en profite également pour remercier Jean-Marc et Sandrine pour votre gentillesse et toutes ces riches discussions qu'on a pu avoir autour de ce beau projet sur les verres métalliques. De la même manière, je souhaiterais dire un grand merci à Sébastien, pour ta franchise, pour la confiance que tu m'as accordée et ce que tu m'as appris sur le plan humain. Merci aussi à Sylvain D., d'avoir relevé au pied levé le défi de porter ce projet sur la simulation éléments finis de mes scaffolds, merci pour ton calme et ta patience mais aussi pour ta gestion organisée !

Au-delà de toutes ces réalistaions sur le plan professionnel, il y a aussi le quotidien, tous les à-côtés, l'ambiance dans laquelle on baigne au jour le jour. Mes années de thèse ont donc été marquées par le temps passer au sein de l'équipe MétAl, équipe dans laquelle on se sent particulièrement bien, si bien qu'on aimerait y rester ou être sûr de retrouver le même cadre ailleurs, ce qui n'est pas garantie.

Il me paraît impossible d'aborder le quotidien de l'équipe sans commencer par remercier sincèrement Frida. Toujours attentive à tous "tes petits jeunes", tu contribues tous les jours à la bonne ambiance de cette équipe que tu fais tourner d'une main de maître et qui te doit beaucoup. Mes remerciements vont aussi à JYB et sa sagesse. Jean-Yves, ou Grand Maître du 21 ème siècle (comme t'appelles tes doctorants), merci pour ta bienveillance quotidienne, pour tes discussions qui nous poussent à réfléchir, pour cette attention (qui frôle parfois la taquinerie) que tu portes à l'avenir de chacun d'entre nous (les thésards), mais aussi pour ces supers balades en vélo vers l'Alpes et la Bérarde. Je souhaiterais également profondément remercier Michel, pour ton optimisme et ton enthousiasme permanent, pour tes encouragements à coup de "dernier virage", pour ta patience et ton endurance face à mes demandes successives de modification de ce fameux modèle de précipitation des TiC, mais aussi pour ton goût pour Khatchatourian et ses tempos intenables, qui m'aura permis d'apprendre à être les troisième et quatrième mains de quelqu'un ! Merci aussi Patrice pour tes "sauvetages" à base de pain d'épice (au demeurant très bon ! !) et tous ces moments partagés fort enrichissants. La liste promettant d'être bien trop longue, je souhaiterais finalement remercier l'ensemble des membres de l'équipe MétAl pour cette bonne ambiance générale, pour ces discussions animées en salle café ou ailleurs et pour ces belles sorties sportives.

Enfin, j'ai eu la chance de partager mon quotidien avec une belle bande de doctorants et j'espère que les liens profonds qu'on aura pu tisser au cours de ces années sauront résister à l'usure du temps. Pour reprendre par chronologie des différentes "fournées", merci aux "anciens" qui nous ont accueillis : Juju pour ton courage à toutes épreuves doublé d'un recul sur les choses, ton attention envers les autres et le lancement de ce fameux groupe de cyclistes, Théo pour ton dynamisme et toutes ces sorties sportives, tes connaissances intarrissables en cinéma et ton sourire toujours au rendez-vous, Oriane pour ta volonté de fer, que ce soit pour les sciences ou pour le zéro déchets, Victor pour ton côté ouvert et

ta fameuse interprétration de “Rude Boy”, Gwen pour ton petit côté têtue et ton accent chantant, et Sib pour tes pauses guitares au deuxième, qui mettaient du baume au coeur de tous les habitants des bureaux voisins.

Merci aussi à tous ceux qui, en plus de nous accueillir, nous ont également accompagnés un an de plus dans cette belle aventure : Alexis pour cette association de bonté et de générosité qui te caractérise, pour tes réponses aux blind tests et tous ces kilomètres parcourus en courant à tes côtés, Gabriel pour ton écoute, ta sensibilité, ces petites piques bien placées que tu sors de temps en temps et ton incroyable lutte contre le stress, François pour ton calme, ta confiance et ton courage sans limite face aux défis du grand Mathevon, Julie pour ta bonne humeur communicative et ton esprit festif, Aléthéa pour la force de tes émotions et ton souci de ne pas déranger, et Amin pour cette résilience incroyable que tu caches derrière ta discrétion.

Mes remerciements vont également “aux nouveaux” qui arrivent chaque année et perpétuent cette bonne humeur générale : Tic et Tac, nos inséparables rois de l’ambiance après quelques verres, Manon pour ta dextérité incroyable avec un tube en quartz et un chalumeau, mais aussi pour ta spontanéité et ton caractère entier si attachant, Mathilde pour cette inépuisable énergie que tu dégages et ton implication dans les “à-côtés” de la vie au labo toujours pleine d’entrain et de bonne humeur, Justine pour ton esprit ouvert et ta constante tranquillité, Théophile pour ton côté décontracté, Marion pour ta gentillesse et ta ténacité, Lucas pour ces sessions courses même à la fraîche, Ce pour ton perpétuel sourire et enfin Maël, pour avoir relevé avec brio (et une incroyable sérénité) le défi de la préparation et de la réalisation de ces fameuses manips synchrotron, et pour tes petites piques d’humour de plus en plus nombreuses depuis qu’on te connaît un peu mieux !

Je souhaite également bon courage à tous les derniers arrivés, Florian, Théotime, Louis et Yohan. Vous avez commencé avec un sacré test de résilience à travers ce “baptême du feu” (littéral) que vous ont gentillements offerts les travaux d’Eiffage, mais je vous souhaite un avenir moins mouvementé (après la fin des travaux) et un retour à l’ambiance de l’équipe d’avant Covid.

Enfin il y a ceux qui ont marqué mon quotidien de la plus belle des façons durant ces trois années (modulo quelques mois), en m’offrant leur présence quotidienne, leur amitié, leur générosité d’âme, et que je souhaiterais remercier du fond du coeur.

Je souhaiterais commencer par remercier ces trois formidables personnes qui constituent le fameux “bureau du bonheur”, qui mériterait parfois d’être rebaptisé en “bureau du dialogue de sourd”, mais qui est gage d’un accueil ressourçant (et de quelques fous rires) dans les périodes de doutes. Merci Lucile pour tout ce qu’on a pu partager depuis ce 2 octobre 2017 (dont quelques heures de manips synchrotron grâce à ton invitation !), merci pour ton écoute, pour ta gentillesse qui semble sans limites (même quand tu nous tacles subrepticement), pour toutes ces discussions qui nous auront fait avancer (et je ne parle pas que d’avancées scientifiques) mais aussi pour ton incroyable niveau d’organisation

qui restera toujours un modèle pour moi ! Quentin, j'ai le regret de t'annoncer que je ne rédigerai pas ta thèse... mais à la place je tiens à te remercier sincèrement pour ton humour aux mille et une facettes, de ton expertise en ironie à ton amour de ce bon vieux comique de répétition, mais aussi pour ta sensibilité, ta confiance et ton soutien qui ne font jamais défaut. Enfin Laurabelle, bien que tu sois en réalité arrivée après, cela ne change rien à la solidité de ces liens créés par tous ces moments de partage sincères et profonds. Merci pour ton caractère plein d'entrain et ton rire que l'on entend si souvent, mais aussi pour l'attention que tu portes aux personnes qui t'entourent et cette capacité que tu as de nous obliger à nous remettre en mouvement quand on patauge pour une raison ou pour une autre. Enfin pour apporter un peu de diversité à tous ces beaux moments sportifs déjà partagés, je te promets que tu l'auras cette initiation aviron !

Celle belle promotion n'était pas en manque de piliers et de modèles. Alex, je voudrais te remercier pour ce rôle clef de rassembleur que tu as et qui naît du cumul de ta grande gentillesse avec ton incroyable force de persuasion. Merci de nous avoir poussé à oser aller toujours un petit peu plus loin dans ces réalisations sportives (ou plus haut selon l'activité !), mais merci aussi pour tes petits moments taquins et ton recul exemplaire par rapport à toutes ces petites (ou grandes) difficultés de la vie. Et en parlant d'exemple, merci Arnaud pour ta maturité fascinante vis-à-vis du monde qui nous entoure, pour ton caractère agréable, à la fois discret, attentionné et taquin, mais aussi pour toutes ces longues discussions que l'on a pu avoir, que ce soit en bas du bâtiment, pendant ces sorties perchés sur nos selles de vélo, ou sur la terrasse de notre cher XB. Merci également à toi Flore, pour tous ces moments partagés pendant ces trois dernières années. Quotidiens les trois premiers mois puis plus ponctuels par la suite, ils n'en ont pas moins alimentés cette belle amitié qui avait déjà une longueur d'avance grâce à notre plaisir commun de "prendre les rames". Mais ces rames physiques ayant déjà prouvé leur faiblesse, c'est avec plaisir que je t'ai retrouvée pour partager quelques coups de rames métaphoriques au côté de ta constante bonne humeur ! Et finalement, un grand merci à toi Qinqin, pour avoir supporté mes allées et venues incessantes entre passages au bureau et manips en tout genre, mais aussi pour ta gentillesse et ton remarquable courage.

Enfin, parce qu'il y a des bases, des fondations si solides qu'elles donnent la force de beaucoup de choses, je souhaiterais remercier ma famille du fond du coeur. Merci pour tout ce que vous m'avez appris, transmis, au fil des années, pour cet amour indéfectible et votre confiance inébranlable, et tous ces beaux moments déjà partagés ou à venir ! A ces fondations s'est rajouté un nouveau pilier, (plus si nouveau que ça depuis le temps d'ailleurs !), à qui je souhaite dédier les derniers remerciements de ces quelques pages. Merci Mathieu pour ces moments de bonheur passés près de toi et pour ta patience infinie durant ces trois dernières années !

A Julie,

Tenter d'apprivoiser la science,
Ne faisait pas partie de tes préférences,
Mais il y a pourtant un petit peu de toi,
Derrière chacun de ces mots-là.

French summary

La croissance rapide couplée au vieillissement de la population induit une demande croissante d'implants orthopédiques. Les métaux sont considérés comme d'excellents candidats pour ces applications de par leur compromis entre résistance et ductilité [KRI 07]. Ils sont, de ce fait, communément utilisés en chirurgie orthopédique depuis plus d'un siècle [CHE 15]. Parmi les matériaux métalliques couramment utilisés en tant qu'implants orthopédiques (aciers inoxydables, alliages à base de cobalt et alliages à base de titane), les alliages de titane présentent la meilleure résistance spécifique et les propriétés mécaniques les plus appropriées. Cependant, il reste encore nécessaire de réduire la rigidité des implants à base de titane pour améliorer leur ancrage et donc leur longévité. En effet, l'inadéquation entre la rigidité de l'implant et celle du tissu osseux environnant conduit généralement à un déchaussement de l'implant après quelques années [GUI 05, GLA 06]. Ce phénomène est lié au fait que le renouvellement du capital osseux est stimulé par la contrainte à laquelle l'os est soumis. Au niveau d'un site d'implantation, si l'implant possède une rigidité supérieure à celle de l'os, alors toute la contrainte sera absorbée par l'implant. L'os environnant n'étant plus sollicité, son remodelage n'aura donc plus lieu, débouchant ainsi sur une diminution de la densité osseuse autour de l'implant, favorisant les micromouvements dans un premier temps, puis augmentant dans un second temps le risque de déchaussement.

Pour résoudre ces problèmes, différentes approches sont possibles. Parmi les solutions envisageables, la fabrication additive attire une attention particulière. En effet, au-delà de l'aspect de personnalisation qu'elle peut apporter au domaine médical, la fabrication additive donne aussi accès à l'élaboration de structures cellulaires. Ces structures de porosité maîtrisée permettent à la fois de moduler les propriétés mécaniques de l'implant mais aussi de favoriser l'invasion cellulaire nécessaire en ingénierie tissulaire.

Ces travaux de thèse portent sur l'élaboration de pièces métalliques par robocasting, qui compte parmi les techniques de fabrication additive métallique les plus versatiles. Cette technique permet, par ailleurs, d'élaborer des pièces présentant différents niveaux de porosités, ce qui peut être intéressant dans le cadre d'implants osseux. En effet, si des macropores (quelques centaines de micromètres) sont effectivement nécessaires pour permettre la vascularisation et donc l'approvisionnement des cellules en oxygène

et nutriments [KAR 05], diverses études ont également montré que les micropores permettent d'améliorer la reconstruction osseuse [HIN 05, O'B 05, LAN 10, CHA 12, POL 13, BOH 17].

Au vu de l'application visée, cette étude a été menée sur deux matériaux différents : le titane, qui est actuellement une référence pour les implants permanents, et le magnésium, dont les alliages sont prometteurs pour des applications comme implants résorbables.

Les micropores ayant été identifiés comme bénéfiques pour l'ostéointégration par différents auteurs, une étude paramétrique a été réalisée sur le TA6V pour faire varier la microporosité résiduelle et évaluer ses conséquences sur les propriétés finales de la pièce (tant du point de vue dimensionnel et structurel que du point de vue des propriétés d'usage). En outre, comme la composition chimique finale et l'assemblage des phases peuvent avoir un impact important sur les propriétés mécaniques des pièces obtenues, l'influence des paramètres de déliantage a également été étudiée en termes d'enrichissement interstitiel et de fragilisation induite.

En ce qui concerne le magnésium, comme sa réactivité rend sa processabilité plus compliquée, l'objectif de l'étude était d'évaluer si le procédé de robocasting pouvait être appliqué aux alliages à base de magnésium. Le problème était donc avant tout de trouver des processus compatibles avec ce matériau pour chaque étape du procédé.

Robocasting de TA6V

Elaboration des structures

La première étape du procédé de robocasting consiste à formuler l'encre. Un moyen facile d'obtenir des encres présentant des propriétés rhéologiques adéquates (extrudables à travers une fine buse sous l'effet d'une pression, mais capable de conserver leur forme une fois imprimées) consiste à disperser la poudre dans un gel thixotrope. Sous l'effet du cisaillement, le gel se déstructure, ce qui lui permet de s'écouler, mais une fois déposé, il se reconstitue, ce qui permet de conserver la forme demandée. Le choix du liant s'est donc porté sur les hydrogels de pluronic F-127, déjà utilisés au laboratoire avec des poudres céramiques.

Les encres ne contenaient ainsi que trois ingrédients : de l'eau, du pluronic F-127 et des particules de TA6V. Il a alors été possible de faire varier les propriétés rhéologiques des encres en faisant varier la proportion de ces trois ingrédients. Il a été constaté que, en utilisant une température d'impression de 25 °C, les encres réalisées en ajoutant entre 45 et 50 vol% de TA6V dans des hydrogels contenant entre 25 et 30 wt% de pluronic F-127 permettent la réalisation d'un empilement de couches tout en conservant les macropores demandés par le design, jusqu'à une taille de buse de 250 µm. Cette capacité à garder la forme demandée, malgré l'ajout des couches suivantes, a été corrélée avec la présence d'une

contrainte seuil dynamique suffisamment élevée (entre 250 et 300 Pa pour ces encres).

Cependant, une caractérisation plus fine, basée sur la comparaison entre la CAO d'origine et les scans des échantillons séchés obtenus par tomographie aux rayons X, a révélé que les encres à 50 vol% de poudre étaient plus fidèles à la CAO d'entrée que celles à 45 vol%. De manière globale, l'impression à partir de ces encres entraîne des écarts dimensionnels par rapport au fichier CAO de moins de 10 % du diamètre de la seringue.

Déliantage

Une fois l'étape de mise en forme terminée, les pièces doivent être séchées, déliantées puis frittées pour atteindre leurs structures et propriétés finales. Afin de réduire le nombre de variables pour ces étapes, une seule encre a été conservée pour étudier l'influence des conditions de déliantage et de frittage. Il a donc été choisi d'utiliser l'encre présentant 50 vol% de poudre de TA6V dispersée dans un gel contenant 25 wt% de pluronic, de manière à minimiser la quantité de liant et donc ainsi faciliter l'étape de déliantage. Contrairement à ce qui est observé pour les céramiques, le séchage ne s'est pas révélé ici comme une étape limitante.

Les conditions de déliantage sont souvent choisies avec une marge importante pour s'assurer que le liant a été correctement éliminé. Cependant, comme le montrent ces travaux de thèse, cette stratégie doit absolument être évitée lors de l'élaboration de pièces en alliage de titane. En effet, plus la température de déliantage est élevée, plus le titane s'enrichit en éléments interstitiels présents dans le liant et se fragilise. Un enrichissement en carbone trop élevé peut même entraîner la précipitation de carbures dans la phase β lors du frittage ou du refroidissement après frittage, selon la température de frittage et la vitesse de refroidissement utilisée. Ce phénomène a pu être observé expérimentalement (diffraction des rayons X (DRX), microscopie électronique à balayage (MEB)) mais également simulé par un modèle thermo-cinétique de précipitation. Il est donc conseillé de toujours utiliser la température de déliantage la plus basse possible pour éviter la fragilisation des alliages de titane.

La température la plus basse à laquelle le pluronic F-127 peut être dégradé a été déterminée par ananlyse thermogravimétrique comme étant de 350 °C. Un traitement de déliantage de 30 min à 350 °C sous vide dynamique primaire (vitesse de chauffe de 1 °C·min^{-1}), suivi d'un frittage de 2 h à 1200 °C sous vide dynamique secondaire (5×10^{-4} mBar) donne le meilleur compromis en taux d'interstitiels finaux mesurés dans cette étude.

Frittage

Avec un procédé tel que le robocasting, la structure finale de la pièce est fortement influencée par le processus de frittage. La température de frittage et la taille initiale des poudres permettent toutes deux de faire varier la densité finale. L'augmentation de la température de frittage de 1000 à 1200 °C, pour des pièces réalisées à partir d'une poudre

grossière (diamètre moyen de 23 µm), a conduit à augmenter la densification des filaments de 73 à 87,5% tout en conservant une interconnexion de ces micropores résiduels. Les tailles caractéristiques de ce réseau microporeux sont en revanche restées similaires, quelle que soit la température utilisée, avec des cous d'interconnexion allant d'un diamètre de 1 à 7 - 8 µm et présentant un diamètre moyen autour de 4 - 5 µm, et une taille moyenne de pores d'environ 15 µm. Une densification supplémentaire des filaments a été obtenue en maintenant la température de frittage à 1200 °C mais en ajoutant une poudre fine dans l'encre (diamètre moyen de 4.3 µm). La densification la plus élevée a été observée pour une encre contenant 100% de poudre fine (0,025 % de porosité résiduelle dans les filaments). La réduction du diamètre de la poudre utilisée a également entraîné une diminution de la rugosité : le R_a est passé d'environ 10 à 2 µm, ce qui est plus faible que la rugosité généralement obtenue par fusion sur lit de poudres.

Propriétés

La densification observée est également accompagnée d'une augmentation du module de Young des filaments, mais aussi d'une augmentation de la microdureté et de la limite d'élasticité des scaffolds. Une légère augmentation du module d'Young des scaffolds a également été observée d'après les courbes obtenues à partir des mesures de déformation par corrélation d'images. Cependant, l'utilisation de la poudre fine a de nouveau induit une fragilisation des filaments constitutifs en raison d'un enrichissement en oxygène plus important au cours du procédé. Cette perte de ductilité a également été observée sur les scaffolds même si ces échantillons atteignaient quand même entre 5 et 10 % de déformation. Globalement, les scaffolds développés dans le cadre de cette étude présentent des limites d'élasticité supérieures à celles de l'os (sauf pour les échantillons frittés à 1000 °C) et des modules de Young suffisamment proches de celui de l'os pour éviter l'arrêt du renouvellement osseux.

D'un point de vue propriétés biologiques, les seules conclusions pouvant être donnée pour le moment sont que les cellules MG-63 sont capables de se développer sur les scaffolds, et qu'elles peuvent effectivement se fixer à l'intérieur des pores laissés par le frittage partiel. De plus, la rugosité des scaffolds permet une meilleure adhérence des cellules, qui peut être visualisée par un étalement plus important de ces dernières que sur les témoins lisses.

Un dernier point intéressant à noter concernant les structures qui peuvent être obtenues est la possibilité d'élaborer des échantillons présentant un gradient de porosité intra-filamentaire, en utilisant différentes tailles de poudre au sein d'un même échantillon. Dans cette étude, des échantillons contenant trois encres différentes (formulées à partir de différents lots de poudre) ont été imprimés pour illustrer cette possibilité. Les échantillons résultants, contenant un gradient échelonné, ont leur comportement régi par les caractéristiques les plus faibles de chacune des couches, comme mis en évidence par les essais de compression.

Robocasting de magnésium

Elaboration des structures

En raison de sa réactivité, le magnésium ne peut pas être imprimé à l'aide de liants aqueux. Cependant, des structures satisfaisantes ont été obtenues en utilisant des liants à base d'éthanol contenant 13 à 17 wt% d'éthylcellulose et chargées de 56,5 à 60 vol% de poudre de magnésium. Ce taux de chargement élevé est comparable ou supérieur aux taux retrouvés dans les matières premières classiques pour le moulage par injection de métaux ou procédés équivalents.

Les structures ont été imprimées à une température de 35 °C pour accélérer le séchage de l'éthanol, ce qui a permis d'aider le maintien de la forme, en amorçant la transition du comportement rhéologique de l'encre, d'un comportement rhéofluidifiant vers un comportement rhéoépaississant. Ces encres fortement chargées se sont avérées extrudables jusqu'à une taille de buse de 400 µm. Il convient toutefois de noter que ce paramètre dépend de la force que la machine peut appliquer sur le piston et peut donc varier d'un robocaster à l'autre. En suivant le même raisonnement que pour le TA6V, l'encre imprimable contenant la plus faible teneur en polymère avec la charge de magnésium la plus élevée a été conservée pour les étapes suivantes.

Déliantage

L'analyse thermogravimétrique effectuée sur le liant contenant 17 wt% d'éthylcellullose met en évidence que la dégradation principale de l'éthylcellulose se produit entre 260 et 330 °C. Toutefois, à 330 °C, la dégradation n'est pas complètement achevée et une perte de masse continue d'être observée jusqu'à 500 °C. Cependant, le magnésium ne peut pas être traité sous vide dynamique à 500 °C car il se vaporise. Une température de déliantage intermédiaire de 400 °C a donc été choisie, mais avec un temps de maintien de 2 h pour être sûr d'atteindre la dégradation complète de l'éthylcellulose. Le traitement a été effectué sous vide dynamique primaire. Le succès de ce traitement de déliantage a pu être mis en évidence par MEB et DRX : le liant avait bien été éliminé sans induire de changements ni structuraux, ni microstructuraux.

Frittage

L'étape de frittage a finalement été la plus compliquée à réaliser. En raison de la volatilité du magnésium, il n'était pas concevable de réaliser ce traitement sous vide dynamique secondaire. De plus, le magnésium est un métal extrêmement réducteur qui forme donc facilement une couche d'oxyde très stable à sa surface et réagit également facilement avec tout matériau contenant de l'oxygène. Mais comme la diffusion du magnésium dans son propre oxyde est extrêmement faible, cette couche de MgO formée à la surface des particules tend à empêcher le frittage.

La première solution trouvée pour surmonter ces difficultés a été d'obtenir le frittage par des phénomènes d'évaporation-condensation, en essayant de maintenir la vapeur de magnésium émise par l'échantillon confinée au plus proche de celui-ci. Pour ce faire, l'échantillon a été complètement immergé dans de la poudre de fer pur, et le creuset contenant à la fois l'échantillon et la poudre de fer a été encapsulé sous vide secondaire. Un traitement de 2 h à 600 °C dans ces conditions a conduit à l'obtention d'un frittage partiel avec environ 28 - 30 % de porosité résiduelle.

Cependant, comme il n'était pas si simple de sceller les tubes de quartz pour encapsuler les échantillons sous vide et que cette méthode limitait la taille des échantillons frittables, d'autres alternatives ont été explorées pour fritter les scaffolds obtenus par robocasting. Un premier essai de frittage en phase liquide a été réalisé, mais sans être concluant. Des caractérisations supplémentaires sont encore nécessaires pour comprendre la raison de cet échec. En revanche, un essai de frittage au SPS réalisé en limitant la charge vue par l'échantillon s'est révélé prometteur et s'avère donc être une piste à explorer.

Contents

General introduction

Rapid growth and ageing of the population induce an increasing demand for bone implants. The high toughness of metals makes them excellent candidates for load-bearing applications [KRI 07], and they have been commonly used in orthopaedic surgery for more than one century [CHE 15]. Among metallic materials routinely used in orthopaedic implants (stainless steels, cobalt-based alloys and titanium based alloys), titanium alloys present the best strength-to-weight ratio and the most suitable mechanical properties. However, it is still needed to reduce the stiffness of titanium based implants and enhance their biological fixation. Indeed, stiffness mismatch between an implant and surrounding bone tissue leads to stress-shielding phenomenon [GUI 05, GLA 06], that may limit osseointegration and may increase relative micro-motions risks (between the implant and the hosting bone tissue). These two phenomena are known to result in aseptic loosening of the implant, which is the most common cause of arthroplasty [1] failures. [GUI 05].

To address these issues, different approaches are possible. Many studies aim at enhancing cell adhesion by modifying implant surfaces in terms of roughness, using sand blasting [GUI 04, ANS 06], machining [XAV 03, LÜT 05] or chemical etching methods [ANS 06, SAN 07], but also with anodisation [ZHA 06, DAS 07] or ion implantation [NAY 05, KRU 07]. Going further in this direction of improving osseointegration, plenty of works have been realised on coating the titanium surface with a bioactive material, such as hydroxyapatite [COO 88, GAR 06, KUR 12], bioactive glasses [GAR 06, PED 08], calcium silicates [LIU 02, BIA 19], titanium nitride [PIS 04] or collagen [RAM 06]. Parts coated with hydroxyapatite by plasma spray are besides commonly used and provide positive results.

In parallel, one of the trends to reduce titanium implants stiffness is to develop metastable β titanium alloys [MAR 06, LAH 10]. However, another leading trend that targets both stiffness decrease and osseointegration improvement consists in developing porous titanium implants with interconnected pores that promote cell invasion, bone formation and vascularisation.

Among the techniques that enable to achieve this type of structure, additive manu-

1. The orthopaedic surgery procedure during which the articular surface of a musculoskeletal joint is replaced by an implant.

facturing (AM) is particularly on the rise, as it also gives access to the production of patient-specific implants. Such implants offer a better fit of the patient anatomy, leading to improved patient outcomes. By making the surgeon's task easier, they also reduce the operating time. Interest for these technologies is reflected by the U.S. healthcare AM market growth presenting on Fig. 1 (a). The global healthcare AM market was estimated at 803.8 million Euros (USD 951.2 million) in 2018 and a compound annual growth rate of 20.8 % is projected for the coming years according to market analysis report from Grand View Research [RES 19a]. Note that this market does not only include patient-specific implants as those presented on Fig. 1 (b), but also anatomic models and surgical guides [BAL 20].

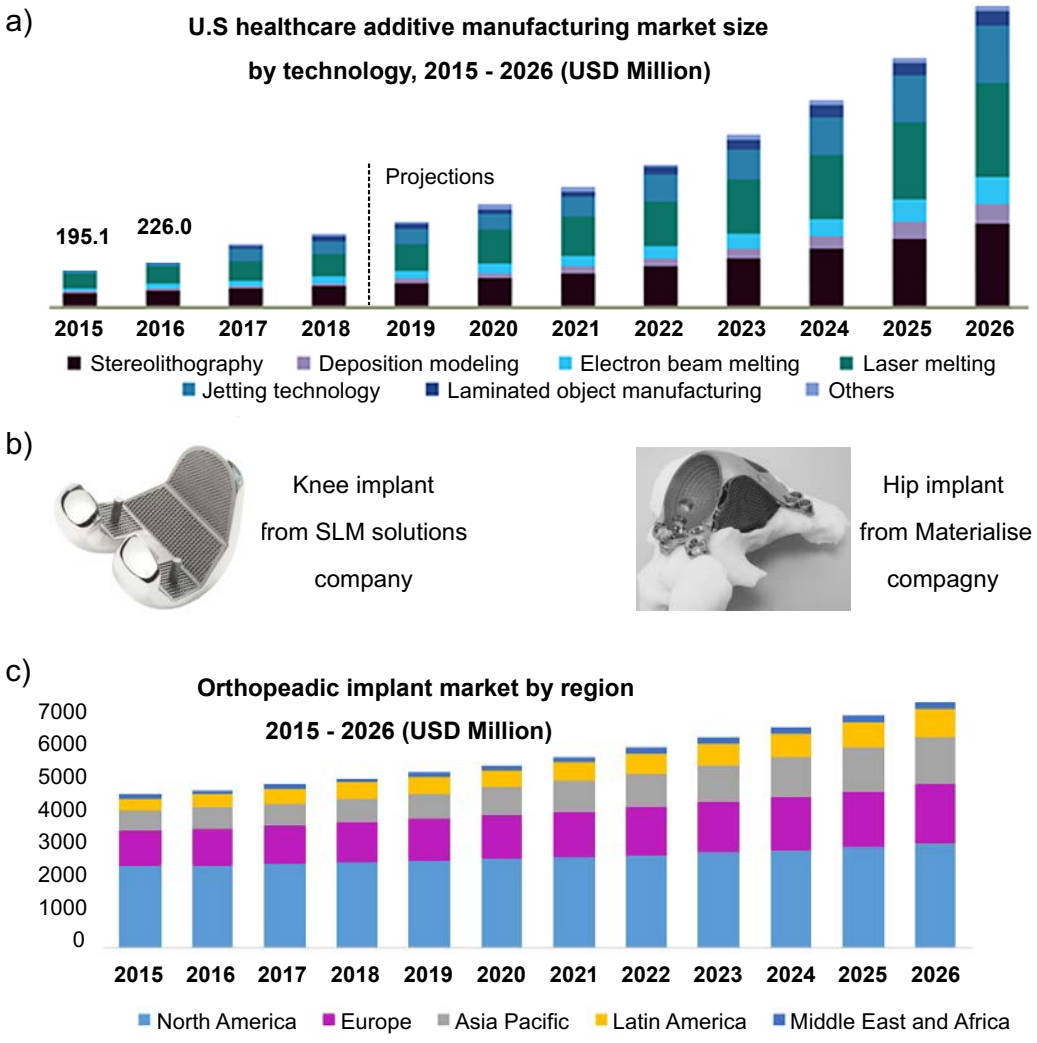

Figure 1: Implant market: (a) U.S. healthcare additive manufacturing market size evolution according to Grand View Research report [RES 19a]; (b) Examples of additive manufactured implants; (c) Orthopeadic implant market by region according to Polaris market research report [RES 19b].

However, as shown by Fig. 1 (c), access to orthopaedic implants is not yet so widespread and the transfer to AM technologies is only likely to amplify this phenomenon. Indeed, for hip arthroplasty, a difference of 2,000 to 3,000 Euros is generally noted between 3D printed custom porous three flanged acetabular implants and classical acetabular implants [TAC 17]. In addition, metallic AM techniques sufficiently developed to be used for implant production rely on expensive and technical equipments that involve large energy consumption (laser, electron beam).

Alternative, simpler and cheaper processes would therefore be welcome to increase the worldwide accessibility of these types of implants. A great versatility is also to be favoured to allow the manufacturing of a large variety of implants by the same machine. Indeed, for temporary reconstruction aid devices, resorbable materials should be preferred to avoid the need for a second operation. In addition, more generally beyond orthopaedics, different materials may be required depending on the location and function of the implant.

By offering the possibility to print each class of material at room temperature, the robocasting process seems promising to reach these requirements [LEW 06a, LEW 06b, SMA 08, COM 14, YET 17, SKY 19]. This process consists in a layer-wise extrusion of a paste, called ink, through a syringe mounted on a robotic arm. In the case of ink containing ceramic or metallic particles, a debinding step is necessary to remove the binder allowing the transport of particles through the nozzle. Then, the parts final properties are reached after a sintering treatment.

Beyond the economic aspect, this process based on a structure obtained by sintering, can also be a way to enhance osseointegration by keeping a microporous network through partial sintering. Indeed, parts obtained by powder bed fusion (PBF) processes can present an interconnected porosity network with a pore size usually above 300 µm [PAR 10, DEW 16, ELD 17, ZAH 18], which is wide enough to allow vascularisation [KAR 05]. But while vascularisation through macropores is actually needed for bone formation and long-term stability, as it ensures the supply of nutrients to the cells (and their oxygenation), numerous studies suggest that micropores (smaller than 100 µm) can also improve bone ingrowth [LAN 10, POL 13]. O'Brien *et al* showed a linear relationship between specific surface area and cell attachment [O'B 05]. This is in agreement with the increased bone volume fraction that has been observed in the presence of micropores [HIN 05, CHA 12]. Bohner *et al* also concluded that mineralised tissue formation requires interconnected micropores with a mean size larger than 1 µm [BOH 17]. Thus, designing parts with both macro- and micro-porosity networks seems of interest.

Robocasting process seems promising to easily build this type of structure as macropores can be designed during the ink deposition, while the microporous network might be obtained through a partial sintering. However, this process is still in its early stage of development meaning that studies are still needed to fully assess the potential and limitations of the technique. Indeed, to produce patient-specific implants, a proper control of the dimensions as well as of the properties (mechanical and biological) is necessary. This

therefore raises a number of questions which it would be essential to be able to answer for each material under consideration:

— How well the ink deposit complies with the computer-aided design (CAD) requested?
— What is the dimensional relationship between the CAD and the sintered part depending on the level of porosity kept in the filaments and the shrinkage behaviour?
— Which combination of design and porosity level leads to the best properties compromise?

And for some more critical materials, the first question that needs to be addressed first may even be: Is the robocasting process compatible with the manufacturing of this material? This thesis work therefore aims to assess what can be achieved by using robocasting to design parts in Ti-6Al-4V alloy, which is an alloy routinely used in orthopaedic surgery. In addition, as magnesium presents the advantage of being resorbable in the human body, a part of this work is dedicated to the study of the suitability of this process for magnesium-based materials.

To do so, this work has been divided as follows:

The first chapter presents a brief literature review of metal additive manufacturing, with a particular focus on robocasting process. The properties that inks must exhibit to be robocasted and the different strategies adopted to successfully print structures are discussed.

The chapter 2 focuses on the Ti-6Al-4V structures that can be printed. First of all, a study on the formulation of the ink and its consequences on CAD compliance is carried out. Then the influence of debinding conditions is evaluated in terms of both final chemical composition and microstructure obtained. Finally, the influences of sintering temperature and powder size on the final structure are quantified in terms of remaining porosity, shrinkage, roughness and microstructure.

The third chapter aims at characterising the functional properties of these Ti-6Al-4V structures. Their mechanical strength is evaluated at two different levels: the intrinsic material properties are obtained through three points bending tests on filaments and microhardness measurements whereas the scaffold structures are tested under compression. A preliminary biological characterisation is also presented in this chapter to highlight the influence of microporosity on cell behaviour.

Tests concerning the transfer of the results obtained on Ti-6Al-4V to the manufacturing of magnesium parts are finally presented in chapter 4. This chapter includes the

ink formulation that has to be adapted to magnesium reactivity, the debinding step and various trials of sintering treatments.

Finally, this manuscript ends with a conclusion that recalls the main results obtained in this study, discusses the strengths and limitations of the process, and brings some perspectives on the further characterisations needed on Ti-6Al-4V structures, as well as on the various approaches that should be explored in greater depth in order to achieve the manufacturing of resorbable metallic parts by robocasting.

Chapter 1

Metal additive manufacturing: towards parts architectured at different scales

Additive manufacturing (AM) is gathering all the technologies that enable to build structure by joining materials according to 3D model data generated by a design software (ASTM F2792-12a and [GIB 10]). It gives thus the opportunity to build geometries that are not accessible by subtractive fabrication techniques. Initially developed for simple prototyping, it is now shifted to actual production [HIR 17]. This is driven by the fact that optimised geometries can be produced by adding material only where it is needed, resulting in light structures. The growing interest in these technologies has given rise to more than 50 AM techniques [G.R 20]. Some of them have already led to the creation of innovative products, such as personalised implants [SIN 16, POP 16], more efficient and conformal cooling systems [ARM 14, ZHA 15], or lightweight and cost-saving components for the aerospace [JOS 15, NAJ 19]. But a number of techniques still require fundamental understanding, and further developments are still needed to achieve more advanced applications.

Although the most widespread techniques concern the additive manufacturing of polymers, metals remain indispensable for certain applications such as structural support, electrical conductivity, heat dissipation or load-bearing implants (to be more specific to our field). Thus, without being exhaustive, the following section attempts to give an overview of the metal additive manufacturing (MAM), keeping bone implants as an application goal.

Contents

1.1 Brief overview of metal additive manufacturing

Among MAM techniques, the most established methods are electron beam and laser beam powder bed fusion (EB-PBF and LB-PBF respectively) [HIR 17]. These two techniques are based on the fusion-solidification phenomenon, so an initial focus is placed on the melting processes.

1.1.1 Additive manufacturing *via* powder melting

AM processes relying on powder melting can be divided into two categories: direct deposition methods and powder-bed based methods (see Fig. 1.1).

In called Direct Energy Deposition (DED), also referred to as Direct Metal Deposition when used for metals, a powder flow is brought where an addition of material is desired. Meanwhile, a melt pool is induced at the same place by a heating source (usually a laser). The added powder is thus absorbed in the melting pool to create the new layer (see Fig. 1.1 a)). This method can also be used with wire as a filler material, which is continuously fed to the melting pool [LEY 15]. The raw material can be added either laterally or coaxially. The later one is less cumbersome and therefore allows greater movement flexibility but it requires a more complex and expensive dispensing head.

This kind of process is widely used for cladding but parts repair with limited access and complete parts manufacturing are also emerging applications [SAB 19]. However, increasing print resolution is at the expense of powder yield: to reach a 30 µm beads width, less that 10 % of the feeding powder is actually absorbed in the melting pool [LEY 15]. In addition, complex structures can hardly be obtained with DED as there is no support to realise spanning structures. This is one of the reasons that led to a greater development of powder bed fusion technologies for parts manufacturing.

As shown on Fig. 1.1 b) PBF technologies, rely on an heating source that locally melts the powder spread on the building platform, to build a structure layer by layer [BHA 17].

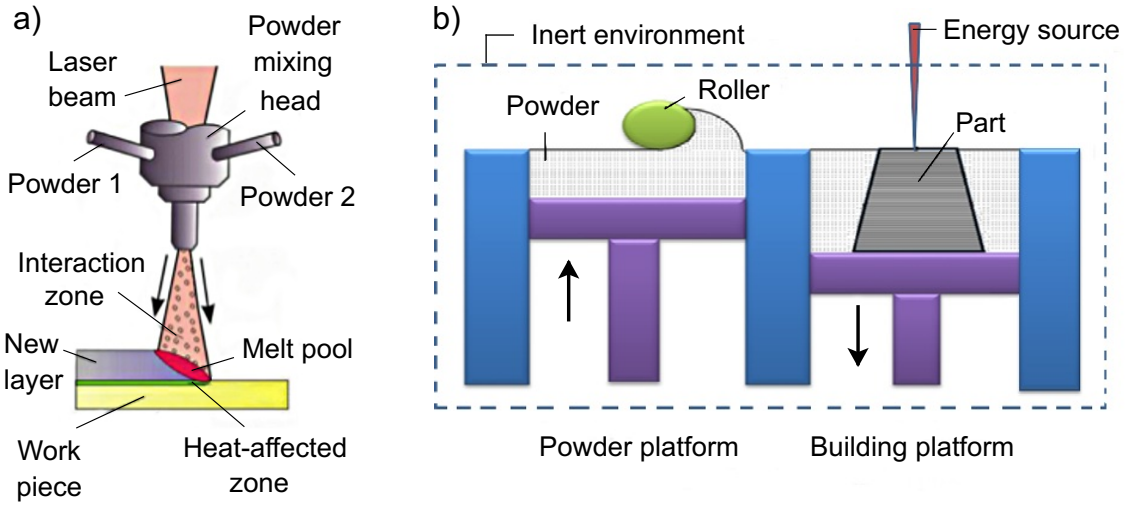

Figure 1.1: Schemes of AM melting processes: (a) Direct energy deposition adapted from [LEY 15], (b) Powder bed fusion adapted from [BHA 17]

Once the heating source has finished consolidating the current layer, a new layer of powder is spread over the previous one by the roller to be consolidated in turn. The whole system has to be held in an inert environment to prevent metal oxidation during the building process. Very complex shapes are reachable through this type of process as the unmelted powders from the powder bed can act as support for the structure being manufactured. However, unmelted powders can remain stuck on strut edges, leading to partial clogging of the drawn pores. This phenomenon can limit the minimum achievable pore size and requires finishing step, such as shot peening, chemical etching or even femtosecond laser postprocessing [MIN 13, DOL 19, PER 19, ATZ 20].

Parts obtained by PBF technologies can present an interconnected porosity network with a pore size usually above 300 µm [PAR 10, DEW 16, ELD 17, ZAH 18], which is wide enough to allow vascularisation [KAR 05]. But while vascularisation through macropores is actually needed for bone formation and long-term stability as it allows cells feeding, numerous studies suggest that micropores (smaller than 100 µm) can also improve bone ingrowth as shown in the introduction. This second microsized porosity network (in addition to the macropores) can hardly be obtained by PBF technologies [AND 17] but might be more easily achieved by AM techniques relying on powder sintering.

1.1.2 Additive manufacturing *via* powder sintering

Selective laser sintering (SLS) can be seen as an extension of the L-PBF process. Indeed the particles in the powder bed are sintered rather than melted by lowering the laser power [LIN 13]. This method enables to obtain pores of a few tens of microns [KRU 05, LIN 13]. With this process it can therefore be imagined to obtain macropores by design

and micropores by partial densification.

A less expensive alternative allowing to reach this bi-modal porosity and also based on the use of a powder bed is binder jetting. In this method, the laser is replaced by a printing head that selectively sprays a liquid binder onto the powder [BAI 15]. The system to supply the new powder between each layer remains the same, as well as the part complexity that can be reached. Once the printing step is completed, the remaining unbound powder on the platform has to be removed with compressed air [BAI 15]. Printed parts then undergoes debinding and sintering treatments to reach their final properties.

An other promising emerging approach consists in directly "write" a mixture containing both the powder of interest and the binder. This concept, known as direct-ink writing, has been developed through different methods. The process studied in this work being one of them, it was therefore chosen to dedicate a specific section to this global approach.

1.2 Direct-Ink writing

Direct-Ink Writing (DIW) consists in the deposition layer by layer through a computer-controlled nozzle, of an ink, to design materials with controlled architectures and composition. The ink can either be a fused filament, or a binder solution (loaded with particles or not). The first case, called fused deposition modeling (FDM), is presented on Fig. 1.2. The second case can be further divided into two categories: extrusion can take place either in the form of droplets (direct inkjet printing) or in the form of continuous filament (robocasting). They are respectively presented on Fig. 1.3 and Fig. 1.4.

FDM is probably the most popular additive manufacturing method as it is not only available for industrial but also for consumer market. This technique enables shaping of thermoplastic material. In this method, the extrusion head is controlled in temperature to extrude a thermoplastic filament in a semi-molten state. The initial filament (with constant diameter) is continuously fed into the heating head by two rollers, and thus acts as a plunger on the semi-molten materials. Extrusion head movements are controlled in X and Y direction according to the chosen CAD design. During the deposition, the polymer solidifies and thus keeps the desired shape. After the completion of each layer, either the platform is moved down or the head is lifted up before beginning the following layer. This new layer fuses with the previous one during deposition [ZEI 02].

This method is used to print polymers and polymers-based composites [ZEI 02, Gon 18] but also ceramic and metallic parts [Gon 18]. To do so, thermoplastic materials are highly-loaded with ceramic or metallic particles (between 45 and 65 vol% particles) before being extruded as filament. Various materials have already been used as filler particles for this process, including mullite, fused silica, titanium dioxide, wood, aluminium, copper and iron [ONA 01, MAS 05, LIU 19]. Then FDM is applied to these filaments by heating them above the melting temperature of the thermoplastic used as binder. As for Metal

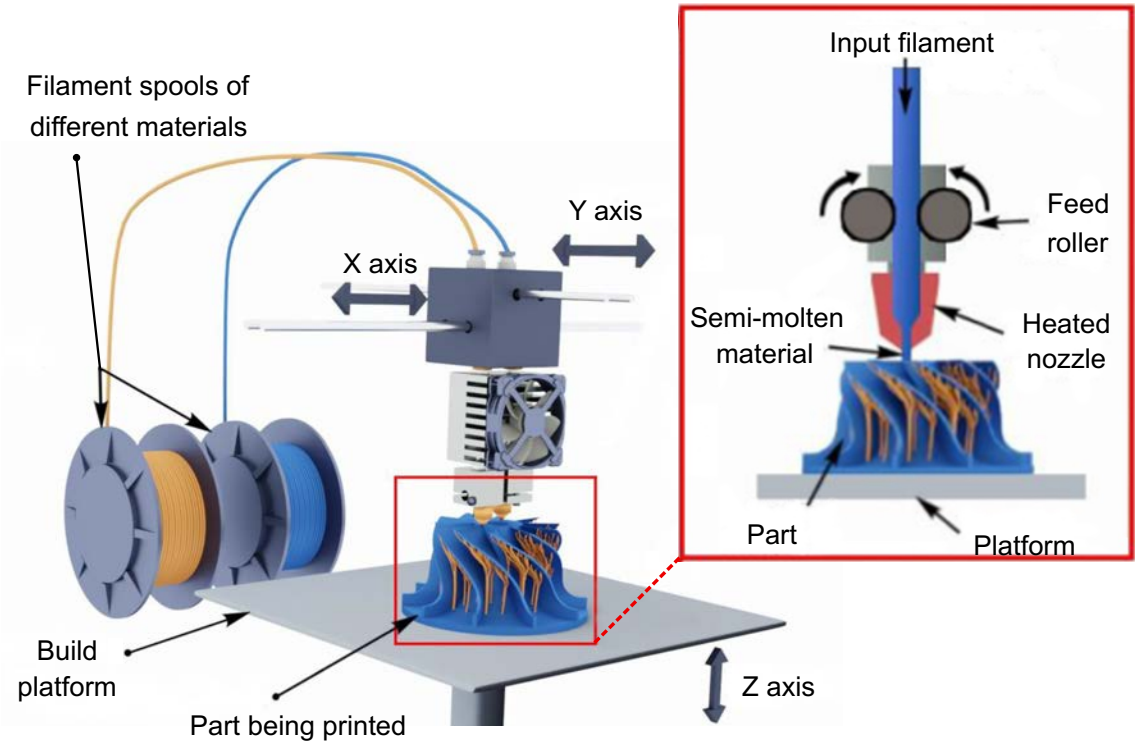

Figure 1.2: Scheme of the fused deposition modeling (FDM) process adapted from [ELK 20]

Injection Moulding and for all the DIW of particles loaded system, the as-printed parts then undergo debinding and sintering treatments to get rid of the thermoplastic and reach the desired mechanical properties.

It should be noted that filaments used in FDM should be rigid enough to act as a plunger to extrude the semi-molten material. But as some material cannot reach this requirement, the extrusion can also be performed using a worm screw, which is able to convey pellets to the melting zone. There, pellets are softened by both temperature and friction before being submitted to high pressure to be extruded through the nozzle.

Direct inkjet printing relies on Rayleigh instability for droplets generations (see Fig. 1.3). In 1878, Rayleigh found that a jet of inviscid fluid can be broken down into a stream of droplets by applying a pulse of pressure to the nozzle [RAY 78]. Nowadays this principle is used with two different approaches to engender droplets within a printing head: the continuous inkjet printing (CIJ) and the drop-on-demand inkjet printing (DOD). Both methods enable to generate droplets with diameters ranging from 10 µm to 150 µm but CIJ is usually used for larger drop diameters than DOD [DER 10].

For CIJ printing, a force is applied to the ink to induce the fragmentation of the stream into a continuous series of droplets of uniform size and spacing. To be able to direct

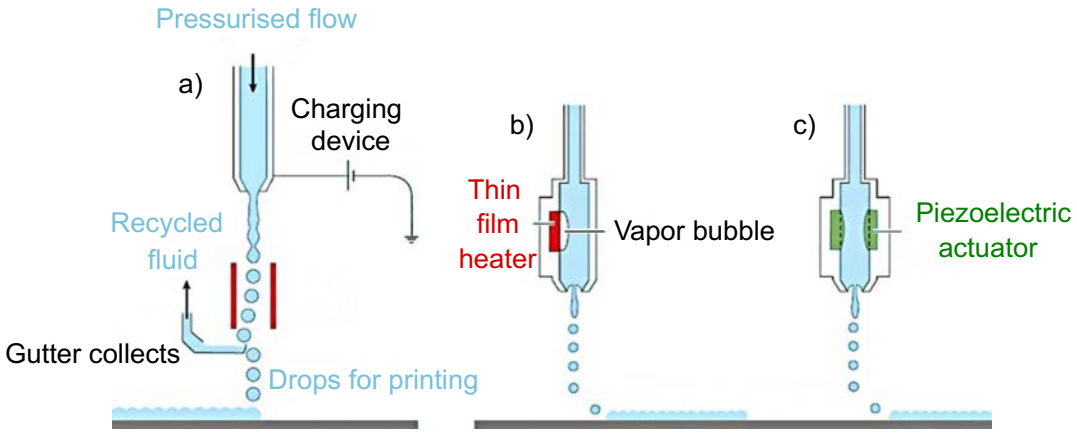

Figure 1.3: Scheme of the different inkjet printing processes adapted from [DER 10]: (a) Continuous Injekt Prinitng, (b) Thermal drop on demand printing, (c) Piezoelectric drop on demand printing

the drops, all of them are slightly charged during their formation thanks to a potential applied on the nozzle. Then a second potential is used to deflect the unwanted drops to a gutter as the created drops stream is continuous but sometimes no printing is required (see Fig. 1.3 (a)). In some cases, the ink collected in the gutter can be recycled but contamination can occurs [DER 10, CUM 12].

Thus DOD appears to be a waste free alternative to CIJ as they generate droplets only when required. In the resting state (without pressure), the ink is held in the needle by surface tension effect. To induce the pressure pulse that will generate the drop, two different techniques are commonly used. The first solution that has been used consists in locally heating the ink above its boiling temperature to create vapour bubble (see Fig. 1.3 (b)). Then the current that creates the temperature rise in the thin film heater (by Joule effect) is removed. The resulting decrease in temperature leads to bubble collapse. This bubble formation and collapse induces the pressure pulse needed to generate droplets. The second solution relies on the use of a piezoelectric transducer to generate the pressure pulse (see Fig. 1.3 (c)). Under the effect of voltage, the piezoelectric electrodes contract, compressing the ink chamber, resulting in the droplet formation. Only dilute polymeric solutions or suspensions containing a low concentration in nano-particles (usually around 10 - 15 vol% of sub-micronic particles) can be printed using all these direct inkjet methods [LEJ 09, DER 10].

To work with larger particles (from the micron to a few tens of microns) or higher solid contents, the ink can be extruded as a filament, using a plunger to generate continuous uni-axial pressure necessary for extrusion. This solution, called robocasting, relies on the rheological property of shear-thinning. To obtain a part by robocasting, the ink is poured in a syringe ended by a nozzle of the desired diameter (see Fig. 1.4). The syringe is fixed

on a robotic arm which can move in the three directions of space. Both robotic arm movements and plunger displacement are computer controlled, to extrude the ink only where and when it is necessary. Without plunger pressure, the ink does not flow through the nozzle. Depending on the robocaster used, the plunger can be either mechanical or pneumatic. Ink rheology enables shape retention but more generally the printing of self-supporting and spanning structures.

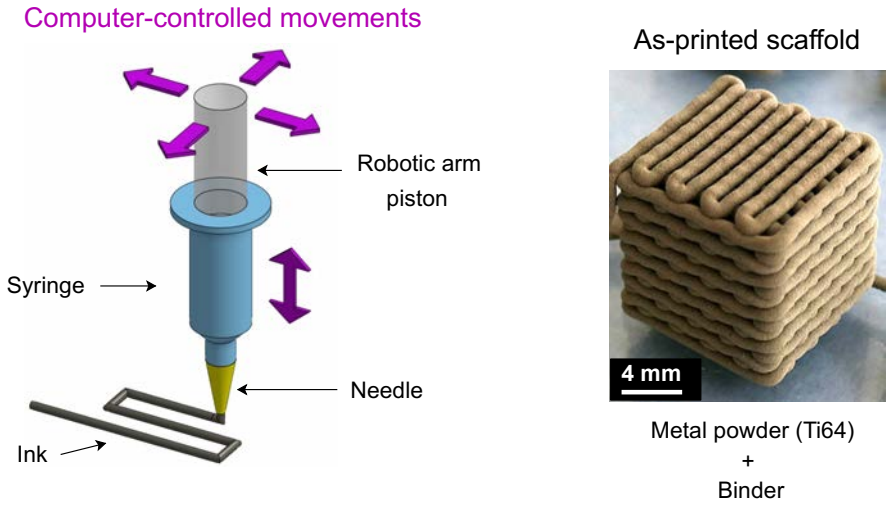

Figure 1.4: Scheme of the robocasting process with a printed scaffold structure

All these DIW techniques involve an ink flow through a nozzle, with an ink that must be able to retain its shape immediately after printing. To do so, the ink must display specific rheological properties. Due to their different extrusion method, the required rheological properties differ for each DIW process presented above. But as this PhD work focuses on robocasting, only the rheological requirements for this specific process are presented in the next section.

1.2.1 Rheological requirements for robocasting

Rheology is the study of the deformation and flow of matter under the effect of an applied stress. The way the ink reacts to the force exerted by the piston and its behaviour after stress release is crucial for the success of the shaping step of the robocasting process.

Dynamic viscosity, often simply referred to as *viscosity*, is a rheological property that describes the resistance of a fluid to irreversible changes in position [SCH 00]. To counteract this resistance, energy (in the form of pressure) must be continuously supplied to a fluid to maintain its flow. In general, the higher the viscosity of a fluid, the greater the pressure required to make it flow. Indeed, this property is defined as the ratio between

shear stress (τ, Pa) and shear rate ($\dot{\gamma}$, s^{-1}):

$$\mu = \frac{\tau}{\dot{\gamma}} \tag{1.1}$$

This term *dynamic viscosity* is only valid for homogeneous shear rates and in cases giving a viscosity independent of the shear rate. However, in other cases the equation 1.1 is still used but the obtained result is refereed to as *apparent viscosity* [SCH 00, RAT 13]. In addition, it should be kept in mind that this property also depends on the temperature. This dependence varies according to the nature of the fluid.

Fluids are usually classified depending on their shear stress / shear rate behaviour (see Fig.1.5). Fluids that present a linear relationship, like water, are called Newtonian. Their viscosity is thus independent of the shear rate gradient, meaning that the viscosity remains the same regardless of the applied shear rate. This kind of fluid is thus inappropriate for robocasting as, once extruded (i.e. at zero-shear) they will go on to flow.

Non-Newtonian fluids can be further divided depending on how their apparent viscosity change with the shear rate and whether they present a yield stress or not. For fluids like polymers in solutions or suspensions, which have interactions or connections between their different constituents (for example hydrogen bond), increasing the shear rate can destroy some of these interactions and thus decrease the viscosity. These fluids are shear-thinning fluids, also called pseudo-plastic fluids. In some rare cases, the inverse phenomenon can be observed (shear-thickening). For example in highly loaded suspensions, liquid phase is only present in void between particles and shearing can cause the particles to block against each other, resulting in an increase in viscosity [CES 97, FAL 08]. To describe these different types of fluids, rheological models have been proposed such as the models oh Bingham (equation 1.2), Ostwald (equation 1.3), or Herschel-Bulkley (equation 1.4) [RAT 13]:

$$\tau = \tau_y + K\dot{\gamma} \tag{1.2}$$

$$\tau = K\dot{\gamma}^n \tag{1.3}$$

$$\tau = \tau_y + K\dot{\gamma}^n \tag{1.4}$$

where n is the pseudoplasticity index ($0 < n < 1$ in shear-thinning fluids), K is the consistency index and τ_y is the yield stress, which can be defined as the stress to apply on the ink to make it flow from a static state.

Moreover, fluids behaviour can also be time-dependent. The best examples of this possible dependence are thixotropic fluids. When a constant stress (or a constant shear rate) is applied on a thixotropic fluid after a period of rest, a decrease in apparent viscosity is observed over time. The structure of the fluid is disorganised by shearing. Once the stress (or the shear rate) is removed, the internal structures of the fluid start to rebuild themselves, leading to a viscosity recovery [SCH 00]. The product can be partially (partial thixotropy) or fully restored to its original state after a fairly long rest. Thixotropy is often associated with rheofluidifying behaviour.

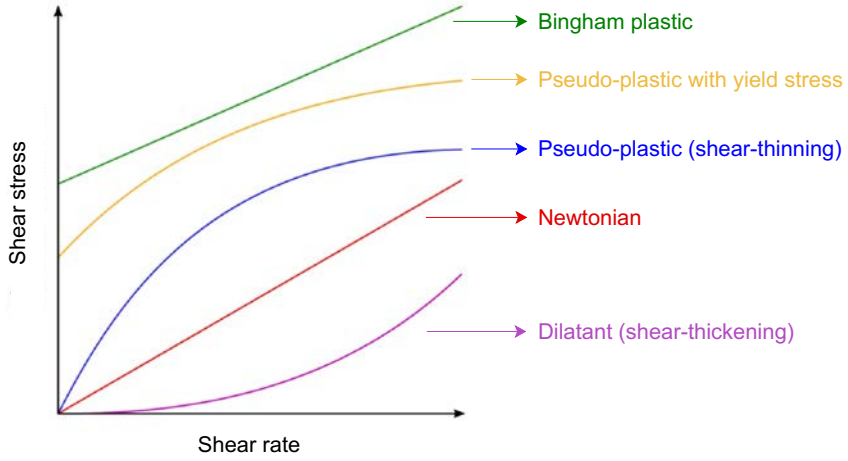

Figure 1.5: Main rheological behaviours presented through shear stress as function of shear rate (adapted from [ŠAF 19])

To be printable by robocasting, an ink must meet different criteria. First, to enable extrusion through a small nozzle under moderate pressure, an ink should present a shear-thinning behaviour. An ink with a yield stress is also preferable to prevent it from leaking when the syringe is held vertically but no printing is desired. Once extruded the ink must behave as a non-flowable structure to be able to keep the desired shape. This capacity to retain its shape can also be obtained thanks to the yield stress. And finally the printed ink must be stiff and strong enough to support the following layers without collapsing. Indeed, when a new layer is dispensed over the former one, the smearing may induced shear stress. This phenomenon added with the increasing weight caused by multilayering may engender enough stress to exceed the yield stress and thus induce flow in previously printed layers. To avoid this effect, two routes have mainly been explored.

The first one was proposed by Cesarano *et al.* with the beginnings of robocasting. They found that a pseudoplastic suspension can be transformed into a shear-thickening suspension by increasing the solid loading as explained earlier and shown on Fig 1.6 (a). Thus their strategy was to print pseudoplastic suspension with solid content just below the behaviour transformation and to dry the just printed ink so that it becomes dilatant, giving a locked structure (see Fig 1.6 (b)). With this strategy, a particular attention must be paid to the drying speed. Indeed if the drying is too slow, slumping may occur but a fast drying can induce cracking and delamination [CES 97, CES 98]. Also, it should be noted that the dilatant transition within loaded suspension can occur for various solid content depending on particles shape, size and size distribution.

The second approach was to used thixotropic gel-based ink. The interactions that held the material in its gel state are broken when the applied stress exceeds the yield point, allowing the ink to flow. But once the ink is printed, the fluid quickly returns to its gel

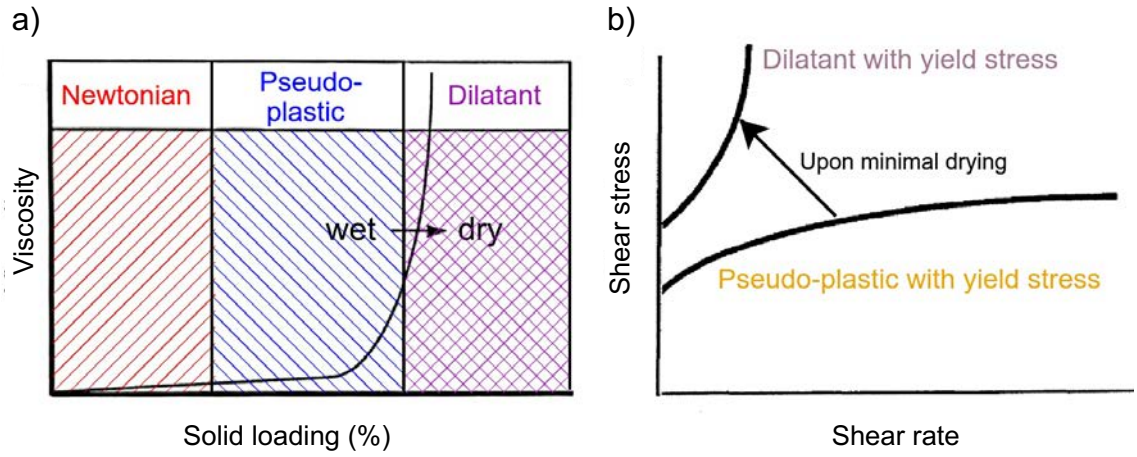

Figure 1.6: Rheology transition: (a) Evolution of an ink viscosity as a function of solid loading adapted from [CES 98], (b) Ink behaviour transition obtained trough drying (adapted from [CES 97])

state. This gives the ink the ability to maintain the required shape without the need for drying [SMA 02, LEW 06a]. This is probably due to the higher yield stress reached by this kind of ink. However, as shown by M'Barki *et al.*, the yield stress reached by such inks after extrusion (called dynamic yield stress) might differ from the stress needed to make them flow from a static state (called static yield stress). Thus it is important to make a clear distinction between them, and well characterise both of them, since they do not represent the same phenomenon. Indeed, the dynamic yield stress, which is the minimum stress required to maintain the flow, represents the limit below which an ink is capable of retaining its shape, whereas static yield stress is linked to its extrudability [M'B 17].

In addition, various parameters can be considered to define a printable domain and the notion of printability as such remains rather ill-defined. Initially, only the inks stiffnesses were considered as a criterion to define inks "printability" (usually a G' around 10000 Pa or above [FEI 17a]) and this printability was appreciated without being measured. Meaning that if an ink was extrudable and offered the possibility to stack layers and keep a shape visually similar to the CAD, the ink was considered as printable. And already a certain number of parameters (solid loadings, polymer content, dispersant content, printing temperature and so on) could play on this printability as shown on Fig. 1.7 (a).

However, two criteria have been recently introduced to approach a definition of printability. The dimensionless value Ξ was defined by M'Barki *et al.* as being:

$$\Xi = \frac{\sigma_{Dyn}}{\gamma R^{-1} + \rho g h} \tag{1.5}$$

where σ_{Dyn} is the dynamic yield stress of the ink, γ is the surface tension of the ink, R the nozzle diameter and $\rho g h$ the gravity effect for a part height h.

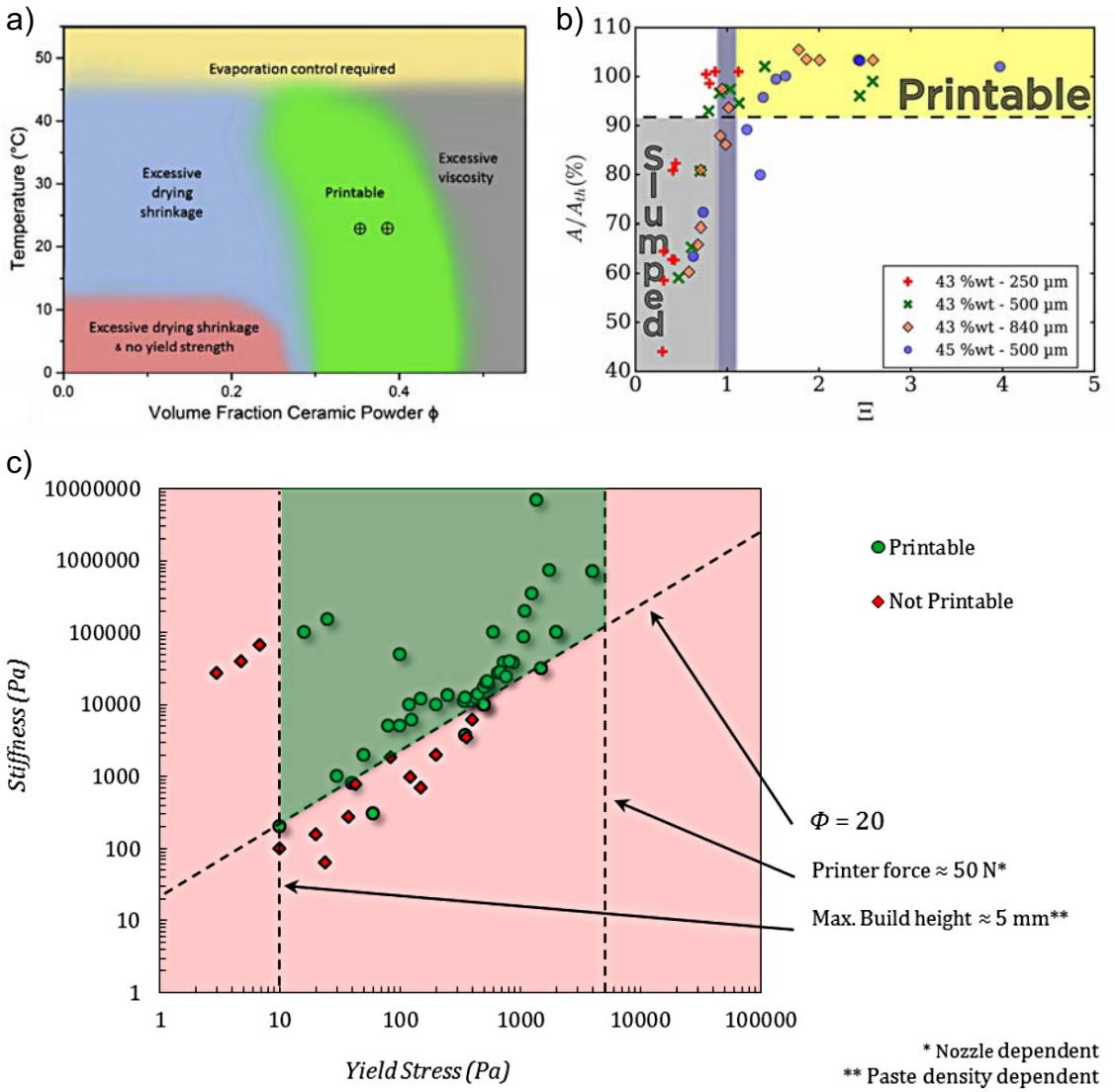

Figure 1.7: Printability: (a) Subjective evaluation of printability as a function of two printing parameters, temperature and the level of particles in the ink [FEI 16a], (b) Introduction of a printability criterion based on the compensation by the dynamic yield stress of the two cumulative phenomena gravity and capilarity. The printability verification is done by comparing the occupied area between the part and the CAD.[M'B 17], (c) Introduction of a printability criterion based on the ratio between the ink stiffness (G' at the plate) and its yield stress.

By considering that a dense structure is successfully printed when the area of one of its side represents at least 90 % of the area of the CAD design side, they found that Ξ should be equal or above 1 to reach printability. It means that the dynamic yield stress have to compensate both gravity a,d capillary forces. This has been verified on various bohemite suspensions printed through different nozzle sizes as shown on Fig. 1.7 (b).

Following the same idea of trying to find a criterion to define printability, Feilden

showed that having a ratio between stiffness and yield stress greater than 20 could be also considered as a printability criterion (see Fig. 1.7 (c)). However, a minimal dynamic yield stress is still required to be able to print part with a given height.

So as presented above, several ways exist to formulate a printable ink. And even though different binders can be considered, this is not the only parameter affecting printability. So in addition to giving an overview of the different binders commonly used in robocasting of particle-loaded inks, the next section also discuss the influence of parameters that are important to bear in mind when formulating such an ink.

1.2.2 Binders and ink formulation

For inks that do not rely on a gelling phenomenon, different lever arms can be considered to increase viscosity and yield stress. First, as slightly discussed with Fig. 1.6 (a), increasing solid loading enables to increase these two properties. Indeed, by reducing the space between particles, the increase in solid content results in more inter-particle interactions but also in more particle collisions. However, increasing solid loading may lead to irregular flow or even nozzle clogging due to flocculation [FEI 16a]. To avoid this effect, inks usually contain a small amount of dispersant (<1 vol.% as mentioned in Cesarano *et al.* study [CES 97]). Different molecules, anionic or cationic, can act as a dispersant and they have to be chosen according to the chemistry of the powder to be dispersed. But once the molecule to be used has been identified, its molecular weight can also be a way to play on both yield stress value and viscosity; the longer the polymer chain, the more entanglement there is [COS 16]. But also a longer chain is more likely to create bridges between particles by being adsorbed on the surface of different particles [EQT 14]. In addition it should be noted that there is an optimum to be found for the amount of dispersant to be added. Going beyond the quantity that gives the best dispersion can decrease again the yield stress. Indeed, the adsorbed layer becomes denser and decreases the probability for one polymeric chain to be adsorbed by several particles.

Different suspensions were thus formulated using various dispersants (polyethlenimine (PEI), poly(methylvinyl ether) known as Easysperse, carboxymethyl cellulose...) [COS 16, EQT 13] but also based on different solvents (water, ethanol...) [CES 97, DEL 12] as it can influence particles interactions [DEL 12]. It should also be kept in mind that the maximal solid loading that can be incorporated in an ink is increasing with a decrease of the suspended particles aspect ratio [DEL 12]. In addition, an optimised particle size distribution, leading to higher packing density with smaller particles able to fit into the gaps left by larger ones, should enhance the reachable solid loadings.

The first gel-based inks were largely inspired by the inks described above. First a highly concentrated but stable dispersion is generated with the help of a dispersant. Then interactions between particles leading to a fluid to gel transition are generated by either inducing

a pH change to reach the point of zero-charge [SMA 02, LEW 06a], or by adding ions of opposite charge to that of the dispersant adsorbed on the particles surface [CON 08]. This type of gel is therefore obtained by adapting the surface chemistry of the particles which finally act as gelling agents. For example, in their study, Smay *et al.* dispersed lead zirconate titanate particles with preadsorbed poly(acrylic acid) on their surfaces (dispersant) in an aqueous solution of 0.5 wt% cellulose. Then they induced particle gelation by lowering the pH via HNO3 titration [SMA 02]. Following the same idea, Conrad *et al.* first induced cationic polyelectrolyte adsorption on the surface of their silica particles before adding an anionic polyelectrolyte to obtain a gel [CON 08].

Later, new gel-based inks allowing to avoid the manipulation of inter-particles forces were developed. This new approach relies on polymeric solutions exhibiting a reversible thermal gelation. The mixing step can thus be realised at a temperature authorising the solution to be liquid and then particles are encapsulated by polymer reorganisation in gel form. This method has first been set up using poly(ethylene oxide)-poly(propylene oxide)-poly(ethylene oxide) triblock co-polymer surfactant, named Pluronic F-127 [FRA 10]. This polymer has both hydrophilic and hydrophobic blocks, which give it the ability to organise itself in the form of micelles. A rise in temperature induces swelling of the micelles which therefore have a greater probability of coming into contact with each other. At the same time, the rise in temperature leads to desolvation which makes the hydroxyl groups more accessible. Thus a cross-linked network can be formed through hydrogen bonds and/or Van der Waals forces [LEN 87]. This mechanism is thus concentration and temperature dependant. As shown by Feilden *et al.*, a 25 wt% Pluronic F-127 solution presents a gelling transition between 15 ans 20 celsius [FEI 16a]. Even though other polymers probably present the same behaviour, the temperature range of pluronic F-127 solutions gelling transitions have placed it among the interesting avenues to study. This technique involves higher polymer content than inks previously described and thus requires a good control of the debinding step. But at the same time it enlarges the robocasting possibilities in term of chemical composition of particles to be printed [FRA 10].

1.2.3 Debinding and sintering

Regardless of the solution chosen to formulate the ink, the printed parts must then be dried, debinded and sintered to obtain their final properties. In the case of robocasting, theses steps are usually only performed using thermal treatments, that should be adapted to the binder and the powder used. For example the Pluronic F-127 is usually removed with temperatures around 500 - 600 °C [FRA 10, FU 11, FEI 16a, FEI 17b, PET 17]. The sintering temperature must then be chosen according to the temperature range in which sintering occurs for the considered material. Following the same reasoning, the sintering atmosphere has to be adapted to the material to sinter.

Sintering consists in the consolidation of a particle assembly. Since it relies on atom

diffusion through the boundaries of particles to create one solid piece, this mechanism is thermally activated. Atom diffusion can take different forms (vapor transport (evaporation/condensation), surface diffusion, lattice (volume) diffusion, grain boundary diffusion, and plastic flow (dislocations motion)), that are often classified in densifying and non-densifying mechanisms [KAN 04]. Indeed, when the moving atoms come from the volume, consolidation is accompanied by densification and the sintering process can then be divided into three stages as presented on Fig. 1.8.

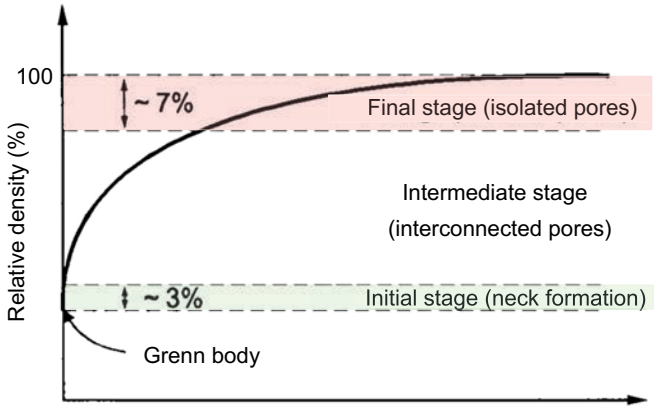

Figure 1.8: Stages of sintering densification according to [KAN 04].

If these steps seem less complex than the formulation of the binder, they must nevertheless be well controlled since they can cause cracking and they necessarily lead to shrinkage. This last one must be mastered in order to be able to control parts sizes. Considering the whole process and the versatility of ink formulation [1], it was foreseen that all sinterable materials can be printed by robocasting. Indeed, while robocasting was initially developed for ceramic printing, a transfer to metals began to emerge.

1.3 Robocasting applied to metals

Robocasting of metallic parts might be interesting for some applications such as load bearing implants or electronic devices. Hence, there is an increasing number of studies in this field involving various metals such as 100C6 [YET 17], silver [ZHO 17], copper [PIN 20] or Ti-6Al-4V [LI 06, ELS 19, ELS 20]. Different binders have already been successfully used to print metals [LI 06, YET 17, ELS 19]. These inks are usually based on high polymer content binders that give the desired properties to the ink rather than inter-particle forces. Indeed, in their study, Yetna N'Jock *et al.* dispersed their steel powder in 30 wt% Pluronic F-127 solutions [YET 17]. In addition, a 28 wt% polymeric aqueous solution of polyethylene glycol plus polyvinyl alcohol was used by Elsayed *et al.*

1. Ink formulation versatility can even be further improved with tricks such as printing in an oil bath, use heated syringe, use UV-light sources to cure polymers [G.R 20]

to print Ti6Al4V part [ELS 19]. Two points that differ from the ceramic process are worth noting regarding these metallic inks. First, metallic particles used are often gas atomised [LI 06, YET 17, ELS 19], meaning that there are round-shaped. This enables a higher packing density than for ceramic, meaning that higher solid loading can be reached. The second interesting point is that the use of dispersant does not seem to be mentioned, whereas for ceramics it could be useful even in the case of gel-based inks [FEI 16a]. As metallic particles are often larger than ceramic ones (a few microns diameter as compared to submicronic or even nanometric size), they present much less interparticle interactions and are therefore less prone to floculate even without dispersant.

In contrast to printed ceramic parts, the debinding step cannot take place in air as it would induce metal oxidation. Despite the inert environment, successful debinding are obtained with a temperature of 500 celsius [LI 05, LI 06, YET 17, ELS 19, ELS 20]. However, for metals with a high affinity to the interstitial elements contained in the binder (C, O), carbide formation were recently observed [ELS 19, ELS 20]. Studies are therefore still needed to find a way to limit the formation of these phases when they are not desired. In addition special care has to be taken to limit the formation of an oxide layer on metallic particles during sintering as it can limit sinterability. Thus sintering is usually performed under high vacuum [LI 05, LI 06, YET 17, ELS 19, ELS 20]. However, an other approach consisting in printing oxide particles which are then sintered in a reductive atmosphere to be converted in their metallic form, has been successfully applied to obtain copper parts [PIN 20], but also iron and nickel [TAY 17]. This method can nevertheless only be applied to oxides that are easy to reduce.

Thus for the transfer from ceramic to metal robocasting, both ink formulation and heat treatments require special attention. In addition, as already mentioned, this process is a cheaper and waste-free alternative to additive manufacturing melting processes to obtain porous parts that allow vascularisation and reduce sress shielding. As a result, titanium robocasting for medical applications is receiving increasing interest: Li *et al* manufactured titanium porous scaffolds that exhibit interesting cells activity [LI 05, LI 06]. In 2019, Chen *et al* developped a promising biocompatible polymer that could be used as binder to obtain Ti6Al4V parts [CHE 19]. Meanwhile, Elsayed *et al* [ELS 19, ELS 20] used DIW to print titanium scaffolds of different strut diameters, with struts as dense as possible. These studies highlight the benefit of using DIW to produce load-bearing implants with relevant biological properties. However, we also mentioned that robocasting can easily enable to obtain multi-scale porosity architectures, which can be of particular interest for biomedical applications. But characterisations of these possible hybrid pore size distributions and of their resulting biological and mechanical properties have not been performed yet. Besides, there are still a large number of parameters to be studied which may have consequences on the final properties of Ti6Al4V robocasted parts (such as debinding and sintering parameters or initial powder characteristics).

In addition to this first observation, it should be noted that titanium alloys are not the only ones to attract attention in the medical field. Indeed, magnesium alloys are at the origin of a large number of studies, as they present the advantage of being resorbable in the human body [STA 06, ZEN 08, LI 13, CHE 14, LI 16]. It would therefore also be interesting to check whether a process such as robocasting could be extended to this type of alloy. Indeed, this could be an interesting way to shape magnesium alloys parts without taking any risk with magnesium exposure to high energy beams.

Chapter 2

Designing Ti-6Al-4V architectured porous structures by robocasting: a structural study

The literature review presented in chapter 1 showed that robocasting might be a simple way to obtain architectures with different porosity scales, which are of interest for tissue engineering. This kind of structure should enable both a reduction in the Young's modulus of metallic implants and a better cell invasion. As Ti-6Al-4V (Ti64) alloy is already routinely used in orthopaedic surgery, this chapter focuses on cellular structures, named scaffolds, that can be obtained by robocasting of Ti64.

First, different water-based Ti64 inks were formulated to optimise the shaping step of the robocasting process. The quality of shapes obtained was correlated to the rheological properties of the inks. Then, the influence of powder size, debinding and sintering conditions has been evaluated in terms of resulting structures (and microstructures). To do so, scaffolds were characterised after each processing step. Finally, the influence of the initial powder size was used to produce structures with graded intra-filament porosity.

Contents

2.1 Background

Ti6Al4V, also known as Grade 5 or Ti64, is the flagship alloy of the titanium industry. This titanium alloy is the most commonly used and accounts for 50% of the world's titanium use. Its success is due to the interesting balance of its mechanical properties. Indeed, this alloy is highly resistant to corrosion and presents a high specific strength (200 - 210 $MPa \cdot g \cdot cm^{-3}$). These properties bring many performance benefits to the transport sector, as evidenced by its use in the aerospace industry [LEY 03]. In addition, Ti64 alloy is biocompatible and present a rather low Young's modulus (110 GPa) as compared to other metals routinely used in orthopaedic implants (stainless steels, cobalt-based alloys), which slightly reduces the stress-shielding phenomenon [1]. This has considerably increased the use of this alloy in the biomedical field over the past two decades [CHE 15]. However, as previously mentioned, Ti64 stiffness still needs to be reduced for bone implant applications [GUI 05]. In this context, additive manufacturing (AM) techniques may enable to achieve several goals including this stiffness reduction, but also patient-specific production and cell adhesion improvement.

The different AM technologies that can be used to produce Ti64 parts give rise to parts with a wide variety of thermal histories. But as Ti64 alloy presents an allotropic transformation, a wide range of microstructures might thus be obtained and influence the final mechanical properties of the parts. Thus the next section is dedicated to Ti64 microstructures and their consequences on mechanical properties.

1. Stress-shielding refers to the reduction in bone density as a result of decreased physiologic loading of bone due to the presence of an implant stiffer than bone. Bones are continuously remodelling themselves in response to the load to which they are subjected. If this load decreases, they stop remodelling.

2.1.1 Ti64 microstructure

The ASTM F1108 standard for Ti64 alloy castings for surgical implants requires the chemical composition given in Table 2.1. An "Extra Low Interstitial" (ELI) version of this alloy, containing reduced amount of carbon, oxygen, nitrogen but also substitutional iron is known to exhibit improved ductility and fracture toughness [WEL 93]. This ELI grade is also used in biomedical the field and its composition has to follow the ASTM F136 standard given in Table 2.1.

Table 2.1: Chemical composition of Ti64 and Ti64 ELI required by ASTM F1108 and ASTM F136 respectively

Element	H	C	N	O	Fe	Al	V	Ti
Ti64 (wt%)	<0.01	≤0.1	<0.05	≤0.2	≤0.3	5.5 - 6.75	3.5 - 4.5	Bal.
Ti64 ELI (wt%)	<0.01	≤0.08	<0.05	≤0.13	≤0.25	5.5 - 6.5	3.5 - 4.5	Bal.

Alloying elements can act as phase stabilisers. Indeed, in pure titanium, the allotropic transformation from the hexagonal closed pack (hcp) structure (α phase) to the high temperature body-centred cubic (bcc) phase (β phase), named β transus, occurs around 882 °C (see Fig. 2.1 (a)). However, some elements (such as aluminium, oxygen or carbon) can increase the temperature of the β transus and thus stabilise the α phase, whereas others decrease this β transus temperature (vanadium, tantalum, molybdenum...). In Ti64, aluminium is stabilising the α phase and vanadium is stabilising the β phase, resulting in an $\alpha + \beta$ duplex structure with a β transus around 980 °C.

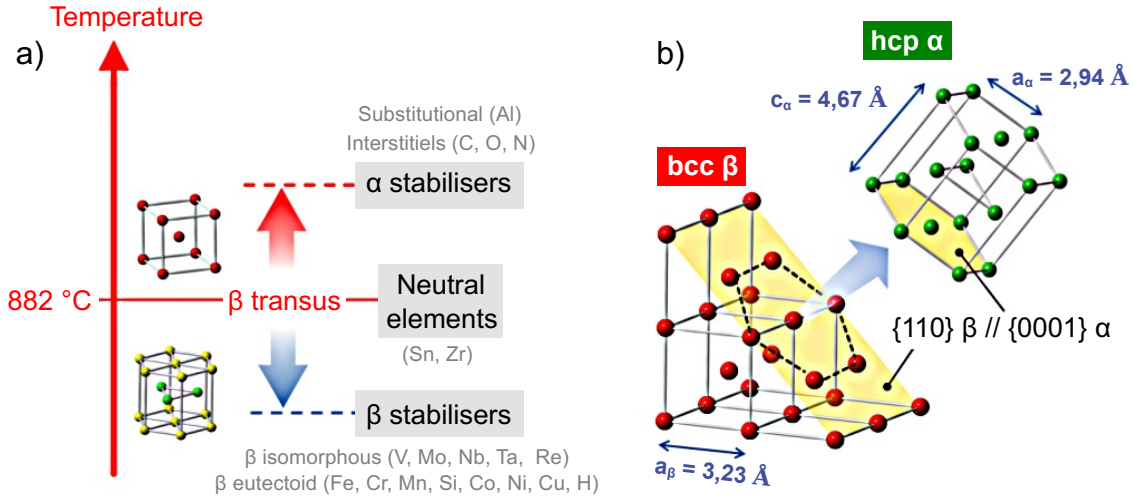

Figure 2.1: Titanium crystallographic structure adapted from [VIL 15]: (a) Allotropic titanium phases with associated influence of alloying elements, (b) Lattice relation between the hcp α phase and the bcc β structure. The lattice parameter given are those reported by Malinov *et al.* for Ti64 after furnace cooling from the β phase [MAL 02].

When cooling down from above the β transus, the β phase dense planes {110} become

the basal planes {0001} of the α phase as shown on Fig. 2.1 (b). This gives 12 possible transformation variants (12 possible orientation relationships between the two phases). Note that Ti64 lattice parameters given on Fig.2.1 (b) were measured after furnace cooling [MAL 02] and can vary with cooling rates [MAL 02] and with interstitials (C, O, N) insertion [MON 08].

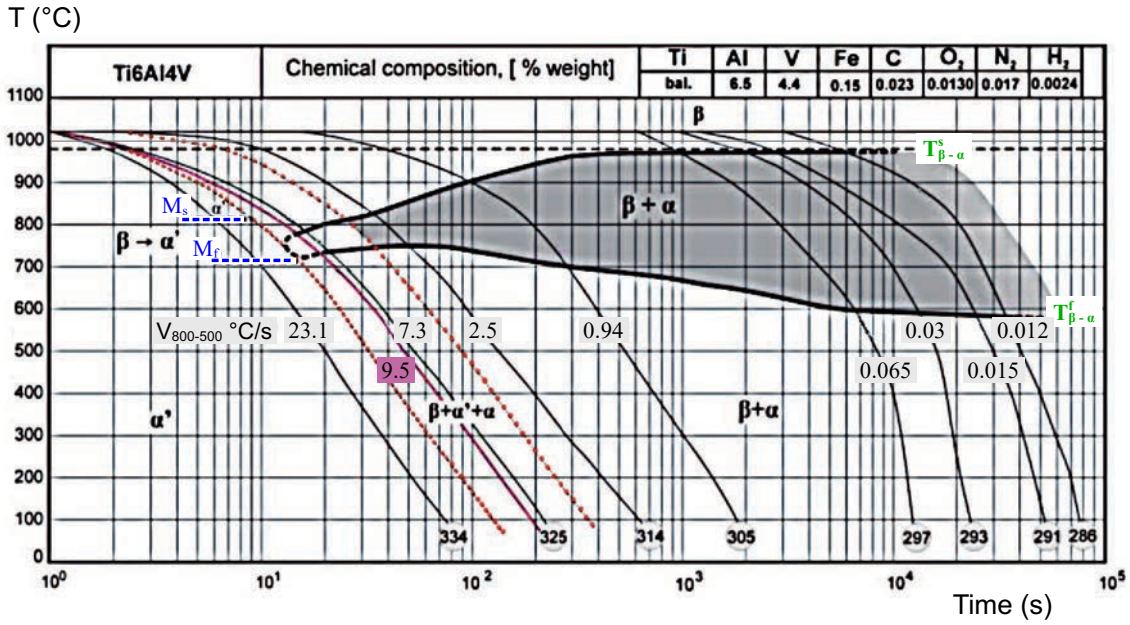

Figure 2.2: Continuous cooling transformation diagram for Ti64 cools down from 1020 °C [DĄB 11a].

In addition, similarly to steels, a high cooling rate can induce a martensitic-type displacive transformation, as it can be observed on the continuous cooling phase transformation diagram (Fig. 2.2). Depending on the cooling rate, samples can be fully martensitic (α') or have a microstructure combining martensite and $\alpha + \beta$ structure. In addition, among $\alpha + \beta$ samples, grain shapes and sizes strongly vary with the cooling rate used, from thin lamellar structures to equiaxed α grains (see Fig. 2.3 (a) to (e)). The higher the cooling rate, the finer the resulting microstructure. A third kind of microstructure can be obtained by performing a recrystallisation post-treatment below the β transus (see Fig. 2.3 (f)). The volume fraction of recrystallised equiaxed α grains in these bimodal samples relies on the time-temperature pair chosen for the recrystallisation treatment [LÜT 98].

In terms of mechanical properties, a thinner microstructure leads to an increase in hardness, yield stress and ultimate stress but it drastically decreases the ductility. Indeed, in their study, Galaraga *et al.* performed additional heat treatment to parts obtained by electron beam melting, in order to increase their ductility. They found a decrease of elongation at break from 12%, for a sample that undergoes a furnace cooling from 1100 °C after

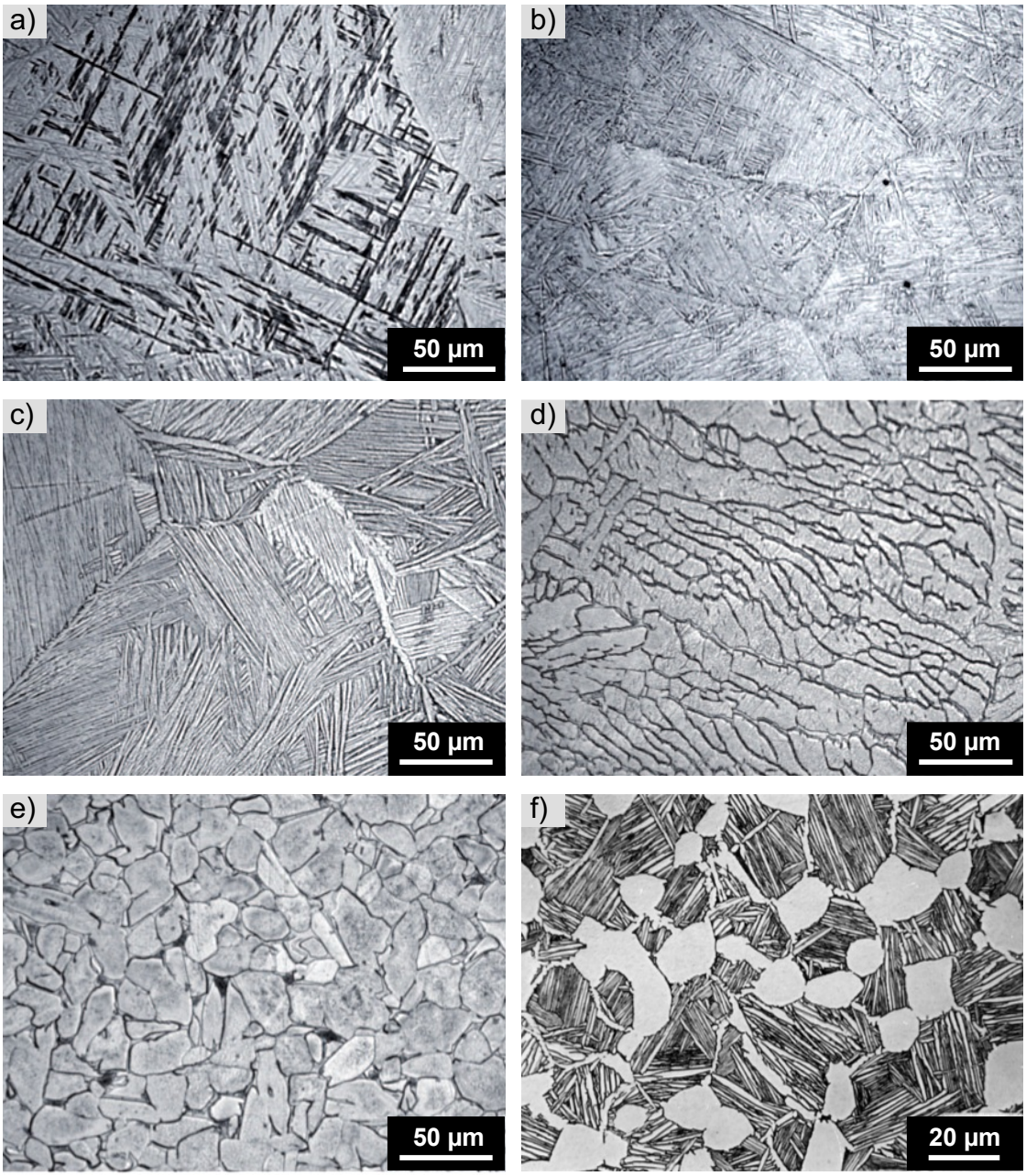

Figure 2.3: Optical micrographs of the Ti6Al4V alloy cooled from $1020\,^{\circ}\mathrm{C}$ by Dabrowski *et al.* [DĄB 11a] at: (a) $23.1\,^{\circ}\mathrm{C}{\cdot}\mathrm{s}^{-1}$,(b) $7.3\,^{\circ}\mathrm{C}{\cdot}\mathrm{s}^{-1}$,(c) $0.94\,^{\circ}\mathrm{C}{\cdot}\mathrm{s}^{-1}$, (d) $0.030\,^{\circ}\mathrm{C}{\cdot}\mathrm{s}^{-1}$, (e) $0.012\,^{\circ}\mathrm{C}{\cdot}\mathrm{s}^{-1}$ and recrystallised structure taken from Lütjering *et al.* work (f) [LÜT 98]

.

30 min of homogenisation, to 1.8% for a water-quenched sample [GAL 17]. In contrast, equiaxed structures often exhibit both high ductility and high fatigue strength [LEY 03]. Finally, bimodal structures usually present a well-balanced property profile by combining the advantages of lamellar structures with those of equiaxed structures, but they require

an additional thermal treatment [LÜT 98].

An advantage of DIW processes compared to powder bed fusion techniques is that the cooling rate after the sintering treatment can be adapted to the desired microstructure. But the structure needs first to be sintered.

2.1.2 Conventional sintering of Ti64

As titanium is a metal easily subject to oxidation, it and its alloys must be sintered in an oxygen-poor atmosphere [QIA 15]. Although argon is widely used for practical reasons, vacuum sintering is to be preferred since it allows the removal of volatile pollutants (H, Mg...). Indeed, it has been reported than hydrogen can be removed above 600 °C under vacuum [QIA 10], which might be interesting as hydrogen is known to lead to titanium and titanium alloys embrittlement [BEC 75]. In addition, even though titanium is easily oxidisable, sintering is not hindered by the surface oxide layer, as this layer might be resorbed by diffusion of oxygen into the bulk above 550 °C [QIA 10], or damage by the difference in the coefficient of thermal expansion.

With conventional sintering (pressureless), temperatures around 1350 - 1450 °C are necessary to reach high densification of Ti64. Indeed, in their study involving powder size distribution below 45 µm, Chávez *et al.* increased the final density of Ti64 compacts from 89 to 96% by increasing the sintering temperatures from 1200 to 1400 °C [CHÁ 17]. However, direct-ink written green bodies density is lower than green bodies density achieved with compaction, which may limit the final density obtained for an identical sintering treatment. However, other parameters can also influence the final density reached. Indeed, particle size is known to impact sintering density by modifying the powder specific surface area and so the sintering driving force [OH 03]. Using finer particles thus enables to reach higher density. In addition the holding time at sintering temperature might also be an important parameter. During sintering of Ti64 compacts, Xu *et al.* showed that an important densification still occurs during the first 4000 seconds of their different holding temperatures (ranging from 900 to 1300 °C), even though the densification began during the heating ramp [XU 14]. Besides, it should be noted that in a recent work on robocasting of Ti64, Elsayed *et al.* reached density above 97% in their printed struts by sintering powder having a mean diameter (D_{50}) of 10 µm for 2 h at 1450 °C [ELS 19].

Thus these different parameters (sintering temperature, holding time and particle size) have to be chosen according to the desired density. Also, while hydrogen enrichment can be avoided by heat treatment under vacuum, this is not the case for other titanium interstitials (C, O, N). This can become an important concern for a process involving a debinding step, like DIW, when the aim is to obtain parts suitable for bone implant applications, and therefore meet the requirements of the standard ASTM F1108 presented in section 2.1.

2.2 Sample manufacturing

All samples presented in this study have been printed using a robocaster (3D Inks, LLC, Stillwater, OK, USA) controlled by the motion software Aerotech A3200 (Aerotech Inc., Pittsburgh, PA, USA). They were printed on glass plates covered with a thin layer of grease to help the removal of dried samples. Inks were extruded at $10\,\mathrm{mm{\cdot}s^{-1}}$ through plastic conical nozzles with internal diameters of 840, 610, 410 or 250 µm. Pictures presenting the robocaster used in this study can be found in Appendix A.

For all scaffolds, the rod spacing (distance between two rod centres) was fixed at 1.5 times the internal diameter of the nozzle to be comparable to the study conducted by Elsayed *et al.* [ELS 19]. Similarly, the space between two layers along the building direction was fixed at 0.8 times the internal diameter of the nozzle, in order not to crush the filaments too much, while ensuring a slight interpenetration [LAN 02]. This geometry results in a relative density of 67.86 %, considering fully dense struts.

To ensure a stabilised flow during scaffold printing, a sacrificial length (few mm) of ink was extruded before printing each sample. For all samples, the temperature was maintained at 25 °C in the printing chamber.

Knowing these chosen printing parameters, the first step was to formulate a printable ink.

2.2.1 Ink formulation and characterisation

As shown in chapter 1, Pluronic F-127, a poly(ethylene oxide)-poly(propylene oxide)-poly(ethylene oxide) triblock copolymer surfactant, has already been successfully used to form hydrogel binders to obtain both ceramic and metallic parts by robocasting. Thus Pluronic F-127 was chosen in this study to formulate binders for robocasting of Ti64. It was used in the form of dried granules supplied by Sigma Aldrich.

Ti64 argon atomised powders used in this study were purchased from TLS Technik GmbH (Germany). Two different batches with different powder size distributions were used, referred to as "coarse powder" and "fine powder" in the following. Their chemical compositions are given in Table 2.2.

Table 2.2: Composition of the Ti64 powders according to the supplier

Chemical element	N	C	H	Fe	O	Al	V	Ti
Coarse powder (wt%)	0.005	0.01	<0.001	0.22	0.08	6.20	3.98	Bal.
Fine powder (wt%)	0.008	0.011	0.002	0.155	0.15	6.10	3.87	Bal.

These powders represent the initial state of the multi-step robocasting process. So in order to know our starting point it is important to start by characterising them.

2.2.1.1 Powder characterisation

The as-received powders were characterised in terms of particle size distribution, morphology and microstructure.

Particle size distribution (PSD) measurements were conducted on the as-received Ti64 powders using the dry dispersion unit "Scirocco 2000" of Laser Diffraction Analyser (Mastersizer 2000, Malvern Instruments Ltd, UK). Three measurements were performed on each powder, using 2.611 as refractive index value. Obtained results are presented on Fig. 2.4.

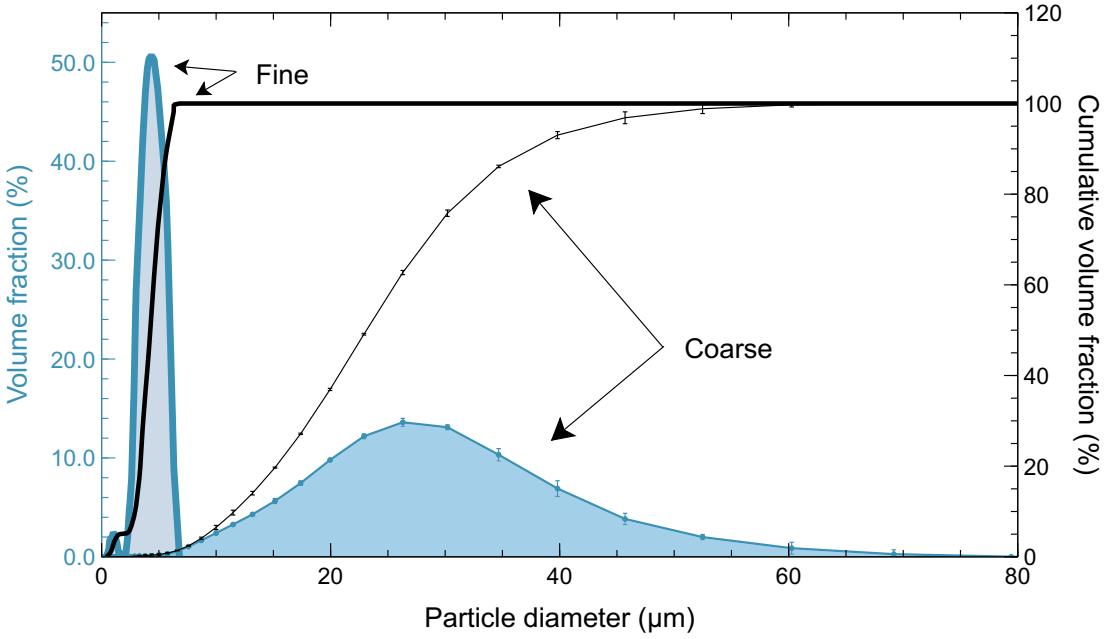

Figure 2.4: Particle size distributions of both Ti64 powders used in this study.

According to the laser diffraction results, Ti64 particles diameters of the fine powder range between 0.4 and 7 µm, while those of coarse powders extend from 2 to 70 µm. PSD of coarse powder is therefore far larger than the one of fine powder. Distribution are characterised as follows: $D_{10} = (2.93 \pm 0.02)$ µm; $D_{50} = (4.31 \pm 0.07)$ µm and $D_{90} = (5.83 \pm 0.07)$ µm for the fine powder, and $D_{10} = (11.6 \pm 0.2)$ µm; $D_{50} = (23.1 \pm 0.1)$ µm and $D_{90} = (37.2 \pm 0.4)$ µm for the coarse powder.

Images of powders (and more generally images of structures presented in this chapter) were acquired within a Tescan Vega3 scanning electron microscope (SEM) equipped with a tungsten filament (Tescan Orsay Holding, a.s., Brno, Czech Republic). Both secondary electrons (SE) and backscattered electrons (BSE) modes have been used.

Electron Backscatter Diffraction (EBSD) map acquisitions were performed in a Zeiss Supra 55 VP SEM with field-emission gun, equipped with an Oxford Instrument EBSD Symmetry camera. EBSD maps were performed using an acceleration voltage of 20 kV, with an aperture size of 120 µm, in the high current mode. The step size was fixed at 200 nm, in order to well detect the β phase. Note that directions defined during an EBSD acquisition are such that the z-axis is perpendicular to the surface being analysed.

EBSD maps were then post-treated using Channel 5 software and a 5° grain boundary criterion to calculate the mean grain size.

Fig. 2.5 highlights powders morphologies in comparison with powder used in electron beam and laser beam PBF processes. All of them are round-shaped due to gas atomisation, the only difference being the size. Note that particle size is a free input parameter in the case of robocasting process.

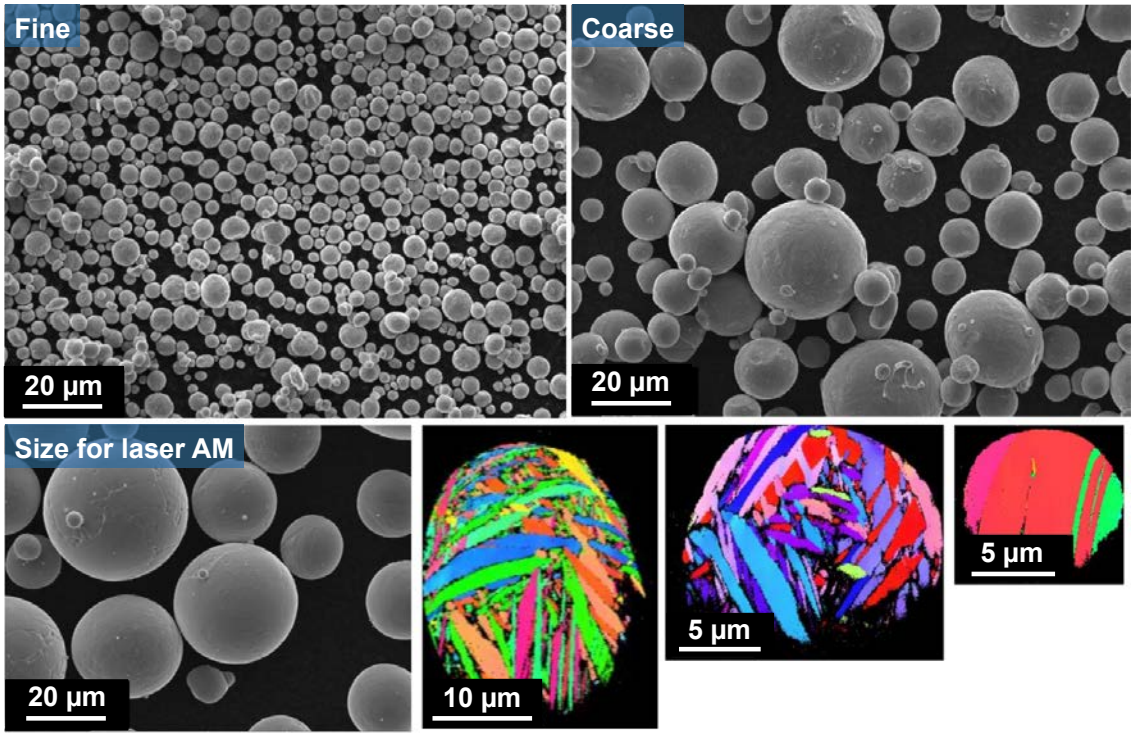

Figure 2.5: SEM images of the two powders used in this study, in comparison with powder used for laser AM processes (top and left). Inverse Pole Figure (IPF) maps obtained through EBSD analysis on powder cross-sections from the coarse batch, highlighting a thin lamellar microstructure (bottom right).

In addition, as shown by Inverse Pole Figure maps obtained on coarse powder particles (Fig. 2.5), Ti64 is in its hexagonal structure (α phase) and presents a lamellar microstructure with micron-thick laths, which is characteristic of a fast cooling rate.

Study on printability (to optimise shaping by playing on ink formulation) was performed using only the coarse powder to keep a reasonable number of conditions.

2.2.1.2 Rheology and printability

In this study, 20, 25 and 30 wt% of Pluronic F-127 were gradually dissolved in distilled water to be used as binder solutions. Before adding the Ti64 powder, those solutions are stored at 4 °C, below the liquid-solid transition temperature, in order to be kept in their liquid state.

To study the printability, each binder has been loaded with 40, 45, 50 and 55 vol% of Ti64 powder. For each ink, Ti64 addition was carried out in three stages. The batches were mixed in a dual asymmetric centrifugal mixer (SpeedMixer DAC 150.1 FVZ-K) for 1 min at 1500, 1700 and 2000 rpm after the first, the second and the last addition, respectively. Before each mixing step, inks were kept for 10 min at 4 °C, in order to be mixed when liquid.

The nomenclature given in Table 2.3 is used to identify the studied hydrogels and inks.

Table 2.3: Inks composition and nomenclature

Ti64 powder content (vol%)	Pluronic content in the gel (wt%)		
	20	25	30
0	P20	P25	P30
40	P20T40	P25T40	P30T40
45	P20T45	P25T45	P30T45
50	P20T50	P25T50	P30T50
55	P20T55	P25T55	P30T55

All studied inks have been printed and SEM images of obtained scaffolds were systematically acquired. In parallel, rheological measurements were performed to obtain both static and dynamic yield stresses and define a printable domain depending on inks compositions. The criterion corresponding to the upper limit of this domain is the robocaster's ability to extrude the ink, while the lower limit is defined by the ability to stack layers while maintaining the macropore design.

Rheological studies were carried out on a Kinexus Pro+ rotational rheometer (Malvern Instruments Ltd., England), fitted with a 40 mm parallel plates geometry, mounted so as to maintain a gap of 1 mm. Plates were roughened to minimise the risk of slip and a solvent trap was used to prevent drying. The temperature was maintained at 25 °C during tests.

Flow curves were obtained using a decreasing shear rate ramp from 200 to 1 s^{-1}. To measure static and dynamic yield stresses, the stress-shear rate loop proposed by M'Barki *et al.* has been used [M'B 17] (see Fig. 2.6 (a)). This loop was chosen to approach the printing conditions, by applying an increasing stress-controlled ramp until ink extrusion, followed by a decreasing shear-rate-controlled ramp. This second ramp enabled to imitate stress release and relaxation that lead to the dynamic yield stress when printing

is completed.

As already described in the literature [Nom 18, FEI 17b], Pluronic-F127 hydrogel rheological behaviour (loaded with particles or not) can be described by the Herschel-Bulkley model, that can account for both the presence of a yield stress and a shear-thinning behaviour (equation 1) [HER 26]:

$$\sigma = \sigma_y^0 + K\dot{\gamma}^n \tag{2.1}$$

where n is the pseudoplasticity index ($0 < n < 1$ in shear-thinning fluids), σ_y^0 is the yield stress ($\sigma_y^0 > 0$) and K is the consistency index.

Thus yield stresses were evaluated by fitting the data to the Herschel-Bulkley equation, and obtained values are reported on Fig. 2.6 (b). Except the 20 wt% F-127 (which does not exhibit a yield stress probably due to incomplete gelation at 25 °C), all studied gels and inks follow a Herschel-Bulkley model with $0.3 < n < 0.7$, meaning that they are shear-thinning. This behaviour is also highlighted by their decrease in viscosity when increasing shear rate, as shown on Fig. 2.6 (c). This decrease in viscosity can be explained by the gel destruction under shear.

Increasing the amount of Pluronic F-127 in the hydrogel, or the solid loading in the ink does not lead to an increase of the shear-thinning character as the slope remains the same. However it leads to an increase of viscosity as already observed in other studies [FEI 16a, Nom 18, YET 17]. This means that the soft network formed by the Pluronic F-127 hydrogel is not affected by the presence of the Ti64 powder but only by the shear stress. The hydrogel might then be able to transport the powder through a nozzle.

It is widely admitted that an ink should present a shear-thinning behaviour to be printable. However, M'Barki *et al.* also emphasised the important role played by both static and dynamic yield stresses in printability [M'B 17]. The static yield stress is the stress to apply on the ink to make it flow from a static state. The dynamic one is the minimal stress needed to maintain the flow when the ink is already moving. Thus, the stress endured by the ink just after printing has to be below this dynamic value to prevent deformation. So the static yield stress gives us information on the ink extrudability, whereas the dynamic one informs us on the ink capacity to retain its shape and support the following layer.

Fig. 2.6 (b) shows that all inks made with the 20 wt% pluronic gel present dynamic yield stresses lower than 50 Pa, and a poor printability (scaffolds collapsed few seconds after printing). Feilden *et al.* [FEI 17b] also considered this value of 50 Pa as a threshold under which the shape cannot be retained after robocasting. Those low dynamic yield stresses might be due to incomplete gelation at 25 °C. Gioffredi *et al.* indeed suggested a Lower Critical Gelation Temperature (LCGT) of 28 °C for this 20 wt% pluronic gel [GIO 16]. These inks might therefore be printable at temperatures higher than 28 °C.

Note that inks containing 55 vol% metallic particles were not printable (static yield

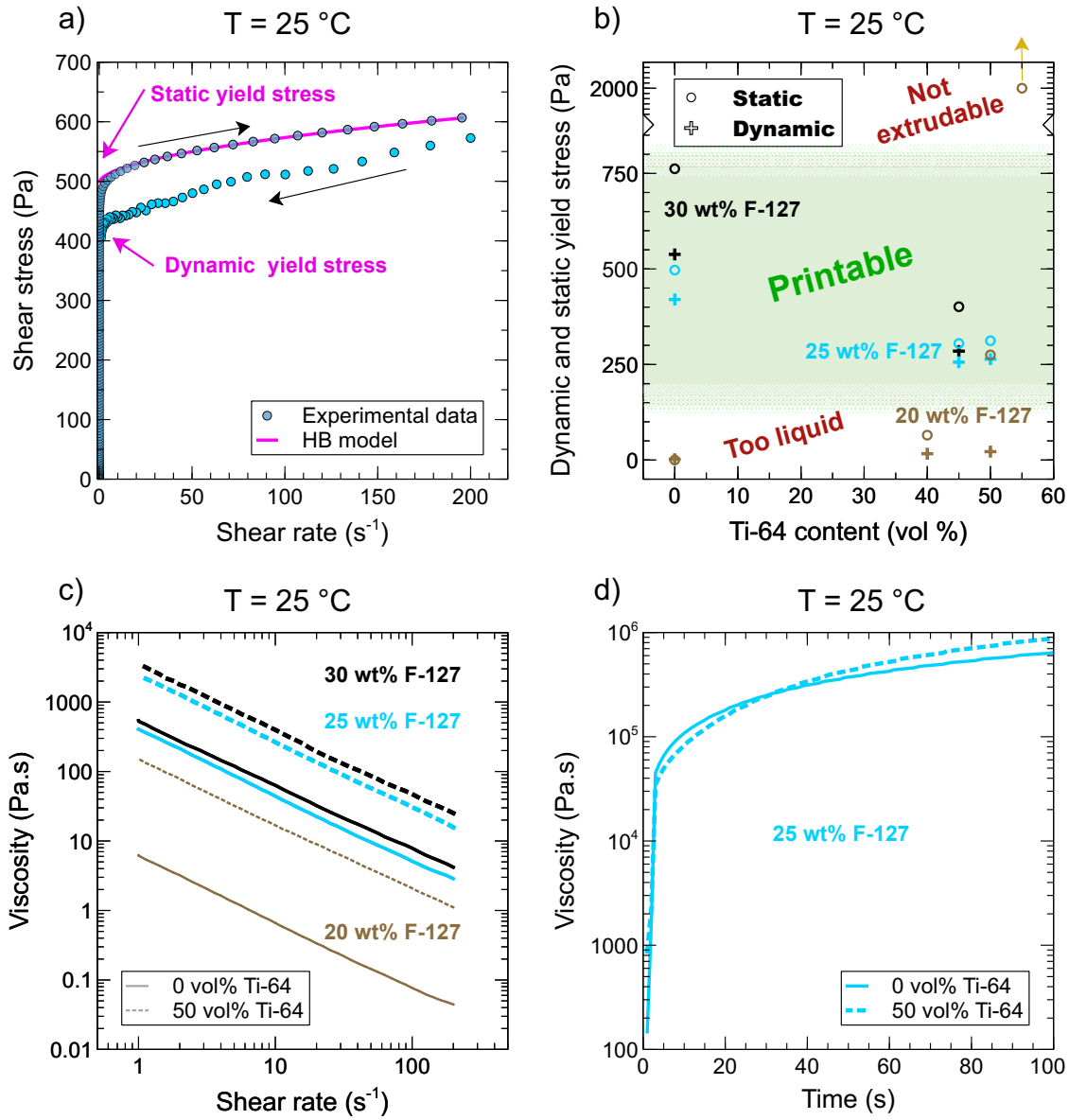

Figure 2.6: Rheology of formulated inks: (a) Example of stress-shear rate loop (P25) applied to all formulated inks; (b) Static and dynamic yield stresses of binders and inks; (c) Viscosity *versus* shear rate of the 3 binders and the 3 inks at 50 vol.%Ti64; (d) Recovery time of P25 and P25T50 (cf Table 2.3 for the nomenclature).

stress cannot be achieved with the robocasting operative pressure). This value of 55 vol% corresponds to the percolation threshold of hard spheres in a fluid [WOO 12], for which stress is also transmitted *via* metallic particles. This point added to a binder which ensures relatively high tangential forces between the particles lead to a consequent increase in the static yield stress.

Inks made with the 25 and 30 wt% pluronic gel lead to acceptable printed scaffolds

for the three larger nozzle size (see Fig. 2.7, (h)-(m)). Their associated dynamic yield stresses are larger than 200 Pa. The lower limit of the printable domain lies between 50 and 200 Pa, as represented on Fig. 2.6 (b). Moreover, the presence of particles tends to slightly decrease both yield stresses. This might be due to the presence of discontinuities in the gel caused by the Ti64 particles that seem to have poor interactions with the hydrogel.

Another important point for printability is the recovery time of the ink: after being sheared in the nozzle, the ink has to recover a relatively high viscosity in a limited amount of time to preserve the scaffold structure. Gel and ink structure recovery was measured by following Gioffredi *et al.* procedure [GIO 16]. First, gel and inks were destructured under a 100 s^{-1} shear rate for 10 s. Then, while they were submitted to a 100 Pa stress, their viscosities were measured as a function of time. Note that the shear rate chosen to destroy gel and ink structures, corresponds to the maximum shear rate that can be seen by an ink printed at 10 $mm{\cdot}s^{-1}$ through a 250 µm nozzle diameter, as estimated using laminar flow model [M'B 17, JAN 20].

Fig. 2.6 (d) shows the time evolution of the viscosity of P25 and P25T50, after applying a step shear rate. It can be observed that the presence of metallic particles does not affect the gel recovery time, as also suggested by the proper structure of just printed scaffolds (see Fig. 2.7, (h)-(m)).

However, down sizing the nozzle diameter leads to less homogeneous extrusion as shown on Fig. 2.7, (b)-(g). This might be due to arches formation within the nozzle (non-constant flows were observed), as the nozzle diameter become too near to the D_{90} of the used powder (ratio < 7 with the nozzle of 250 µm). Indeed arches formation that leads to clogging has been observed in both silos [ZUR 14, GEL 17] and narrow vertical pipes without constrictions [JAN 15] and is known to depend on both outlet diameter and particle size [ZUR 14, GEL 17, JAN 15].

In regards of rheological properties and structures of dried scaffolds, the three inks made with 25 wt% pluronic hydrogel and the three made with 30 wt% pluronic hydrogel seem printable. However for P25T40, P30T40 and P30T45, the nozzle diameter cannot be lowered to 250 µm without affecting printability. Thus, only P25T45, P25T50 and P30T50 inks were kept for deeper investigation of printability using 3D characterisation. Also, as samples printed with the 840 µm diameter nozzles were easier to handle, the further characterisations were performed on this sample size.

2.2.2 Printing accuracy

To quantify the robocaster precision associated which each ink, X-Ray tomography scans of dried scaffolds were compared to the CAD design files. Parts printed with a needle of 840 µm diameter were analysed by X-Ray computed tomography. Whole scaffolds were scanned using a V|tome|x device (GE Sensing & Inspection Technologies Phoenix X-Ray GmbH, Boston, MA, USA) (0.1 mm Cu filter, 100 kV X-Ray tube voltage, 1200 projections

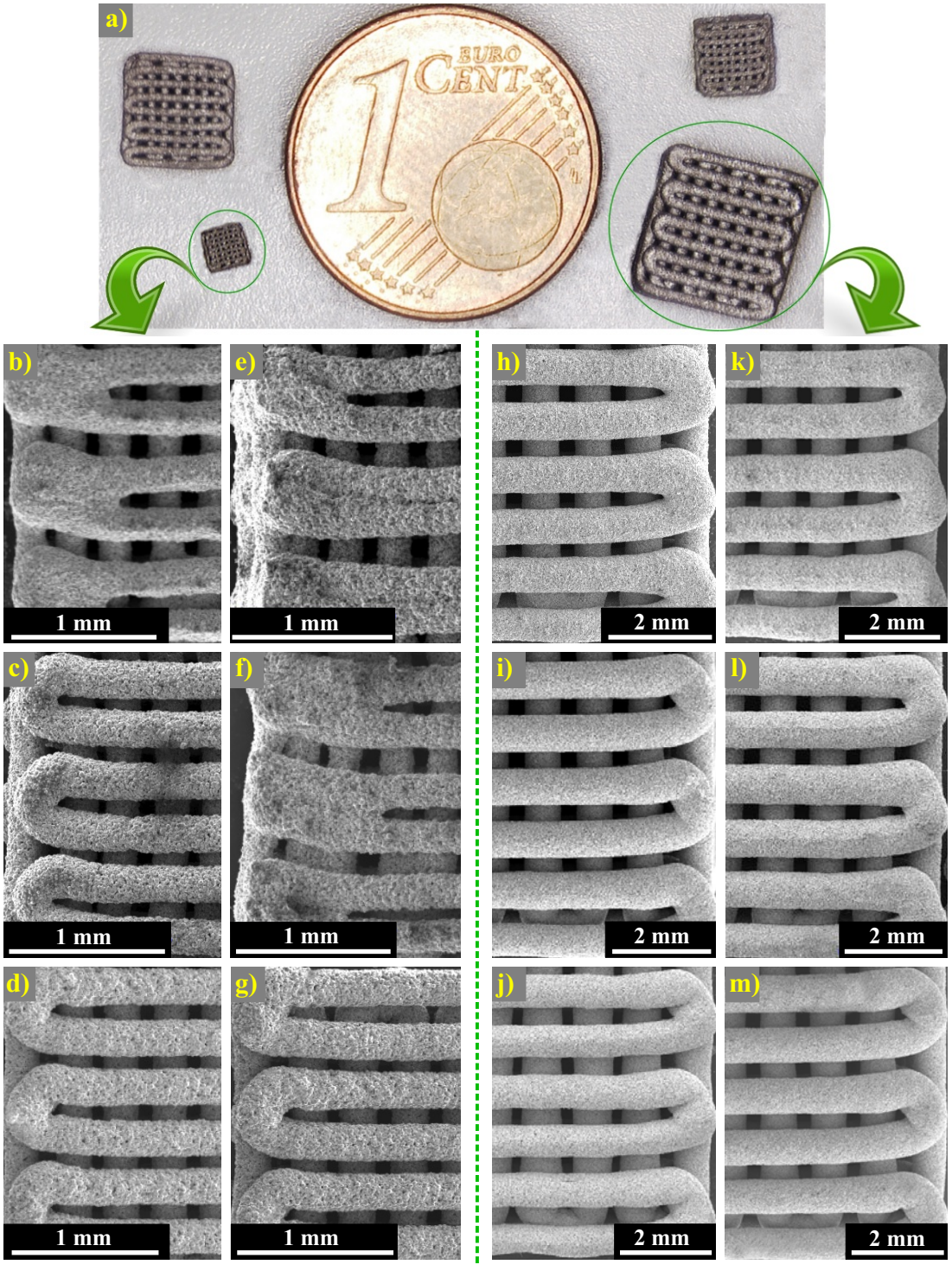

Figure 2.7: Morphology after printing: (a) Picture showing the four scaffold sizes, printed with respectively 840, 610, 410 and $250\,\mu m$ nozzle diameter; (b)-(d) Dried scaffolds printed using P25T40 (b), P25T45 (c) and P25T50 (d) inks and the $250\,\mu m$ nozzle; (e)-(g) Dried scaffolds printed using P30T40 (e), P30T45 (f) and P30T50 (g) inks and the $250\,\mu m$ nozzle; (h)-(j) Dried scaffolds printed using P25T40 (h), P25T45 (i) and P25T50 (j) inks and the $840\,\mu m$ nozzle; (k)-(m) Dried scaffolds printed using P30T40 (k), P30T45 (l) and P30T50 (m) inks and the $840\,\mu m$ nozzle.

over 360° rotation, 3 images per projection, 667 ms exposure time, 8 µm voxel size). 3D volumes were reconstructed from the collected radiographs using a filtered back projection Feldkamp-algorithm. Images analysis was then performed using the free and open-source Fiji software [SCH 12].

First, the two structures were aligned by authorising the rigid-body translation/rotation. Then, signed Euclidean distance transform operator was applied to the CAD design to get, at any point in space, the closest Euclidean distance to the surface of the CAD design. This distance was considered as positive for voxel outside of the CAD struts and negative for voxel included in CAD struts. Finally, the value of this distance field was extracted for any point on the actual surface, giving the signed Euclidean distance from the ideal surface closest to the observed actual surface point.

An example of a distance map obtained by comparing the volume obtained from X-Ray tomography with the CAD file is given on Fig. 2.8 (a). This technique also enables to quantify the dispersion of this discrepancy, normalised here by the total surface area Fig. 2.8 (b)).

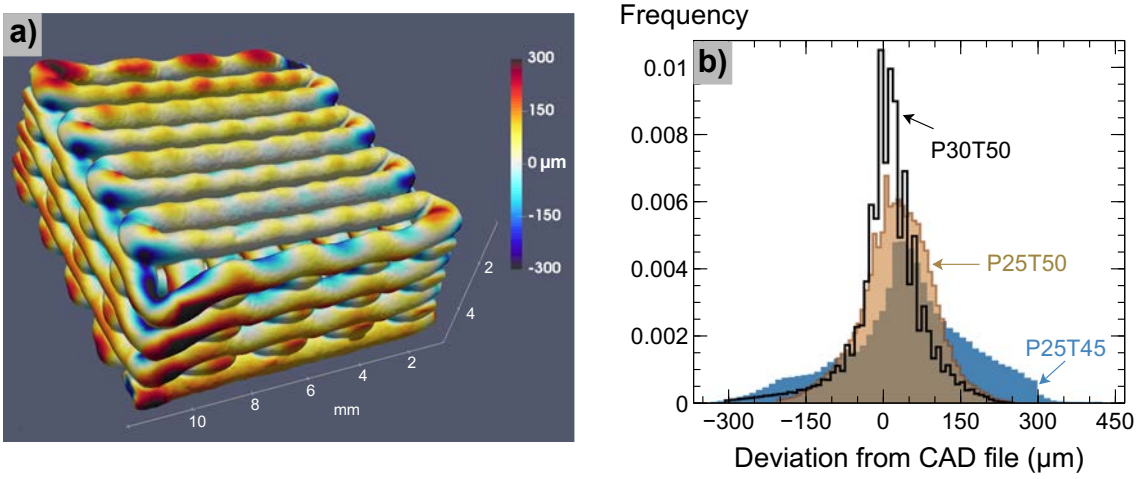

Figure 2.8: Discrepancy from CAD file: (a) Calculated distance map of a reconstructed scaffold printed with the P25T50 ink; (b) Measured discrepancy for the same scaffold and scaffolds printed with the P25T45 and P30T50 ink.

Fig. 2.8 (a) shows that the largest deviations from CAD file are located around corners, and when moving from one layer to the next one. This leads to an important standard deviation on the measured value, as presented in Table 2.4. Note that CAD files used in this study were asking for two closely spaced right angles, where a circle arc would have been easier to draw. Also, we used in this study the same printing speed for all printed segments. However, it might be relevant for the future to verify if slowing down when cornering enhances the precision.

Standard deviations given in Table 2.4 reflect the distribution width of the discrepancy

Table 2.4: Deviation from CAD file depending on the ink used

Ink	P25T45	P25T50	P30T50
Mean discrepancy from CAD (μm)	50	30	10
Standard deviation of discrepancy from CAD (μm)	130	80	80

from CAD file for each ink (see Fig. 2.8 (b)). Thus these values provide a good overview of printing precision, and the ideal case would be to have the narrowest possible distribution.

It should be noted that, if the increase from 45 to 50 vol% of Ti64 particles in the 25 wt% pluronic gel leads to a refinement of the distribution, this is not the case for an increase from 25 to 30 wt% of pluronic in the gel, keeping the solid loading at 50 vol%. It seems that the distribution of the deviation from CAD file can not be more refined without playing on printing parameters or design.

Thus both P25T50 and P30T50 lead to the best printing accuracy obtained in this study. But to minimise the pluronic content in order to facilitate the debinding step, only the P25T50 ink was kept for further characterisations.

2.3 Scaffold structure evolution during process

Once the desired shape is obtained, structures have to be debinded and sintered to reach their final properties. Both steps can highly impact the structures (and microstructures) obtained, as well as mechanical properties. This section is thus focusing on the influence of process parameters on final structures and microstructures. To limit the number of studied conditions, the effects of both debinding and sintering parameters were evaluated on the coarse powder only. Then, the influence of initial powder size was investigated through only one set of debinding and sintering conditions.

2.3.1 Influence of debinding conditions

2.3.1.1 Set up of debinding thermal cycles

Printed scaffolds were dried 48 h at room temperature (above 22 °C) before being removed from the glass substrate to undergo thermal treatments. To choose the debinding temperature, thermogravimetric analysis (TGA) was performed on a dried sample to be as close as possible to the debinding conditions. It was conducted using a TGA Q50 analyser, equipped with an EGA furnace (TA Instruments, New Castle, USA). Mass losses were recorded during a heating ramp of $1\,°C{\cdot}min^{-1}$ from room temperature to 500 °C under a $150\,mL{\cdot}min^{-1}$ nitrogen flow (after a purging step).

The observed mass loss on Fig. 2.9 is due to the Pluronic F-127 degradation. Considering the density of the P25 hydrogel ($\rho_{gel} = 1100\,kg{\cdot}m^{-3}$), the density of Ti64 alloy ($\rho_{Ti64} = 4430\,kg{\cdot}m^{-3}$), and the presence of 50 vol% of each in the considered ink, the

P25T50 ink contains 19.9 wt% of hydrogel. In addition the hydrogel contains 25 wt% of Pluronic F-127, meaning that the ink contains 4.98 wt% of Pluronic F-127. So the debinding step is fully completed at 350 °C. Thus, even though previous parts printed with pluronic F-127 were usually debinded at 500 °C or above [FEI 16b, PET 17, YET 17], a temperature of 350 °C should be enough. Consequently, two debinding cycles were studied here: 30 min at 350 °C (minimal temperature for a complete debinding), and 2h at 500 °C (usual debinding cycle).

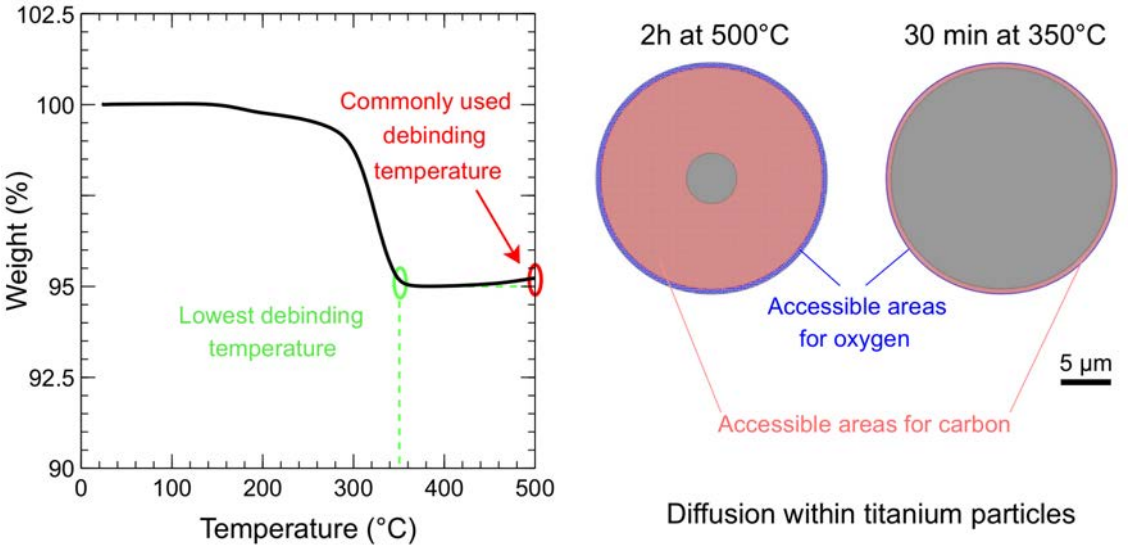

Figure 2.9: Thermogravimetric analysis with the two debinded temperatures studied and their consequences on carbon and oxygen diffusion. Debinding at 500 °C gives a large accessible area for carbon.

These two pairs of debinding parameters (30 min at 350 °C and 2 h at 500 °C) are supposed to lead to very different carbon and oxygen enrichments, as shown on Fig. 2.9. Indeed, using the diffusion coefficient of carbon within Ti64 measured by De Barros *et al.* [DEB 99], carbon diffusion length decreases from 9 µm to 0.2 µm by reducing the debinding treatment from 2 h at 500 °C to 30 min at 350 °C. As the mean diameter of Ti64 particles used in this study is about 23 µm, a diffusion length of 9 µm would lead to a carbon enrichment of a significant proportion of the total volume (see Fig. 2.9). Similarly, oxygen diffusion length decreases from 0.6 to 0.03 µm, using the diffusion coefficient determined by Poquillon *et al.* for Ti64 studied between 600 °C and 750 °C [POQ 13].

Although TGA was performed under nitrogen flow, this atmosphere was not kept for debinding treatments. Indeed, titanium might easily interact with nitrogen to form titanium nitride, which might be the reason of the small mass gain observed above 450 °C on Fig. 2.9. Thus debinding treatments were tried both under dynamic vacuum and under argon flow as this parameter might impact the debinding step efficiency.

In addition, heating rate of the debinding step might also influence the final structure in various ways. Indeed, instinctively, a slow heating rate may be preferred to avoid the

structure collapse thanks to a gradual removal of the binder. It also seems promising for the effectiveness of this debinding step. However it leaves more time for the diffusion of elements contained in the binder. Thus two different heating rates ($1\,°C{\cdot}min^{-1}$ and $5\,°C{\cdot}min^{-1}$) have been studied.

To summarise, the different debinding conditions studied in this work were obtained by combining the following parameters:

- debinding temperature (350 and 500 °C),
- holding time (30 min and 2 h),
- heating rate ($1\,°C{\cdot}min^{-1}$ and $5\,°C{\cdot}min^{-1}$),
- atmosphere (primary dynamic vacuum (5×10^{-2} mbar) or $0.2\,L{\cdot}min^{-1}$ argon flow).

Then, samples were sintered 2 h at 1200 °C under dynamic secondary vacuum (below 5×10^{-4} mbar), using a heating rate of $10\,°C{\cdot}min^{-1}$ and the natural cooling rate of the furnace that decreases from $50\,°C{\cdot}min^{-1}$ to less than $1\,°C{\cdot}min^{-1}$ as the temperature drops. These two thermal treatments took place in a Nabertherm N 11/hr furnace with an in-house set up enabling a controlled atmosphere.

This part of the study aimed at understanding the influence of debinding parameters on the development of the microstructure of robocast Ti64 alloys, in particular from the point of view of oxygen and carbon enrichments.

2.3.1.2 Interstitial contents

To measure interstitials enrichment under the different debinding conditions, oxygen and carbon quantifications were performed on raw powder, debinded and sintered samples for each case.

Carbon content measurements were carried out using an inductar CS cube analyser from Elementar Analysensysteme GmbH (Langenselbold, Germany). Samples were weighed into ceramic crucibles with W/Sn and Fe as accelerators. The equipment performed sample combustion under oxygen flow using an induction furnace. The carbon extracted from the sample was transformed into carbon dioxide, quantified by infrared spectroscopy. Measurements were performed on three samples of each condition. TiC powder was also used as a sample to verify the system ability to burn TiC and therefore to detect carbon involved in these carbides. In addition, 58A SY13001-1 and 173c titanium based standard reference materials (HRT Labortechnik GmbH Buchholz, Germany) were used to verify the analyser calibration. Datasheets giving their chemical composition can be found in Appendix B.

Oxygen contents were obtained using an EMGA 620 W analyser from Horiba Jobin Yvon company. Samples were weighed into nickel capsules and three measurements were performed for each condition. To obtain the oxygen content, the system used melting in a helium (He) impulse furnace to extract oxygen. Nickel capsules containing samples were

brought into a graphite crucible raised to high temperature (between 2500 and 2800 °C). The oxygen which was transformed into carbon monoxide (CO) by combining with the carbon in the crucible was quantified by a non-dispersive infrared cell. Then the carbon monoxide was oxidised into carbon dioxide and trapped. The 173c standard reference material was also used to verify the analyser calibration.

In addition, hydrogen and nitrogen contents were measured on the raw powder and both debinded and sintered samples corresponding to the two extreme carbon and oxygen enrichment. Measurements were performed by Elementar Application Laboratory (Langenselbold, Germany). Samples were weighed into nickel capsules and analysed using an inductar EL cube in ONH mode (Elementar Analysensysteme GmbH, Germany). Four measurements were performed on each batch.

All these chemical element quantifications give a full overview of the pollution induced by the binder (which includes carbon, oxygen and hydrogen), but also include the pollution induced by debinding and sintering atmosphere. All these interstitials contents are gathered in Table 2.5.

First of all it can be observed that debinding 2 h at 500 °C does induce a higher carbon and oxygen uptake than debinding 30 min at 350 °C, as expected according to diffusion coefficients. Also, the decrease in carbon content after sintering for all samples debinded at 350 °C (compared to their as debinded state) tends to suggest that a small amount of binder remains after debinding. This seems confirmed by hydrogen evolution for both debinding temperatures. Indeed, while there is no hydrogen uptake at the end of the whole process, the hydrogen content is slightly higher after the debinding step, even for a debinding of 2 h at 500 °C. Thus, whatever the debinding temperature used, it is the sintering step which makes it possible to get rid of the binder completely.

Fig. 2.10 is also in line with the hypothesis that a very small proportion of binder is still present after debinding. Images (a) and (b) show a dried structure. The higher magnification of image (b) reveals the significant presence of Pluronic-F127 between each particle. On the basis of images (c) and (d), it can be considered that the structure has been successfully debinded. Indeed, the scaffold structure has not been lost (Fig. 2.10 (c)) in spite of the fact that the binder was eliminated (Fig. 2.10 (d)). However some small dark areas are still visible at the points of contact between particles (highlighted by red ellipse on Fig. 2.10 (d)). This is believed to be residues of Pluronic-F127 not fully degraded during heat treatment.

This not quite complete degradation means that the C, O and H contents measured in debinded samples include Pluronic-F127 residues in addition to what has diffused into the Ti64 powder. As the stoichiometry of the residue is not known, the two contributions cannot be separated. However it should be noted that the difference in oxygen uptake during debinding at 350 °C compared to that during debinding at 500 °C is in agreement with the difference in diffusion length.

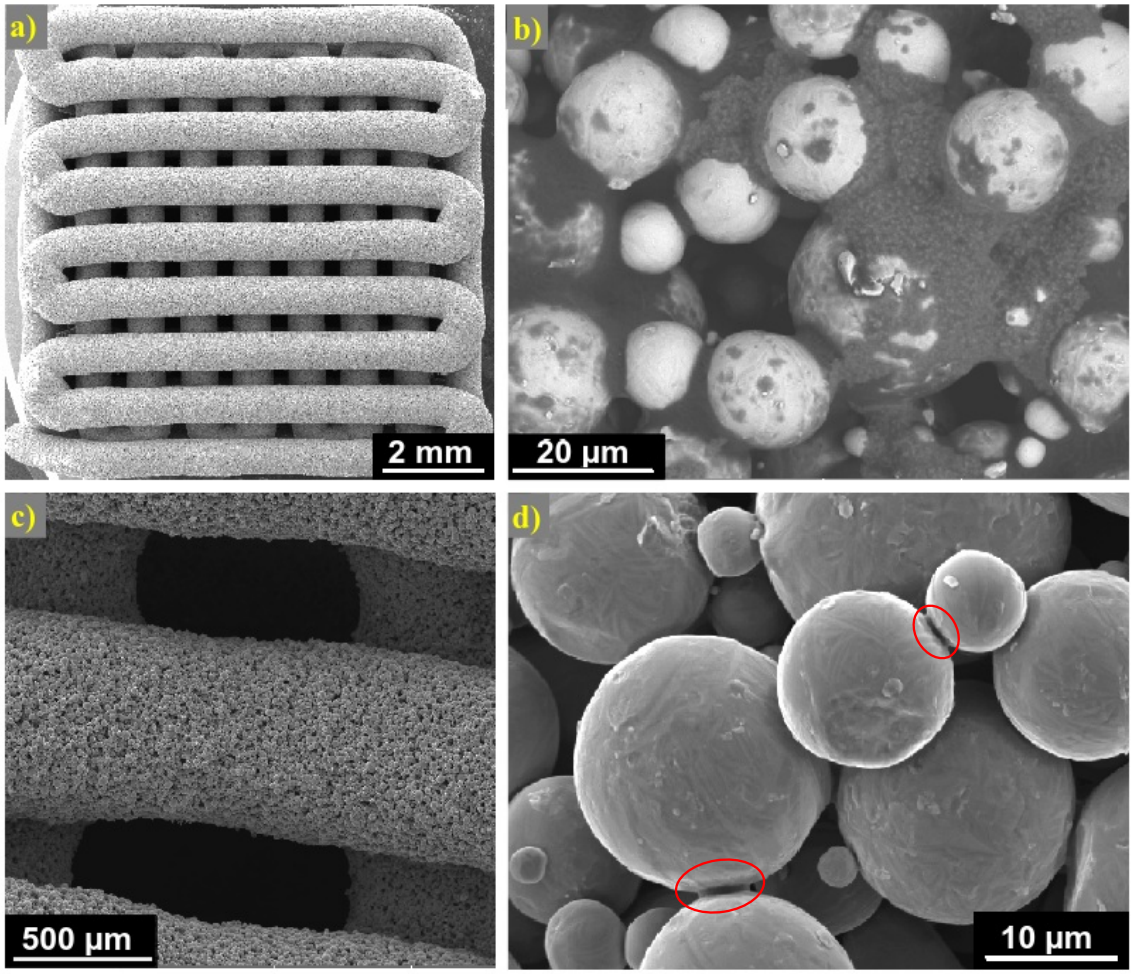

Figure 2.10: Structure evolution during debinding: (a) Dried scaffold; (b) Focus on few particles surrounded by Pluronic F-127 in a dried scaffold; (c) Rods of a debinded scaffold; (d) Focus on few particles of a debinded sample presenting residues of Pluronic F-127, as highlighted by red ellipses.

Another important point highlighted by Table 2.5 is the influence of carbon content on oxidation. While carbon uptake only takes place during debinding (as the only carbon source is the binder), oxidation occurs at each step. And oxidation during sintering might be limited by the presence of carbon, as shown by D350Ar-S1200 samples. Indeed, at 1200 °C under vacuum, carbon is able to reduce titanium oxide [JAC 09], and this positive effect of a high carbon pick-up on further oxidation control, has already been observed in powder injection moulding of titanium [BAR 10].

Also, as sintered samples containing the lowest amount in carbon present a too high oxygen content to be fully interesting, the same debinding and sintering heat treatments were performed in presence of zirconium. According to Ellingham's diagram, zirconium is supposed to act as an oxygen getter for titanium samples [BAL 16]. But this was not relevant (as shown in Table 2.5), probably due to the use of a too coarse zirconium powder

Table 2.5: Measured interstitials contents for different conditions associated with their nomenclature

Sample	Debinding conditions	Sintering conditions	[C] (wt%)	[O] (wt%)	[N] (wt%)	[H] (wt%))
Powder	-	-	0.011	0.102	0.009	0.003
D500	2 h, 500 °C 1 °C·min^{-1} vacuum	-	0.187	0.335	0.009	0.012
D500-S1200	2 h, 500 °C 1 °C·min^{-1} vacuum	2 h, 1200 °C 10 °C·min^{-1} vacuum	0.184	0.488	0.011	0.002
D350	30', 350 °C 1 °C·min^{-1} vacuum	-	0.130	0.125	0.008	0.017
D350-S1200	30', 350 °C 1 °C·min^{-1} vacuum	2 h, 1200 °C 10 °C·min^{-1} vacuum	0.094	0.219	0.010	0.002
D350Ar	30', 350 °C 1 °C·min^{-1} Ar flow	-	0.221	0.222	-	-
D350Ar-S1200	30', 350 °C 1 °C·min^{-1} Ar flow	2 h, 1200 °C 10 °C·min^{-1} vacuum	0.157	0.244	-	-
5-D350	30', 350 °C 5 °C·min^{-1} Vacuum	-	0.092	0.166	-	-
5-D350-S1200	30', 350 °C 5 °C·min^{-1} Vacuum	2 h, 1200 °C 10 °C·min^{-1} vacuum	0.088	0.273	-	-
5-D350Zr	30', 350 °C 5 °C·min^{-1} Vacuum + Zr	-	0.099	0.187	-	-
5-D350Zr-S1200Zr	30', 350 °C 5 °C·min^{-1} Vacuum + Zr	2 h, 1200 °C 10 °C·min^{-1} vacuum + Zr	0.090	0.308	-	-

compared to the Ti64 powder studied.

It is believed that these differences in interstitals amount can lead to differences in microstructures. It is therefore on this aspect that the next section focuses.

2.3.1.3 Microstructural analysis

Crystallographic evolution during the process was followed performing X-Ray Diffraction (XRD) analysis on raw powder, debinded and sintered samples. X-Ray diffraction (XRD) patterns were acquired using a Bruker AXS D8 Advance Diffractometer with a Cu tube (40 mA, 40 kV) and a 0.6 mm diffusion slit. Diffracted X-rays were collected with a Lynxeye detector, between 20 and 60° 2θ (since this range includes all the highest intensity Ti diffraction peaks), with steps of 0.02° at 1s/step. XRD patterns were then analysed using Eva software (Brucker). Lattice parameters and phase quantification were obtained after Rietveld Refinement (Topas 4.0 Software, Bruker, Germany). Distortions were quantified through the strain-G parameter, which measures the widening of the Gaussian part of diffraction peaks and is related to the distortion ϵ by: strain-G = 4 ϵ (Topas 4.0 technical reference, Brucker). Fig. 2.11 shows XRD patterns for debinded and sintered samples in comparison with the initial powder. Different debinding parameters were compared but all the debinded samples were submitted to the same sintering treatment of 2 h at 1200 °C under secondary vacuum.

Like for the initial powder, XRD patterns of debinded samples only show the presence of the α titanium phase (Powder Diffraction File (PDF) 00-044 1294), indicating that there was no crystallographic transformation during the debinding step, regardless of the debinding conditions.

Debinding at 500 °C leads to higher and thinner peaks than debinding at 350 °C. This can be explained by the recovery phenomenon induced by the debinding treatment. Indeed, gas-atomised powders have fine martensitic structure with a potentially high dislocations density, which debinding treatment at least partially decreases. A treatment of 2 h at 500 °C eliminates more dislocations than a 30 min treatment at 350 °C. This is confirmed by the decrease of the strain-G parameter (obtained from Rietveld refinement) with increasing thermal treatment temperature.

After sintering, α phase remains predominantly present within all samples, together with around 10 wt% of beta-titanium phase (estimated by XRD, using lattice parameters compatible with those given by Malinov *et al.* [MAL 02]). After sintering at 1200 °C, samples debinded at 350 °C contain no other phase. However, D500-S1200 samples contain also a small amount of titanium carbides. These peaks can be fitted both by considering the cubic TiC lattice (PDF 01-1222) as well as by considering the cubic $TiC_{0.62}$ lattice (cif file number 1532224 from the crystallography open database) and the hexagonal $Ti_6C_{3.75}$ lattice (cif file number 1540227). These last two lattices are in agreement with the chemical composition given as thermally stable by Thermocalc TTTI3 database (Ti_6C_4).

Thus precipitates are only detectable through XRD in D500-S1200 samples after sintering. This means that in other conditions carbides are either non-existent or too small or too few in number to be detectable. Indeed, 3 % of TiC smaller than 30 nm gives a signal of the order of magnitude of background noise.

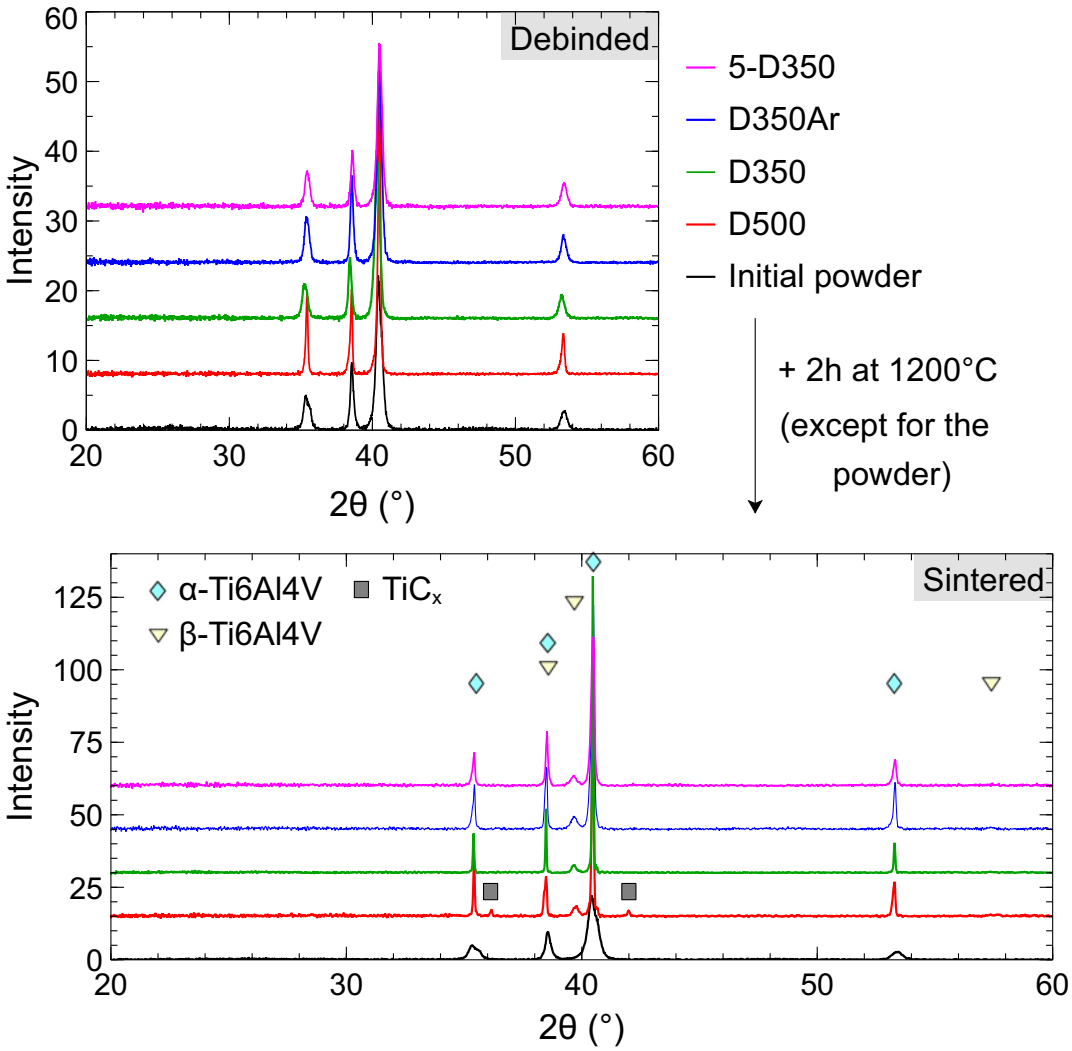

Figure 2.11: Evolution of XRD patterns after debinding and sintering for different debinding conditions. Ti_6C_4 are observed in sintered samples that were previously debinded at 500 °C.

Two conditions must be met to allow the carbides precipitation: the carbon concentration must be above the carbon solubility limit in Ti64, and the mobility of solute atoms must be high enough. According to the XRD patterns, these two conditions are met for D500-S1200 samples. However carbon solubility limit at 1200 °C in Ti64 containing 0.5 wt% of oxygen is about 0.33 wt% as given by Thermocalc software using the TTTI3 database. Thus global carbon concentration measured in all the samples studied here, including those debinded at 500 °C, is below this solubility limit (see Table 2.5). In addition, carbon solubility in the α phase is decreased below 0.18 wt% around 500 °C. But at this temperature the mobility is not sufficient to allow precipitation as no carbides are observed in D500 samples. Thus precipitation may occur during the cooling ramp but in

the β phase.

To get a better overview of these precipitates, surfaces and cross-sections of both D350-S1200 and D500-S1200 have been imaged by SEM as shown on Fig. 2.12. Surface structure of the two samples is completely different. D500-S1200 surface has a granular appearance with "granule" sizes smaller than the size of Ti64 particles (Fig. 2.12 (a)). This might be due to the formation of a contaminant layer on the surface as suggested by the cross-section (Fig. 2.12 (c)). In comparison, D350-S1200 surface is much smoother, titanium particles are directly visible. However, it should be noted that they present faceted surfaces, probably due to anisotropic surface diffusion as explained by Joo *et al.* [JOO 20]. In addition, cross-section shown on Fig 2.12 (d) confirms that there is no additional phase formation on D350-S1200 surface.

Fig. 2.12 (e) focuses on the surface layer of D500-S1200 sample and enables to see that this layer can be almost 10 µm thick in some areas. However, its thickness is not homogeneous and the layer even presents discontinuities as shown on Fig. 2.12 (c). These discontinuities added to the surface topology are more reminiscent of a precipitation phenomenon than a simple oxidation. EDX analysis shown on Fig. 2.12 (e) suggests that this is a carbon-rich layer which might also contain oxygen. In addition to this carbon-rich layer, titanium carbides can also be found in D500-S1200 bulk (Fig. 2.12 (f)), whereas higher oxygen concentrations were only detected around the pores. These carbides present globular shapes to reduce their interface energy, whereas precipitates on the surface keep more elongated shapes as they only have one side in contact with Ti64 matrix. Also, it should be noted that no carbides were observed in D350-S1200 bulk, and that carbides observed in D500-S1200 bulk were non-homogeneously distributed. This seems in agreement with the hypothesis of a precipitation in β phase during the cooling ramp, in parallel with the allotropic transformation.

To complete the microstructural study, Fig. 2.13 shows inverse pole figure maps obtained for both D350-S1200 and D500-S1200 samples, with their associated phase maps. First it can be observed that D500-S1200 presents, on average, twice smaller α grains than D350-S1200. This can be explained by the presence of titanium carbides, which might either limit grain growth [KIM 02] or serve as nucleation sites for the α phase. In addition, these smaller α grains are fully equiaxed, whereas coarser grains of D350-S1200 are still lamellar. Once again this equiaxed morphology might be due to the presence of titanium carbides as it has been reported by Badini *et al* [BAD 00]. In view of the microstructures obtained with the fine powder (which will be described in section 2.3.3.3), oxygen cannot be blamed for these phenomena.

Also, the difference in α grains morphology induces a difference in morphology of the inter-granular beta phase but does not seem to change the α / β ratio, with an estimation through EBSD remaining around 4 - 4.5 % of β phase. The difference between this value and the one estimated through XRD measurements can be explained by several factors.

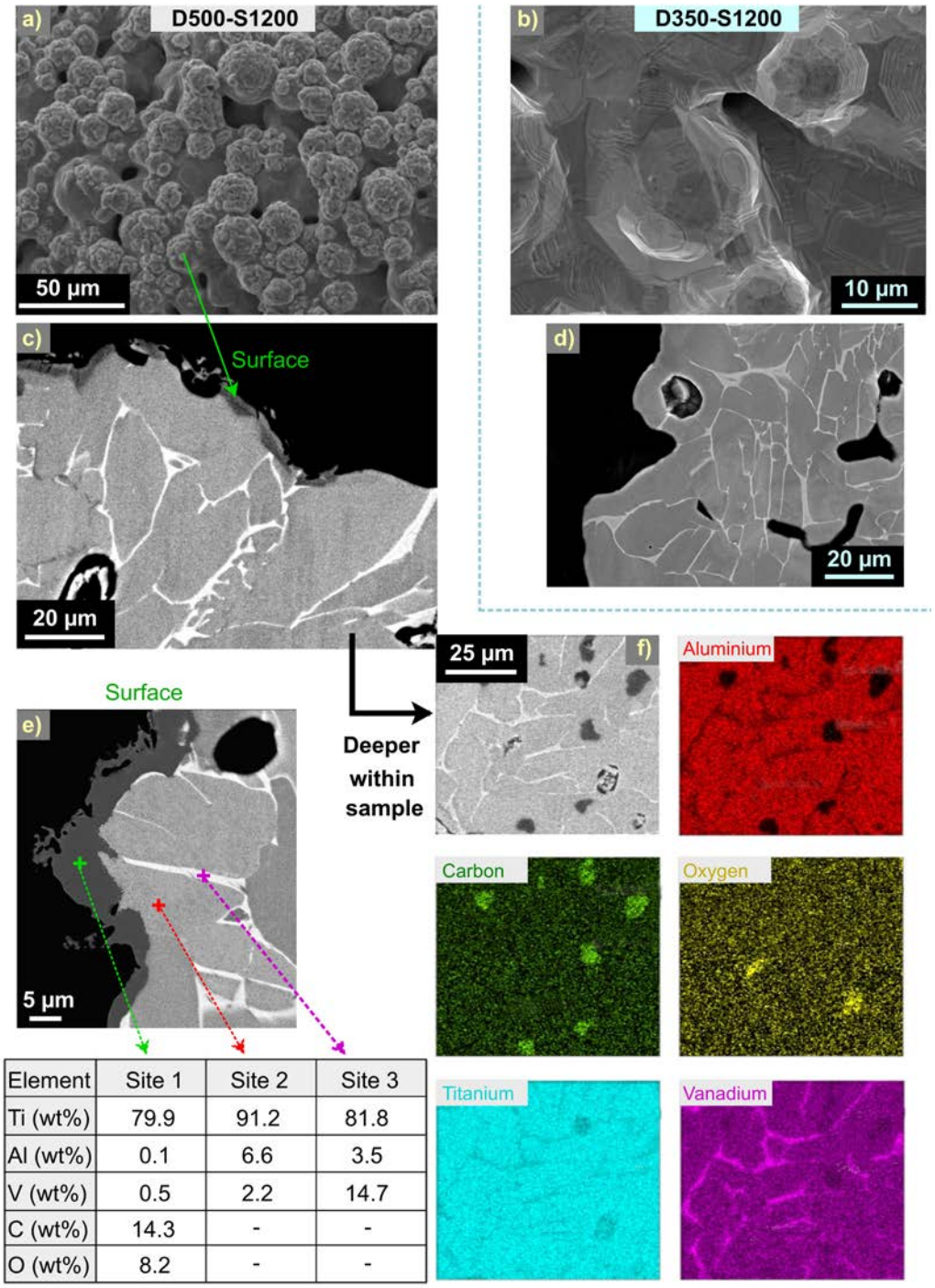

Element	Site 1	Site 2	Site 3
Ti (wt%)	79.9	91.2	81.8
Al (wt%)	0.1	6.6	3.5
V (wt%)	0.5	2.2	14.7
C (wt%)	14.3	-	-
O (wt%)	8.2	-	-

Figure 2.12: Surface aspect of (a) D500-S1200 and (b) D350-S1200; Cross-section showing the surface of (c) D500-S1200 and (d) D350-S1200 ; EDX analysis showing carbide formation on the surface (e), as well as in the bulk (f).

First β being the finest phase it may be less well indexed and therefore slightly underestimated by EBSD. In addition, EBSD is a surface analysis carried out on a relatively small

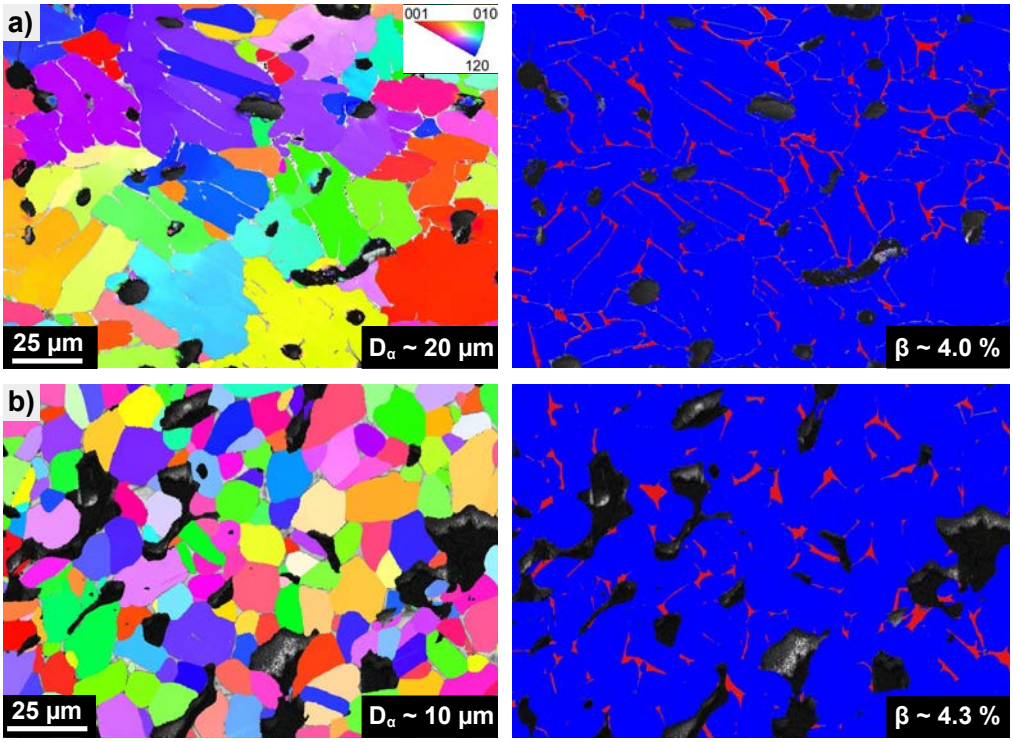

Figure 2.13: As-sintered microstructure : EBSD inverse pole figure map and its associated phase map of: (a) D350-S1200, showing thick but still lamellar grains; (b) D500-S1200 samples presenting smaller and equiaxed grains.

area. Finally, DRX quantification can lead to an overestimation of the β phase, as the presences of aluminium in the α phase and vanadium in the β phase were not taken into account and preferential orientation effects were neglected.

In view of this microstructural analysis, it seems that no carbide precipitation occurs during the debindig step. However, during sintering of samples debinded at 500 °C, precipitation seems to occur in the β phase during the cooling stage. So first, to verify the consistency of the C and O uptake measured, diffusion simulations were performed on a Ti64 powder particle. Then, to validate the precipitation scenario mentioned, precipitation simulations were performed on the same system. These models were created in collaboration with Michel Perez.

2.3.1.4 Diffusion and precipitation modelling

Mean field modelling methods

Precipitation of titanium carbides has been modelled using in-house software PreciSo [PER 08b, PER 08a], a multi-class, Kampmann-Wagner Numerical (KWN) precip-

itation model [WAG 05] based on Classical Nucleation and Growth Theories (CNGTs). For more details on the implementation of CNGTs, please refer to ref. [TOF 20].

Entry parameters of the precipitation model are the temperature profile, the diffusion coefficients of C and O in Ti64 phases and the thermodynamic properties of precipitates (chemical composition of precipitates *i.e.* Ti_6C_4 from TTTI3 [THE 18] database, surface energy γ, solubility products $K^{\alpha}_{Ti_6C_4}$ and $K^{\beta}_{Ti_6C_4}$ in α and β phases). The output parameters are the precipitate size distribution ($N_i(r_i)$, the number density of precipitates of size r_i) and the remaining solute content.

Nucleation ΔG, which is given by equation 2.2, represents the potential energy to be minimised.

$$\Delta G = \frac{4}{3}\pi r^3 \Delta g + 4\pi r^2 \gamma \tag{2.2}$$

where r is the precipitate radius and Δg is the driving force, given here by the TTTI3 thermodynamic database [THE 18]. This driving force must be negative for allowing the precipitation to occur.

The critical size r^*, above which precipitates are stable and grow (and can thus decrease the potential energy) corresponds to the value of r for which the derivative of ΔG function is zero:

$$r^* = \frac{-2\gamma}{\Delta g} \tag{2.3}$$

The nucleation energy barrier ΔG^* is the potential energy obtained for $r = r^*$ so:

$$\Delta G^* = \frac{16}{3}\pi \frac{\gamma^3}{\Delta g^2} \tag{2.4}$$

By applying Boltzmann's statistical analysis to the ΔG function, the nucleation rate dN/dt giving the flux of precipitates reaching the critical size r^* can be obtained [WAG 05]:

$$\frac{dN}{dt} = N_0^j Z^j \beta^{*j} \exp\left[-\frac{\Delta G^{*j}}{k_B T}\right] I(t) \tag{2.5}$$

where j stands for either α or β Ti64 matrix, N_0^j is the nucleation site number density, Z^j is the Zeldovich factor, β^{*j} is the condensation rate, k_B is the Boltzmann constant, T is the temperature and $I(t)$ is an incubation coefficient varying from 0 to 1 with $I(0) = 0$ and $I(\infty) = 1$.

The energy barrier ΔG^{*j} depends on surface energy and driving force for precipitation that is calculated from TTTI3 [THE 18] thermodynamic database *via* solubility products.

Growth The growth equation of spherical precipitates is given solving Fick's diffusion equation assuming a stationary solute concentration profile:

$$\frac{dr}{dt} = \frac{D_{\mathrm{C}}^{j}}{r} \frac{X_{\mathrm{C}}^{0} - X_{\mathrm{C}}^{eq}(r)}{\alpha X_{\mathrm{C}}^{P} - X_{\mathrm{C}}^{eq}(r)} \tag{2.6}$$

where α is the ratio of atomic volumes of matrix and precipitates: $\alpha = v_{at}^{\alpha/\beta}/v_{at}^{P}$, X_{C}^{0} is the C solute content and $X_{\mathrm{C}}^{eq}(r)$ are the equilibrium solute concentrations at the interface. They are given by the Gibbs-Thomson equation (adapted from [PER 05, DU 12]):

$$(X_{\mathrm{Ti}}^{eq})^{6} \, (X_{\mathrm{C}}^{eq})^{4} = K_{\mathrm{TiC}}^{j} \exp \left(\frac{20 \gamma v_{at}^{P}}{r} \right) \tag{2.7}$$

Solubility products were fitted from TTTI3 [THE 18] thermodynamic database for various O contents:

$$K_{\mathrm{Ti_6C_4}}^{j} = \frac{C^{j}}{T^{2}} - \frac{A^{j}}{T} + B^{j} \tag{2.8}$$

where A^j, B^j and C^j are constants depending of the O content of the matrix $[O]_{wt\%}$ *via* $A^j = a_A^j [O]_{wt\%} + b_A^j$, $B^j = a_B^j [O]_{wt\%} + b_B^j$ and $C^j = a_C^j [O]_{wt\%} + b_C^j$.

In this approach, the surface energy γ is the only fitting parameter. All model parameters are summarised in Table 2.6.

Implementations At each time step, if the number of nuclei is larger than a critical value, a new class of precipitate is created with number density $N_i = dN/dt \times \Delta t$. Then all existing classes grow according to the solution of the non-linear system formed by eqs. (2.6) and (2.7), leading to $r_i(t + \Delta t) = r_i(t) + dr/dt \times \Delta t$. Finally, the mass balance is performed to update the solute content of all solute species.

Coupled diffusion/precipitation model In its most recent version called NodePreciso [BAR 16, ROU 18], the software has been improved to be able to model precipitation within a chemical gradient of diffusing solute atoms. At the beginning of the simulation a mesh is defined.

In this simulation, we used 3 nodes. The two first ones [node 0] and [node2] represent the bulk and the surface of a powder grain (of size 25 µm), respectively. The third one [node 1] represents a C/O rich layer of the binder (of thickness 1 µm) (see figure 2.14 (a)). All nodes have a given initial solute content X^0 and are connected to their neighbouring node via a given surface. Each time step of the simulation starts with a diffusion step during which a node can exchange atoms with its neighbour. Fluxes of atoms are given by Fick's law. Note that precipitation is allowed to occur only in the Ti64 particle bulk [node0].

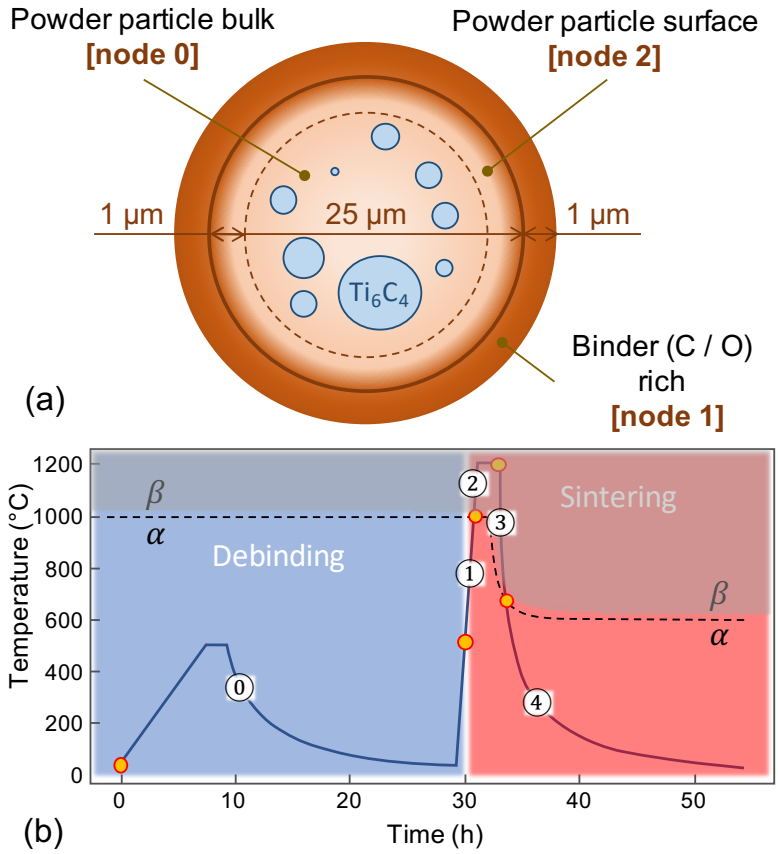

Figure 2.14: (a) A simulated Ti64 powder particle: the precipitation model is applied on 3 nodes exchanging solute atoms: [node 0] represents the bulk of a Ti64 powder particle, [node 1] represents a C/O rich layer issued from the binder and [node 2] is the surface layer of the Ti64 particle. (b) Simulated thermal profile composed of a debinding stage [stage ⓪], heating to the α/β transformation temperature [stage ①], heating and holding at the sintering temperature [stage ②], cooling from sintering temperature to the β/α transformation temperature [stage ③] and cooling in α phase to room temperature [stage ④].

Thermal treatments Thermal treatments were modelled by a succession of 5 stages: a debinding stage [stage ⓪], heating to the α/β transformation temperature $T_{\alpha\beta}$ [stage ①], heating and holding at the sintering temperature T_s [stage ②], cooling from sintering temperature to the β/α transformation temperature $T_{\beta\alpha}$ [stage ③] and cooling in α phase to room temperature [stage ④] (see figure 2.14 (b)). Note that $T_{\beta\alpha} < T_{\alpha\beta}$, because the cooling rate is high compared to the transformation kinetics, leading to a shift in the transformation temperature [DAB 11b] (see Fig 2.2 presented in section 2.1).

Isothermal precipitation

The model behaviour was initially evaluated with an isothermal treatment at 500 °C. For this study, only [node 0] and [node 2] were kept and a carbon concentration of 1 wt%

was attributed to the 2 nodes to avoid supplementary effect of diffusion. The evolution of precipitation over time is observed in [node 0] for different interface energy values (fitting model parameter). In addition, the evolution of the solute concentration is followed over the whole system by weighting the average by the volume of each node. Results obtained are shown on Fig. 2.15.

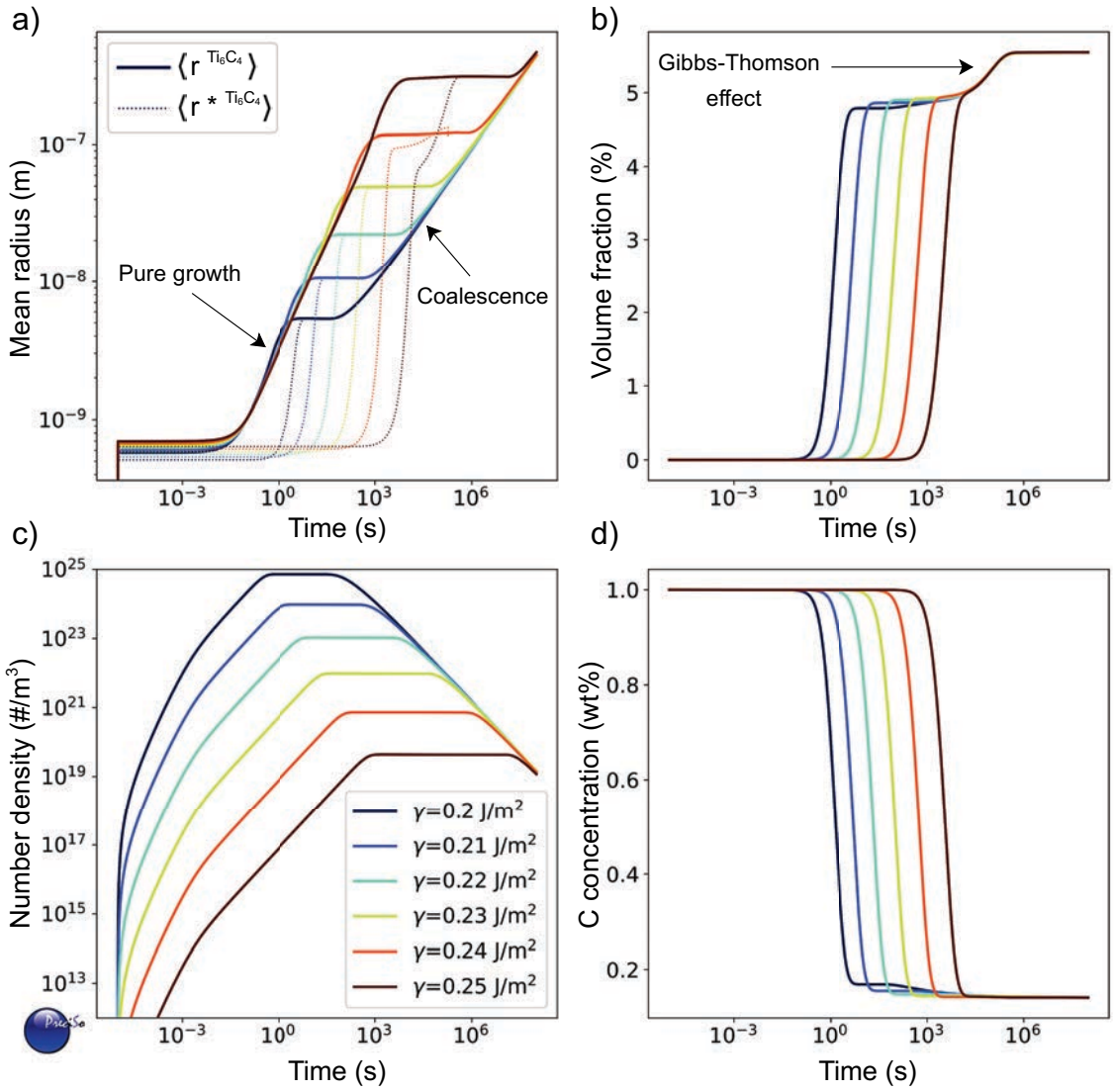

Figure 2.15: Isothermal precipitation: (a) Evolution of the Ti_6C_4 mean radius as a function of time for various interface energies; (b)Evolution of Ti_6C_4 volume fraction with time for different interface energies, highlighting the Gibbs-Thomson effect; (c) Evolution of the number of precipitate with time depending on the interface energy chosen; (d) Evolution of the carbon solute content in the whole system as a function of time for various interface energies.

As the concentration in carbon (1 wt%) is far above the solubility limit in the Ti64

α phase at 500 °C (0.18 wt%), Ti_6C_4 nucleation occurs almost immediately as shown by Fig. 2.15 (a) and (c). The precipitates then follow a classical evolution, with a first domain of pure growth, where their radius is proportional to $t^{1/2}$, followed by a transient regime before entering the coalescence regime (r proportional to $t^{1/3}$).

When the interface energy is increased, precipitation requires more energy. Thus to be stable, Ti_6C_4 have to be larger to reduce the amount of interface to be created. The initial radius of the nuclei is therefore larger when the interface energy is higher (see Fig. 2.15 (a)). But larger precipitates imply a greater distance for the carbon to travel to be integrated into the nucleus. This is thus increasing the nucleation time, as shown by the slower initial increase in number for higher γ (see Fig. 2.15 (c)). This difference in diffusion length also induces a slower growth for the bigger nucleii. In addition, as they are fewer in number, they need to grow more to consume the same amount of solute, explaining the higher mean radius observed during the transient regime for higher γ.

During this transient regime, there is no more nucleation, the number of precipitates remains constant. In addition, the mean radius is also staying stable as the large precipitates grow larger at the expense of the smaller ones, which diminish in size. When the smaller precipitates become too small to remain stable, they dissolve in the matrix continuing to feed the larger ones. This is the coalescence domain, characterised by a decrease in the number of precipitates and an increase in their average radius.

These precipitates begin to be visible in terms of volume fraction (and therefore in parallel in terms of decrease in solute content) only when the product of their number by the cube of their mean radius begins to be significant. Both volume fraction and carbon solute content present a first plateau before reaching their final value. This is due to the variation of the solubility limits with the mean radius of the precipitate, known as Gibbs-Thomson effect. Indeed, larger precipitates are more profitable in terms of energy. The amount of precipitates that can be formed to reduce the potential energy of a material therefore depends on the size of the precipitates formed. Note that the solubility limit given by the TTTI3 [THE 18] thermodynamic database (at equilibrium) is finally reached for an average radius that can be considered as infinite.

C and O uptakes

The two pairs of debinding parameters (30 min at 350 °C and 2 h at 500 °C) lead to very different carbon and oxygen enrichments, as shown in Table 2.5. These values are the result of C and O diffusion from the binder to the Ti64 particles during the debinding treatment. In order to verify the consistency of these C and O uptakes, diffusion simulations were performed on a Ti64 powder particle (bulk: [node0] and surface: [node2]) coated with C and O rich binder layer [node1] (see fig. 2.14(a)). All parameters used in this simulation are recalled in Table 2.6.

As a first step, no precipitation was allowed within the Ti64 particle and only diffusion

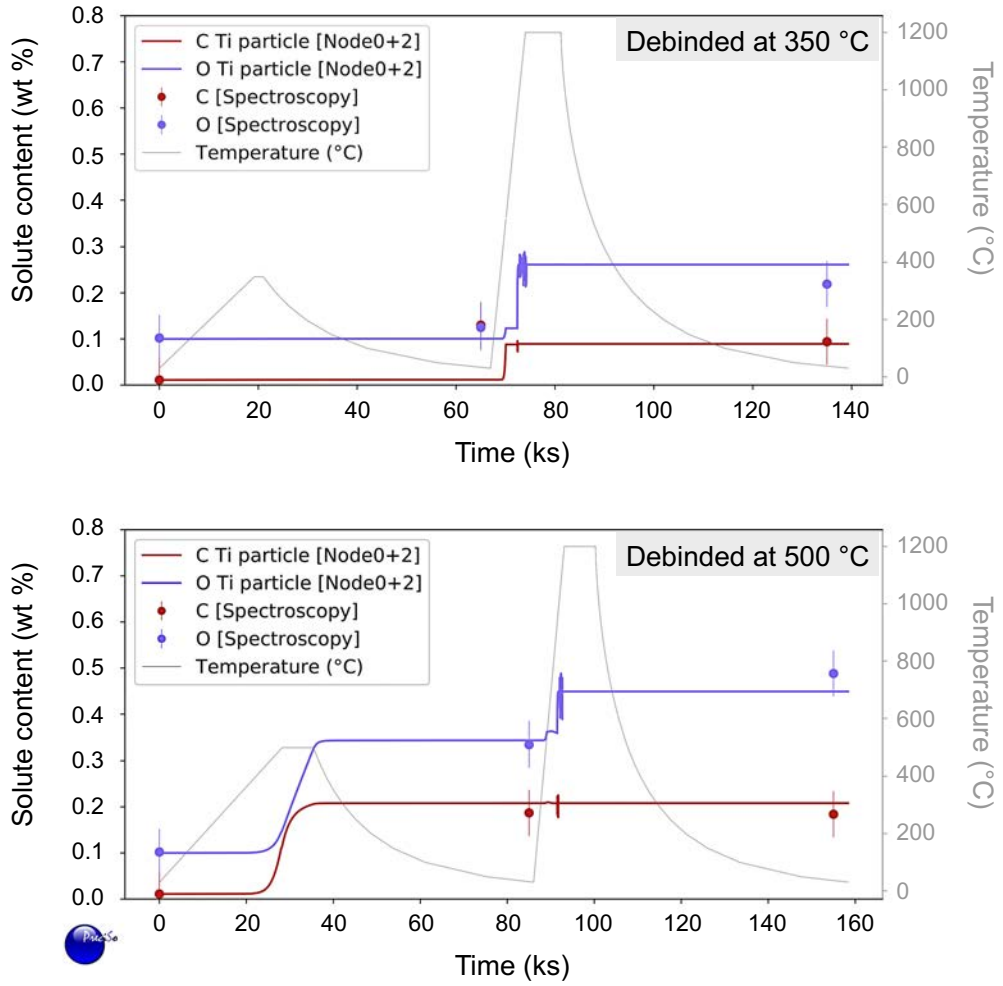

Figure 2.16: Total amount of C and O in a Ti64 particle ([node0]+[node2]) during the debinding and sintering processes. The model is based on a C/O rich layer present during debinding [node1] (see fig. 2.14(a)). The oscillations observed at the beginning of the sintering plateau are due to numerical instabilities.

of C and O was allowed. Fig. 2.16 compares the predicted values of total C and O contents in the powder particle ([node0] and [node2]) with the amounts that were measured with spectroscopy.

Starting from the initial C and O contents measured in the powder, the simulation shows a fast enrichment in C and O during the debinding treatment at 500 °C and a moderate increase in C content during the debinding at 350 °C. The presence of remaining binder noticed after this debinding treatment at 350 °C explains the higher amount of measured C compared to the simulated one. It can even be assumed that all the carbon detected by spectroscopy after debinding at 350 °C is due to Pluronic F-127 residues. As the C can diffuse from this remaining binder to the Ti64 particle during the ramp up of the sintering treatment between 350 and 500 °C, simulated and measured C content rejoin

Parameter	Value	Unit	Ref.
$D_0^{C/\alpha}$	5.06×10^{-4}	m^2/s	[OGD 55]
Q_C^{α}	182	kJ/mol	[OGD 55]
$D_0^{C/\beta}$	1.08×10^{-2}	m^2/s	[OGD 55]
Q_C^{β}	202	kJ	[OGD 55]
$D_0^{O/\alpha}$	1.23×10^{-7}	m^2/s	[POQ 13]
Q_O^{α}	150	kJ/mol	[POQ 13]
$D_0^{O/\beta}$	1.6×10^{-4}	m^2/s	[OGD 55]
Q_O^{β}	201	kJ/mol	[OGD 55]
γ^{α}	0.2	J/m^2	fitted
γ^{β}	0.2	J/m^2	fitted
a_A^{α}	-1978	K/(wt%)	[THE 18]
b_A^{α}	7665	K	[THE 18]
a_A^{β}	1241	K/(wt%)	[THE 18]
b_A^{β}	7754	K	[THE 18]
a_B^{α}	-1.827	1/(wt%)	[THE 18]
b_B^{α}	-0.210	—	[THE 18]
a_B^{β}	0.295	1/(wt%)	[THE 18]
b_B^{β}	-1.593	—	[THE 18]
a_C^{α}	-9.133×10^5	K^2/(wt%)	[THE 18]
b_C^{α}	8.596×10^5	K^2	[THE 18]
a_C^{β}	5.362×10^4	K^2/(wt%)	[THE 18]
b_C^{β}	-9.479×10^5	K^2	[THE 18]
v_{at}^{P}	1.029×10^{-29}	m^3	
v_{at}^{α}	1.743×10^{-29}	m^3	
v_{at}^{β}	1.679×10^{-29}	m^3	
$X_C^0\|_{node1}$	6	wt%	fitted
$X_O^0\|_{node1}$	40	wt%	fitted

Table 2.6: Parameters of the diffusion/precipitation model

after sintering. Note that O enrichment of Ti64 particles during the sintering stage at 1200 °C is attributed to the presence of the quartz tube, which could act as an O source at such high temperature.

This first step of the simulation is in agreement with experimental values and can therefore quantitatively explain the C and O uptake during debinding and sintering treatments.

Carbides precipitation

In order to verify the observations (no precipitation during debinding stages and precipitation of carbides after sintering of the D500-S1200 sample), precipitation simulations

were performed on the same system as previously (a Ti64 powder particle (bulk: [node0] and surface: [node2]) coated with C and O rich binder layer [node1] (see fig. 2.14(a))).

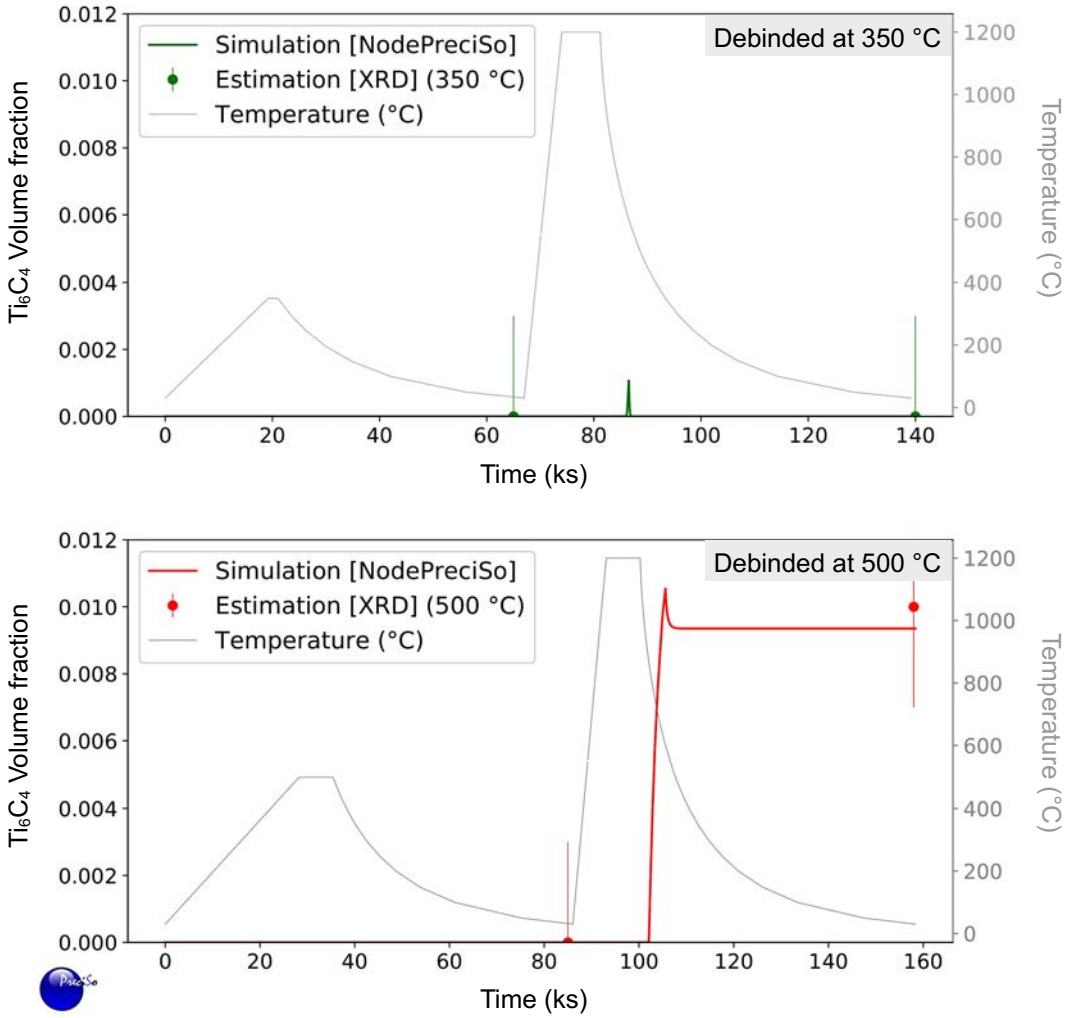

Figure 2.17: Evolution of Ti_6C_4 precipitates volume fractions during the debinding and sintering processes. Precipitation is predicted during cooling from the sintering stage in the Ti-β phase of the sample debinded at 500 °C.

In this second simulation step, precipitation was allowed to occur within the bulk of the Ti64 particle [node0]. Figure 2.17 presents the evolution of precipitate volume fraction during the debinding and sintering treatments for both debinding temperatures (350 and 500 °C). Not surprisingly, no precipitation occurs during debinding stages, neither at 350 °C, nor at 500 °C. However, the evolution of mean radius and r^* value shown in Fig. 2.18 is helpful to fully understand what is happening. For both holding temperatures (350 °C and 500 °C), the solubility limit of C is higher than the maximum amount of C present in the Ti64 particle, so that no precipitation can occur. But the rise of r^* for both debinding treatments during the heating and the cooling shows that there is a driving

force for precipitation. However, nucleation is not occurring due to the low mobility of C (at the temperature for which this rise in r^* is observed). Indeed, the (dynamic) evolution of temperature does not give enough time for precipitation to occur.

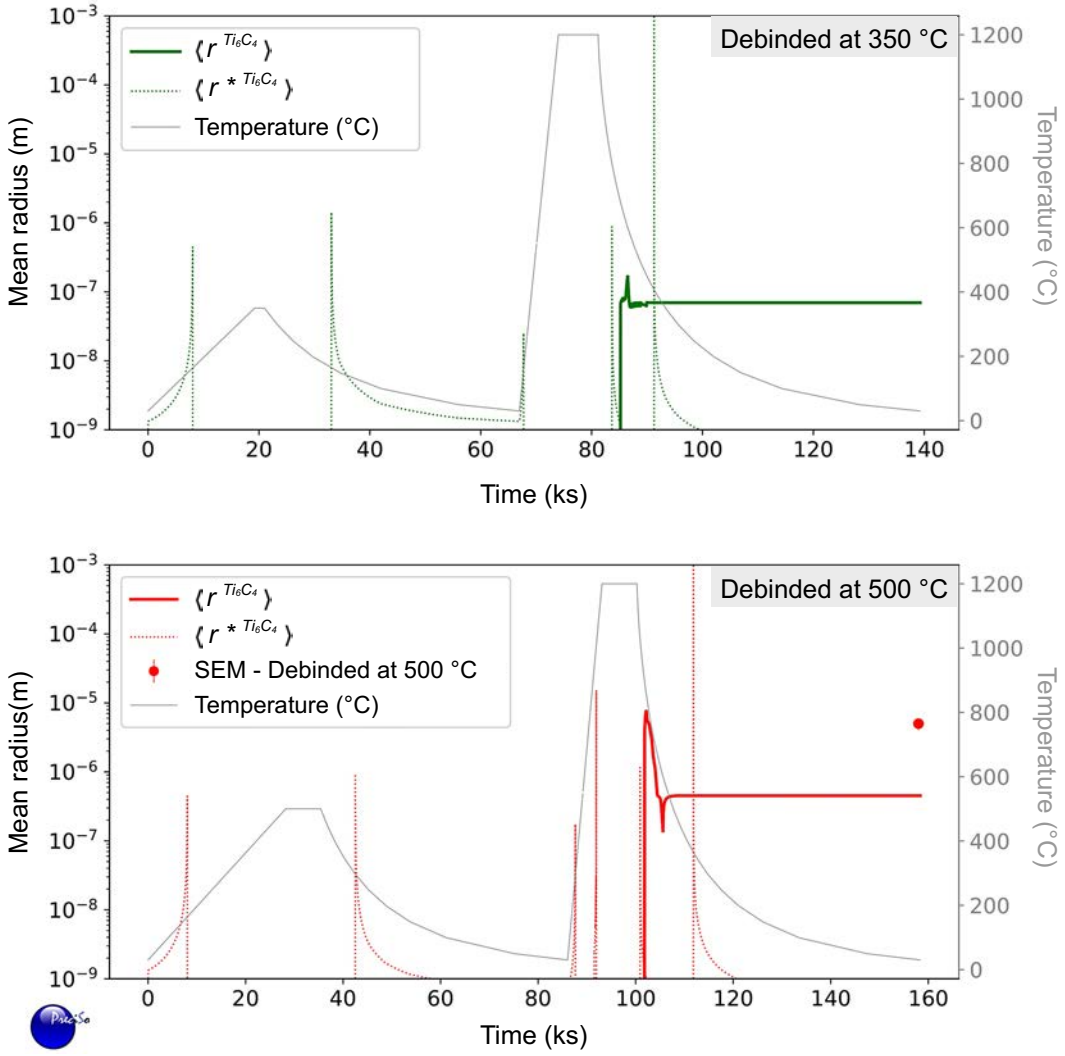

Figure 2.18: Evolution of critical radius and mean Ti_6C_4 radius during the debinding and sintering processes.

Precipitation is not observed either during the ramp up to reach the sintering temperature because the temperature domains for which both mobility and precipitation driving force are high enough are very limited and the heating rate is also too high. At 1200 °C, precipitation is still not observed because the solubility limit of C in the Ti-β phase is once again too high (0.32wt%) compared to the C content (0.2wt%). However, during the cooling, as the $\beta \rightarrow \alpha$ transition temperature is lowered by the transformation kinetics (as shown in the TRC diagram of Ti4Al4V of Dabrowski [DAB 11b]), a temperature domain ranging from 1000 to 700 °C exists where mobility and driving forces are high enough for

precipitation of Ti_6C_4 carbides to occur during cooling in the Ti-β phase of both samples. This is highlighted by both volume fraction and mean radius evolution.

However, after a first precipitation, a decrease in the mean radius but also in volume fraction are observed, showing that the β to α phase transformation leads to a partial dissolution of these precipitates due to the associated increase in solubility limit. Despite the non-zero radius present until the end of the sintering treatment in the case of a debinding at 350 °C, the final precipitate content remains insignificant as shown by the volume fraction but also by the number of precipitates evolution shown in Fig. 2.19. The sample debinded at 500 °C exhibits a much larger volume fraction of precipitates, as observed experimentally. This is induced by its higher enrichment in C during the debinding stage. Note that an additional increase in r^* is observed around 400 °C but do not lead to any supplementary precipitation as the mobility is too low.

With regard to the mean radius presented on Fig. 2.18, it would appear that there is a non-negligible difference between the size of the precipitates predicted by the model and that of the precipitates observed by SEM. However, by plotting the size distribution of the precipitates, both in number and volume, it can be seen that the number of small precipitates gives them a non-negligible weight in the calculation of the mean radius, but that the volume distribution is in agreement with SEM observations, as highlighted by Fig. 2.20

These precipitation simulations are fully consistent with all experimental results and therefore validate the following scenario: (i) High C uptake during debinding at 500 °C and (ii) precipitation of carbides in the β phase during the cooling after sintering before and during the $\beta \rightarrow \alpha$ phase transformation. Note that these simulations were rather performed to validate a possible scenario than quantitatively fully predict a precipitation state (volume fraction and radius distribution), which would require extensive additional characterisations (precipitate size distribution by TEM, precipitate volume fraction from chemical analysis).

To focus on changes induced by debinding parameters variation, all the samples studied in this section were sintered at 1200 °C. However, variation in sintering temperature are also known to induce structural changes in terms of remaining porosity, shrinkage or even crystallographic structures. Thus the next section gives the characteristics of the different structures that can be obtained by varying the sintering temperature.

2.3.2 Influence of sintering temperature

To assess the influence of sintering temperature, only one set of debinding conditions was kept in this section: 30 min at 350 °C under dynamic vacuum, with a heating rate of 1 °C·min^{-1}.

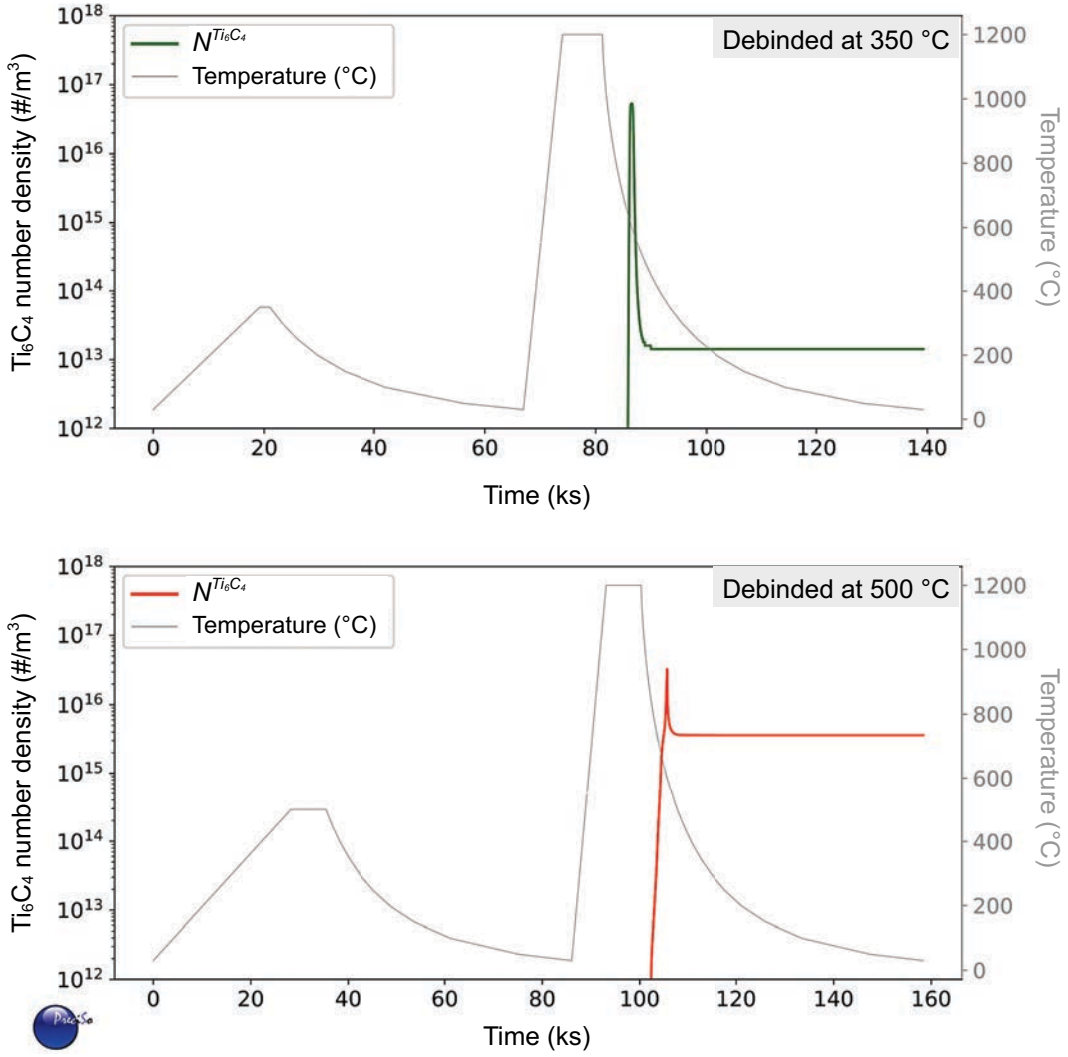

Figure 2.19: Ti_6C_4 number density evolution during the debinding and sintering processes. Precipitation is predicted during cooling from the sintering stage in the Ti-β phase of the sample debinded at $500\,^{\circ}\mathrm{C}$.

2.3.2.1 Architecture and porosity

An important concern associated with sintering is to control the shrinkage in order to predict the final dimensions of the sintered part from the initial CAD file. Thus, as-sintered dimensions were measured thanks to X-Ray tomography (Fig. 2.21 (a) and (b)). Measurements were performed on X-Ray tomography scans of sintered scaffolds and filaments, and compared with CAD dimensions to obtain the shrinkage related to the whole process. Sintered scaffolds were scanned using the same parameters as for dried scaffolds (see section 2.2.2). Sintered mono-filaments (printed with a nozzle of 840 µm) were imaged at high resolution using an EasyTom Nano tomograph (RX Solutions, Chavanod, France) (100 kV X-Ray tube voltage, 1248 projections over a 360° rotation, 3 images per projection,

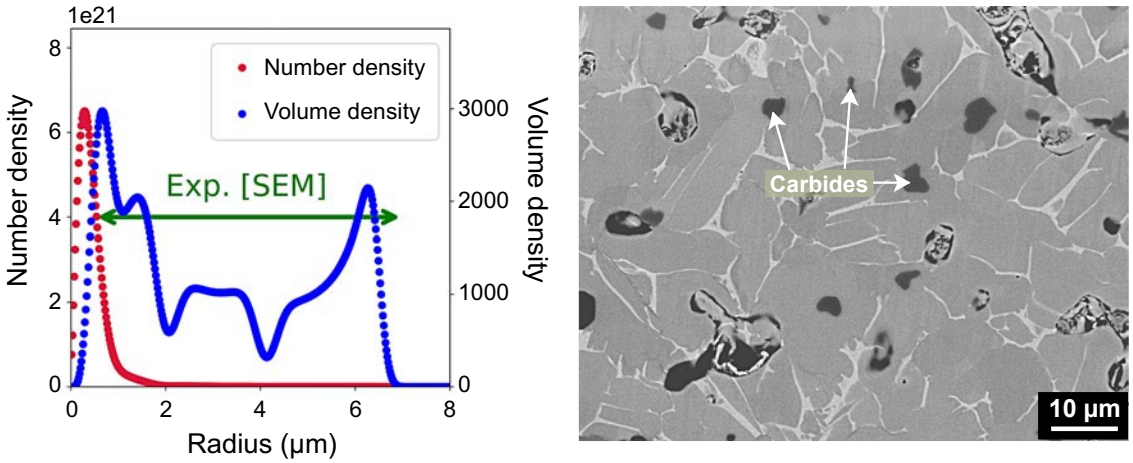

Figure 2.20: Calculated size distributions (in number and volume) of Ti_6C_4 precipitates for the sample debinded at $500\,°C$ accompanied by a SEM image showing titanium carbide in a D500-S1200 sample. The simulated volume density is in agreement with SEM observations.

4 s exposure time, 0.45 µm voxel size). In both cases, 3D volumes were reconstructed from the collected radiographs using a filtered back projection Feldkamp-algorithm. Images analysis was then performed using the free and open-source Fiji software [SCH 12].

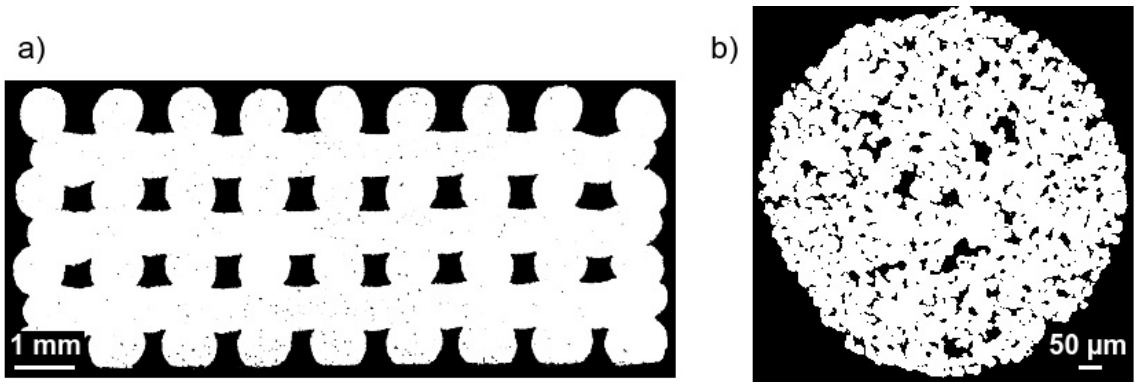

Figure 2.21: Final structure after sintering at $1200\,°C$: Example of tomographic section of: (a) the whole structure, (b) a constitutive strut.

To be sure to work on structures completely perpendicular to the observation axis, sintered structures were first aligned with CAD design files as explained in section 2.2.2. This alignment is important to measure the right dimensions as an angle would introduce a bias (sine or cosine). Once the structure is well oriented, Fiji software enables to sum all the projections in the stack. This gives the enveloping outer shell of the structure in the plane of observation, whose dimensions can be accurately measured at pixel level

(0.45 µm). This is repeated for the three plans of observation: (x,y); (x,z) and (y,z).

Note that as-sintered dimensions obtained by X-Ray tomography were in agreement with measurements realised on SEM images, and shrinkage obtained for filaments was as well in agreement with shrinkage obtained on scaffolds. Results are summarised in Table 2.7. Scaffolds used to determine shrinkage were also weighed. Each mass obtained was divided by the corresponding scaffold volume (measured by X-Ray tomography) to get their density. The Ti64 density used to calculate scaffolds relative density was $4.43\,\mathrm{g{\cdot}cm^{-3}}$.

Table 2.7: Process shrinkage and relative density obtained for the different sintering conditions

Sintering temperature	Shrinkage (%)				Relative density (%)	
	Along X	Along Y	Along Z	Volume	Measured	Designed*
1000	10.4 ± 0.1	10.4 ± 0.1	10.4 ± 0.2	28.1 ± 0.1	48.9 ± 0.3	49.22
1100	13.1 ± 0.2	13.1 ± 0.2	13.1 ± 0.2	34.4 ± 0.2	53.8 ± 0.5	54.97
1200	15.3 ± 0.3	15.3 ± 0.4	15.2 ± 0.3	39.2 ± 0.3	57.3 ± 1.0	59.38

* Calculated considering remaining porosity within struts.

It can be observed that shrinkage is homogeneous in the 3 spatial directions. Also, even for the higher sintering temperature, final macropores size is about 350 µm which remains wide enough to allow vascularisation [KAR 05].

X-Ray tomography high-resolutions scans ((Fig. 2.21 (b)) were also used to determine constituent filament density. After binarisation, a mask is obtained from each scan of filaments by filling all pores. The initial binarised scan is then subtracted from this mask to keep only the pores. Then pores are labelled (one label per pore) to get dimensional information on each of them, authorising to plot a pore size distribution. Labels containing eight voxels or less are considered as noise and are not kept for characterisations. The porosity is obtained by comparing the number of voxels included in the mask with the number of voxels included in the labelled pores. In addition, Fiji is able to detect edges. Thus by adding the edges of the mask to the stack of pores, it is possible to determine which ones are open (in contact with the edge of the mask), and which ones are closed.

In addition, the plugin "local thickness" enables to assess the thickness of objects contained in a 3D volume, by filling this object with spheres. For each point, this plugin gives the largest sphere that fits inside the object and contains the point. It is then possible to access to sphere thickness distribution. And as one point cannot be counted in two different spheres, the thickness distribution obtained is really representative of the thickness variations of the 3D object considered. This has been for example used to determine the thickness of trabecular bone structures [DOU 07].

Fig. 2.22 gives an overview of this remaining intra-strut porosity as a function of sintering temperature with associated pore size distributions. This volumetric distribution

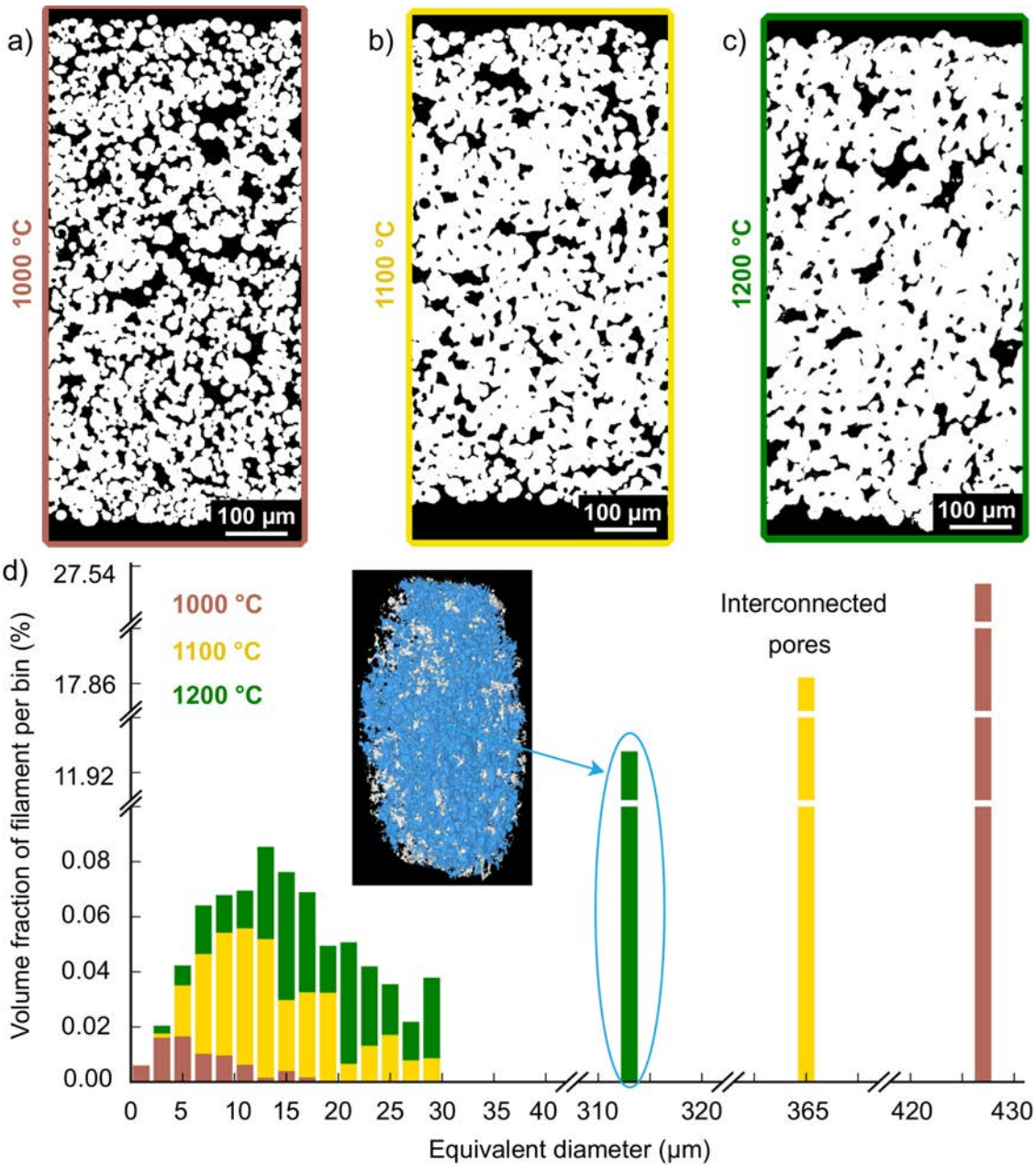

Figure 2.22: Remaining porosity after sintering: Example of tomographic section of constitutive filament sintered at: (a) 1000 °C; (b) 1100 °C; (c) 1200 °C. (d) Pores volume distribution for the three temperatures illustrated with the porosity network 3D reconstruction of a filament sintered at 1200 °C.

is plotted as a function of the equivalent pore diameter, which is the diameter that a sphere of the same volume would occupy. In addition, a 3D reconstruction of a portion of a filament sintered at 1200 °C was performed with the larger label (corresponding to the larger pore) coloured in blue. For a better 3D rendering, see video here. This highlights the presence of an interconnected porosity present all along the strut. The presence of this

interconnected network is representative of an intermediate sintering stage as described by Kang *et al.* [KAN 04]. In addition, porosity levels obtained, represented on Fig. 2.23, are also in agreement with this stage. But even though densification observed with increasing temperature is mainly resulting from a volume reduction of the interconnected network (see Fig 2.22 (d)), pore closure also occurs. Indeed, Fig. 2.23 shows a slight increase in the proportion of closed pores (as a ratio of total porosity).

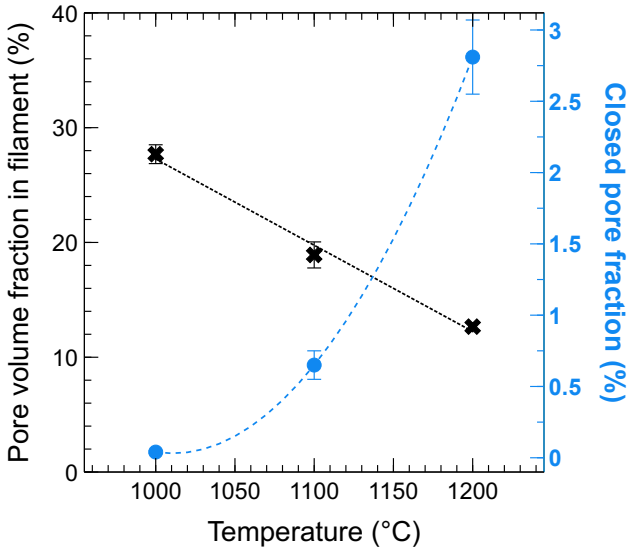

Figure 2.23: Pore volume fraction in the filament and closed pore volume fraction (as a ratio of total porosity) evolutions with sintering temperature.

However, characteristic sizes of this interconnected pores network does not really vary with sintering temperatures, as shown by Fig. 2.24. Indeed, spheres used by the local thickness plugin to fill interconnection necks are ranking from 1 µm diameter to $\sim 7-8$ µm with a maximal number of spheres for a diameter of $\sim 4-5$ µm whatever the sintering temperature. In addition, the mean diameter of the spheres required to fill the pores (without considering the interconnection necks), is also stable around 15 µm, regardless of the temperature. However the maximal sphere size required slightly decreases with an increase from 1000 °C to 1200 °C. But this small decrease is not sufficient to explain the porosity evolution. The main change lies in the total number of spheres needed in each case, which decreases sharply with temperature (almost divided by 3 with an increase from 1000 °C to 1200 °C). Characteristics of this second porosity network seem then in accordance with requirements mentioned by Bohner *et al.* for the formation of mineralised tissues [BOH 17].

Thus, scaffolds with two interconnected porosity networks were successfully obtained through robocasting and partial sintering from 1000 °C to 1200 °C.

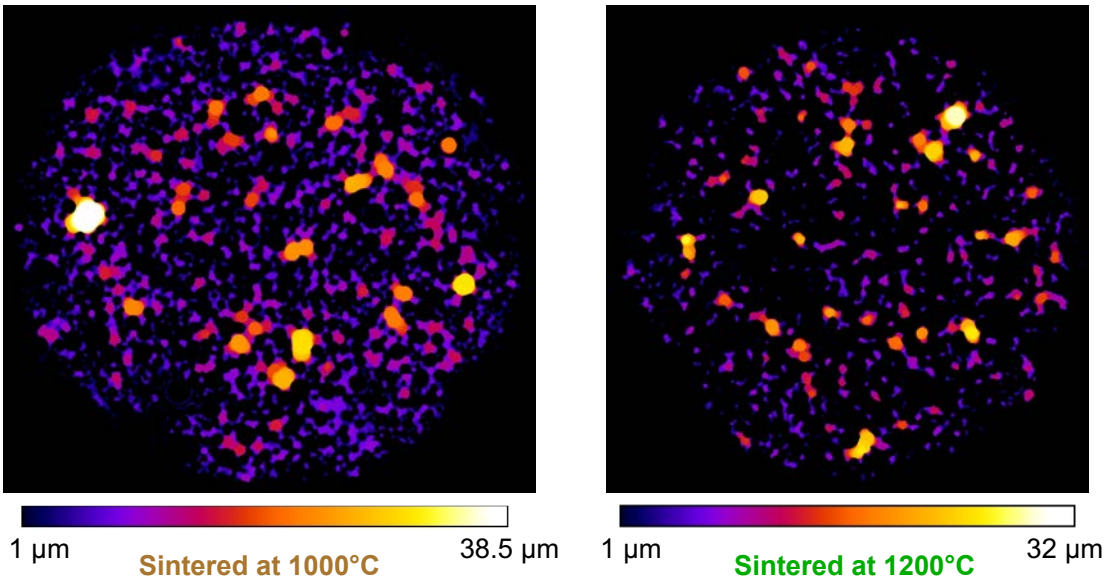

Figure 2.24: Porous network dimensions: Local thickness plugin applied on X-Ray tomography scans of filaments sintered at 1000 °C (left) and 1200 °C (right).

2.3.2.2 Crystallographic structure

Fig. 2.25 shows the microstructure obtained for the different sintering temperatures. Maps of crystallographic phases highlight the presence of the β phase at grain boundaries (yellow phase). The sintering temperatures used do not seem to really impact the beta phase amount as all of them were above the beta transus (see section 2.1).

Inverse pole figure maps of the α phase were obtained using a 5° grain boundaries criterion. These maps highlight the grain growth induced by a rise in sintering temperature. In coarser microstructure, it can be observed that thick but unclosed lamellae are still present. In addition to the grain growth induced by the sintering process, it is the applied cooling rate that gives this microstructure much coarser than that obtained by powder bed fusion technologies. In this study, maximum cooling rates after sintering are around $0.5\,°C{\cdot}s^{-1}$ whereas LB-PBF process induces cooling rates in range of $(10^5$-$10^6)\,°C{\cdot}s^{-1}$ that lead to martensitic transformation. The preheating of the powder bed during EB-PBF process slightly reduces the cooling rates, allowing the martensite transformation into α+β structure after solidification to occur. However, the final microstructure reached by EB-PBF remains fine, with Windmanstätten α laths presenting submicronic thickness [GAL 17, ZHA 16].

As microstructure obtained can also be tailored by cooling rates after sintering, the main influence induced by an increase of sintering temperature from 1000 °C to 1200 °C is an increased density and associated shrinkage. However varying the powder size used (and the powder size distribution) might be another way to play on final density obtained.

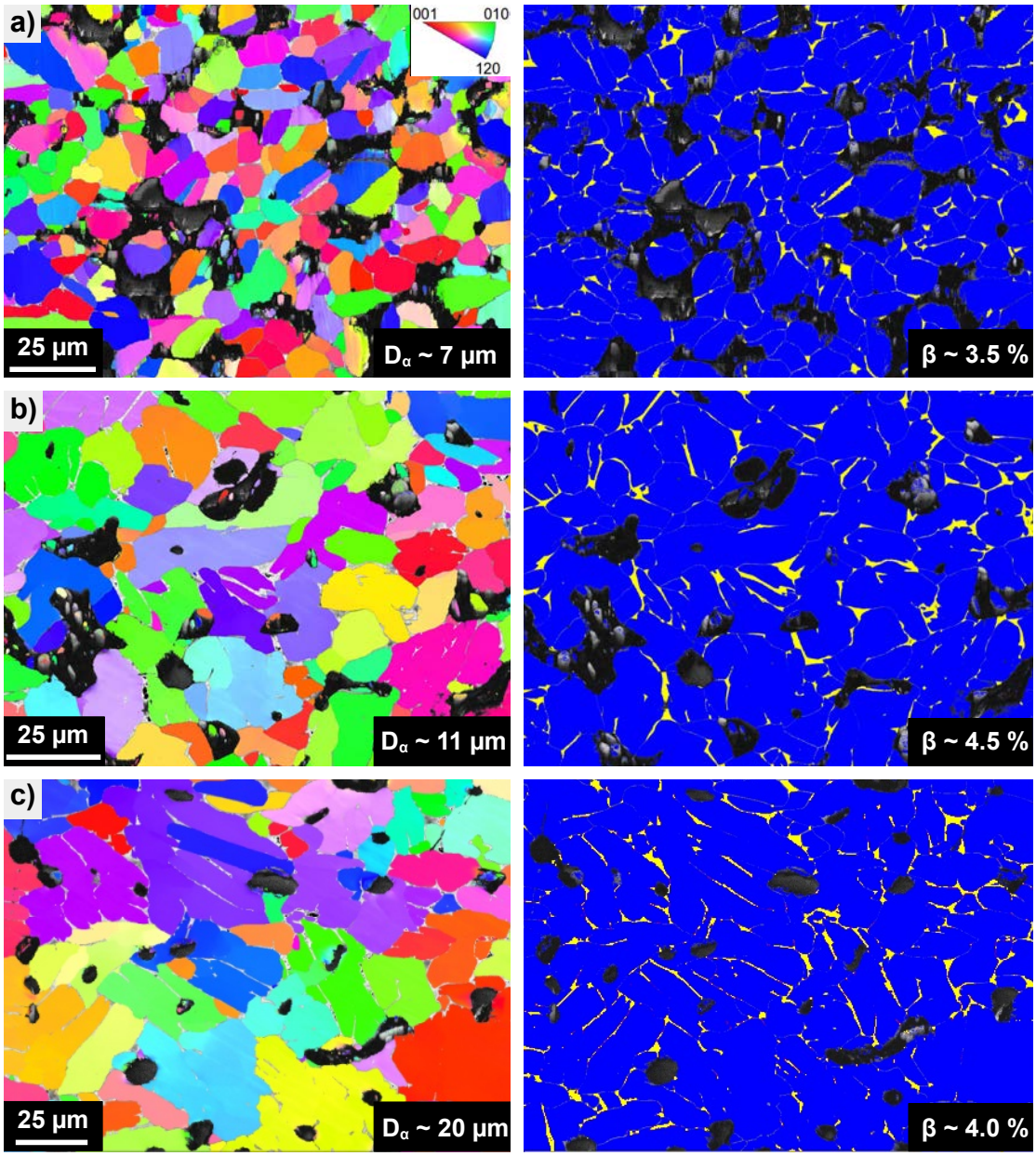

Figure 2.25: Microstructure evolution with sintering temperature: EBSD IPF maps and their associated maps of phase for samples sintered at: (a) 1000 °C, (b) 1100 °C and (c) 1200 °C.

2.3.3 Influence of powder size

To study the influence of the powder size on final structure obtained, three different P25T50 inks were compared:

- one containing 100% of coarse powder (D_{50} = 23 µm)
- one containing 100% of fine powder (D_{50} = 4.3 µm)
- the last one containing a blend: 30% fine powder - 70% coarse powder

All the structures designed with these inks (scaffolds and filaments) were debinded for 30 min at 350 °C and sintered for 2 h at 1200 °C before being analysed. As the powder size is known to influence the driving force of the sintering process, a characterisation of the densities and shrinkages obtained was first carried out.

2.3.3.1 Shrinkage and density

Remaining porosity within filaments was quantified by high resolution X-Ray tomography (voxel size of 0.45 µm) using the same method as described in section 2.3.2.1. X-Ray tomographic sections presented on Fig. 2.26 underline the significant effect of the powder size on the density obtained. Indeed, decreasing the particles mean diameter from 23 to 4.3 µm enables to decrease the remaining porosity within filaments from 12.5 % to 0.025 %. However the use of the powder blend leads to an improvement in densification compared to coarse powder but not compared to fine powder (remaining porosity of 4.4 %).

Bimodal particles size distributions are usually used as they enable to reach higher green density, as shown in German *et al.* work reported on Fig. 2.27(a) [GER 92]. However, with processes such as robocasting, particle rearrangement that takes place during drying and debinding steps probably does not lead to the most optimal stacking. In addition, a higher green density obtained through bimodal distribution does not necessarily lead to an increase in post-sintering density. This intermediate effect observed here, with improvement compared to the 100 % coarse powder case but a decrease in density compared to the 100 % fine powder case has already been observed as shown on Fig. 2.27 (b). Two factors may explain this lower density than with fine powder. The first one is the decrease in coordination number (number of neighbouring particles to a given particle) caused by the addition of large-size powder, which decreases the sintering driving force [GER 16]. The second reason is related to the faster densification of fine particles (compared to coarse ones). This difference in densification rate results in a constrained shrinkage for small particles powder near large particles. This is reflected in the presence of large residual pores near large particles, as schemed on Fig. 2.27 (b) according to German *et al.* [GER 92].

In addition to this global remaining porosity evolution, pore size distributions shown in Fig 2.26 (d) highlight the closure of the interconnected pores network for the two samples containing fine powder. These two samples are thus in their final sintering stage according to Kang (isolated pores only), which is also in agreement with the remaining percentage of porosity being below 7 % for both samples [KAN 04]. However, the filaments made from the powder blend present larger pores than the two others, due to the constrained shrinkage mentioned above.

Also, it should be noted that larger pores can sometimes be observed in samples printed with the ink containing 100 % of fine powder, as reveal by the SEM image presented on Fig. 2.26 (d). This is a result of air bubbles trapped in the ink when it is mixed, and kept despite the printing stage. This problem could be avoided by carrying out the mixing

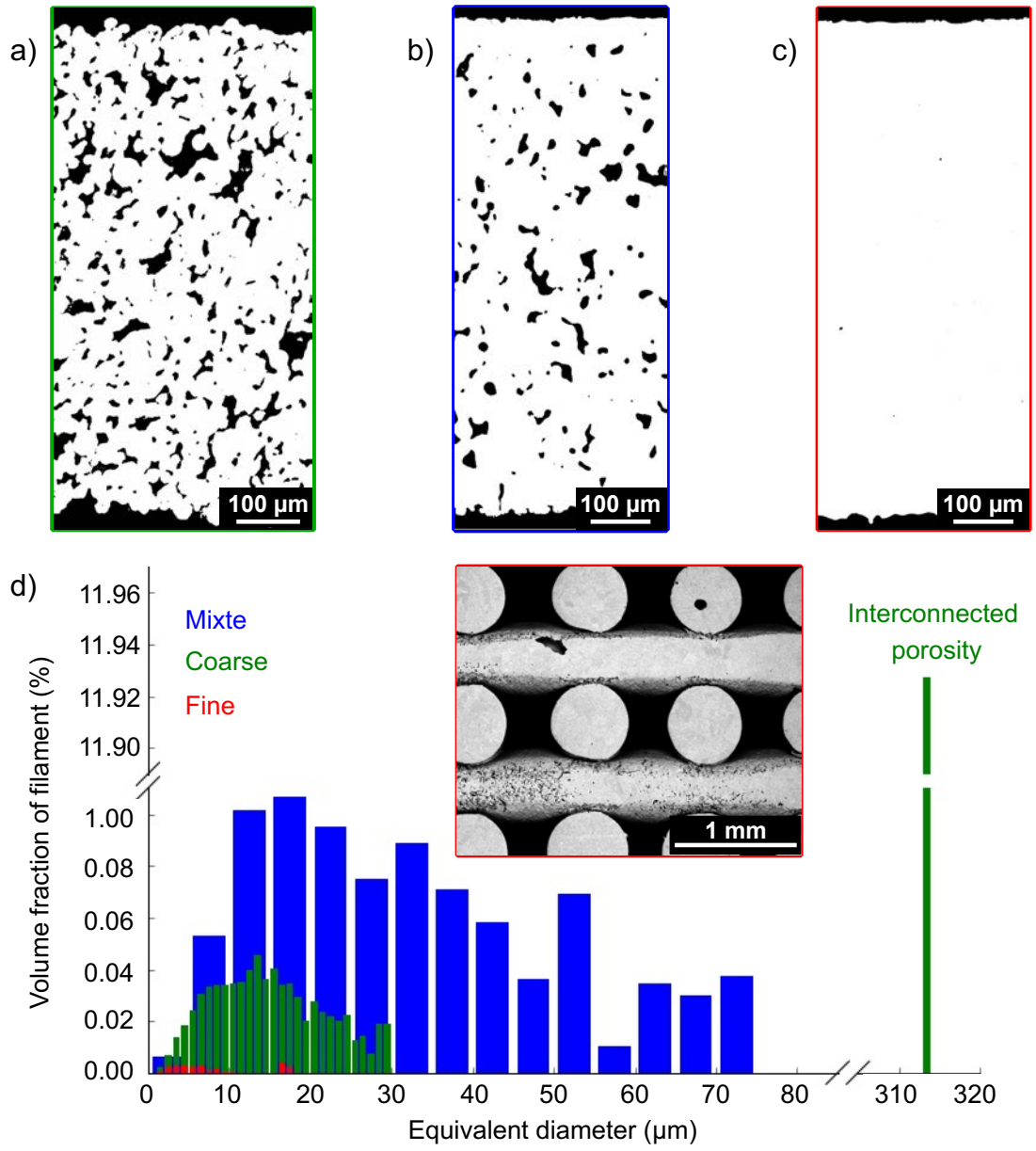

Figure 2.26: Remaining porosity after sintering: Example of tomographic section of sintered filament containing: (a) Coarse powder only; (b) The powder blend; (c) Fine powder only. (d) Pores volume distribution for the three powder batches illustrated with a SEM image of a fine powder scaffold presenting local air bubbles.

steps under vacuum and by using a dedicated transfer system to convey the ink into the syringe.

The observed differences in densification are also accompanied by varying shrinkages. These latters were determined using the method described in section 2.3.2.1. Results are gathered in Table 2.8. Scaffolds used to determine shrinkage were also weighed to access to their density. Relative densities were calculated using $4.43\,\mathrm{g{\cdot}cm^{-3}}$ as reference density

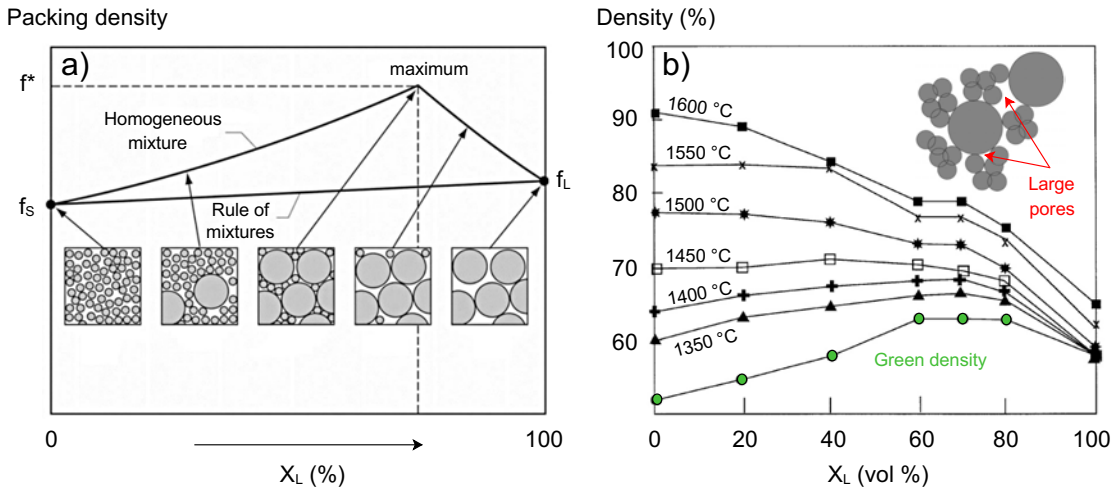

Figure 2.27: Bimodal powder sintering: (a) Packing density evolution with composition of a bimodal powder blend, illustrated with five possible structures. The maximum density for a homogeneous mixture f* occurs at a composition X* which depends on the particle size ratio. Adapted from [GER 92]. (b) Sintering density for mixtures of small ($0.56\,\mu m$) and large ($4.5\,\mu m$) alumina particles. The bimodal large-small particle mixture leads to a higher green density near 70 vol% large particles. However large particles degrade sintering due to constrain shrinkage for small particles next to the large one, as schemed. The highest sintered density comes with small particles alone. Adapted from [GER 16]

for Ti64.

Table 2.8: Process shrinkage and relative density obtained for the different powder size distribution used

Powder used	Shrinkage (%)				Relative density (%)	
	Along X	Along Y	Along Z	Volume	Measured	Designed*
Coarse	15.3 ± 0.3	15.3 ± 0.4	15.2 ± 0.3	39.2 ± 0.3	57.3 ± 1.0	59.38
Blend	16.3 ± 0.3	16.2 ± 0.2	15.3 ± 0.4	40.7 ± 0.6	$60,0 \pm 0.4$	62.84
Fine	18.6 ± 0.2	18.5 ± 0.2	17.0 ± 0.3	44.8 ± 0.2	63.5 ± 0.6	67.84

* Calculated considering CAD design but also remaining porosity within struts.

Contrary to what was observed on more porous samples, the shrinkage here seems to lose isotropy with the addition of fine powder. For the blend and the fine powder, the shrinkage in the stacking direction of the layers is lower than those in the layer deposition plane. In view of the feeling when printing these different inks, it is thought to be linked to an increase in ink stiffness with the addition of fine powder, which prevents the interpenetration of the layers required by the CAD from being respected. Indeed, the same CAD file was used for the three inks, asking for a distance of $672\,\mu m$ between two layers, but the interpenetration seen by both SEM and X-Ray tomography seems to differ depending on the ink used, as shown on Fig. 2.28. It would therefore be interesting to perform oscillatory rheological test to control the evolution of the modulus of conservation

G' according to the powder used in the inks.

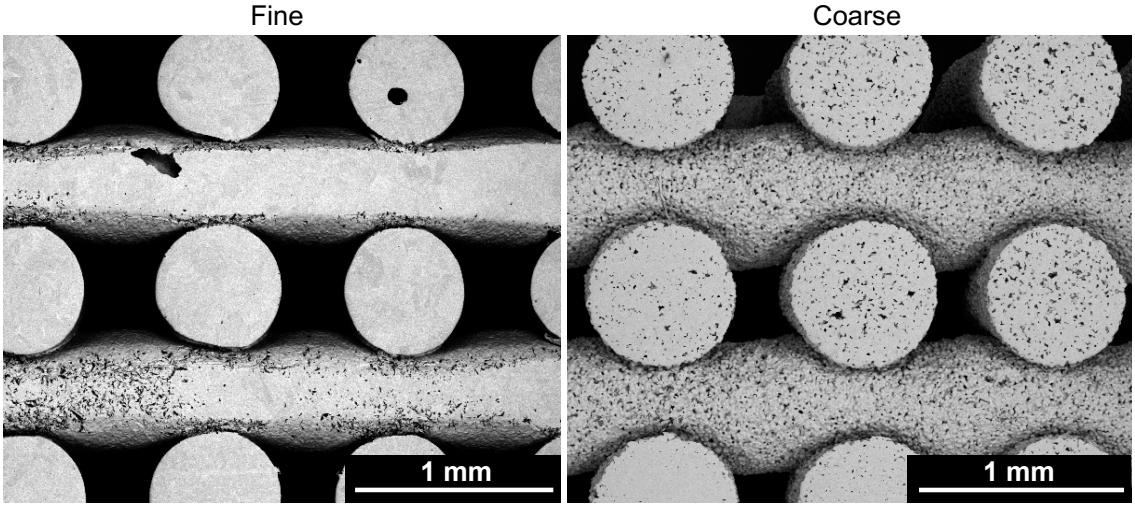

Figure 2.28: Layers overlap: SEM images of samples printed with inks containing fine powder (left) and coarse powder (right). The overlap between layers of the sample with coarse powder is more important than the one of the sample with fine powder.

The variation in density of scaffolds filaments, in addition to the change in the size of the constituent powders, should tend to have a strong impact on the surface roughness of the filaments.

2.3.3.2 Roughness

The parameters commonly used to quantify linear roughness and defined by the IS0 4287 standard are shown on Figure 2.29 and can be defined as follows:

- R_a is the arithmetic mean roughness. It refers to the average of the absolute values of the profile heights with respect to the mean line, over the sampling length.
- R_p is the maximum peak height, given by the highest point of the profile over the sampling length and the mean line.
- R_v is the maximum depth of the valleys, given by the distance between the lowest point of the profile over the sampling length and the mean line.
- R_z is the maximum profile height. It indicates the absolute vertical difference between the maximum height of the peaks and the maximum depth of the valleys over the sampling length ($R_z = R_p + R_v$).

All these parameters for representing the roughness obtained along a line can be extended to surface analysis. They are then referred to as S_a, S_p, S_v and S_z respectively according to the ISO standard 25178.

Beyond these local sequences of peaks and valleys, surfaces may also present waviness motifs that should be removed to avoid distortion of the measurement. The waviness

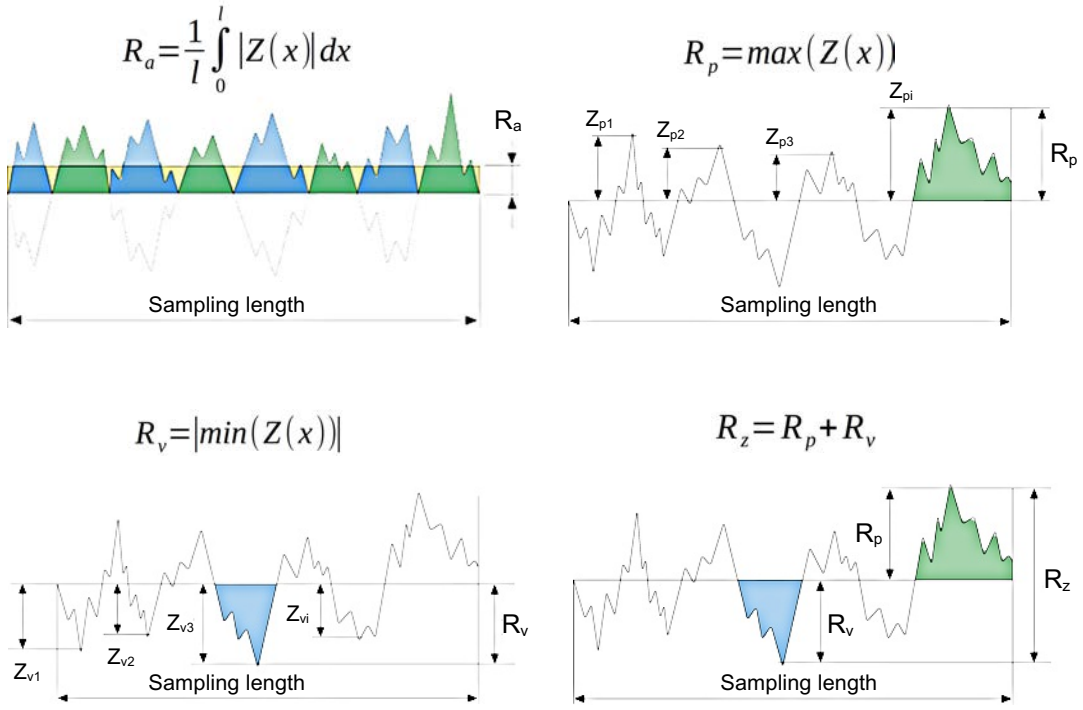

Figure 2.29: Schemes representing the different linear roughness parameters, adapted from [OLY].

motifs are at much lower frequencies than roughness (they represent larger elements) and are therefore eliminated using high-pass filters.

The difference in roughness induced by the different powders batches can be visualised on the 3D reconstructions of the volumes acquired by high-resolution X-ray tomography presented on Fig. 2.30. Surface roughness measurements were performed following filaments and using a Hirox Nano Point Scanner - White Light Confocal system. No tilt correction was necessary for the surfaces analysed, however, a Gaussian filter with a wavelength of 0.8 mm was used to suppress the wave effect. Results are summarised in Table 2.9

Table 2.9: Roughness

Powder	$D_{50}(\mu m)$	**Area** (μm^2)	S_a	S_p	S_v	S_z	R_a	R_v	R_z
Coarse	23	289*2636	9.86	63.0	41.0	104	9.65	38.0	75.5
Mixed	-	225*3880	8.02	40.0	58.2	98.2	6.43	36.8	63.5
Fine	4.3	176*3246	2.54	25.3	30.4	55.6	1.94	11.8	23.0

Linear values were taken along the lines separating the analysed surfaces into two halves. Profiles obtained along these lines are shown on Fig. 2.30. The red line on each of the graphs represents the wave pattern that has been subtracted from the profile to obtain the values.

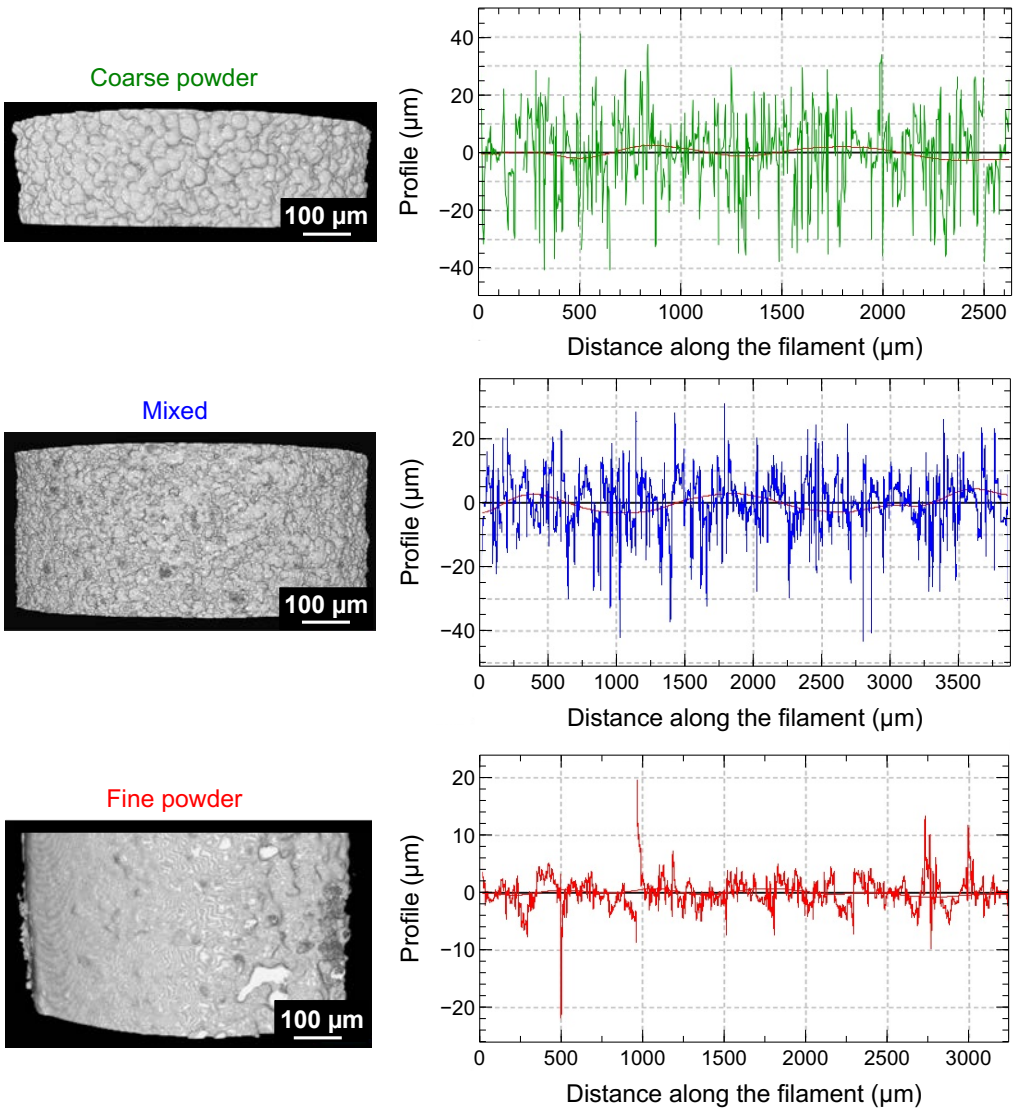

Figure 2.30: Linear roughness profile obtain following a strut of samples from each powder batch with associated 3D reconstructions from X-Ray tomography showing surface aspect.

As expected, roughness is considerably decreased with the use of fine powder leading to almost full densification. Also, it should be noted that linear measurements tend to underestimate the different values compared to surface measurements, simply because of the smaller area of analysis they represent. However, they are still widely used and are therefore interesting for comparisons. It may be worth noting that the roughness obtained from the robocasting process is lower than that obtained by both electron beam and laser beam PBF even in the case of interconnected residual porosity. Indeed, it seems that as-built LPBF parts can present R_a ranging from 10 - 15 to 30 - 40 µm depending on the printing parameters and the building orientations [EDW 14, SIM 14, MIL 16]. In addition, R_z up to 150 - 180 µm have been observed [EDW 14]. Parts obtained by EB-PBF present

even slightly higher values (R_a between 30 and 45 µm and R_v around 200 µm), as shown by Persenot measurements along constitutive struts of a porous structure [PER 18]. Note that keeping a low roughness can be interesting for fatigue resistance properties [PER 18].

2.3.3.3 Microstructure

To complete structural analysis, sample microstructures were investigated through EBSD analysis as shown on Fig. 2.31.

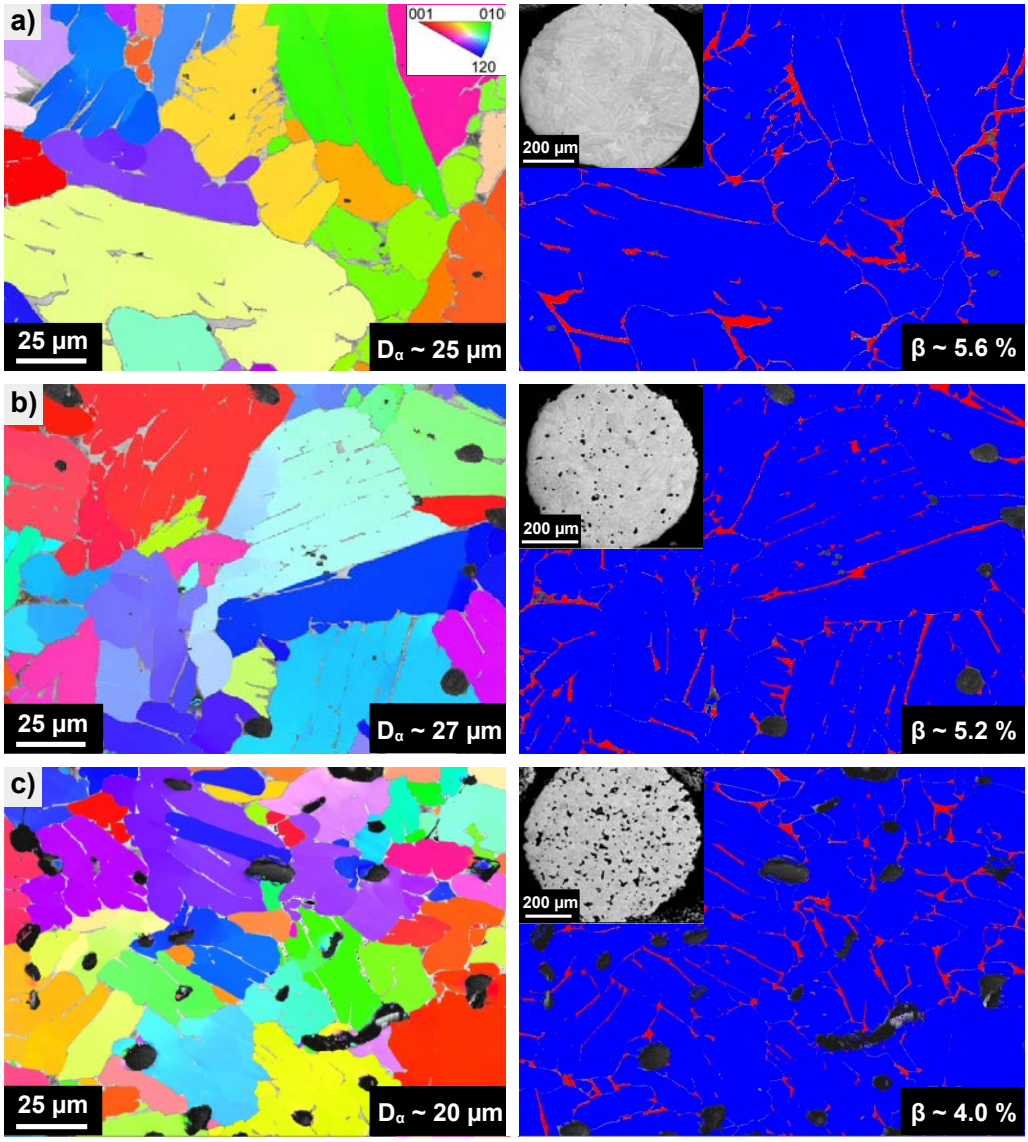

Figure 2.31: Microstructure evolution with sintering temperature: EBSD IPF maps and their associated maps of phase for sintered samples made of: (a) Fine powder; (b) Mixed powder; (c) Coarse powder.

All three types of samples have a similar grain morphology, presenting thick unclosed

lamellae. Of the approximately 300 grains analysed for each case, no major changes in terms of proportion of phases are to be reported, but only a moderate increase in alpha grain size for samples containing fine powder. This might be due to a higher oxygen content reached by fine powder, oxygen being an alphagene element. Indeed, β transus is shifted from 942 °C for a sample containing 0.2 wt% of oxygen, as with the coarse powder, to 1050 °C for a sample containing 1 wt% of oxygen which is the order of magnitude measured for samples made of fine powder. In addition, pores can also impede grain growth. So the fastest densification obtained with fine powder can enable a more important crystal growth.

The difference presented here in terms of density and roughness are obtained for a single temperature meaning that obtaining a material with an intra-filament porosity gradient could be considered.

2.3.3.4 Toward graded material

As a first approach, and as a robocaster can often include several syringe holders, the three inks were successively printed through three different syringes to form a single scaffold. The as-sintered result is shown on Fig. 2.32. Particular attention should be paid to the alignment of the different syringes to avoid the formation of a misalignment when changing the ink.

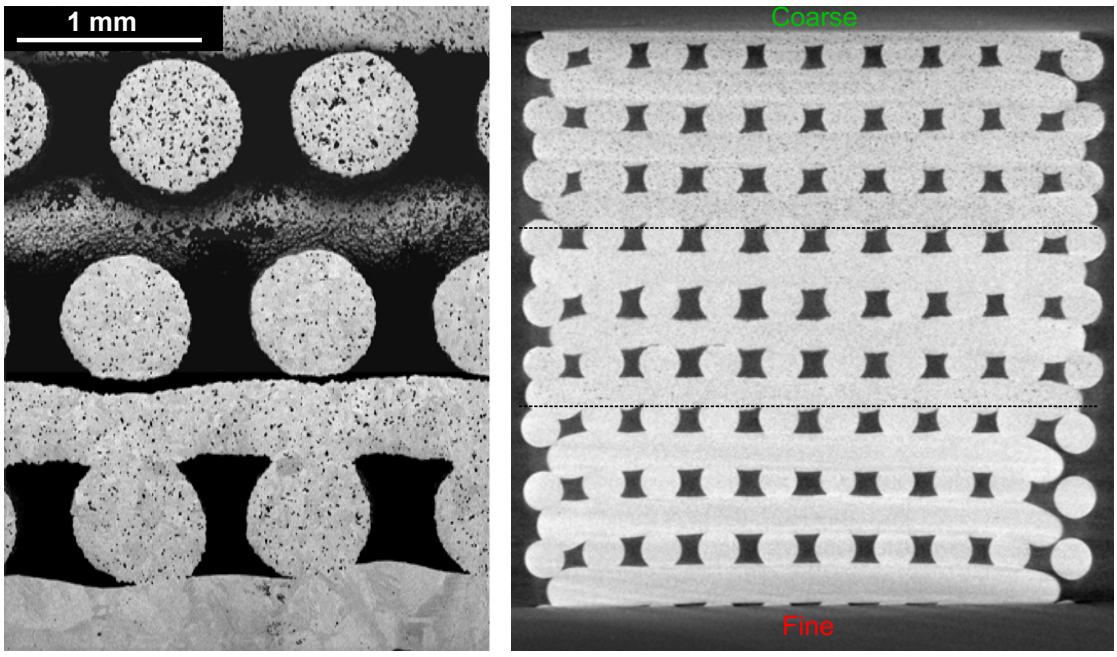

Figure 2.32: SEM image and X-Ray tomographic section of two different scaffolds presenting graded microporosity (within filaments) The right sample being one of the samples dedicated to the compression test, it has a larger number of layers.

Despite the difference in shrinkage between each ink, no crack formation was observed by X-ray tomography. However, the filaments of the ink with the highest shrinkage show a curvature probably related to the stresses exerted by this difference in shrinkage. This type of deformation could be avoided by adding intermediate cases. Gradual mixing can even be envisaged using systems such as the ink mixer directly feeding the nozzle as proposed by [ORT 19].

2.4 Conclusion and perspectives

The main findings to be retained at the conclusion of this chapter are presented in the figure 2.33.

First, a printability study was conducted by varying both the amount of Pluronic F127 and the solid loading. Comparison between the volumes obtained by scanning the dried samples through X-Ray tomography and the CAD input file showed that P25T50 and P30T50 inks gave the best printing accuracy. However, to facilitate the debinding step and limit the contamination risk only ink P25T50 was retained to continue the study.

The risks of contamination during debinding are indeed not negligible. This study revealed that the debinding temperature commonly used for ceramics shaped using pluronic is not suitable for Ti64. Indeed a debinding of two hours at 500 °C leads to high oxygen and carbon uptakes that further lead to carbide precipitation in the beta phase during the cooling from sintering temperature. The final carbon and oxygen content are in this case far above the ASTM standard F1108 requirements. Decreasing the debinding treatment time and temperature to 30 min and 350 °C enables to decrease the final carbon content below the 0.1 wt% required for surgical implants. However the oxygen level remains slightly above the required value (0.219 wt% for 0.2 wt% asked).

However, it should be noted that efforts to limit oxygen uptake have only been concentrated here on the debinding stage. It would be interesting to check what can be achieved by extending this effort to paste composition and sintering stage. Indeed, interactions have sometimes been observed at the points of contact between sample and quartz tube used to work under vacuum. Local changes in colour were correlated to Silicium and Oxygen presence according to EDS analysis. Similar problems of interaction with the support or the sintering mould have already been observed and it appears that yttria supports should be preferred [BAR 10, REI 12]. In addition, initial powder used, in terms of both size and composition, also plays an important role on the final oxygen content obtained [BAR 10]. These two lever arms should therefore be studied in order to continue to reduce oxygen intake.

Then structural analyses were conducted to assess the impact of both sintering temperature and powder size. As expected, increasing the sintering temperature leads to an increase in density. However, with the coarse powder (mean diameter around 23 µm),

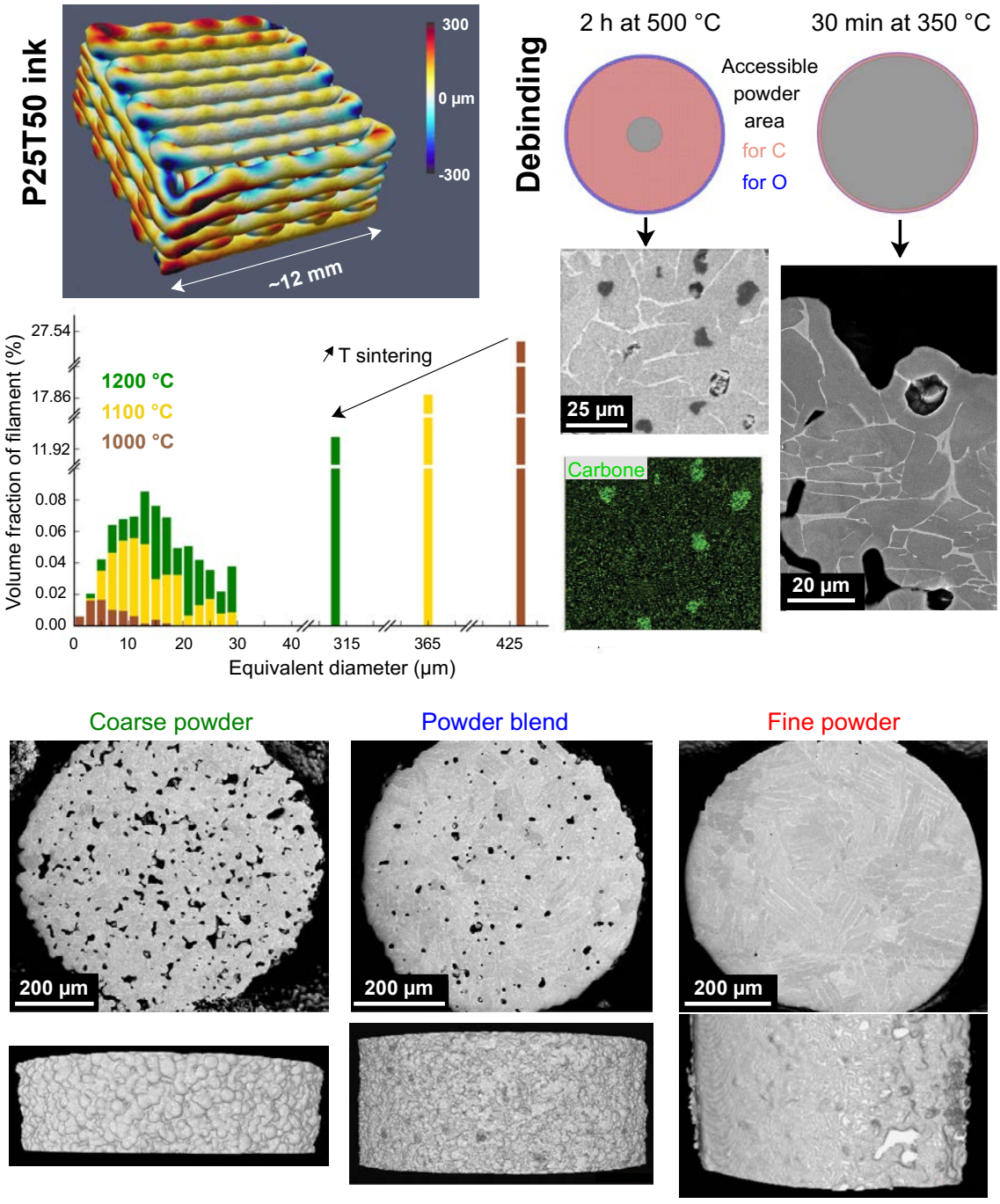

Figure 2.33: Graphical summary containing main results presented in this chapter.

the three temperatures used enable to keep an interconnected microporosity within filaments. The interconnection neck mean size remains stable around 4-5 µm, which might be suitable for the formation of mineralised tissues [BOH 17]. Decreasing the powder size (at the same sintering temperature) also increases the densification of the filaments while

reducing the surface roughness. In this way, it is possible to obtain almost dense filaments (0.025 % porosity) by sintering fine powders (mean diameter: 4.3 µm) for 2 h at 1200 °C. Using a powder blend at 30 vol% of fine powder leads to a intermediate densification state between what can be obtained with only fines and only coarse. This therefore opens up the possibility of creating materials with a microporosity gradient in the filaments.

However, some additional characterisations are still needed to understand the difference in shrinkage in the stacking direction of layers for inks containing fine powder. Indeed, these inks seem to retain their shape particularly well after printing, reducing interpenetration between layers compared to what is required by the CAD file. Performing oscillatory rheological tests would be a way to ascertain the influence of powder size on ink stiffness (G'). This should also be completed with an evaluation of discrepancy from CAD file for these inks. Asking a lower layer overlap (for example by using a distance between layers of 0.9 times the nozzle size instead of 0.8) should be enough for these inks and might lead to a better compliance with the CAD file than the one measured for ink with coarse powder. A complete understanding of shrinkage phenomena is in fact necessary in order to be able to choose the dimensions to be entered in the CAD file according to the dimensions desired for the final part.

Once the structural characteristics of the different obtainable scaffolds have been evaluated, it is necessary to verify that their mechanical and biological properties are in accordance with the intended application.

Chapter 3

Functional properties of Ti-6Al-4V scaffolds manufactured by robocasting

Contents

3.1 Background

3.1.1 Mechanical properties of Ti64 for medical application

Ti64 mechanical properties strongly depend on its thermal history, as it influences final microstructural characteristics of the alloy (phase distribution, crystallographic grain morphology and size), as shown in section 2.1. However, for biomedical applications, Ti64 and Ti64 ELI are usually used in their annealed and mill-annealed state respectively, leading to the properties given in Table 3.1 [NII 98].

Table 3.1: Mechanical properties of Ti64 for biomedical application according to [NII 98]

Alloy	Tensile strength (MPa)	Yield strength (MPa)	Elongation (%)	Young's Modulus (GPa)
Ti64	895 - 930	825 - 869	6 - 10	110 - 114
Ti64 ELI	860 - 965	795 - 875	10 - 15	101 - 110

With its density of $4.43\,\mathrm{g cm^{-3}}$, Ti64 presents an interesting strength-to-weight ratio. However, with regard to an application as a bone implant, its Young's modulus of 110 GPa is still much higher than that of bone (3 - 20 GPa). Although the use of Ti64 already represents a reduction in the stiffness mismatch encountered with other alloys used in orthopaedic surgery, it is not yet sufficient to overcome the phenomenon of stress shielding [GUI 05]. Porous structures might thus be a way to avoid this phenomenon that is one of the most common causes of arthroplasty failure [GUI 05]. However, care must be

taken to ensure that the introduction of porosity does not impair the strength properties too much. However, one of the most important risks in terms of mechanical property compromises with robocasting of Ti64 could be the enrichment in interstitial contents, linked to the presence of the binder.

3.1.2 Embrittlement by interstitial elements

Unlike hydrogen atoms, that can be found in the tetrahedral vacancies of the β phase, oxygen, nitrogen and carbon atoms are located in octahedral sites of the α phase. However, as hydrogen, these interstitials have been reported to highly affect titanium alloys ductility and mechanical properties in general. As they are acting in a similar way by strengthening titanium and titanium alloys structures, their contributions can be gathered together in the form of an equivalent oxygen content. This oxygen equivalent is defined as [OGD 55, YAN 14]:

$$O_{eq} = [O](wt\%) + 2[N](wt\%) + 0.66[C](wt\%) \tag{3.1}$$

This definition leads to maximal oxygen equivalents of 0.366 and 0,2828 wt% for Ti64 and Ti64 ELI respectively, considering the maximal content allowed for each element by ASTM F1108 and F136 standards respectively.

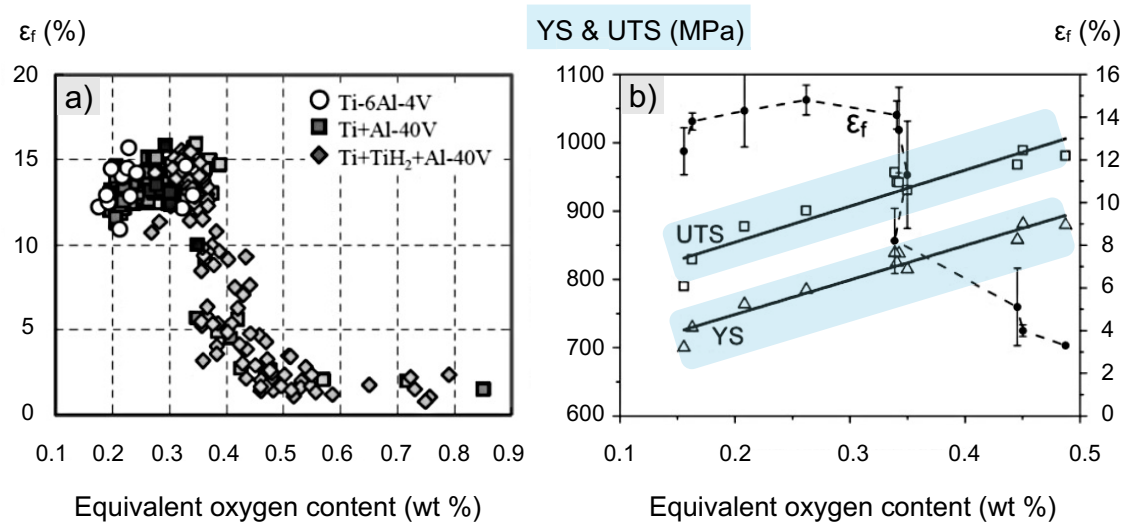

Figure 3.1: Tensile elongation of as sintered Ti64 *versus* equivalent oxygen content as presented in Yan *et al.*'s review: (a) Samples obtained by MIM of either prealloyed powders or different powder blends, (b) Samples obtained by MIM of prealloyed Ti64.

Its effect on mechanical properties, and especially on elongation at break, was extensively studied on Ti64 parts obtained by Metal Injection Moulding (MIM). Indeed this process involves the use of large amount of binder and therefore debinding and sintering

treatments, which increases the risks of interstitial enrichment. Thus numerous studies are conducted to try to define an acceptable limit in terms of equivalent oxygen content [BAR 10, YAN 14, EBE 17]. Results usually show a drastic decrease in ductility for an equivalent oxygen content around 0.35 wt% as highlighted by Fig.3.1 taken from Yan *et al.*'s review.

As seen in the previous chapter, varying the parameters of the process (and in particular of the debinding step), can lead to extremely variable interstitial contents. This would therefore have consequences on mechanical properties that have to be quantified.

3.2 Evolution of mechanical properties with process parameters

3.2.1 Methods

To access to the intrinsic material properties, three-points bending tests were conducted on 10 constitutive filaments of each condition, using an Electroforce 3200 test machine (Bose, Eden Prairie, MN) equipped with a 22 N load cell. Tests consisted in a preload of 0.2 N, followed by a loading rate of $0.05\,\mathrm{N{\cdot}s^{-1}}$. The length between the two support points was fixed at 10 mm. Since the cross-sectional area may vary slightly from one sample to another, the actual cross-sectional area of each sample was measured using a RH-2000 microscope (Hirox Europe, Limonest, France) to enable the calculation of the quadratic moment corresponding to each sample. Calculations were performed at the point of rupture, considering the quadratic moment of the fracture surface. It was then possible to plot stress-train curves for each sample considering the following relations:

$$\sigma = \frac{FL}{4I}y \tag{3.2}$$

And

$$\epsilon = \frac{6Dy}{L^2} \tag{3.3}$$

with F the force applied on the sample, L the distance between support points, I the quadratic moment, y the distance to the neutral axis and D the deflection.

In addition, Vickers hardness tests were performed on previously polished scaffolds cross-sections. The load used was sufficiently low (500 gf) to characterise only filaments and not whole structures, as highlighted on Fig.3.2. Average values were calculated on more than 10 measurements.

Finally, compressive tests were conducted on approximately cubic scaffolds, using an Instron 8502 universal testing machine, equipped with a 100 kN load cell. Tests consisted in a preload of 100 N, followed by a strain rate of $0.05\,\mathrm{min^{-1}}$. Tested samples were made

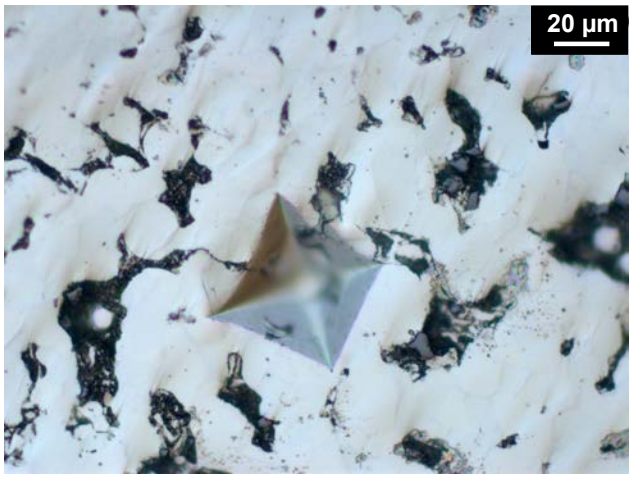

Figure 3.2: Example of an indent obtained during micro-hardness measurements on a sample sintered for 2 h at 1100 °C.

of 18 layers of 10 struts, to follow Ashby's advice on preventing size effect by having at least 7 times the foam cell size in each direction [ASH 00]. Upper and lower surfaces were polished prior to tests, in order to get flat and parallel surfaces. Stress-strain curves were then obtained after correcting the data from the machine stiffness (measured on a sample with known stiffness: aluminium alloy 2017A at T4 with a Young's modulus of 74 GPa). One side of the tested sample was filmed using a mvBlueFox camera, to follow sample surface damages. In addition, one compressive test per sample type was interrupted several times at different loads, to enable the evaluation of damage in 3D by X-Ray tomography.

Images obtained by filming the samples and X-Ray tomographic volumes acquired after each interruption can allow to perform Digital Image correlation (DIC) and digital volume correlation (DVC) respectively. The purpose of correlating digital images (or volumes) is to digitally reconstruct the field of movement that describes the evolution of the reference image towards the distorted image. To do so, the whole region of interest (ROI) must be divided into sub-images (or sub-volumes) identifiable by a unique greyscale pattern. The optical flow equation (3.4) then allows to consider that the variations of the grey levels between the two images are only due to the displacement of the material points.

$$f(x) = g(x + u(x)) \tag{3.4}$$

where f corresponds to the reference ROI and g to the distorted ROI, x is the vector giving the current point position (with respect to the ROI coordinate system) and u the unknown displacement vector field.

The method of least squares is then used to solve this problem. The technique consists

in minimising, by taking into account a displacement u, the following residue :

$$\phi_c^2\ (u) = \frac{1}{2} \iiint_{ROI} [f(x) - g(x + u(x))]^2 \mathrm{d}x \tag{3.5}$$

Since the residue is dependent on u in a non-linear way, the resolution method consists in solving this problem iteratively by displacement increments du. To find more details on resolution method, please refer to chapter 3 of Lachambre's thesis [LAC 14]. The criteria for validating the solution over a number of iterations are:

— Error stabilisation $\phi_c^2\ (u) \rightarrow \epsilon$

— Convergence of the displacement increment du towards 0

If the difference between the two images is too great, there is a risk that the calculation will not converge. It was therefore tried to target around 0.2 mm of displacement only, between two interruptions to scan the sample by X-Ray tomography.

In this study, DIC was used in a second step, to check and, if necessary, correct what was obtained from the displacement measured by the compression machine. DVC was rather used as a means of visualising possible inhomogeneity of deformation in the samples, allowing the location of damage to be predicted. These two techniques could be used thanks to the precious help of Joël Lachambre.

3.2.2 Influence of rheology

While the control of the rheology is important for the shaping stage, it can also influence the properties obtained. This phenomenon has only been highlighted through compressive tests performed on samples printed with the coarse powder (P25T50 ink).

Two different conditions were used for these tests: the first scaffold was printed shortly after taking the ink out of the fridge, whereas the two other scaffolds have been printed after reaching temperature equilibrium at 25 °C. The first case (below 25 °C) was used as a way to assess the robustness and limitations of the process by giving an overview of the rheology impact on final properties. The three scaffolds were then debinded for 30 min at 350 °C under dynamic vacuum and sintered for 2 h at 1200 °C before being tested. Stress-strain curves under compression are presented on Fig. 3.3.

First it can be observed that evolutions of stress-strain curves are really similar except for the stress drop on the blue curve representing the first scaffold (Fig. 3.3 (a)). This drop in stress can be explained by the preferential densification of the last two printed layers, as shown on Fig. 3.3 (d). This phenomenon highlights the importance of controlling temperature with precision when printing pluronic based ink. Indeed, a temperature a little bit too low can lead to a not stiff enough ink, thus to a compaction of the first printed layers under the weight of the following ones, inducing a density gradient between the top and the bottom of the sample. This leads to a preferential densification of the less dense layers under compressive load, before getting a more homogeneous densification.

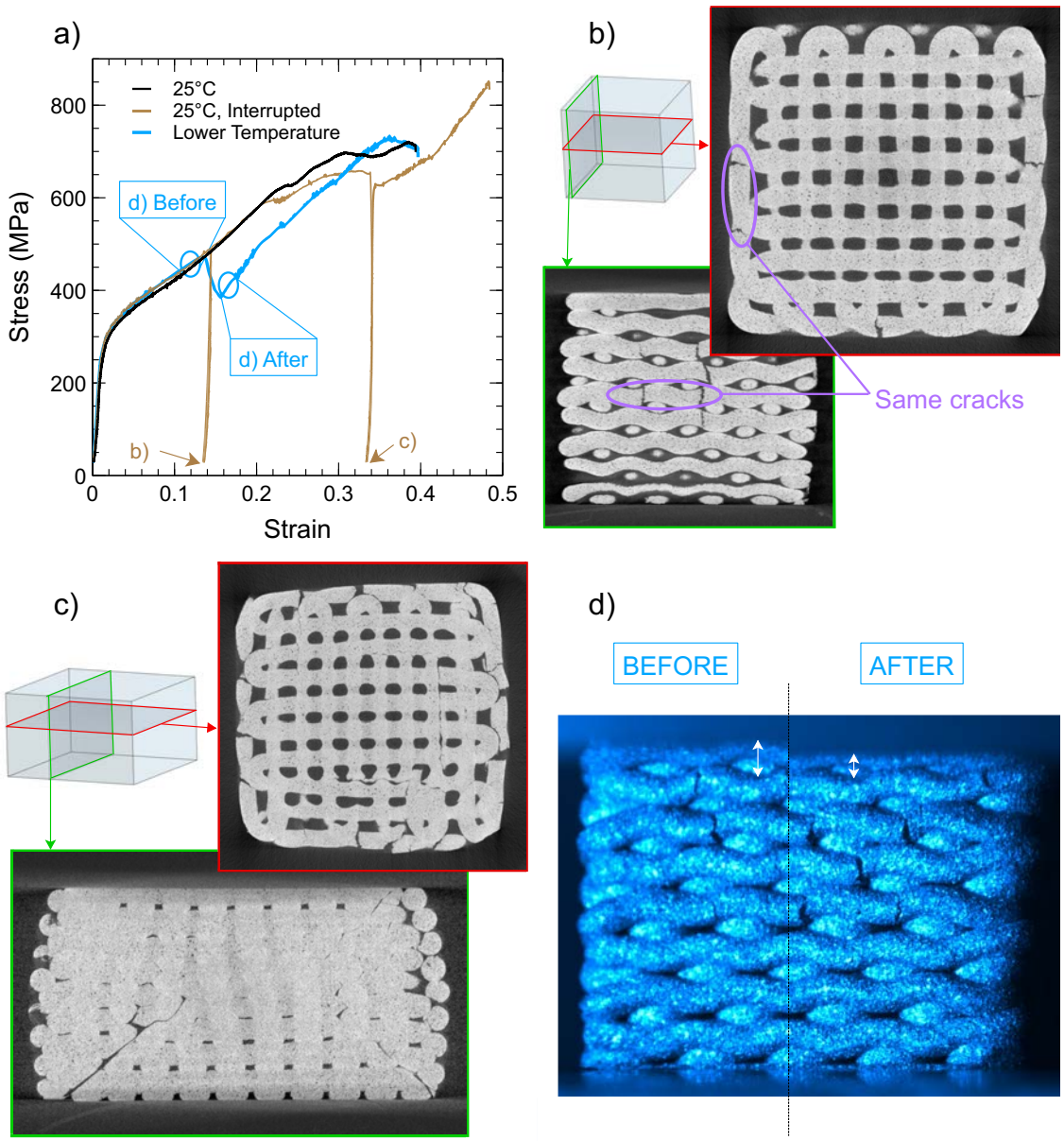

Figure 3.3: Importance of ink rheology highlighted by compressive tests : (a) Stress-strain curves obtained for the 3 samples printed with the P25T50 ink; (b) X-Ray tomographic sections showing only surface cracks for a $\sim 14\%$ strain; (c) X-Ray tomographic sections showing internal cracks at $\sim 33\%$ strain; (d) Images registered by the camera before and after the stress drop.

Formation of vertical cracks were observed on surfaces of the three samples, during the densification that follows the elastic domain. The first crack was formed for a 5-6 % strain and was then followed by other cracks. X-Ray tomography performed during interrupted compression, and realised in this densification domain confirms that these cracks are only located in outer filaments (see Fig. 3.3 (b) that shows one example of scan

during densification domain). They are parallel to the loading direction and propagate only across one strut. At this stage, interfaces between layers seem sufficient to stop their propagation. Note also that their initiation does not lead to a stress drop or a plateau (Fig. 3.3 (a)) as the stress continues to rise with increasing strain. This phenomenon might be related to the ink/process combination, which leads to greater sagging of the external filaments than the internal ones.

This densification domain is followed by a plateau on the stress-strain curve that occurs when the scaffold is almost fully dense in the compression direction (Fig. 3.3 (a) and (c)). According to Fig. 3.3 (c), this plateau is due to the initiation of larger cracks that cross several struts at the same time and propagate at 45° to the compression direction. These cracks appear a little bit later for samples printed with a less stiff ink, as sample density after homogenisation through last printed layers densification is globally higher than density of the two other samples. At this stage, it can be considered that the sample failure is reached, even though no stress drop is observed yet.

Rheology can therefore have consequences not only on the compliance with the required shape but also on the mechanical properties. In order to follow the progress of the robocasting process, the next parameters that can lead to differences in mechanical properties are the debinding conditions.

3.2.3 Influence of debinding temperature

As shown in section 2.3.1, debinding conditions strongly influence interstitial contents in Ti64. But oxygen and carbon enrichments (and resulting microstructure) have detrimental consequences on mechanical properties. As mentioned in section 2.3.1.2 a carbon enrichment during debinding can help to prevent oxidation during sintering. But as both carbon and oxygen can affect ductility, a compromise between carbon uptake and oxidation should be found. Thus the use of an equivalent oxygen content, calculated according to the contribution of each interstitial element on mechanical properties, might be helpful. This equivalent oxygen can be calculated according to the equation 3.1, given in section 3.1. As the range of measured nitrogen concentration is really narrow (see Table 2.5 of section 2.3.1.2), O_{eq} values were calculated using a concentration of 0.01 wt% of nitrogen for all sintered samples that were debinded at 350 °C.

To access to the interstitial content consequences on intrinsic mechanical properties of printed Ti64, without being influenced by structural effects, 3-points bending tests were first performed on filaments. These tests were performed on the three conditions D500-S1200, D350-S1200 and D350Ar-S1200, these materials representing respectively the largest, lowest and an intermediate value of O_{eq}. Stress-strain curves presented on Fig.3.4 show that D500-S1200 samples are fully brittle whereas the two other conditions lead to a bit of ductility. The ultimate stress decreases with increasing interstitial amount. As a result, the ultimate strength of the least brittle sample (D350-1200) is twice higher

than that of the most brittle one (D500-1200).

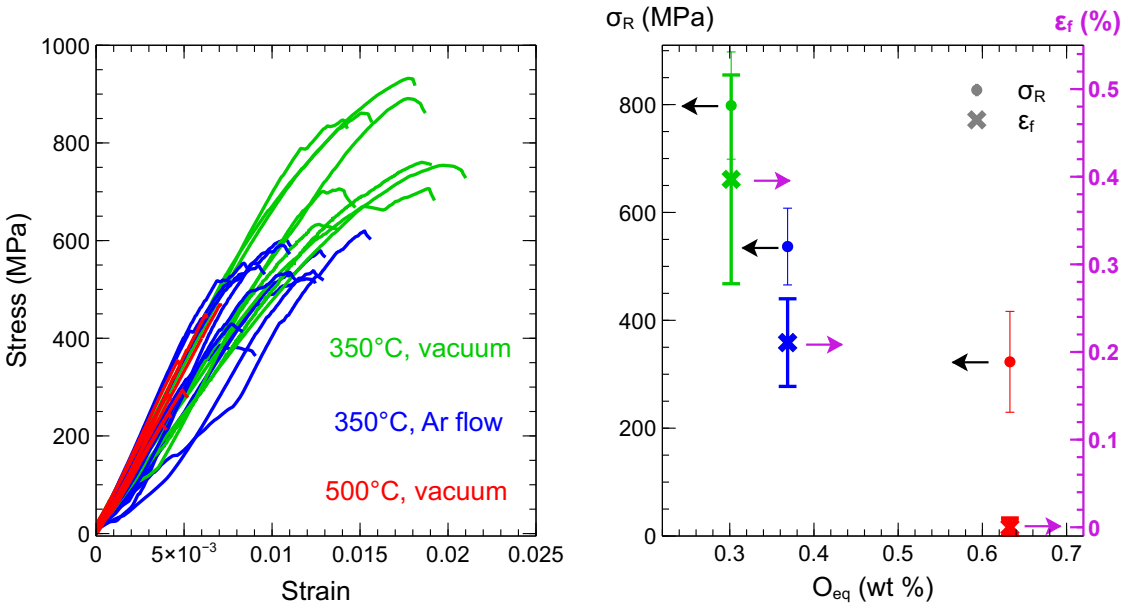

Figure 3.4: Three-points bending tests: Stress-strain curves obtained for D500-S1200, D350Ar-S1200 and D350-S1200 with their associated ultimate stress and elongation at break as a function of O_{eq}.

While the use of $0.2\,\mathrm{L{\cdot}min^{-1}}$ argon flow does not lead to mechanical strength as high as the dynamic primary vacuum due to higher oxygen and carbon contamination, it seems to reduce scattering of the results. Thus it would be interesting to check whether increasing the flow would reduce carbon and oxygen pollution or not.

Young's modulus measured with the stress-strain curves are (60 ± 9) GPa, (70 ± 9) GPa and (68 ± 7) GPa for D350-S1200, D350Ar-S1200 and D500-S1200 respectively. Considering the high standard deviation, no obvious influence of debinding conditions on the Young's modulus can be determined here. However, it should be mentioned that these Young's moduli are consistent with the remaining porosity measured within filaments (12.5 vol%) [OH 03].

Fracture surfaces shown on Fig.3.5 confirm both the brittle behaviour of D500-S1200 samples which are fully cleaved, and the mixed brittle-ductile behaviour of samples debinded at 350 °C which present dimples in addition to cleavage. Zooms on cleavage sites have been performed and EDX analysis presented on Fig.3.5 (c) and (d) shows that carbides can be found for D500-S1200 samples. Carbides could not be detected at cleavage sites of samples debinded at 350 °C (fig 6 (c)), neither by XRD nor by SEM.

Carbides presence on the cleavage site shown on Fig. 3.5 (d) highlights their role in initiating the cleavage, in agreement with cracks location observed in Ti64/TiC composites [da 05]. However, oxygen is also known to decrease the ductility of titanium, although only present in solid solution [YAN 14]. Thus for samples containing high con-

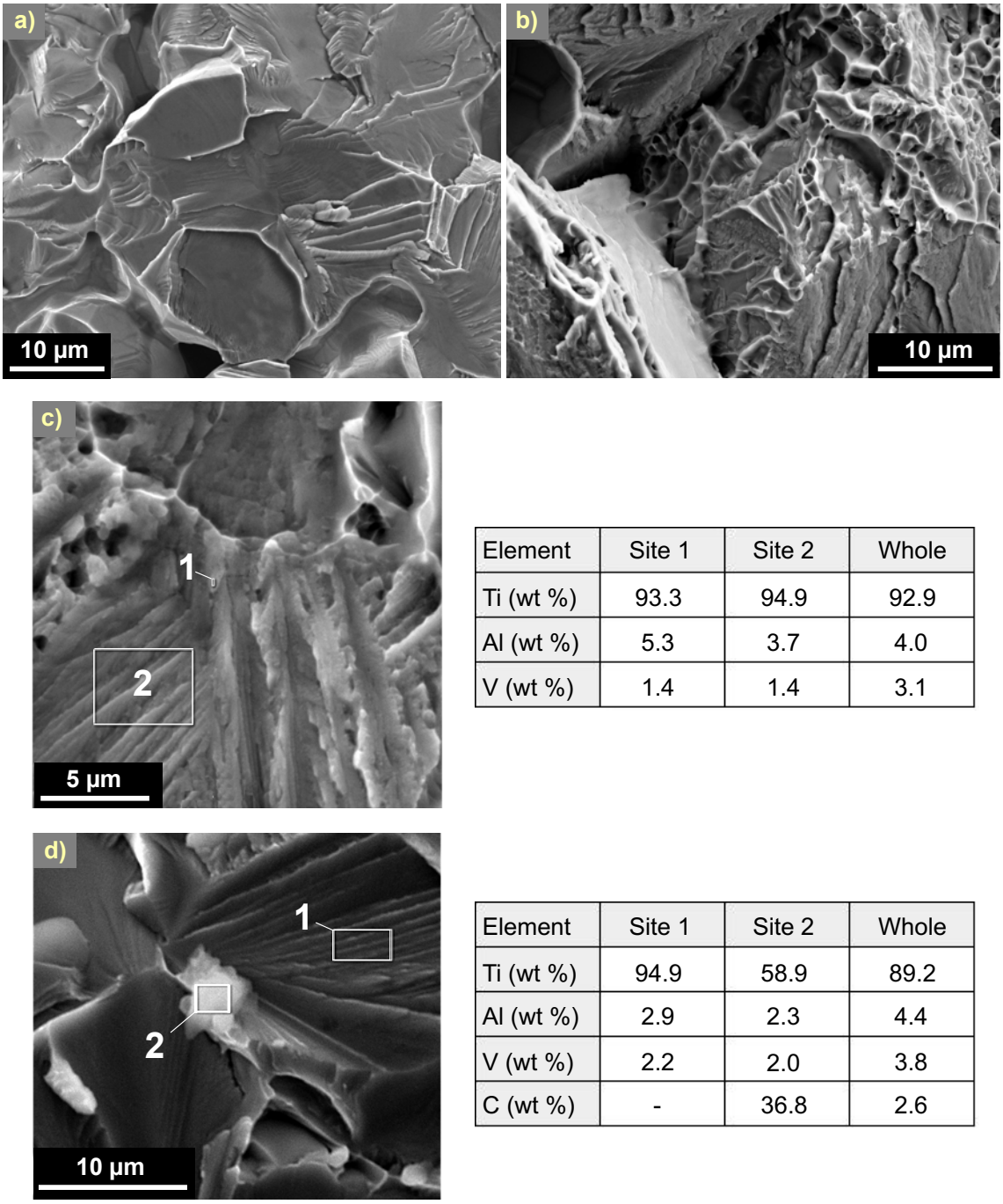

Element	Site 1	Site 2	Whole
Ti (wt %)	93.3	94.9	92.9
Al (wt %)	5.3	3.7	4.0
V (wt %)	1.4	1.4	3.1

Element	Site 1	Site 2	Whole
Ti (wt %)	94.9	58.9	89.2
Al (wt %)	2.9	2.3	4.4
V (wt %)	2.2	2.0	3.8
C (wt %)	-	36.8	2.6

Figure 3.5: Fracture surfaces: (a) Surface of D500-S1200 showing brittle behaviour (cleavage); (b) Surface of D350-S1200 showing mixed ductile-brittle behaviour (cleavage and dimples); (c) Focus on a cleavage site of D350Ar-S1200 showing the presence of an oxide (EDX analysis); (d) Focus on a cleavage site of D500-S1200 showing the presence of a carbide.

tents of different interstitial atoms, elongation at break is usually represented as a function of equivalent oxygen content to try to define an acceptable limit.

In order to get rid of the differences in absolute values obtained due to the difference in porosity of the tested samples, behaviours obtained in this study were compared to behaviours obtained by MIM by plotting ϵ_f / ϵ_0 ; ϵ_0 being the elongation at break obtained for the most ductile sample. This enables to highlight the similarity of behaviours with a ductility drop for an equivalent oxygen content around 0.35 wt% (see Fig. 3.6).

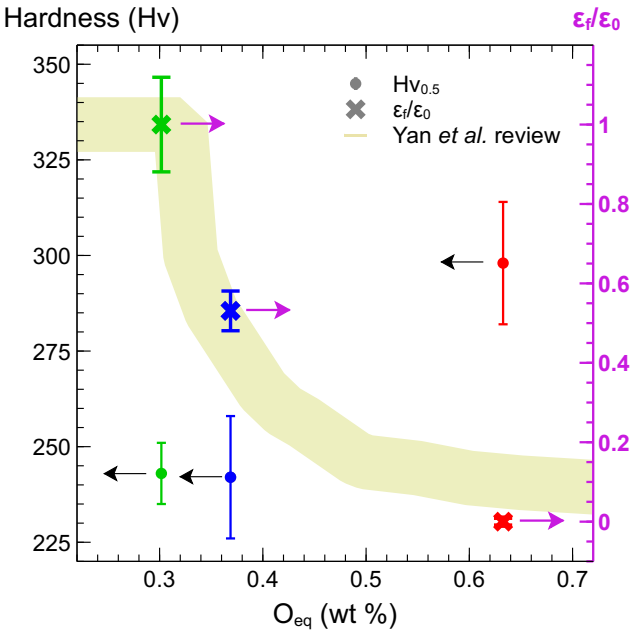

Figure 3.6: Hardness and elongation at break evolution as a function of equivalent oxygen content.

In addition to three-points bending tests, Vickers hardness was measured for the same three conditions. D350-S1200 samples present a $HV_{0.5}$ of 243 ± 8, which is in agreement with values already observed on Ti64 samples with similar sintering density [CHÁ 17, SON 12, OH 13]. However, D500-S1200 sample presents a higher hardness, (298 ± 16) $HV_{0.5}$, which can be attributed to the higher equivalent oxygen [BAR 10].

These two kinds of tests (3-points bending tests and Vickers hardness) highlight the impact of interstitial amounts (and so the impact of debinding conditions) on intrinsic properties of printed Ti64. However, as the purpose is to get architectured structures, it is also important to measure the consequences of these interstitials on scaffolds mechanical response.

Compression tests were performed on scaffolds from the two extreme debinding conditions, D500-S1200 and D350-S1200. Stress-strain curves are shown on Fig. 3.7.

First it can be observed that the global behaviour of the two kinds of samples is similar. The elastic domain is followed by densification during which vertical cracks are formed on sample outer filaments, as shown for D500-S1200 on Fig. 3.7. This phenomenon has been previously observed on D350-S1200 (section 3.2.2). Then an internal crack is initiated

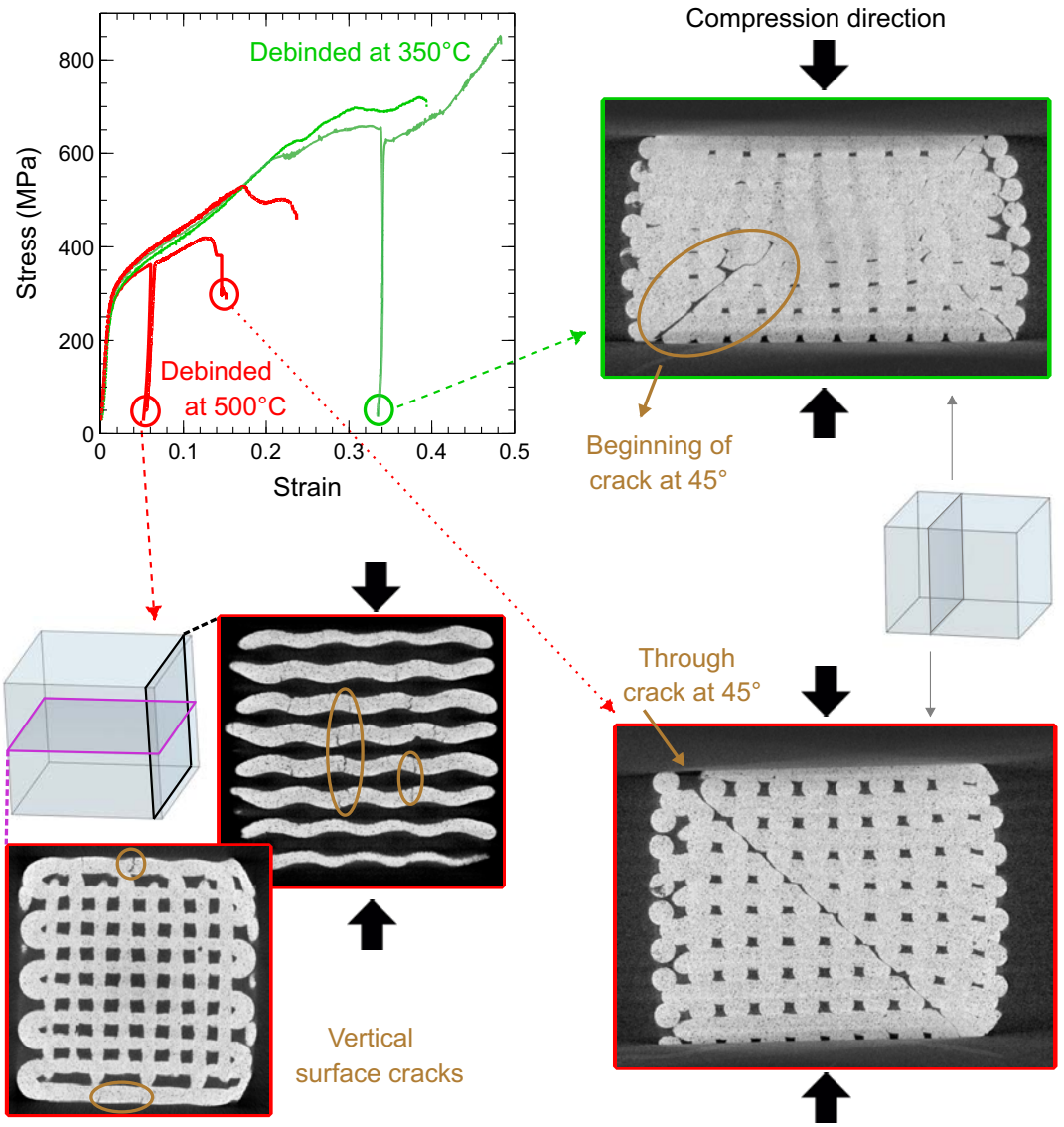

Figure 3.7: Compressive tests : Stress-strain curves obtained for both D500-S1200 and D350-S1200; X-Ray tomographic sections of both cases showing internal damage for different strain levels.

and propagates at 45° throughout the sample. However, vertical cracks formed in outer filaments are initiated earlier in D500-S1200 samples than in D350-S1200. Indeed first crack is observed for a strain of 3-4 % in D500-S1200 samples (5-6 % in D350-S1200). In the same way, the crack that propagates at 45° to the direction of compression is initiated earlier and propagates faster for the D500-S1200 scaffolds than for D350-S1200 as highlighted on Fig. 3.7. For D350-S1200 samples, tests were stopped at 90kN to prevent damage to the load cell, thus the ultimate strength was not measured.

Both D350-S1200 and D500-S1200 present similar Young's Modulus (around 30 GPa)

and yield stress (around 250 MPa). Although the yield stress of D500-S1200 seems to be a bit lower and more scattered than the one of D350-S1200 (246 vs 265 MPa), further statistics are needed to confirm this difference.

In light of both bending tests on constitutive filaments and compressive tests, scaffold structures allow to recover some ductility. However, the difference in interstitial amount between D500-S1200 and D350-S1200 scaffolds still leads to an important difference in ductility. Thus debinding temperature used after DIW of titanium should always be chosen as low as possible. It could then be interesting to work on ink formulation to use an amount of binder as low as possible with organic content that can be burned at lower temperature.

3.2.4 Influence of sintering temperature

To study the effect of sintering temperature, all scaffolds were debinded for 30 min at 350 °C under dynamic vacuum, with a heating rate of 1 °C·min^{-1}.

Compressive tests were only conducted on scaffolds sintered at the lowest and the highest temperature used in this work (1000 °C and 1200 °C respectively). Stress-strain curves obtained under compression are shown on Fig. 3.8 (a).

The overall evolution of the two types of scaffolds follows the same pattern: elastic domain, densification domain and stress recovery. In addition the vertical cracks observed in outer filaments of scaffolds sintered at 1200 °C (see section 3.2.2), were also observed for scaffolds sintered at 1000 °C. However, scaffolds Young's modulus decreases from 28 - 30 GPa to 15 GPa when decreasing the sintering temperature from 1200 °C to 1000 °C, due to lower filament density. This also leads to a drastic decrease of structures yield stress from 265 MPa to 130 MPa. On the other hand, it delays the transition from densification domain to stress recovery as the potential for densification is greater.

It should be noted that for both conditions, tests were stopped at 90kN to prevent damage to the load cell, thus the ultimate strengths were not measured. However, for all scaffolds, large cracks are already formed at this stage. They are initiated in scaffolds corner and propagate through several struts at 45° to the compression direction. But, as it can be seen on Fig. 3.8 (b), the middle of each sample is not affected by these cracks. Also, they seem to propagate on a shorter distance for samples sintered at 1000 °C. In contrast, these scaffolds present more damage on outer struts (some small pieces are even ejected from the structure).

In addition, Fig. 3.8 (b) highlights a high structure densification in the compressive direction. But densification also occurs at the strut scale as shown on Fig. 3.8 (c). Sample sintered at 1000 °C that was used to visualise 3D damage was also scanned in local tomography, to access a voxel size small enough to detect filament porosity (3 µm voxel size, *versus* 10 for the whole structure). Indeed, local tomography performed at the initial state enables to visualise a part of the pores present in the filaments (Fig. 3.8 (c)). These

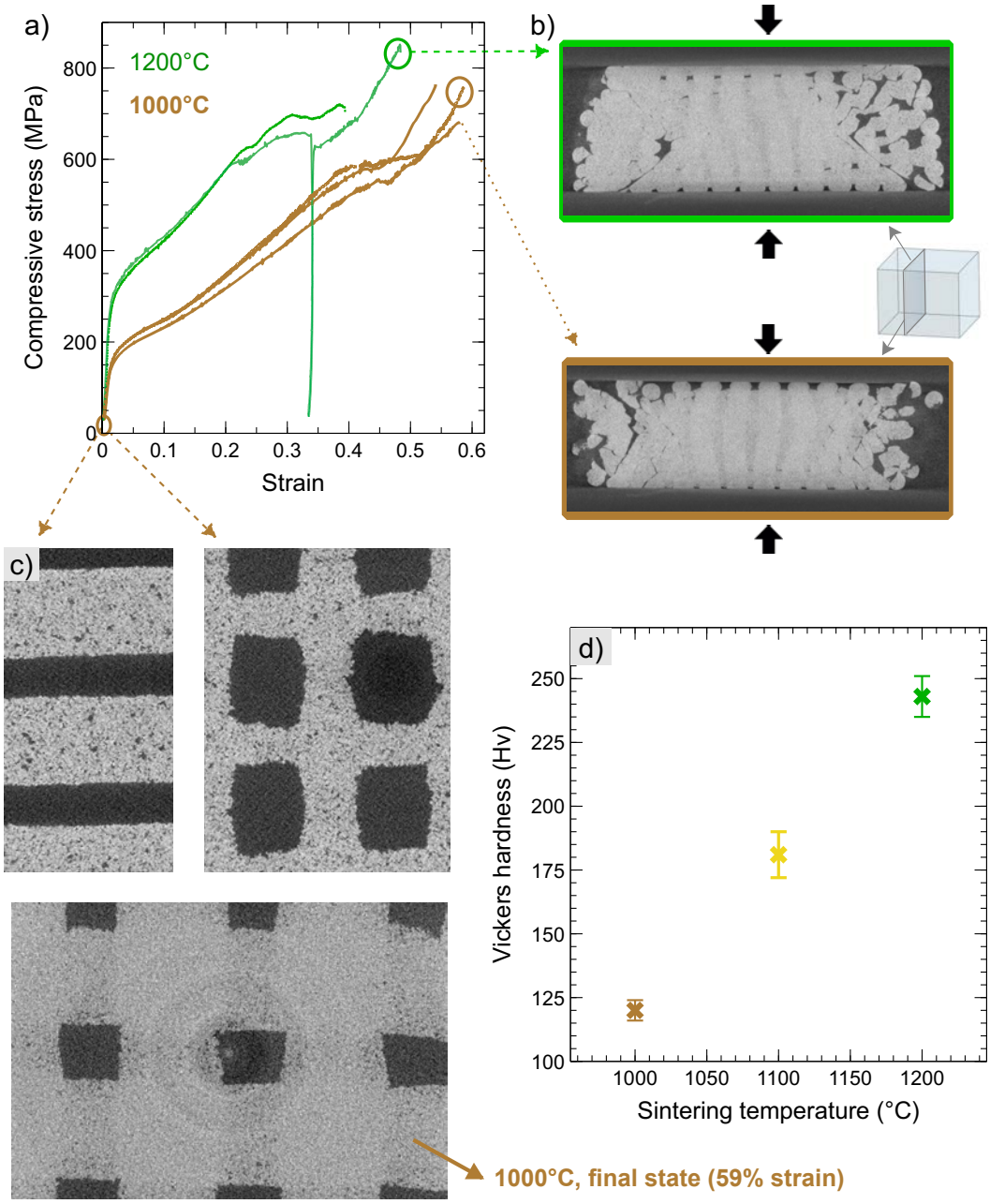

Figure 3.8: Effect of sintering temperature on mechanical properties : (a) Stress-strain curves under compression; (b) X-Ray tomography sections showing internal damage at the end of the test for each sintering temperature; (c) X-Ray tomography sections highlighting filament densification during the test; (d) Vickers hardness evolution with the sintering temperature.

pores are mainly collapsed at the end of the compressive test. In addition, initially, the overlap between two layers is low. Thus only few slices (perpendicular to the compression direction) are showing intersection between layers, with the two strut directions on the same image. In addition the filaments size where these intersections take place is

much smaller than their diameter. After compressive tests, the overlap becomes so high that intersections are visible on each slice and filament size remains almost constant. So a large number of micropores is removed during compression and macropores sizes are considerably reduced, leading to a high final strain.

Vickers hardness measurements were performed for the three sintering temperatures (1000 °C, 1100 °C and 1200 °C). Obtained values are reported on Fig. 3.8 (d). The linear evolution with temperature is in agreement with the linear increase of filament density and corresponds to what has been previously observed [OH 13, CHÁ 17]. In addition, value obtained for filaments dense at 87.5 % (sintering temperature of 1200 °C) is in accordance with commonly observed values on Ti64 samples with similar sintering density [OH 13, CHÁ 17].

These improvements in strength and hardness due to the densification of the filaments with the sintering temperature are also expected with the decrease in powder size, since it allows even greater densification.

3.2.5 Influence of powder size

To study samples from the same conditions as in the previous chapter, the influence of powder size was evaluated on samples sintered at 1200 °C.

Fig. 3.9 (a) shows the compressive curves obtained for samples from the three powder batches. The expected improvement in yield stress was indeed observed with an increase from 265 MPa for scaffolds made with coarse powder to 425 MPa for scaffold containing only fine powder. Note that yield stresses of scaffolds made from powder blend seem more scattered even though additional statistics are required to confirm this observation. This could be due to a difference in the ratio of the two powders between the two scaffolds.

This improvement in strength is also accompanied by a loss of ductility. Indeed, a crack propagating at 45° to the direction of compression appears for strains between 5 and 10 % in the case of samples containing fine powder (partially or totally). X-ray tomography analysis confirmed that this crack does indeed damage the entire sample as shown on Fig. 3.9 (a). Slippage of one half of the specimen relative to the other occurs along this crack. This behaviour is similar to what has been observed for samples debinded at 500 °C.

Three-points bending tests performed on filaments made from the three powder batches highlight that behaviour under compression observed for scaffolds containing fine powder is related to the fragile behaviour of the filaments of which they are composed. This result could be attributed to an increase in oxygen content owing to the greater specific surface area of the fine particles. To verify this hypothesis, carbon and oxygen contents were also measured on samples from the blend and the fine powder batches. No real consequences of the powder size were observed on the carbon uptake, with a final amount kept at 0.1 wt% (against 0.094 wt% previously found for samples made from coarse powder). However, oxygen uptake was far more important, even higher than the one observed on D500-S1200

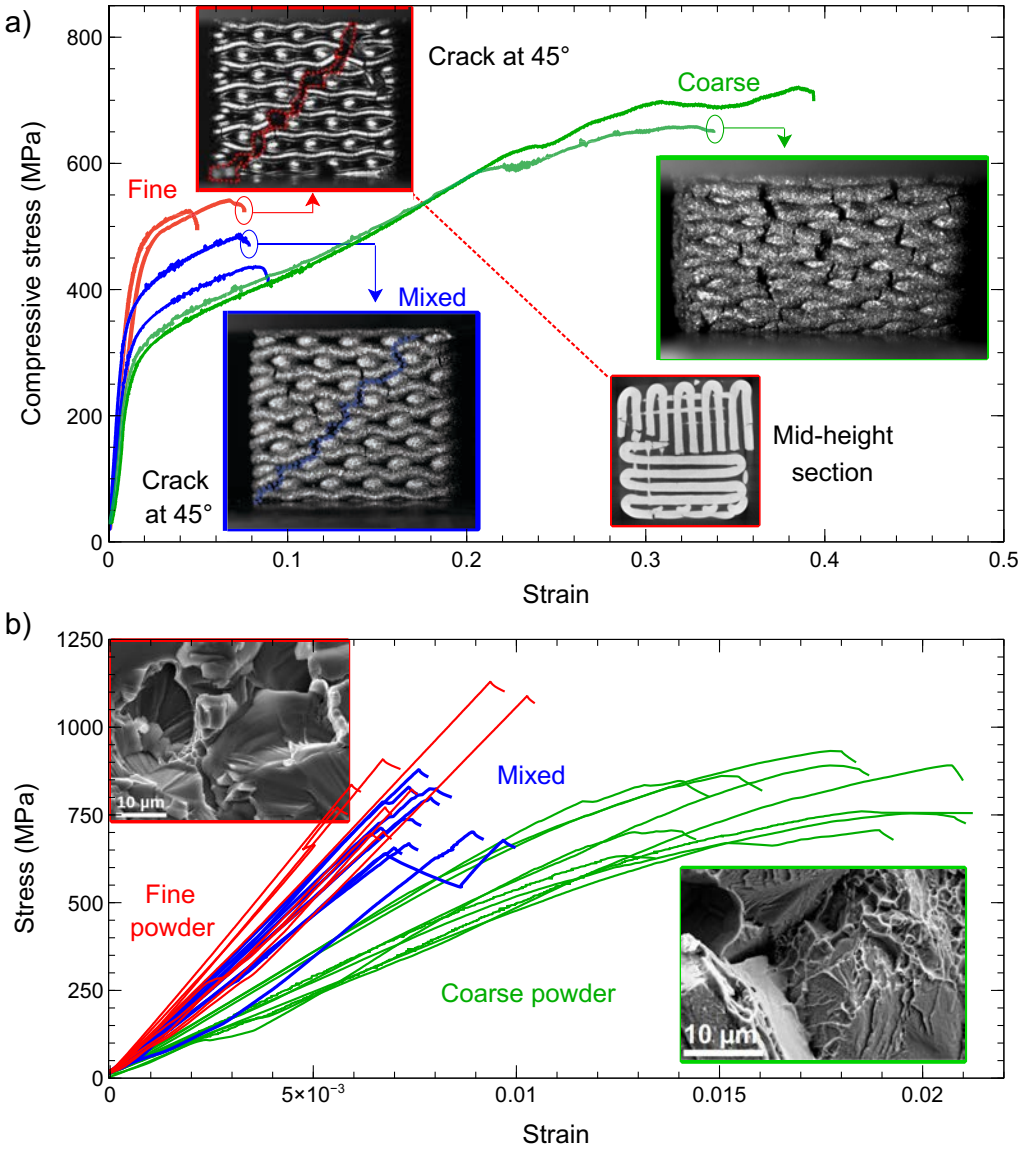

Figure 3.9: Effect of initial powder size on mechanical properties : (a) Stress-strain curves obtained under compression and illustrated with scaffold structures at the end of tests; (b) Stress-strain curves obtained by 3-point bending on filaments and illustrated with fracture surfaces. Samples containing fine powders show brittle fracture surfaces (cleavage) whereas dimples can be found on sample containing coarse powder only.

samples. The whole process intake was indeed evaluated at roughly 8000 ppm (+ 0.8 wt% between the initial and the finial state). Besides, this influence of powder size on oxygen uptake had already been observed for MIM process [BAR 10].

In addition, Vickers hardness increases with the filament density as shown on Fig. 3.10. However, the observed trend is not only due to the increase in density but also to the increase in oxygen content.

As shown in the previous chapter, varying the powder size within the same sample en-

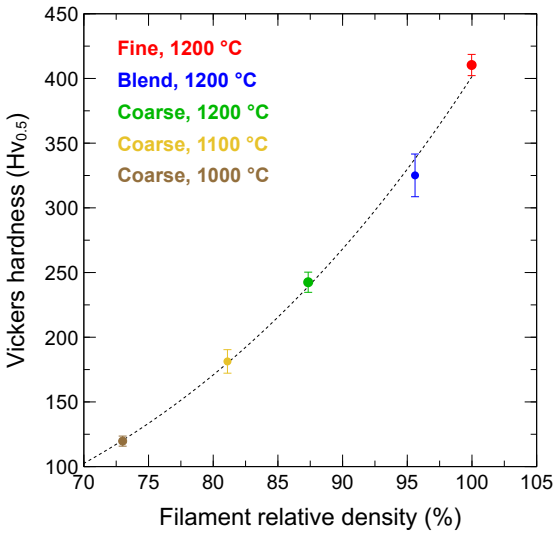

Figure 3.10: Vickers micro-hardness evolution with filament density.

ables to obtain a gradient of intra-filament porosity. Fig. 3.11 shows what happens during the compression of such a sample. From a macroscopic point of view, the sample shows overall the weak points of each layer: a yield strength identical to that of the most porous layers and the low ductility of layers containing fine powder. However, it should be considered that the strain is likely to be non-homogeneous in these samples. DVC performed using the interrupted test on one of these samples shows that the maximum deformation is located in the layers made with the powder mixture. This might be explained by the fact that these layers are the only ones that are constrained both above and below by layers with a different shrinkage from their own.

All the steps for which the convergence of the DVC calculation has been obtained are shown Fig. 3.11. The further stage, after the last one presented at the bottom right, led to the formation of a crack making the correlation too complicated. This crack, propagating at 45° to the compression direction, is as expected located in the most deformed layers, as shown by the X-Ray tomographic section (see Fig. 3.11).

Producing a more gradual gradient would then probably be beneficial to avoid preferential damage to the layers most stressed by the difference in shrinkage.

Having gone through what can be achieved depending on the process parameters, it remains to consider these mechanical properties with regard to the intended application.

3.2.6 Overview

First, a verification of all the results obtained using the data from the compression machine was carried out by tracing the deformation of the samples via a DIC calculation

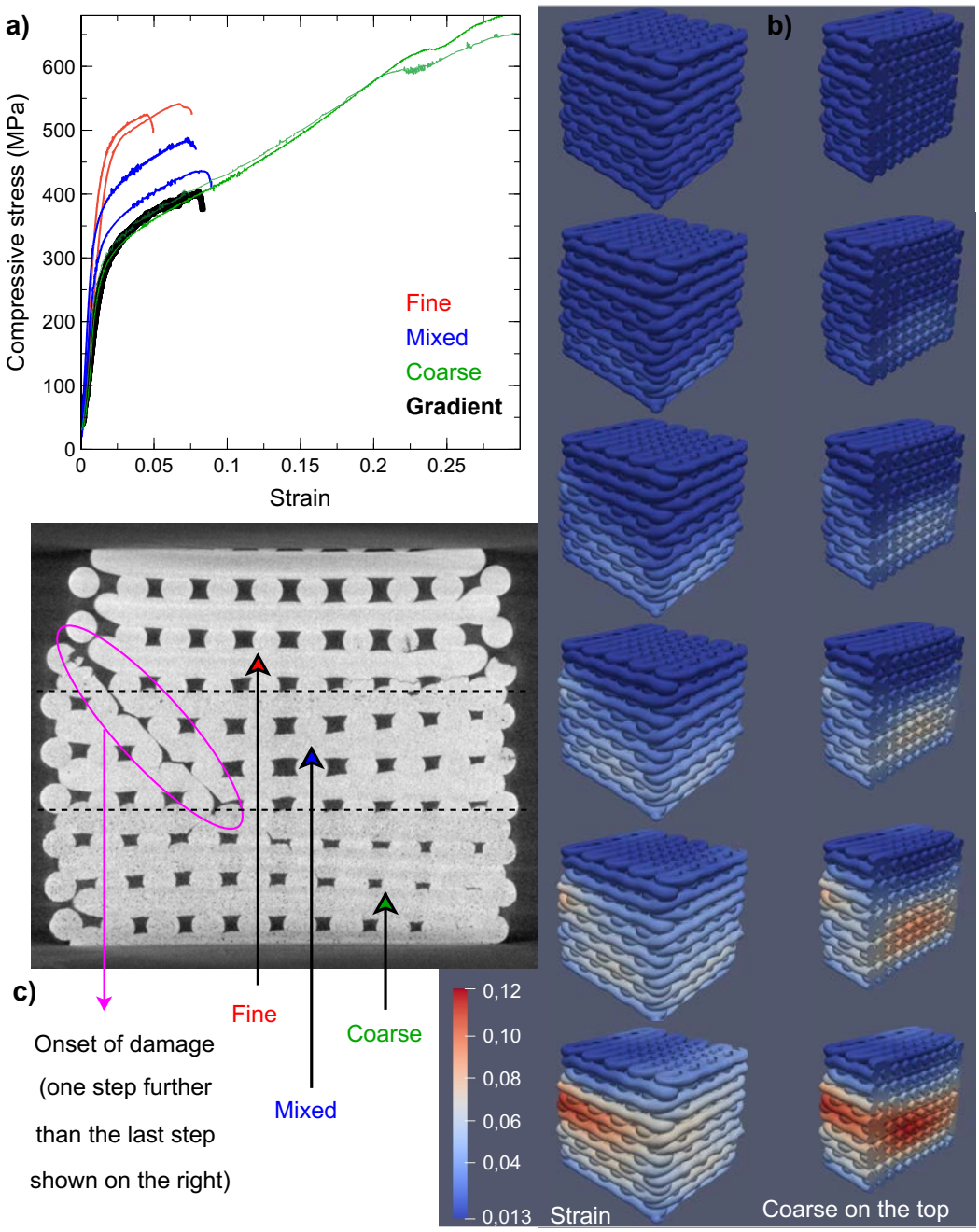

Figure 3.11: Mechanical properties of gradient samples: (a) Stress-strain curve obtained under compression in comparison with behaviour of each type of layer; (b) Evolution of the sample strain during the test obtained by DVC from the tomography scans. The highest strain is located in layers made from mixed powder batch. (c) X-Ray tomography slice showing the formation of a crack at 45° to the direction of compression in the most deformed layers.

on the images from the camera [see video here]. A comparison of the different data can be seen in Fig. 3.12. Overall, the two ways of proceeding give very similar results. However, it

is worth noting the small differences in Young's moduli observed between the two methods for samples containing fine powder.

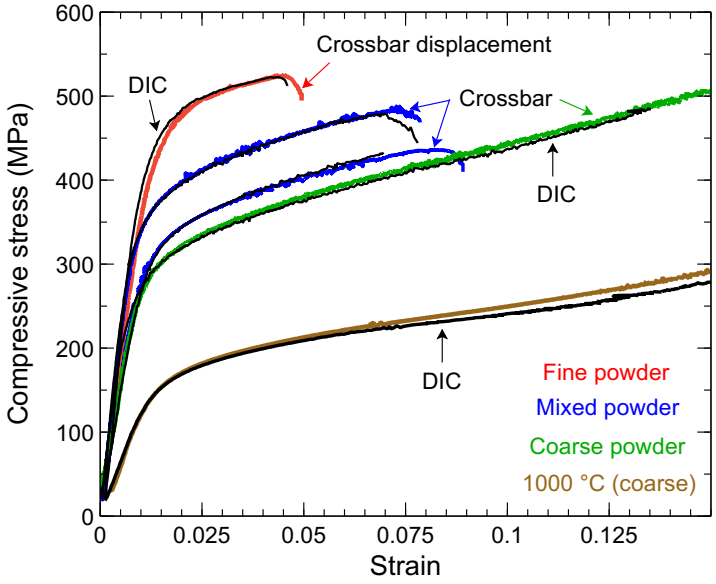

Figure 3.12: Comparison between stress-strain curves obtained using strain either from the crossbar displacement or by DIC. In order to keep a good readability, only one sample per condition is represented except for the samples from the mixed powder batch, whose results are more dispersed.

As the DIC enables to overcome the issue of machine stiffness correction by directly measuring sample strain, it was decided to consider the moduli values measured by this technique. A slight increase in scaffolds Young's modulus is therefore observed with the addition of fine powder due to filament densification, as it was already observed with an increase of sintering temperature. Indeed, according to the curves obtained with DIC, this value increases from 28 - 30 GPa for scaffolds made of coarse powder to 35 - 45 GPa for scaffolds obtained using the mixed powder batch and to 55 GPa for scaffolds containing only fine powder.

Once these corrections have been taken into account, the properties obtained can then be compared both to what is generally obtained on Ti64 foams made by additive manufacturing and also to the properties of the bones. Without being exhaustive, Table 3.2, gives an overview of mechanical properties shown by Ti64 scaffolds obtained through different techniques, in comparison to natural bone. Except for the results of this study, all other values given in the table are for structures with dense filaments, comparable to the case obtained with fine powder here.

Table 3.2 highlights that our scaffolds present one of the highest specific mechanical strength among Ti64 3D printed porous structures, even compared with others, well-established techniques such as EB-PBF or L-PBF. The debinding and sintering kinetics are of primary importance to optimise strength and ductility, and the absence of brittle

Table 3.2: Mechanical properties of various Ti64 cellular structures in comparison to natural bone

	Strut size (µm)	Density (g/cm^3)	E (GPa)	E/ρ (GPa.cm^3/g)	YS (or UCS) (MPa)	YS (or UCS)/ρ (MPa.cm^3/g)
EB-PBF [PAR 10]	940	2.18	3	1.4	(160)	(73)
EB-PBF [PAR 10]	465	2.22	0.6	0.3	(7)	(3)
L-PBF [Sal 13]	610	1.60	9	5.5	170	106
DIW [LI 05]	570	1.99	-	-	(280)	(140)
DIW [ELS 19]	685	2.09	-	-	120	57
DIW [ELS 20]	708	1.83	-	-	125	68
DIW [ELS 20]	713	1.42	-	-	120	84
This work	**750**	**2.16**	**15**	**6.9**	**130**	**60**
This work	**710**	**2.52**	**28 - 30**	**11.4**	**265**	**105**
This work	**704**	**2.66**	**35 - 45**	**13 - 17**	**280 - 335**	**105 - 124**
This work	**684**	**2.81**	**55**	**19.6**	**425**	**151**
Bone [GIB 99]	-	1.8 - 2.1	3 - 20	2 - 10	130 - 180	70 - 100

carbides in sintered parts may explain the enhanced properties compared to Elsayed *et al.* Except for the least sintered case, the strength obtained is greater than that of the bone.

In addition, structure stiffnesses are sufficiently similar to that of bone to avoid stress shielding. Only the Young's modulus of samples containing 100 % fine powder could be too high. However, increasing the porosity by adjusting strut size or interstrut distance would lead to a better stiffness match. In the case of powder bed fusion technologies, an excessive down sizing of the constitutive struts may lead to drastic embrittlement caused by the microstructures induced by extreme cooling rates (Table 3.2). We expect a more moderate effect using direct-ink writing and subsequent sintering that involves lower cooling rate, independent of the strut size. In addition, with their 2020 study, Elsayed *et al.* showed that, contrary to what happens by varying the microporosity, reducing scaffold densities by increasing macropores size has no real effect on the yield strength achieved.

The mechanical properties obtained in this study are therefore of interest for the intended application, including samples with interconnected microporosity in filaments. As previously mentioned, this microporosity can be an advantage in the context of bone repair by favouring anchoring. In view of the wide range of filament densification permitted by the process, it seems important to carry out cellular tests to verify the influence of these different levels of porosity on their behaviour. This would enable to find a compromise between mechanical resistance and cellular activity.

3.3 Biological response

3.3.1 Study design

As the effect of macropores and their necessity for vascularisation is already well documented, it was decided to focus on the effect of micronic interconnected network on some biological responses. Thus, three different cases were selected: coarse powder sintered 2 h at 1000 °C, coarse powder sintered 2 h at 1200 °C and fine powder sintered 2 h at 1200 °C, leading to 27, 12.5 and 0.025 % of remaining micronic porosity respectively.

Scaffolds were printed with a 610 µm needle size and the number of printed struts by layer were reduced to obtain parts fitting in 1 cm diameter wells. To prevent all the cells from falling directly to the bottom of the well at the time of deposition, robocasted samples were designed using the following characteristics:

— A first dense layer (without macropores)
— A contour present over the entire height of the part
— Two additional layers composed of 7 filaments separated by 310 µm (920 µm between two filament centres) with the second layer oriented at 90 ° to the first.

The overlap between layers was kept as 0.8 times the needle diameter. An example of a resulting structure is shown on Fig. 3.13.

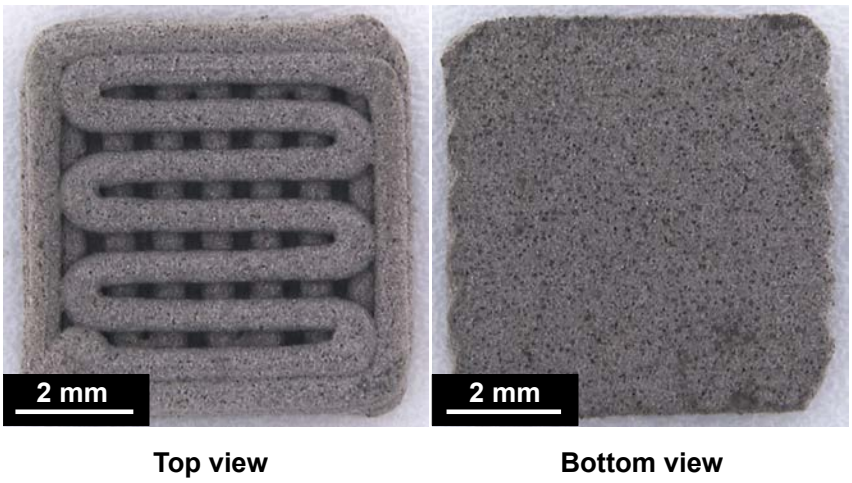

Figure 3.13: Binocular magnifying glass images of a sample for cell culture, presenting a first layer without macropores and a contour around the two additional scaffold layers.

In order to separate the effects of macropores from those of micropores, three other types of samples were added to the study. The same couples (Powder - Temperature) were kept but the sintering was applied this time to small cylinders free of macropores (obtained by casting in moulds). In addition, dense commercial Ti64 discs were included to be used as controls to validate the study.

The first and unavoidable step in testing the behaviour of cells in contact with a material is the cytotoxicity test, which enables to evaluate cells viability when they are brought into contact with a material for a short period of time (24 h). However, this test alone does not answer the question: which microporosity is the most interesting for bone implants? In order to provide elements of an answer to this question, this test must be supplemented by tests aiming at characterising the behaviour of bone cells in contact with the material. While MG-63 cells (a line derived from an osteosarcoma, so a cancer cell line) is usually used for cytotoxicity tests, cells that are more representative of healthy bone should be favoured for the characterisation of cell behaviour. Primary human osteoblasts were thus chosen.

In order to evaluate the behaviour of osteoblasts in contact with these materials, it was first envisaged to study their morphology by phaloidin marking (phaloidin reveals the cytoskeleton of the cells). This study could be coupled with the localisation of focal adhesions, which serve as mechanical links to the extracellular matrix and can be revealed by fluorescent marking, using anti-bodies specific to proteins involved in the focal adhesion such as actin, vinculin, talin or integrin [HUM 07, THI 13]. Knowing whether the cells are able to adhere well to the material represented the first step. To go further, their activity related to bone matrix synthesis should be quantified. To this end, it was foreseen to follow alkaline phosphatase and osteocalcin expressions as these are two components known to be involved in osteogenesis and mineralisation process [GOL 07, CUN 14]. In addition, an analysis with red alizarin would enable, as a complement, to detect calcium deposits [PUC 69].

Unfortunately, this study was not able to see the light of day, because the thawing of the ordered osteoblasts was scheduled for the day before the beginning of the lockdown related to the COVID-19 crisis (16 march 2020). Only preliminary cytotoxicity tests with MG-63 have been started.

3.3.2 Cytotoxicity and cell proliferation tests

Samples previously described were sterilised by dry heat with a 30 min treatment at 180 °C. Tests were carried out in 24-well plates specifically treated for cell culture. Empty wells have therefore been used as controls (plastic reference P-Ref) in addition to Ti64 discs control (Ti64-Ref).

A suspension of 5000 cells was deposited on each sample. A period of 2 hours was left to allow cell adhesion before adding the culture medium. Cells proliferation was measured after 24 hours of culture in contact with the materials (cytotoxicity) but also after 3, 7 and 10 days of culture (cell proliferation). Incubations were carried out at 37 °C under humid atmosphere with 5% CO_2. Evaluations of cell proliferation were carried out using the PrestoBlue technique: the blue, non-fluorescent resazurin is reduced by the metabolic activity of the cells in fluorescent resafurin. The desired day, 1 mL of medium containing

10 vol% PrestoBlue was added to each well. After 1h30 of incubation, 100 µL of medium was taken from each well and transferred to a black-bottomed plate. Results were read using the INFINITE PRO 200 fluorimeter (excitation 535 nm, emission 610 nm, gain 40).

This study was carried out in triplicate and repeated three times (independently of each other).

Results obtained are shown on Fig. 3.14. Fluorescence measured after one day has been separated from the others since it is supposed to represent the cytotoxicity of the samples. These results after 1 day of incubation show an absence of proliferation for cylinders with 27 % microporosity and very low proliferation also for robocasted samples with 27 % porosity in the filaments. However, these results should be seen in the light of the observations made on these two types of samples. The drop containing the cells quickly disappears in these two sample cases after deposition (in less than 10 min) while it remains as a drop in the other cases. The cells are therefore sucked into the microporous network by capillary forces. The stress represented by this phenomenon may impact cell viability. It should be possible to avoid it by soaking the samples in culture medium before depositing them at the bottom of the well and placing the cells on top.

Still related to this phenomenon, it was observed after a few days of incubation, the presence of cells on the plastic at the bottom of the well for robocast samples containing 27 % of porosity within filaments. This means that the cells were able to pass completely through the sample. The fact that the cells could only be observed to pass through the robocast samples and not through the cylinders is not surprising since in some places, the cells only had to pass through one layer of the robocast samples to reach the bottom of the well ($\sim$ 600 microns) while the cylinders were about 3 mm high. However, this means that the results obtained at 3, 6 and 10 days for the most porous robocast samples are distorted by the presence of proliferating cells on the well plastic. Being aware of this limitation, the rest of the test can be validated by significant cell proliferation on both types of controls (plastic and Ti64).

To confirm these results and better visualise what is occurring, one sample from each case was observed by SEM for each incubation time. The cells were fixed on the samples using a 2 % Glutaraldehyde solution in which they were left for 1 hour before being rinsed with a buffer solution. A comparison of images obtained on each scaffold after 6 days is shown on Fig. 3.15.

It can be noted that the quantity of cells observed on the most porous scaffolds is indeed lower than for the other samples. It is only from the 10th day of incubation that the cells begin to really invade the surface and come into contact with each other, whereas the confluence [1] is already reached after 6 days for the other scaffolds. This highlights two things:

— The most porous samples (cylinders and scaffolds) are therefore non-toxic despite

1. In cell culture, confluence refers to the fact that the surface is completely covered by the cells

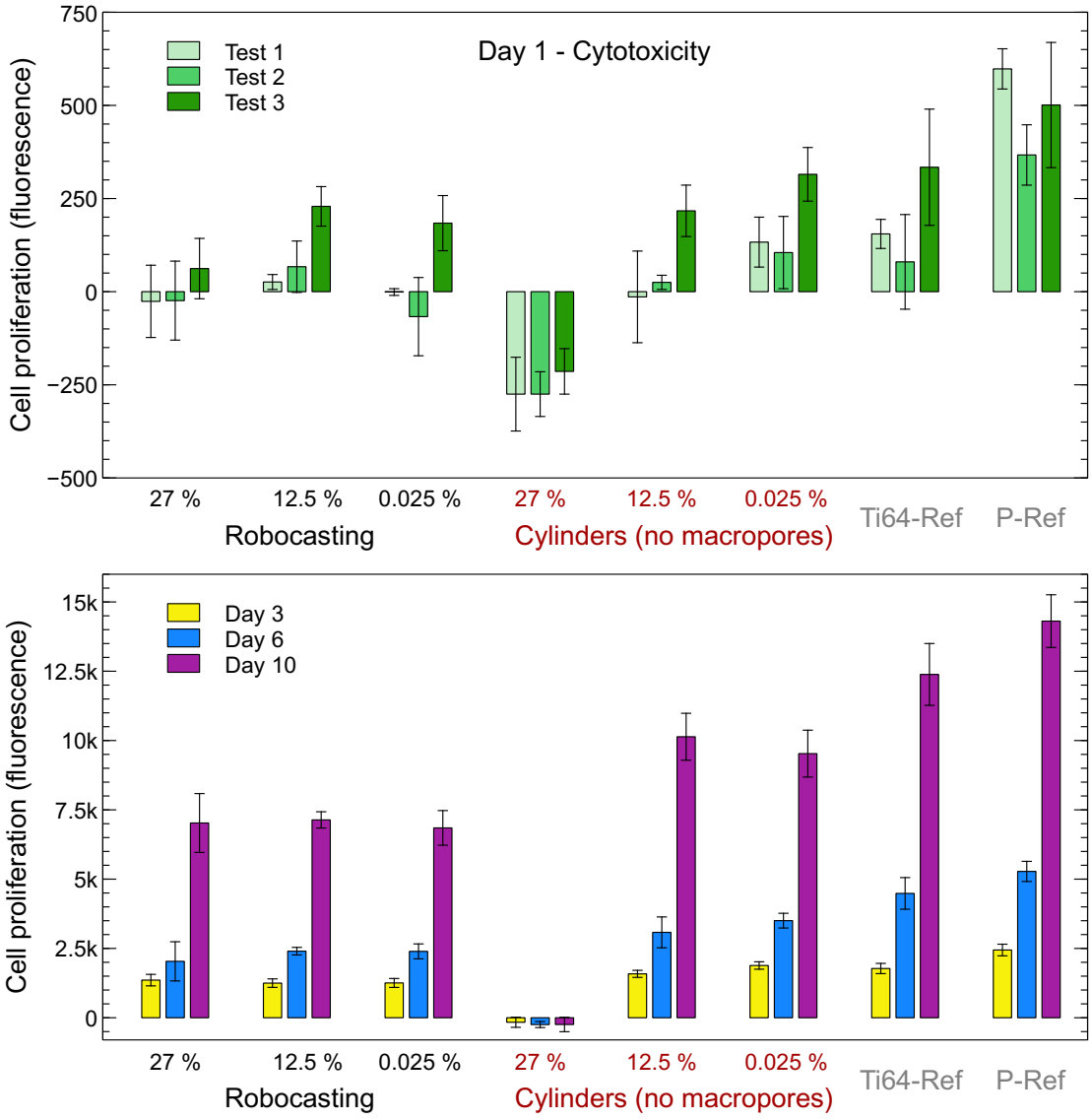

Figure 3.14: Cell proliferation measured by fluorescence: (a) Results after one day allowing cytotoxicity evaluation; (b) Results after 3, 6 and 10 days of incubation.

the first day fluorescence results. It is indeed a question of protocol with regard to the capillary aspiration that these samples can exert which is to be blamed.

— Fluorescence results on the most porous scaffolds after several days of incubation are indeed probably overestimated by the proliferation of cells at the bottom of the well.

It might be possible to avoid this overestimation by applying a hydrophobising product to well surfaces, such as Sigmacote, known to limit the adsorption of proteins and cells [LEE 88].

Fig. 3.16 also highlights the evolution over the incubation period. After the confluence

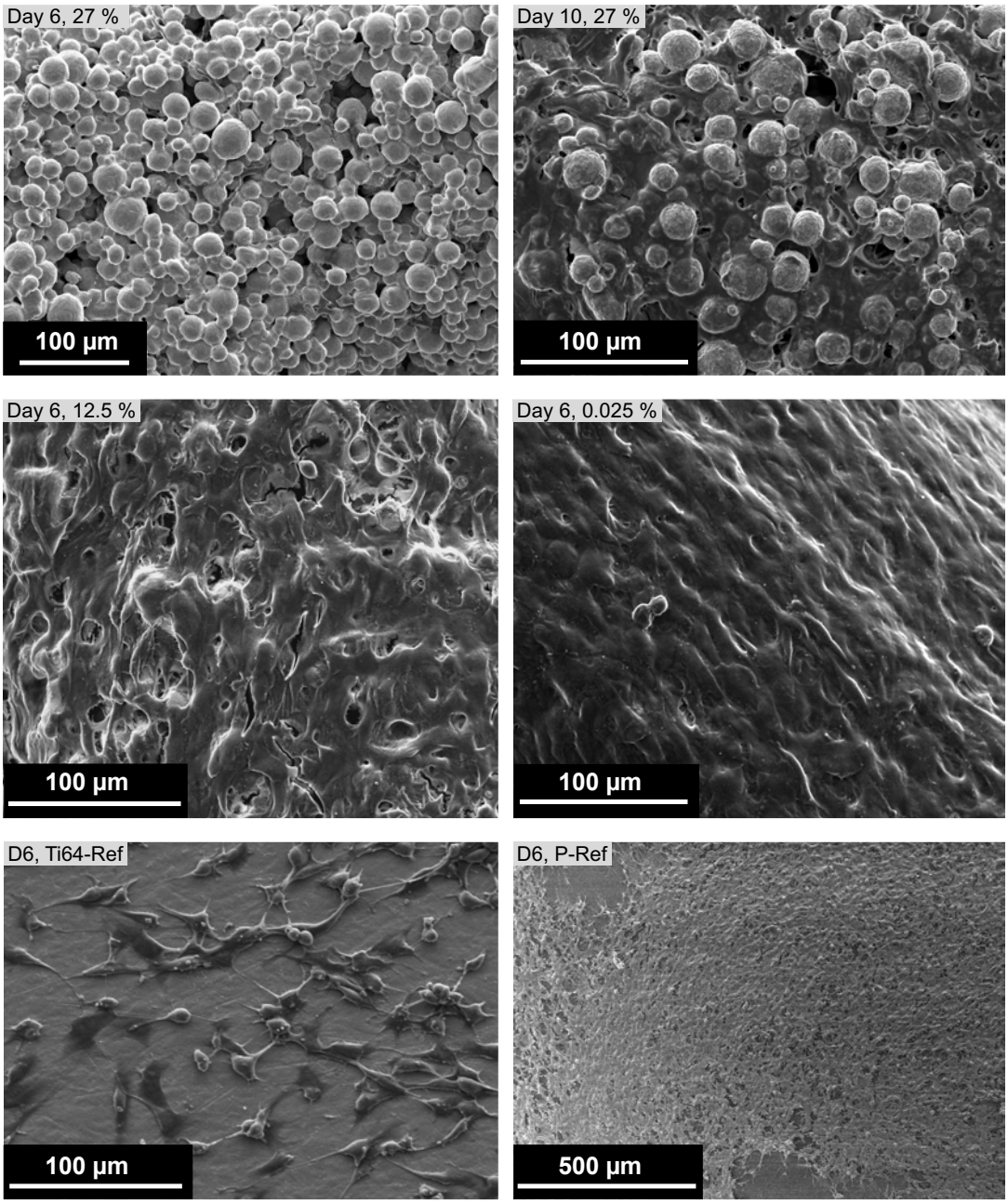

Figure 3.15: SEM images showing the cells spreading on the different samples after 6 or 10 days of incubation.

is reached, the cells continue to grow on top of each other, forming several layers above the surface. It can also be observed that they build bridges between the filaments of the same layer, by following the filaments of the layer underneath.

In addition, SEM image of the most porous cylinders confirms that the cells did not develop on these samples. But despite the effect of the first phenomenon of capillary suction which could be harmful, other questions deserve to be asked:

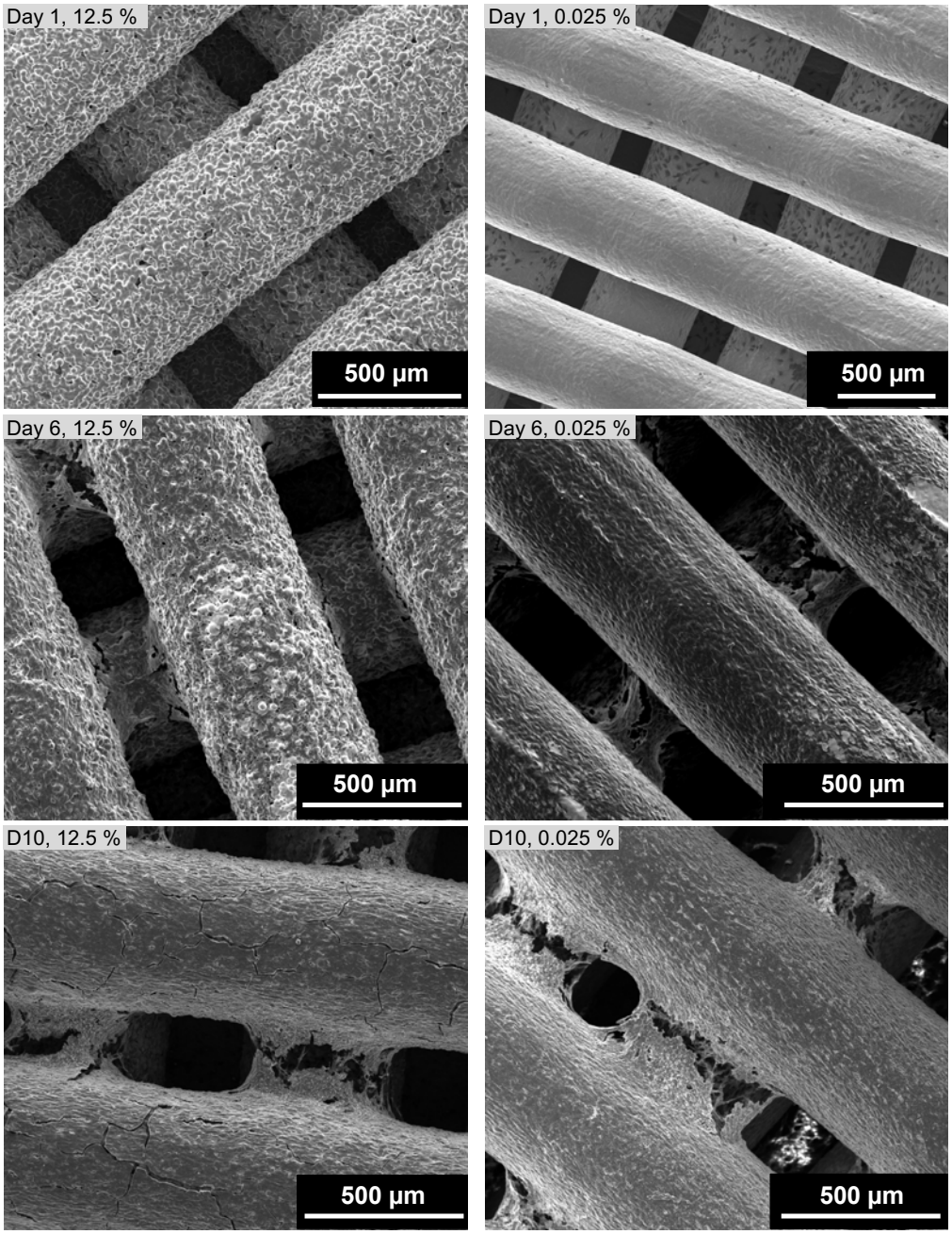

Figure 3.16: SEM images showing the cells spreading evolution over the incubation period, for scaffolds presenting 12.5 % and 0.025 % of remaining porosity in filaments (left and right respectively).

— Do the cells present in the porous network benefit as much from the change of medium as the cells present on the surface if no circulation is applied?
— Following the same reasoning, do these cells really see the PrestoBlue added? And if so, is the resulting resafurin really taken out?

In the human body, it is the blood flow that brings the necessary nutrients to the cells.

When testing porous structures, a circulation of the culture medium would then probably be beneficial and more representative of what can happen *in vivo*. However, it must be kept in mind that a critical distance of 150 microns around the blood capillaries is generally observed for cell viability. Beyond this limit, phenomena of cellular hypoxia can be encountered [BOH 17].

Two other interesting observations can be made from the SEM images. Firstly, it is confirmed that the cells can indeed slip and adhere inside the pores left by sintering as shown in Fig.3.17. In addition, cells are well spread out and flat on the surfaces of scaffolds, synonymous with proper adhesion, while they are more rounded on the surface of the reference Ti64. This is due to the difference in roughness that enhances cell adhesion [NEB 04, DOC 08], the Ti64 reference being the smoothest sample. However, a too great increase in roughness can again reduce cell adhesion. Thus, before going further in testing, it would be interesting to add a sample to the study to get rid of too big differences in filament roughness between samples to be compared. This could be either a sample made from fine powder but sintered at a lower temperature to keep an interconnected microporosity of 12.5 % with low roughness, or a sample made from coarse powder but sintered at a much higher temperature to have nearly dense filaments with important roughness. This would make it possible to study the effect of microporosity and roughness at the same time, since comparisons with almost identical roughness would then be possible.

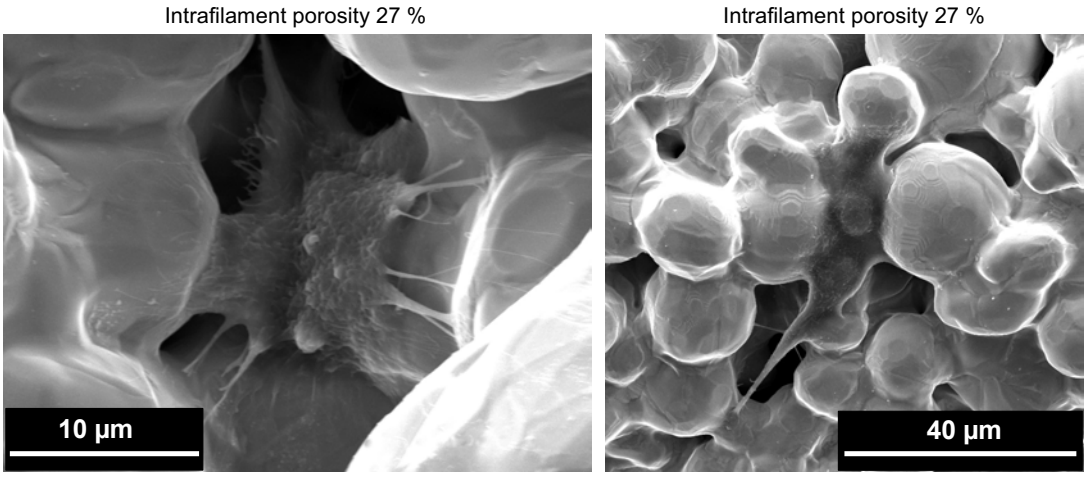

Figure 3.17: SEM images showing cells located in pores or nesting in the hollows between particles.

3.4 Conclusion and perspectives

The main findings to be retained at the conclusion of this chapter are presented in the figure 3.18.

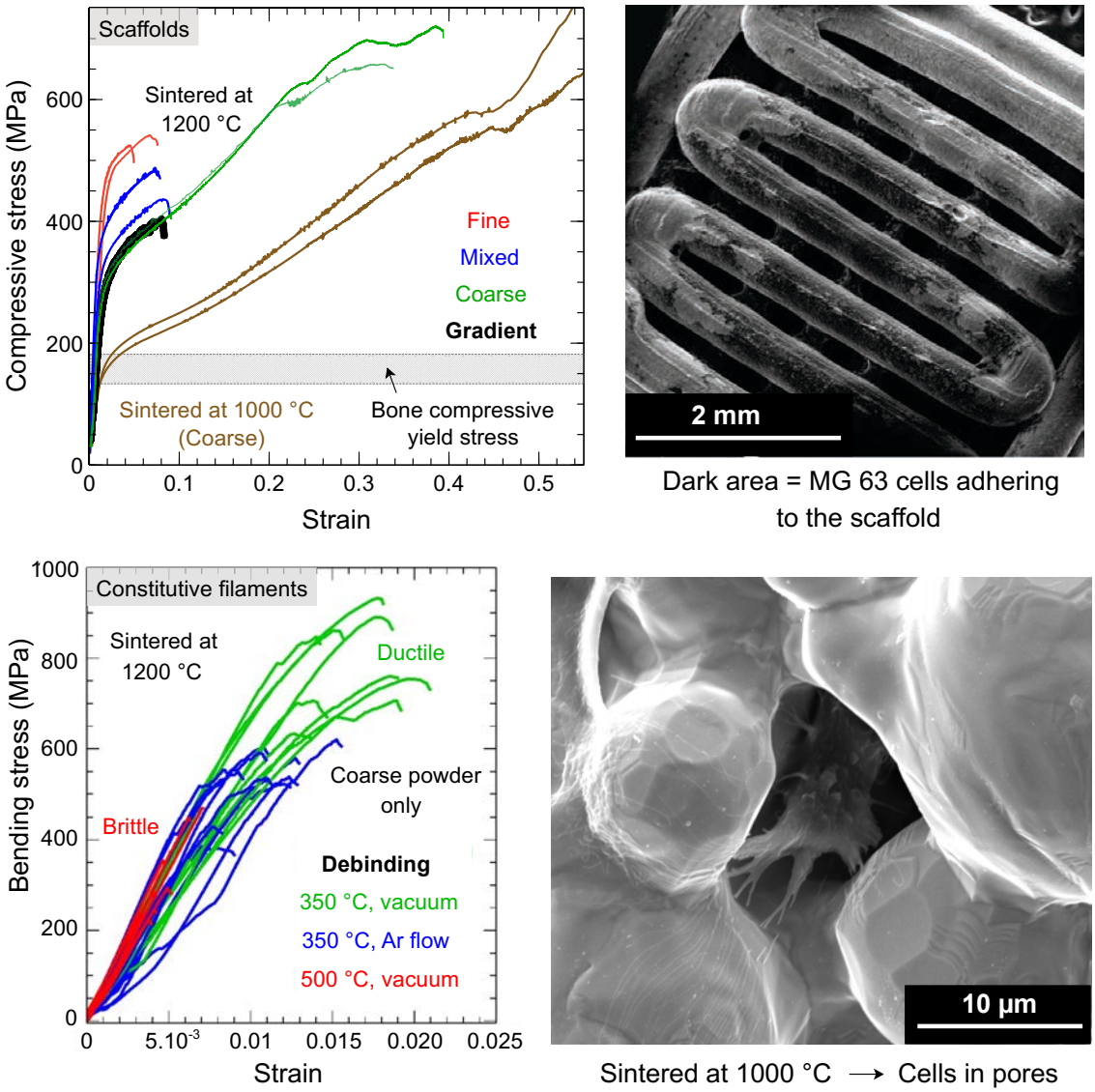

Figure 3.18: Graphical summary containing main results presented in this chapter.

Compressive tests performed on scaffolds highlight interesting mechanical properties with yield stresses usually higher than that of bone and Young's modulus close enough to that of the bone to limit stress shielding. However, a disparity in ductility is observed due to difference in oxygen (or even oxygen and carbon) intake during thermal treatments. For high interstitial contents, the filaments become completely brittle, also reducing the ductility of the scaffolds. It is therefore recommended to use the lowest possible debinding temperature.

Since bending tests give access to the intrinsic behaviour of the constituent filaments, it could be interesting to model the compression of the scaffolds by finite elements using the bending results as input data for material properties. If the model reproduces well what

is observed, it could make it possible to "virtually" test a whole range of configurations (changing pore sizes or filament diameters, for example), so that in the end only the most promising configurations would be tested in practice.

After having optimised as much as possible the parameters to limit interstitial intake (ink formulation, debinding and sintering), it would also be necessary to investigate the tensile and fatigue properties that can be obtained by this type of structure. Reduced surface roughness compared to powder bed fusion processes could be an advantage for fatigue properties.

Concerning the biological properties, tests had to be stopped after their preliminary phases. Thus it can only be confirmed that MG-63 cells can be found within micropores left after sintering, and that the non-zero roughness of the samples gives them plenty of anchoring points giving them a more spread out morphology. However, this initial study has raised a whole set of points to be improved for future tests on this type of material.

To try to evaluate the influence of this microporosity, the initially planned study (including cytotoxicity, morphological evaluation, cellular adhesion and calcium deposition assessment) should therefore be carried out, taking care of:

- *Treating the wells in such a way as to prevent the cells from adhering anywhere other than on the samples.*
- *Soaking the samples in culture medium before depositing them at the bottom of the well, so as to avoid aspiration of the cells by capillary forces when depositing them.*
- *Circulating the culture medium for a better supply of nutrients to the cells.*
- *Adding a supplementary type of sample to overcome the large difference in roughness. (Either a sample made from fine powder but using a lower sintering temperature to keep interconnected micropores, or a sample made from coarse powder but sintered at* 1400 °C *to close pores.)*

The number of dense layers at the bottom of the sample may also be increased to limit the risk of cells being passed through.

Such a more complete evaluation would then make it possible to produce an Ashby's map of the biological properties (cell adhesion, matrix synthesis) as a function of the mechanical properties (E/ρ ; σ_E/ρ). This would give an overview of the best possible compromises for this type of sample.

Chapter 4

Robocasting of bio-resorbable magnesium scaffolds

Due to their permanent renewal, bones are relatively well able to repair themselves. However, devices can be used to facilitate this repair, for example by maintaining the alignment between two fractured halves, or by filling a defect that was initially too large for the repair to be successful. In all these cases where the implant is only useful until healing is sufficiently advanced, the use of resorbable materials seems more appropriate. It effectively lightens the process for the patient, by eliminating the need for a second surgery to remove these reconstruction aids. In some cases it even allows the patient to get rid of the foreign body that could not have been removed otherwise, and could thus have been a source of further complications.

As one of the bioresorbable metals, magnesium is very attractive due to its high tolerance in the human body and its Young's modulus close to that of bone [STA 06, CHE 14]. This chapter is therefore dedicated to the study of the feasibility of architecturing magnesium structures by robocasting. The first task is to formulate an ink that is compatible with magnesium reactivity. Then, once satisfying structures can be printed, scaffolds have to be debinded and sintered. This latter treatment represents the second difficulty to overcome due to the strong tendency of magnesium to oxidise.

Contents

4.1 Background: additive manufacturing of magnesium

In the field of bone regeneration, resorbable materials are attracting increasing interest. As they are gradually eliminated *in-vivo*, they avoid the need for a second surgery, which is necessary when the temporary reconstructive support is made of permanent, non-resorbable material. Biodegradable metallic alloys are being considered for load-bearing applications due to their interesting combination of ductility and strength compared to polymers and ceramics. Magnesium based alloys are among the studied candidates [STA 06, LI 13, CHE 14, LI 16], alongside Zinc and Iron alloys [SCH 10, BOW 13, FEN 13, LI 19].

Magnesium is one of the essential elements provided by the daily nutrition and is abundantly present in the human body (it represents 24 - 25 g of an adult body) [Jah 12]. The human body is therefore tolerating elevated levels of magnesium, with a maximum allowable daily dosage of 400 mg [CHE 14], which is well above the 15 mg recommended for zinc and iron [GIL 04]. In addition, the level of magnesium in the body is controlled by the kidneys, which eliminate the excess in the urine [Jah 12]. This tolerance and possible elimination by the human body are interesting in the context of resorbable implants and lead to numerous studies on magnesium alloys for implantable devices applications.

Despite the success of some devices such as the DREAMS^{TM} stents [JOH 14] or the Magnezix screws which have received the CE mark [CHE 14], the marketing of magnesium implants remains in its infancy due to the difficulties imposed by the very nature of magnesium. Indeed, magnesium is an extremely reducing metal presenting a standard potential of -2,372 V (compared to the normal hydrogen electrode) [LID 04] leading to really fast and important oxidation. In addition, the formation of MgO and that of Mg_3N_2 are strongly exothermic (-606.1 and $-461.08\,\mathrm{kJ{\cdot}mol^{-}1}$ respectively), making magnesium

inflammable in air [LID 04]. Processing magnesium is thus requiring special care from a safety point of view. In addition, in presence of water, magnesium forms a passive film of $Mg(OH)_2$ with di-hydrogen as a by-product, following the chemical reaction:

$$Mg + 2OH^- \longrightarrow Mg(OH)_2 + 2e^-$$

$$2H_2O + 2e^- \longrightarrow 2OH^- + H_2$$

$$\text{Resulting in :} \quad Mg + 2H_2O \longrightarrow Mg(OH)_2 + H_2$$

The release of dihydrogen can again lead to difficulties from a safety point of view. But this gaseous emission also induces cracking or even detachment of the passive layer, resulting in further corrosion. This phenomenon is further amplified by geometrical mismatch between the passive layer and the magnesium hexagonal lattice [KAI 03]. Magnesium corrosion rate is therefore really fast. To obtain degradation rate compatible with implantable devices applications, different approaches are studied, such as purification, alloying, refining microstructure, surface modification [LI 16]. However, the community would greatly benefit from a systematisation of this corrosion rate characterisation by defining common protocols. Indeed different methodologies are used from one study to another, limiting the possibilities for comparison and thus slowing down the development and implementation of biodegradable magnesium based implants [KIR 12]. In addition, the understanding of *in vivo* mechanisms and their relationship with *in vitro* measurements are still to be deepened. *In vivo* degradation may be totally different from what could have been expected based on *in vitro* results. Witte *et al.* showed that in some cases, *in vivo* degradation can be considered as suitable, while samples showed too fast *in vitro* corrosion rates [WIT 06]. However, in parallel with these needs to control the degradation rate, mechanical properties and other biological concerns such as nontoxicity, biocompatibility, or bone attachment must be considered to meet clinical needs.

The development of porous structures is receiving increasing interest due to the cellular invasion and vascularisation they allow. Osteoblasts from the patient's own hard tissues can even be seeded on scaffold structure, promoting the invasion of the structure by new bone tissue [LI 16]. However, this kind of structure presents increased free-surfaces, for which the above-mentioned problems of too high degradation kinetics become even more pronounced. But surface treatments, such as Plasma Electrolytic Oxidation, have been successfully applied to scaffold structures to make their degradation compatible with the intended application [KOP 19].

Among techniques to produce porous magnesium-based structures, AM is attracting an increasing number of studies, due to its ability to manufacture geometrically complex parts with patient-specific design [MAN 16]. The first studies on the additive manufacture

of magnesium focused on the L-PBF process [NG 10]. Beyond the necessary attention to the safety aspects of magnesium melting, other difficulties also seem to be encountered. Undesired remaining pores are generally observed in the fusion beads [MAN 16, GAN 19]. They are probably caused by the large volume contraction that takes place when magnesium solidifies, as previously observed during other solidification processes [KAI 03]. In addition, the volatility of magnesium at high temperatures also leads to chemical inhomogeneities in the parts manufactured by L-PBF [WEI 15, GAN 19]. Flake-shaped phases can also be observed in the workpieces and are believed to be a consequence of the presence of oxide shells around the initial particles [ZUM 19].

Direct-Ink Writing thus appears as an alternative presenting the main advantage of operating in ambient atmospheric conditions. It also removes the problem of the recyclability of the powders present in the powder bed, which are probably too rich in impurities due to the reactivity of the magnesium. Progress has also been made in this direction in parallel with this thesis work. Indeed, Salehi *et al.* proposed a method based on the binder jetting process, but keeping only the solvent (without binder) to create capillary bridges between particles. Their parts were then consolidated by liquid sintering with or without microwave assistance [SAL 19b, SAL 19c, SAL 19a]. Fig.4.1 shows an example of structure obtained by this technique in comparison with a WE43 scaffold structure obtained by L-PBF.

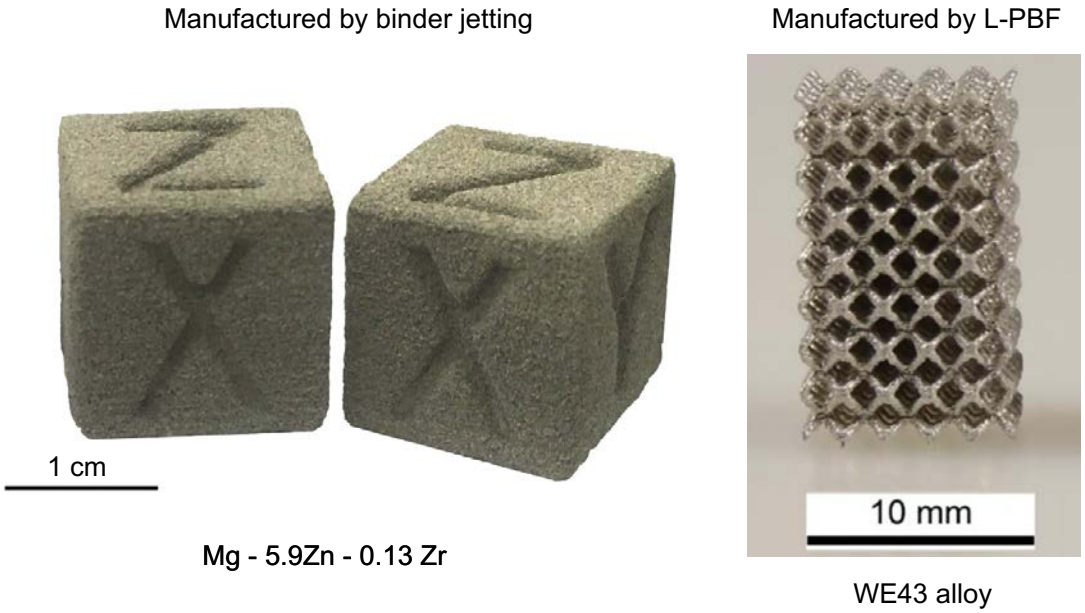

Figure 4.1: Examples of magnesium based structures obtained by additive manufacturing, adapted from [SAL 19c] and [KOP 19]

4.2 Pure Mg sample manufacturing

Alloying elements are known to strengthen the magnesium matrix and reduce its corrosion rate, leading to more appropriate properties for orthopaedic applications [STA 06, CHE 14]. However, the aim was, first of all, to check the feasibility of the robocasting process for magnesium-based materials. Thus, in order to simplify the chemistry of the initial state and to limit the risks of interaction, the study was first started on pure magnesium.

4.2.1 Powder characterisation

Pure magnesium argon atomised powder used in this study was furnished by SFM SA (Martigny, Switzerland). Its chemical composition is given in Table 4.1.

Table 4.1: Composition of the Mg powder according to the supplier

Element	Al	Cu	Fe	Mn	Ni	Ca	Si	Zn	Mg
Powder (wt%)	0.01	<0.001	<0.001	0.012	<0.001	0.05	<0.001	0.093	99.87

The as-received powder was characterised in terms of particle size distribution and morphology (Fig. 4.2). Particle size distribution measurements were performed using the same equipment and protocol as for Ti64 but with a refractive index value of 0.351. Secondary electron (SE) images of Mg powder particles were collected using a Tescan Vega3 scanning electron microscope (SEM) equipped with a tungsten filament (Tescan Orsay Holding, a.s., Brno, Czech Republic). A low acceleration voltage (5 kV) was used to avoid charging effects.

According to the laser diffraction results, Mg particles diameters range between 1 and 70 µm and exhibit a log-normal distribution (Fig. 4.2 (a)). This distribution is characterised as follows: $D_{10} = (7.3 \pm 0.1)$ µm; $D_{50} = (16.2 \pm 0.2)$ µm and $D_{90} = (32.0 \pm 0.8)$ µm.

Powder particles are mainly round-shaped due to gas atomisation (Fig. 4.2 (b)). A zoom on particles surface reveals the presence of small non-conductive particles adhering to the Mg particles. An EDS analysis performed on these small particles showed that they contained a high proportion of oxygen and can therefore be considered as magnesium oxides.

4.2.2 Ink formulation using rheology measurements

Due to its high reactivity with oxygen, magnesium cannot be printed using an aqueous binder. Owing to its non-toxicity and volatility, ethanol can be considered an interesting candidate to be used as ink solvent. Indeed, as explained in Chapter 1, a fast drying can help to retain the shape during the stacking of layers by allowing the transition from a shear-thinning behaviour towards a dilatant behaviour. Moreover, ethanol has already been used to formulate inks that were successfully robocasted [DEL 12]. In this work, the

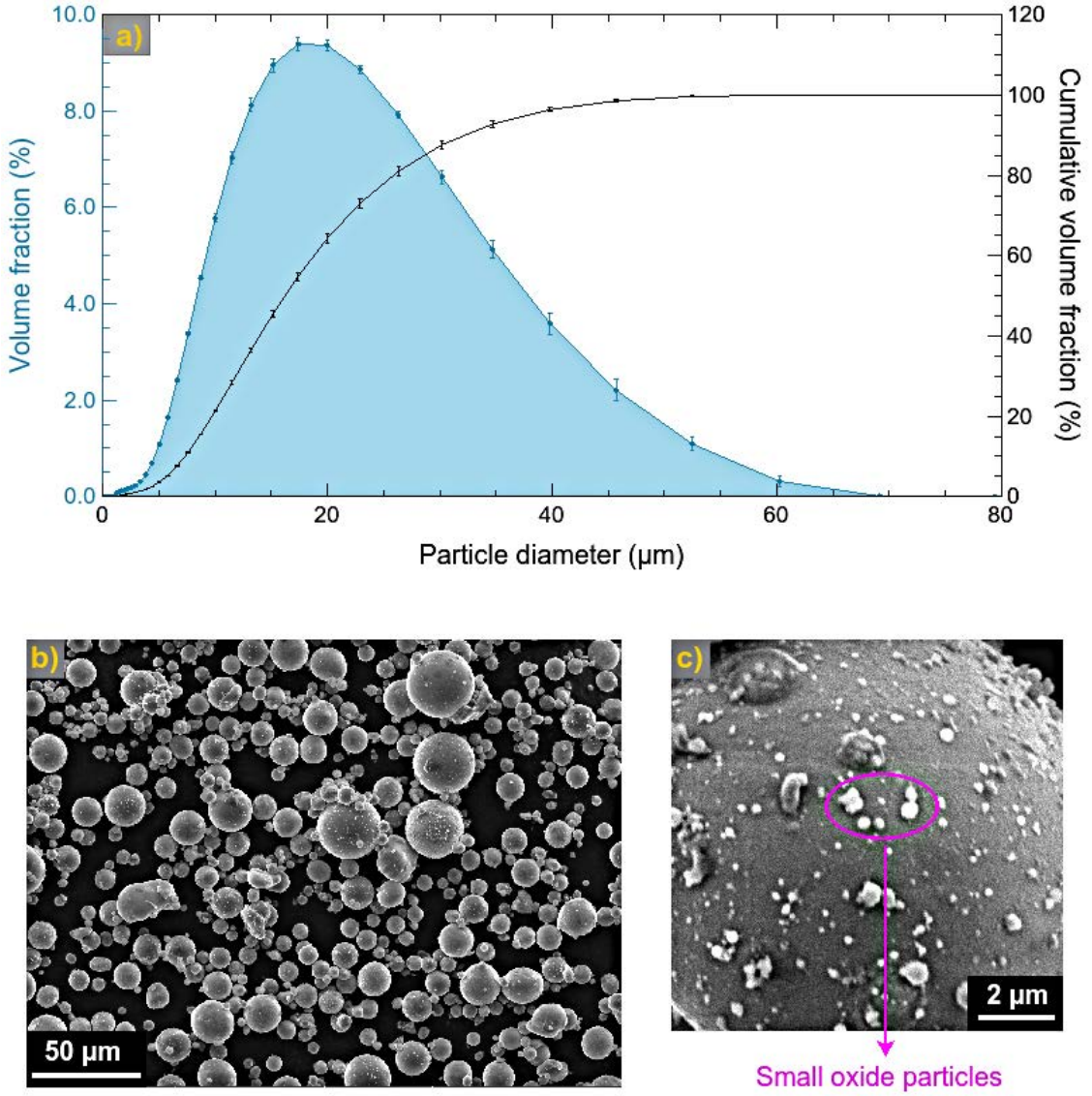

Figure 4.2: As-received powder: (a) Particle size distribution; (b) SE image of the Mg powder; (c) Focus on one particle with oxides on its surface.

binder was composed of both ethyl cellulose and poly-ethylene glycol (PEG) dissolved in ethanol. In their composition, the PEG has two different roles. This molecule usually acts as a plasticiser, meaning that it decreases the viscosity of the solution. However, in their inks it was also used for its capability to be adsorbed onto silica particles surfaces *via* hydrogen bonding. This phenomenon enabled them to obtain inks with yield stresses and shear-thinning behaviour, thus suitable for DIW [DEL 12].

The first attempt was therefore to test this binder composition, hoping for creating hydrogen bonding between PEG and the oxide present at the Mg particles surfaces. Ethyl

cellulose with an ethoxyl content of 48% and a viscosity grade of 22 cps (Acros Organics), and PEG presenting a molecular weight of 300 g·mol^{-1} were used to be in the same conditions as Deliormanli *et al.*. However, it has been observed with Ti64 study that round shaped particles enables higher solids loadings than irregular ones. Thus, although the proportions of the solution were kept identical to those used by Deliormanli *et al.*, the amount of powder was increased to 50 vol%. But the ink obtained was too fluid and did not present any yield stress meaning that not enough hydrogen bonds were formed between PEG and Mg particles. So PEG mainly acted as a plasticiser resulting in a really low ink viscosity.

The second approach was thus to eliminate the PEG from the formulation, retaining only ethyl cellulose, ethanol and magnesium. This left two possibilities to play on ink rheology: the amount of ethyl cellulose in the binder and the powder loading. As there was no plasticiser left in the formulation, the amount of ethyl cellulose used was decreased compared to Deliormanli's *et al.* study. Different binders, containing from 9 to 17 wt% of ethyl cellulose (w/w ratio from 10 to 20 %), were prepared by progressively dissolving the polymer in ethanol. During preparation, the solution was gently stirred by magnetic stirring. The stirring was prolonged until the following day to obtain a very homogeneous solution. Then magnesium powder was added in three stages in the binder, following the method used for Ti64. The batches were mixed in a dual asymmetric centrifugal mixer (SpeedMixer DAC 150.1 FVZ-K) for 1 min at 1500, 1700 and 2000 rpm after the first, the second and the last addition, respectively. Different amounts of powder were tested leading to different inks that are named according to both the content of ethyl cellulose in the binder and the amount of powder in the ink. Non-exhaustive nomenclature is given in Table 4.2 to show the principle of ink identification. The number following "EC" represents the amount of ethyl cellulose in the binder in wt% and the number following "Mg" gives the volume content of magnesium particles in the ink.

Table 4.2: Example of ink compositions and their associated nomenclature

Mg powder content (vol%)	Ethyl cellulose content in the binder (wt%)		
	9	13	17
0	EC9	EC13	EC17
50	EC9-Mg50	EC13-Mg50	EC17-Mg50
55	EC9-Mg55	EC13-Mg55	EC17-Mg55

First, binders were loaded with 50 vol% of magnesium powder. Rheological measurements were conducted prior to printing, using the same methods as for Ti64. The stress-shear rate loop approaching the printing conditions (as described in section 2.2.1.2) was applied to EC9-Mg50 ink as shown on Fig. 4.3 (a). This ink is presenting a shear-thinning behaviour with a static yield stress around 60 Pa. However it should be mentioned that here, this behaviour is not due to the binder. Indeed, both EC9 and EC13 exhibit quasi-

Newtonian behaviour as highlighted by Fig. 4.3 (b). Thus in this case, powder addition increases the viscosity but also enables the transition from a Newtonian to a shear-thinning behaviour as explained by Cesarano *et al.* [CES 98].

In addition, Fig. 4.3 (c) shows that the two binders do not present any yield stress. So the addition of particles leads to the appearance of a yield stress. However, while the static yield stress of EC9-Mg50 is clearly visible around 60 Pa, the dynamic yield stress cannot be determined clearly. And even considering that there is one, its value would be of the order of 30 Pa, which is too low for the ink to be printable (considering results obtained on Ti64). However, this is without counting on the drying effect to change from a shear-thinning to a shear-thickening behaviour. Indeed, the volatility of ethanol proves to be a real problem when carrying out rheological measurements since a number of tests had to be carried out before obtaining a complete measurement without drying, despite the use of a home-made solvent trap. However, as shown by Cesarano *et al.*, this can become an advantage when printing a structure by robocasting, as this drying process can allow layers to stack up due to the induced change in ink behaviour [CES 97, CES 98].

To maximise this phenomenon, temperature, which was held at 25 °C for rheological measurements, was increased to 35 °C for a printing test with EC9-Mg50 ink. The drying speed obtained was fast enough to allow the layers to be stacked but too slow to prevent the macropores from being closed, as shown on Fig. 4.3 (d). By comparing this structure to the "puddles" that were obtained with titanium inks presenting similar yield stresses, it is considered here that there is indeed an effect of drying on the printability of this ink. This means that the printable domain defined for Ti64 according to yield stresses will not apply identically here. In addition, as rheological data were really complicated to obtain due to ink drying, it was decided that the ink formulation would be established directly by printing tests rather than using rheological properties. Measurements of the rheological properties were therefore stopped, so no data other than those presented in Fig 4.3 have been acquired.

4.2.3 Printing tests

Printing tests were carried out using the same scaffold geometries and printing speed as for Ti64 ($10\,\mathrm{mm{\cdot}s^{-1}}$).

To improve post-print form retention, which was not sufficient with EC9-Mg50 ink, both ethyl cellulose and magnesium contents were increased. The two binders with 13 and 17 wt% of ethyl cellulose were gradually loaded with 52 to 60 vol% of magnesium powder. For each intermediate state (from 52 to 60 vol%), printing tests were carried out with all four nozzle sizes (840, 610, 410 and 250 µm diameters) at 35 °C. Some of the obtained structures are presented on Fig. 4.4.

Using the 13 wt% ethyl cellulose binder, it is possible to obtain well-shaped structures from 56.5 vol% of magnesium powder, as illustrated by the central photo in Fig. 4.4, to

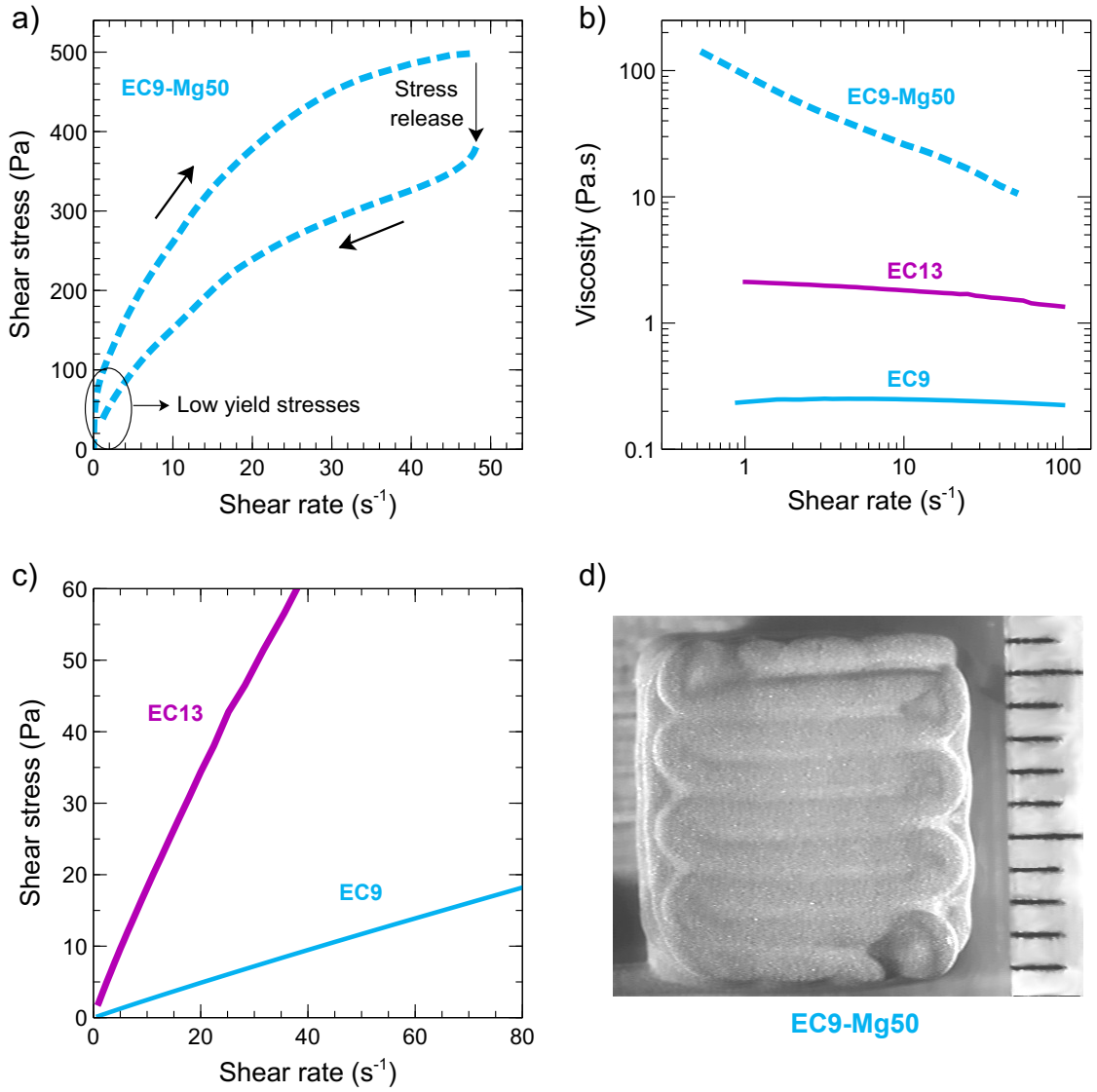

Figure 4.3: Rheology and printability: (a) Stress-shear rate loop applied to EC9-Mg50 ink, the ramp up is controlled in shear stress and the ramp down in shear-rate; (b) Viscosity evolution with shear rate for the two binders EC9 and EC13 and the EC9-Mg50 ink; (c) Shear stress evolution with shear rate for the two binders, (d) Binocular magnifying glass image of a scaffold printed with EC9-Mg50 ink. Thanks to the ethanol drying, layers are stacked despite low yield stress, but the macropores are not maintained.

60 vol%. However EC13-Mg60 ink was not extrudable through the 250 µm diameter nozzle. The high solid content might lead to nozzle clogging due to arch formation as mentioned in section 2.2.1.2. On the other hand, even if a lower particle ratio allows extrusion, the ink flow remains unstable and the resulting structures do not well respect the required geometry. Indeed, EC13-Mg56.5 ink is printable through a 250 micron needle, but ink flow was not constant throughout the structure, as shown on Fig. 4.4 (b). The EC13 loaded with a particle content ranging from 56.5 to 60 vol% is therefore considered printable to

a minimum nozzle diameter of 400 µm.

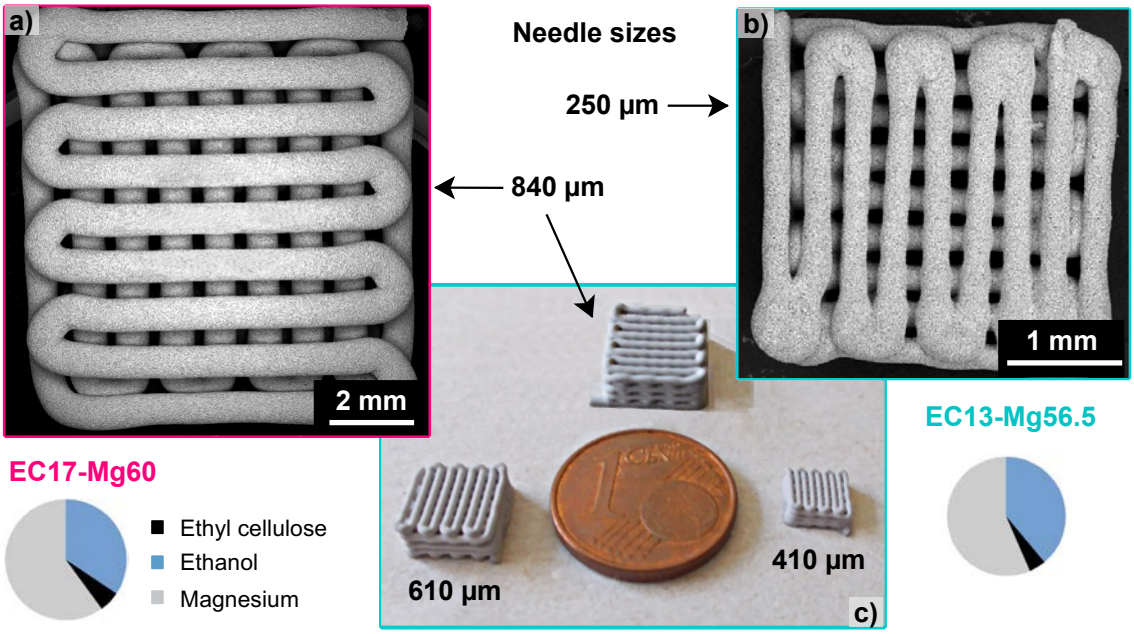

Figure 4.4: As printed scaffolds: SEM images (left and right) and picture (middle) of scaffold structures obtained with various inks and needle sizes.

Using the 17 wt% ethyl cellulose binder enables to keep macropores design for lower solids loadings. Acceptable structures are obtained from 55 vol% powder. With this solids loading, a needle diameter of 250 µm can be used but seems to lead to macropores closure again. Increasing powder ratio enables better shaping but limits again the minimum nozzle diameter that can be achieved. Indeed, EC17-Mg60 ink leads to really nice scaffolds when printed with a 840 µm diameter nozzle (see left SEM images of Fig. 4.4), but it can hardly be printed with 610 µm needles and it is unthinkable to go below. The printability window appears thus narrower with this binder and so EC13-Mg60 ink was kept for further printing.

Note that magnesium content reached here (up to 60 vol%) are far above Ti64 content added in Pluronic hydrogel (50 vol%). This may be due to the greater tendency of this binder to act as a lubricant, due to the lower surface tension of ethanol with air ($22\,mN{\cdot}m^{-1}$ at 25 °C) compared to that of water with air ($72\,mN{\cdot}m^{-1}$ at 25 °C) [ADA 67]. Once the desired shapes are obtained, the next step in the robocasting process is to debind the structure.

4.2.4 Debinding

In order to know which temperature should be used to debind these magnesium structures, thermogravimetric analysis (TGA) was first performed on EC13 binder. For practi-

cal safety reasons, this analysis was not carried out in the presence of magnesium particles. It was conducted using a TGA Q50 analyser, equipped with an EGA furnace (TA Instruments, New Castle, USA). Mass losses were recorded during a heating rate of $1\,°C{\cdot}min^{-1}$, from room temperature to 500 °C, under a $150\,mL{\cdot}min^{-1}$ nitrogen flow (after a purging step). Obtained results are reported on Fig 4.5.

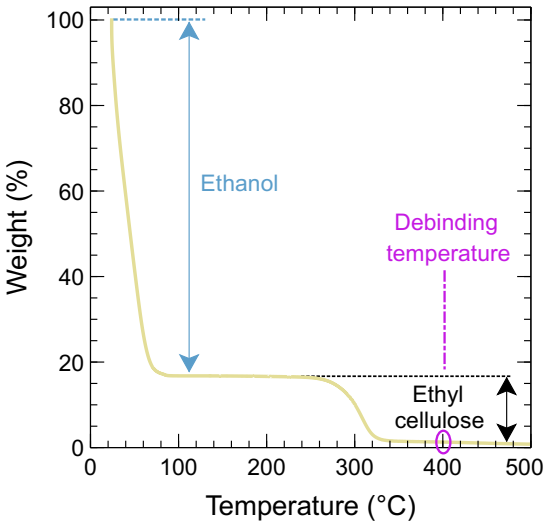

Figure 4.5: Thermogravimetric analysis of the 17 wt% ethyl cellulose binder justifying the choosen debinding temperature.

TGA of the EC17 binder shows two successive mass losses. The first, below 70 °C, corresponds to ethanol vaporisation. Then degradation of the ethyl cellulose occurs from 250 °C. Most of this degradation takes place between 260 and 330 °C. However, at 330 °C the degradation is not completely finished and a slight decrease in mass continues to be observed up to 500 °C (see Fig. 4.5). Nevertheless, this measure was performed with a continuous heating ramp, without adding holding time. Thus it has been chosen to perform debinding treatments at 400 °C only, but to add a 2 h plateau at this temperature after the heating ramp to be sure to reach complete ethyl cellulose degradation. The heating ramp was kept at $1\,°C{\cdot}min^{-1}$ and the treatment was performed in the same Naberthermn N 11/hr furnace as for Ti64, with the in-house set up enabling to work under primary dynamic vacuum (5×10^{-2} mbar).

Samples were characterised after debinding to check whether this stage had been carried out correctly. XRD patterns were acquired between 20 and 60° 2θ since this range includes the five main Mg diffraction peaks, using the same equipment as for Ti64, with the same parameters (40 mA, 40 kV and a 0.6 mm diffusion slit). XRD pattern of debinded samples presented on Fig. 4.6 (a) shows the 5 same peaks as initial powder pattern, meaning that no crystallographic transformation occurs during the debinding step.

In addition, the SEM image of a dried sample shown on Fig. 4.6 (b) highlights the

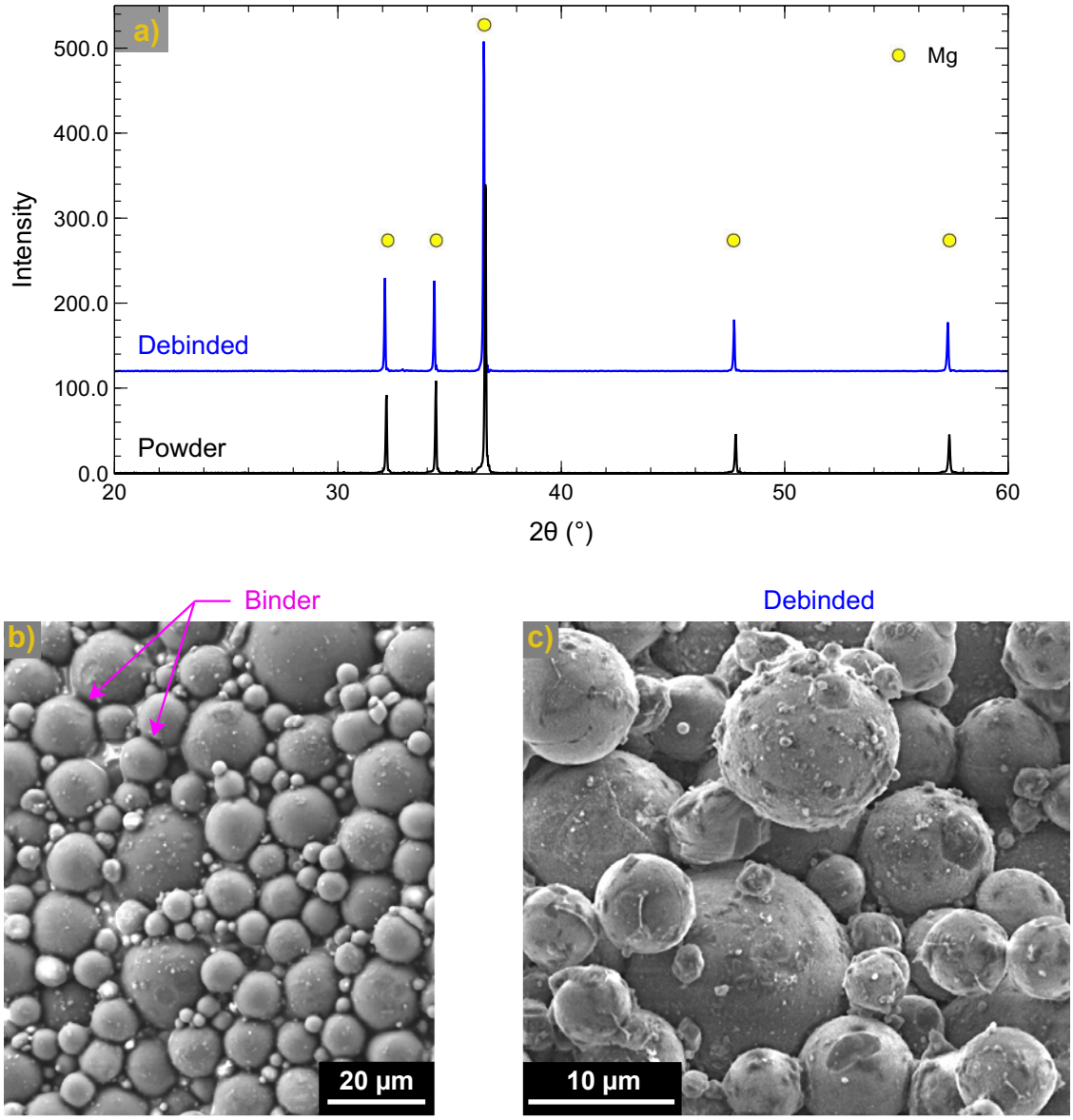

Figure 4.6: Characterisation of the debinding step: (a) XRD pattern of both as-received powder and debinded sample showing only magnesium peaks; (b) SEM image of a dried sample highlighting the presence of ethyl cellulose around the points of contact between particles; (c) SEM image of a debinded sample highlighting the success of the debinding step.

presence of ethyl cellulose around points of contact between particles. Its comparison with the debinded sample image (Fig. 4.6 (c)) emphasises the success of the binder degradation. Also, no transformation in terms of particle morphology is observed here. It is thus considered that the debinding step is successfully performed and that only the sintering stage remains to obtain the final properties.

4.2.5 Sintering and characterisations

To enable a better understanding of the different choices adopted in this section, some additional information on both equipment used and magnesium properties must first be provided.

4.2.5.1 Preliminary considerations

The Naberthermn N 11/hr furnace with its in-house set up enabling to work under various atmosphere conditions is presented on Fig. 4.7. During this thesis work, modifications were introduced on this equipment. Initially the assembly only enabled to work under vacuum. The sealing flange, into which the quartz tube is slid, was directly connected to the left-hand valve serving as a connection to the pump, and there was no gas supply. This left two possibilities: working under dynamic vacuum (both primary and secondary vacuum could be used) or working under static vacuum by closing the connection valve to the pumps. However, when it comes to heat treatment on Mg, the usual preference for a dynamic vacuum, which ensures that the atmosphere is kept as clean as possible whatever happens, may be called into question by the volatility of Mg. Indeed, at 600 °C the vapour pressure of magnesium has been reported to be comprised between 10^{-3} and 10^{-2} atm so between 1 and 10 mBar [GRA 72]. This means that a dynamic vacuum, even a primary vacuum, would result in the disappearance of the sample. Continuous pumping would not allow the sample to reach equilibrium with its partial pressure and it would therefore vaporise continuously. Note that this problem was not encountered during the debinding stage as at 400 °C, the vapour pressure of magnesium is comprised between 10^{-3} and 10^{-2} mBar, whereas the primary pump makes it possible to reach vacuum levels in the order of $5*10^{-2}$ mBar.

As for the sintering step, temperatures of around 550 - 600 °C are considered (Mg melts at 650 °C), dynamic vacuum was not kept as an option. When the valve is closed, the quality of the vacuum maintained is mainly based on the seal obtained at the flange. When all parts have been threaded onto the tube, the clamping ring is screwed onto the second part of the flange, compressing the joints between the tube and the inside of the flange (see Fig. 4.7 (c)). It is the compression of these joints that provides the seal. Although this assembly works very well in a dynamic vacuum, some doubt remains as to its effectiveness in maintaining a static vacuum. However, before embarking on more complicated set-up modifications, it seemed worth checking what could be achieved with this assembly. Thus a first sintering test was performed at 550 °C under static secondary vacuum, using a heating ramp of 10 °C·min^{-1} and a holding time of 2 h.

This first attempt was a complete failure due to both oxidation and interactions between quartz and magnesium. Indeed, as shown by Fig. 4.8, the sample came out highly oxidised from this heat treatment. On the XRD pattern obtained after this treatment, the intensity of the five Mg peaks strongly decreased in favour of the appearance of a consequent MgO

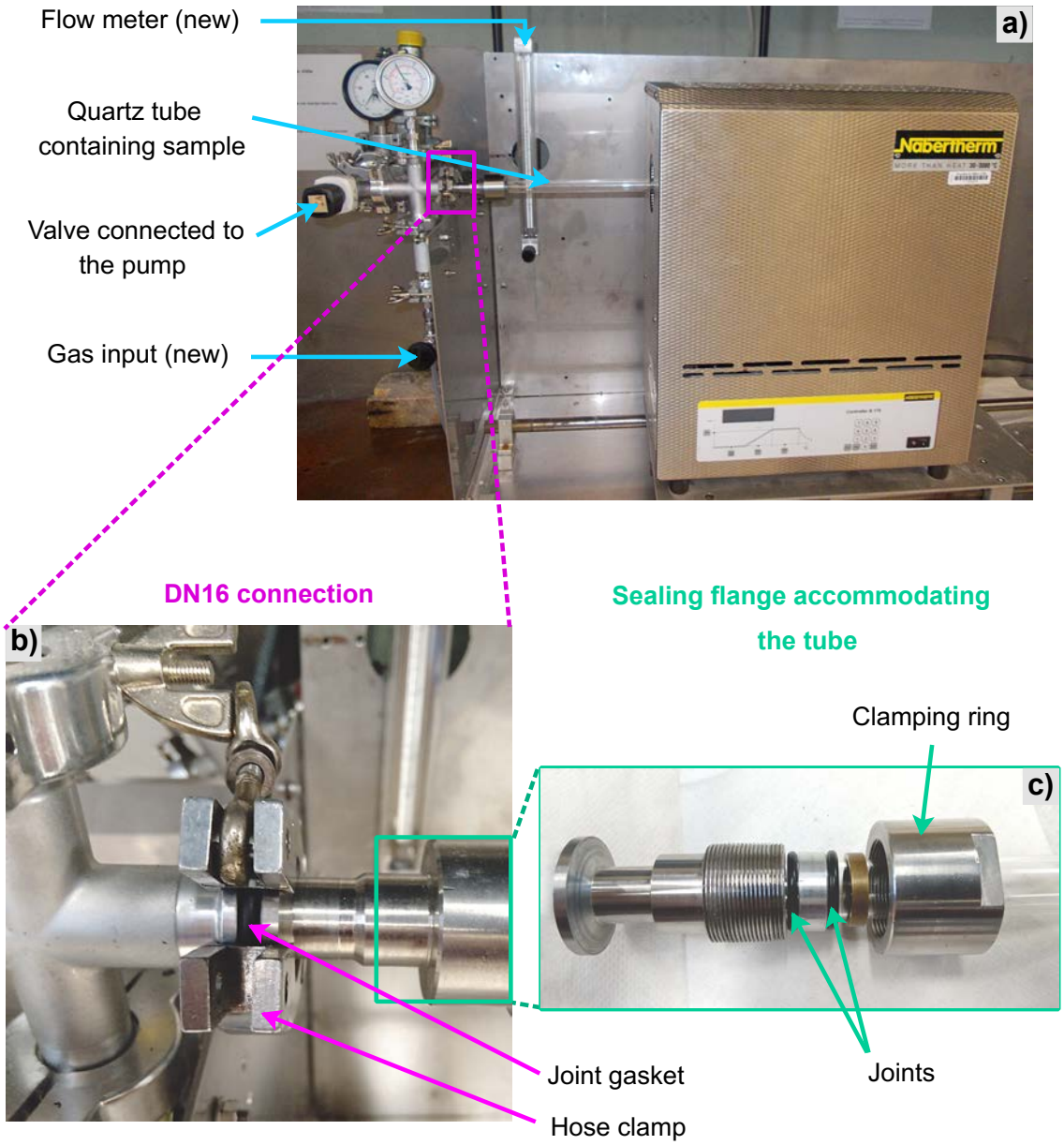

Figure 4.7: Illustration of the assembly used to carry out heat treatments in a controlled atmosphere: (a) Whole system; (b) Focus on the DN16 connection; (c) Focus on the system that enables sealing with the tube.

peak. The MgO layer formed is in addition easily visible on SEM image of the sample (white shells) and has prevented the particles sintering.

Besides the particle oxidation, an interaction between quartz and magnesium is observed as shown by the tube picture on Fig 4.8. In view of the areas concerned, it is thought that this interaction takes place with magnesium vapour, as previously observed [DEF 18, BRA 79]. This interaction is due to the highly reducing nature of magnesium (standard potential of -2,372 V), which allows it to reduce silica [LID 04]. In

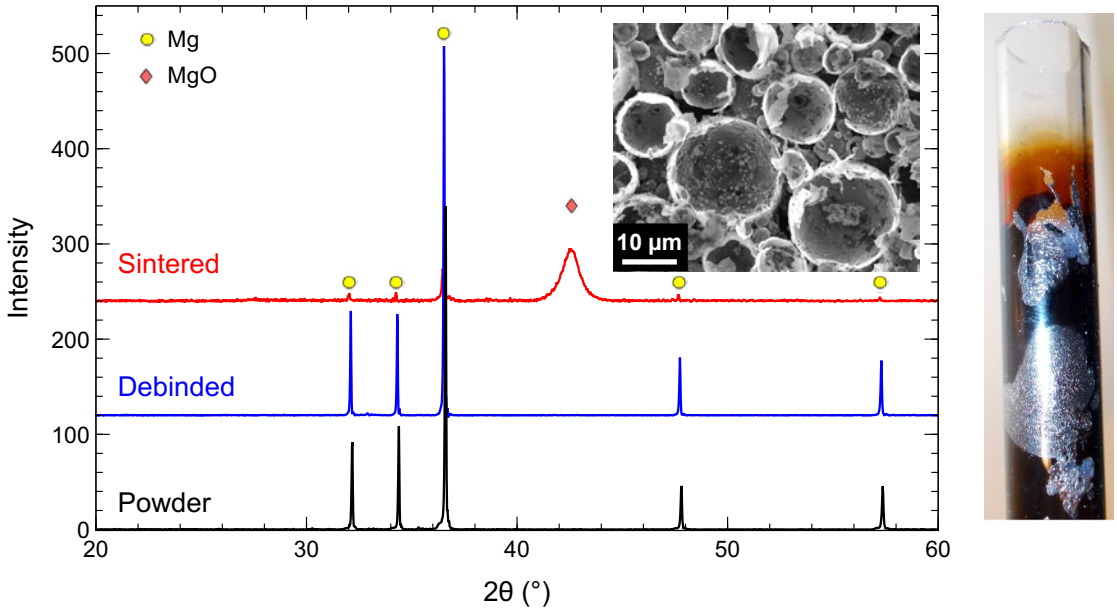

Figure 4.8: Illustration of specimen characteristics and quartz tube used condition after sintering for 2 h at 550 °C under static vacuum.

addition, as the side of the tube that is connected to the pumps remains cold (so as not to melt the joints), the Mg vapours created to form the equilibrium partial pressure can be recondensed on the wall of the tube.

This experiment highlights two important points: contact with quartz should absolutely be avoided and solutions must be found to work in cleaner atmosphere. Indeed if most of the sintering success of pure Mg involves the use of pressure to break the oxide layer [BUR 09], Wolff's *et al.* study showed that it was possible to achieve pure magnesium conventional sintering with the help of a very clean atmosphere [WOL 10].

To overcome these experimental difficulties, the first need was to find a material which remains inert with magnesium up to at least 650 °C. According to Deffrennes' study, both iron and carbon can be considered as excellent candidates [DEF 18], meaning that steel might be an interesting option. This is confirmed by the successful sintering treatment performed in steel crucibles by Wolff*et al.* [WOL 10].

In parallel an improvement of the sintering atmosphere purity was necessary. A way to achieve a reliable static atmosphere is to seal quartz tubes under secondary vacuum. This allows the sample to be enclosed in a small volume and contact with quartz can be avoided by using a steel sheet to line the inner wall of the tube. Results obtained with this technique (that have been tried first) are detailed in the following section.

4.2.5.2 Sintering in quartz tubes sealed under vacuum

With this vacuum encapsulation of the sample, the volatility of Mg is no longer a major concern. In fact, the entire quartz bulb is heated to the same temperature, so no condensation will take place during the treatment but only during cooling. And due to the small volume, the saturating vapour pressure will be easily reached. However, isolating the sample and its vapours from the quartz walls is still needed. The first test was carried out by lining the wall of the tube with a steel sheet. To vacuum encapsulate the sample in the tube, after placing the sample at the bottom of the tube, the tube is worked with a blowtorch to form a neck as thin as possible. Once the neck obtained is satisfying, the tube is connected to the pump and then closed with the blowtorch when the vacuum is below 5×10^{-4} mbar. For all the samples described in this section, sintering treatment applied consisted in a heating ramp at $10\,°C{\cdot}min^{-1}$ followed by a 2 h plateau at 600 °C and a furnace cooling.

Fig. 4.9 (a) shows a picture of the sample obtained after sintering on the steel sheet within a quartz tube sealed under vacuum. Two different areas can be observed. The sample is sintered in the area that was in contact with the steel sheet but oxidised (and therefore not sintered) elsewhere. However, quartz bulb was a bit coloured but not damaged, meaning that the interactions were indeed limited by the presence of the steel sheet. Note that the sample used for this sintering test was obtained with the EC9-Mg50 ink. So the cross-section shown here also confirms that this ink is not suitable for retaining macropores.

This semi-sintered sample was encouraging enough to dig a little deeper in this direction. As the contact with steel seemed to be helpful, it was decided to try to increase this contact. The best way to achieve this was to fully immerse the sample in powder. As pure iron powder was already available in the laboratory and as this powder ensured that there was no risk of reaction with the alloying elements, it was decided to use this one. Thus sort of crucible was created by bending the steel sheets, and filled with a little of pure iron powder. Then the sample was placed on the powder bed and the crucible was completely filled with iron powder. This crucible was afterwards vacuum encapsulated. With this set-up magnesium vapours are even more confined, further limiting the risks of interactions with quartz.

These new conditions enabled to obtain sintered samples. Fig. 4.9 (b) shows SEM images of the resulting sample cross-section, highlighting that densification has been achieved despite the presence of residual pores. However, the BSE image presented on Fig. 4.9 (c) reveals the presence of an oxide layer all around each particle, which is supposed to prevent sintering. This is confirmed by the XRD pattern obtained on this sample which shows a small peak of magnesium oxide (see Fig. 4.9 (d)). This peak was considerably reduced compared to the pattern of the sample sintered directly in the quartz tube under static vacuum, but is still present. A known solution allowing sintering to take place in spite

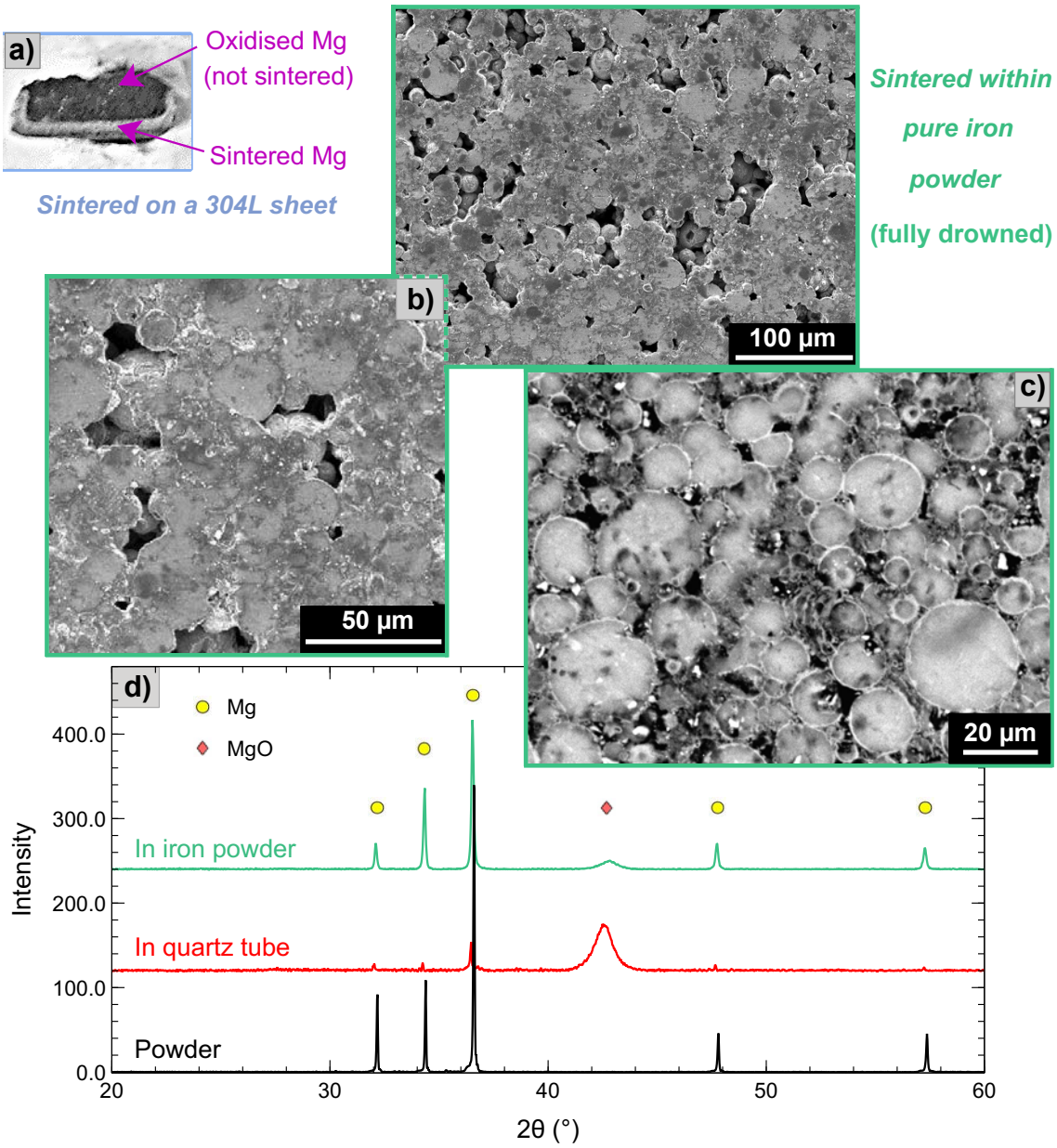

Figure 4.9: Sintered samples : (a) Sample obtained after 2 h at 600 °C on a steel sheet within a sealed quartz tube; (b) SE image of a sample sintered by being immersed in pure iron powder; (c) BSE image of the same sample highlighting the oxide layer present around the particles (white shells); (d) XRD pattern evolution with sintering conditions.

of the oxide layer on the surface of the particles is to have cracks within this oxide layer allowing the diffusion of Mg. However these cracks are usually formed under the effect of a pressure deliberately applied to the particles [BUR 09], so the conditions for forming them are not met here. It is thus supposed that the observed sintering is more likely to be due to evaporation-condensation phenomena, made possible by the confinement of the

vapour phase around the sample.

To quantify the remaining porosity after sintering, high-resolution X-Ray tomography was performed on a small part cutted from the sample. The sample was scanned with a voxel size of 0.7 µm and pore analysis were performed using the same methods as for Ti64 filaments.

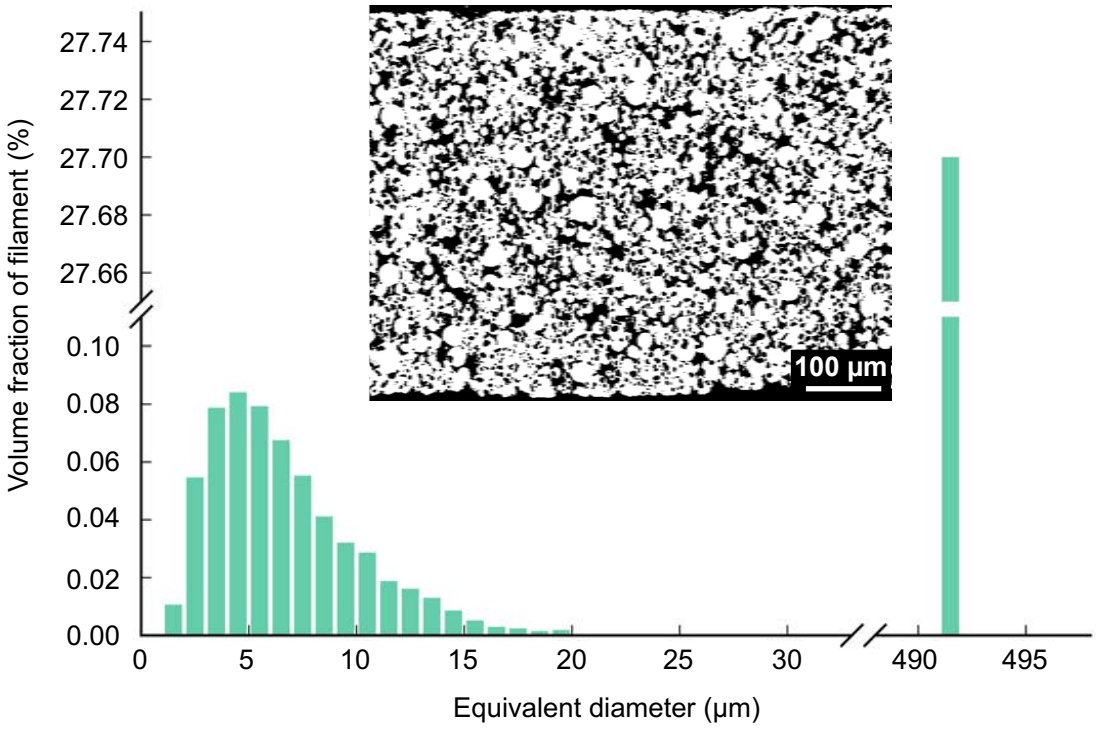

Figure 4.10: Remaining porosity: Pore size distribution with an example of sample section obtained by X-Ray tomography, where magnesium appears in white and pores in black.

Fig. 4.10 shows the pore size distribution with an example of sample section. Remaining porosity after sintering was evaluated between 28 and 30 vol%. As previously shown, this important porosity leads to an interconnected network and almost no closed pores. Such a level of remaining porosity is consistent with the hypothesis of vapour phase sintering. Indeed, material transport by vapour phase does not give rise to shrinkage. The material evaporates at the top of a particle (surface) and is recondensed on the surfaces at the points of contact between particles. This transport phenomenon therefore does not involve diffusion from bulk, preventing densification from occurring [KAN 04].

To complete structural analysis, sample microstructure was studied by EBSD using the same equipment as for Ti64. Prior to acquisition, the sample is polished using SiC grids to P4000 with ethanol lubrication, and then a finishing step is carried out using a mixture containing 50 vol% MasterMet (Buheler, ITW Test & Measurement GmbH, Esslingen,

Germany) and 50 vol% ethanol. Immediately after polishing, the sample is placed in a glove box to be stored (even for a short time) and then transported to the SEM in an inert atmosphere. Inverse Pole Figure (IPF) maps obtained using a 5° grain boundaries criterion are shown on Fig 4.11 (a). The mean grain diameter was evaluated at 5 µm. In addition a preferential orientation of the basal planes {0001} in the direction normal to the polished surface seems to be observed, according to the IPFZ map. This texture is confirmed by the pole figures presented on Fig. 4.11 (b). However, the robocasting process is not supposed to result in preferential orientation and no such texturing has been observed on Ti64, which might point towards a polishing-induced texture.

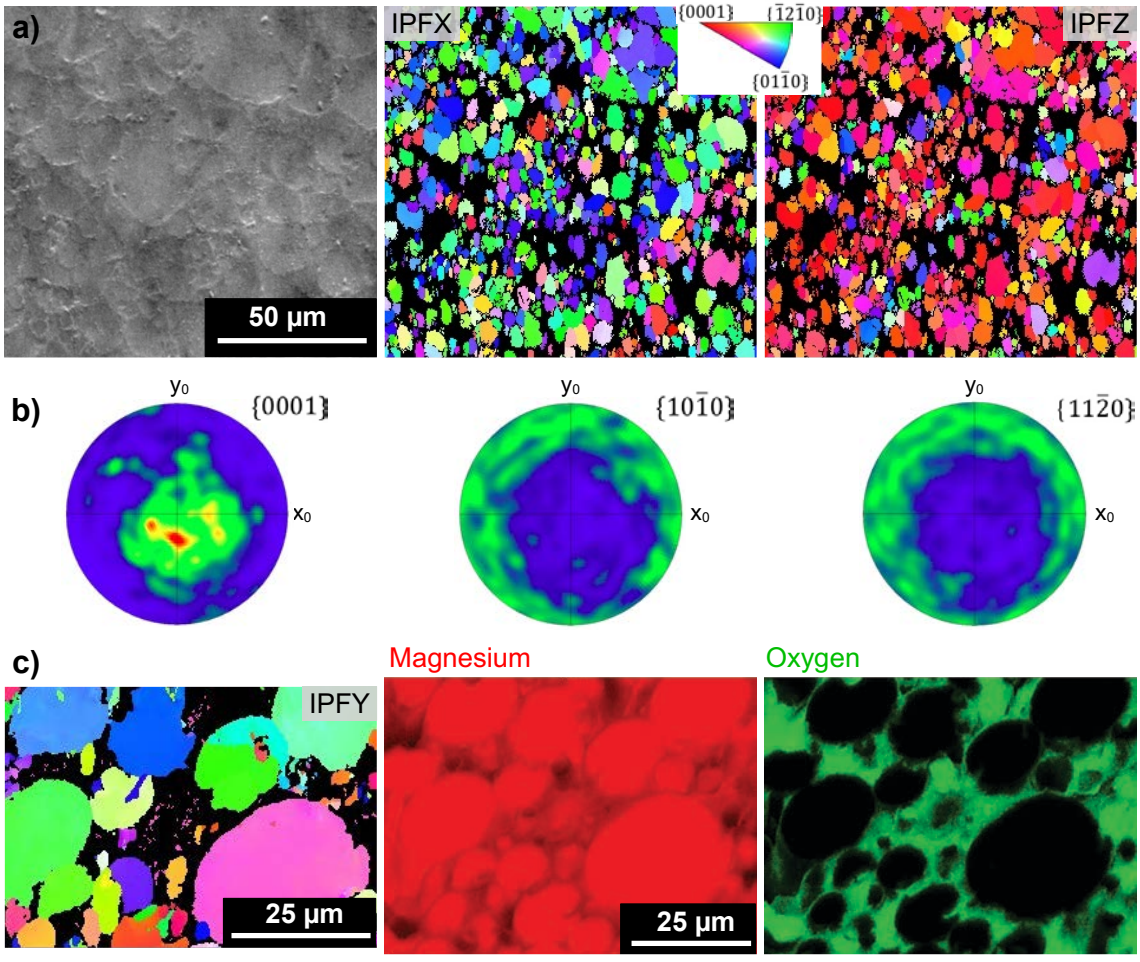

Figure 4.11: As-sintered microstructure: (a) IPFX and IPFZ maps obtained by EBSD with the associated SE image of the analysed area; (b) Pole figures showing a preferential orientation of {0001} planes in the Z direction (normal to the polished surface); (c) IPFY map associated with maps of the same area obtained by EDS, showing that only the least oxidised grains are indexed by EBSD.

However, a fact not to be forgotten when considering the question of the representativeness of this texturing is the 40% non-indexing obtained on an almost dense area of

the sample. To understand the origin of this non-indexing, an area was analysed by both EBSD and EDS at a higher magnification. Results obtained are presented on Fig. 4.11 (c) and it is clear that the difficulties of indexing are linked to the presence of an oxide layer. It can then be hypothesised that it is not the sample that is textured but the oxidation of the latter which occurs according to preferential orientations. This would mean that the {0001} planes allowing Mg indexing would be those with the thinnest oxide layer, which is in agreement with previous observations on magnesium corrosion [BLA 17].

However, initial results regarding grain size should be taken with caution and have yet to be confirmed. Indeed SE image showing the area used for EBSD indexing, gives the impression that the analysis is carried out on an almost dense sample. This is due to the fact that the polishing stage closes the surface pores because of the Mg softness. This phenomenon (verified by tomography on a piece of polished sample) can induce a deformation of the grains. Thus sample microstructure should be observed after an ionic polishing to be sure to access to the real grains shape and size.

In addition to these structural characterisations, Vickers hardness was performed to get a first glimpse of the mechanical properties obtained. Tests were carried out by applying a 100 gf load, and indentations were made on two different samples to obtain a minimum of 10 measurements. The measured value of (22 ± 2) HV is lower than the Mg bulk hardness (35 - 40 Hv [SAH 15]) due to remaining porosity.

While this method of confining the sample in iron powder in a vacuum-sealed ampoule does produce sintered samples, it has a significant limitation in terms of achievable sample size. Indeed larger quartz tubes are more difficult to close with a blowtorch. A solution must therefore be found to move to a more viable scale.

The first idea was to perform set-up modifications to enable working in an inert gas atmosphere. These modifications had to be coupled with the use of a steel tube (instead of quartz) ending directly with a DN16 connector, to allow the use of slight overpressure without the risk of ejecting the tube (see Fig. 4.12). In this configuration the condensation of Mg vapours in the cold zone of the tube can still take place, inducing a mass loss for the sample. To minimise this phenomenon, sacrificial Mg can be placed at the end of the tube, in the hottest zone of the oven, while the sample would be voluntarily placed in the gradient zone. This would allow the sacrificial Mg to be brought to a higher temperature than the sample, causing it to vaporise first to reach equilibrium pressure. This sacrificial magnesium would then also play the role of oxygen getter, which should facilitate sintering [WOL 10].

4.2.5.3 Sintering in steel tubes under slight argon overpressure

Once everything was in place to modify the set-up associated with the oven, tests could be carried out in the stainless steel tube under slight argon overpressure. Magnesium powder has been added at the bottom of the tube to be preferentially vaporised and play

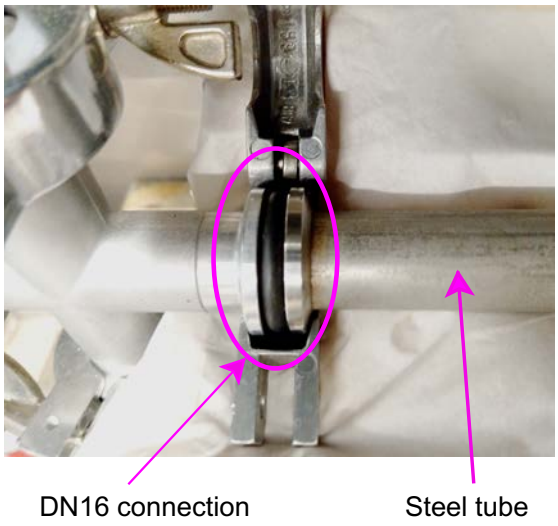

Figure 4.12: Stainless steel tube ended by a DN16 connection.

the role of oxygen getter. The sintering treatment has been kept identical: a heating ramp at 10 °C·min^{-1} followed by a 2 h plateau at 600 °C and a furnace cooling. Results obtained with this treatment are presented on Fig. 4.13.

Despite a diffraction pattern showing almost no magnesium oxide (see Fig.4.13), the sample was not sintered, not only in terms of densification, but also in terms of consolidation. Powder remained on the glove after passing the finger over the sample. And even though some small sinter necks can be guessed between the finest particles (see Fig. 4.13), this was not enough to consolidate the structure. However, the sintering time used here was really short compared to the 64 h used by Wolff *et al.*. Thus a second trial was performed with a sintering plateau of 60 h. This change in holding time resulted in no change other than the formation of a thin layer of Mg_2Ni on the surface that was in contact with the steel tube.

Comparison of these results with those obtained in the previous section reinforces the hypothesis on the role of the vapour phase. Indeed, in this current case, the accessible volume for the vapour phase is important. In addition, despite a continuous supply thanks to the sacrificial Mg powder, the vapour can still recondense in cold areas of the tube. Whereas in the previous case, the Mg steam was kept close to the sample thanks, on the one hand, to the small volume of the quartz bulb and, on the other hand, to the labyrinth created by the iron powder in the crucible. This hypothesis seems also in agreement with Wolff *et al.* observations. Indeed in their study they showed that the presence of the Mg getter near the sample did not really enhance sintering (isolated necks only) whereas the sample fully surrounded by Mg getter were truly consolidated and reached a density of 85 %. And even if they only considered this magnesium getter in terms of surface to absorb impurities, their specimen No.1 was also completely surrounded by Mg vapour,

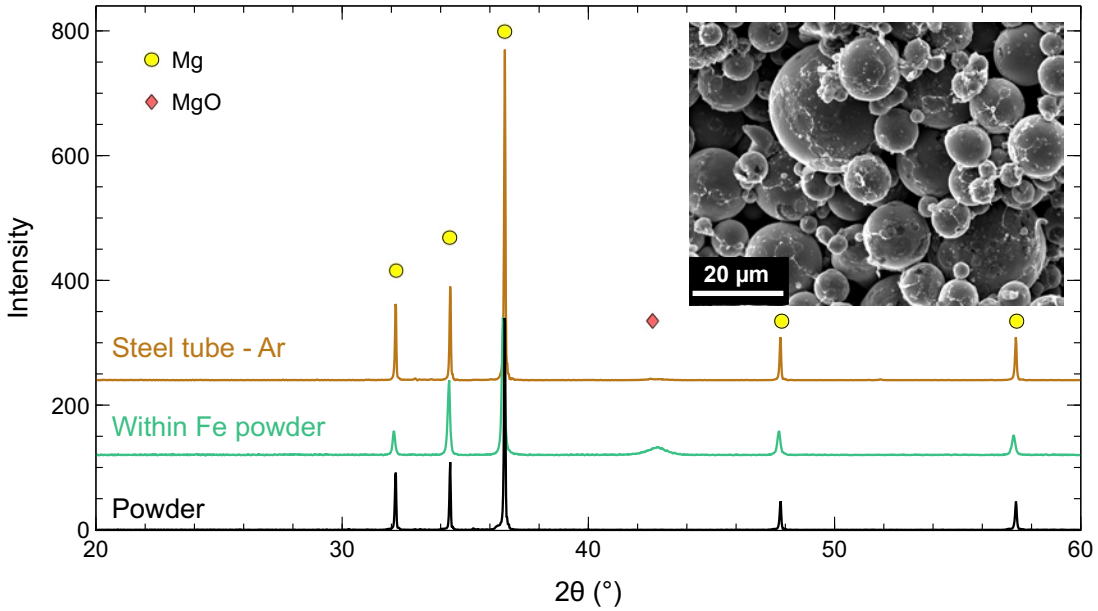

Figure 4.13: Evolution of XRD pattern with sintering conditions, associated with a SEM image of the sample "sintered" in the steel tube under slight Argon overpressure.

which could help neck formation but prevent shrinkage. And considering the results of these thesis works in addition to their study, it appears that this sintering phenomenon can be observed in a less pure but vapour-laden atmosphere, whereas a purer atmosphere (without surrounded Mg vapour) is not sufficient to obtain sintering.

In the absence of a suitable assembly such as the one presented in Wolff's study (labyrinth crucible to saturate the environment with magnesium vapour) and of sufficient Mg powder to be sacrificed to create the vapour phase, other alternatives should be considered to obtain the sintering of magnesium or its alloys.

4.3 Sintering alternatives

Unless being able to maintain a very high purity with very low contents of critical elements such as iron, nickel, copper or cobalt, the corrosion of pure Mg is too rapid to use it as a support for bone reconstruction [SHA 03]. Properly selected alloying elements can be a means of reducing this rate of degradation [LI 16] and at the same time strengthen mechanical properties [STA 06, CHE 14]. In addition alloying elements can assist sintering by the formation of a small proportion of liquid phase at the chosen temperature (for eutectic alloys) [WOL 10, SAL 19c]. Liquid phase sintering can therefore be considered as an alternative for sintering magnesium alloys following robocasting.

4.3.1 Liquid phase sintering of Mg alloys

Sintering relies on diffusion mechanisms (e.g. volume, surface, or grain boundary) that allow atoms to be transported to (and through) the points of contact between particles. Depending on materials, the oxide layer formed on particles surface can either improve or slow down this diffusion [MUN 79]. The difficulties encountered in sintering magnesium are related to the low diffusion of magnesium in its own oxide. Indeed, at 650 °C, self-diffusivity of magnesium is considerably faster than its diffusivity in MgO ($3.01 * 10^{-12}$ [SHE 56] and $5.25 * 10^{-24}$ $m^2 \cdot s^{-1}$ respectively [LIN 14]). It should be noted that MgO is a stable compound which has no chance of decomposing during the sintering of Mg alloys and which also cannot dissolve in the Mg matrix due to the low solubility of oxygen in Mg. That is the reason why the formation of cracks within the oxide layer is needed to improve the sintering process.

Cracking of this layer can be achieved by applying mechanical pressure as commonly used in the literature [BUR 09]. However, Salehi *et al* showed that the increase in the proportion of liquid in Mg alloy particles can also lead to the rupture of the oxide shell due to the overpressure created within the particles [SAL 19c]. The leaking liquid is then accelerating densification thanks to capillary forces that pull powder particles together. In addition the liquid phase offers a hundreds of times faster diffusion path than the solid phase [GER 16]. However, a too high proportion of liquid phase can lead to the loss of the sample shape [GER 97, SAL 19c]. This problem could be even more critical for fine structures with macropores than for denser structures such as the one studied by Salehi *et al.* [SAL 19c]. On the other hand, a small proportion of liquid may not be sufficient to crack the oxide layer, which must be thicker in the case of the robocasting process than in the case of the binderless process used by Salehi *et al.* [SAL 19c].

Thus, before going further in the reflections on the alloy that would give the best compromise of properties for bone implantation while allowing liquid sintering above the solidus, it may be preferable to check the compatibility of such a technique with scaffold type structures and robocasting process. To do so, it was first envisaged to test the liquid sintering of scaffold using a Mg - Zn powder blend, as this bio-compatible system presents a liquid phase at low temperature as shown on the phase diagram of Fig. 4.14. This choice was also supported by the fact that Zn is less oxidisable than Ca and less controversial than Al for use as a resorbable implant.

As this test was only intended to test the viability of such a perspective, it was decided to use proportions that would give the least experimental complications. The idea was therefore to prepare different mixtures of powder allowing to reach different liquid volume fraction at 380 °C, a temperature at which there is no interaction between Mg and quartz.

To find out the correspondence between the mass percentage of Zn added in Mg and the volume fraction of liquid formed at 380 °C, the evolution of the molar fraction of liquid according to the molar fraction of Zn in the powder mixture was extracted from

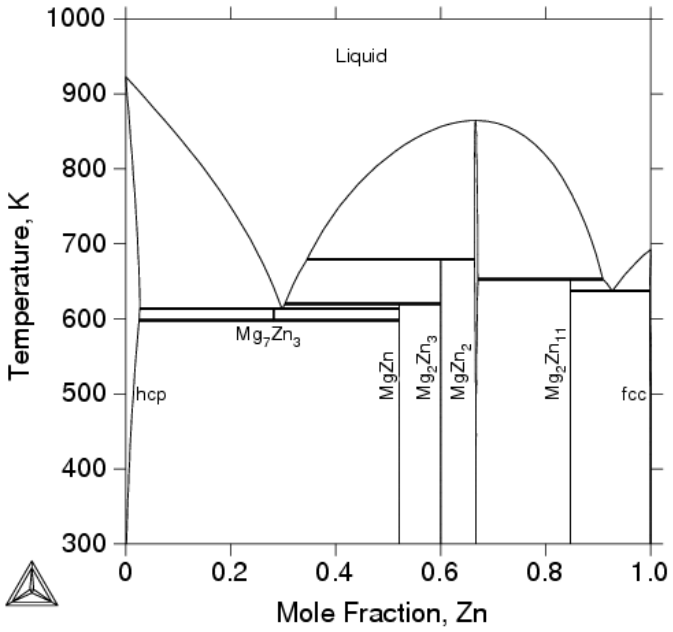

Figure 4.14: Mg-Zn phase diagram calculated by Zhong [ZHO 05].

Thermocalc software. The associated amounts (in mole) of both Mg and Zn in each phase (n^l_{Mg}, n^l_{Zn}, n^s_{Mg} and n^s_{Zn}) were extracted too. Then for each initial mole fraction of Zn, the liquid volume fraction obtained is calculated from:

$$f^l_v = \frac{V_l}{V_l + V_s} \tag{4.1}$$

$$Where: \quad V_l = V^l_m * n^l = \frac{M^l_{Zn}}{\rho^l_{Zn}} * n^l_{Zn} + \frac{M^l_{Mg}}{\rho^l_{Mg}} * n^l_{Mg} \tag{4.2}$$

$$And: \quad V_s = V^s_m * n^s = \frac{M^s_{Zn}}{\rho^s_{Zn}} * n^s_{Zn} + \frac{M^s_{Mg}}{\rho^s_{Mg}} * n^s_{Mg} \tag{4.3}$$

In addition, liquid density differs from that of corresponding solid and varies with temperature. The density of both liquid Mg and liquid Zn has been shown to evolve linearly with temperature. By extrapolating the obtained straight lines down to 380 °C, it gives a density of 1.67 g·cm^{-3} for liquid Mg [MCG 62] and of 6.61 g·cm^{-3} for liquid Zn [WAN 03]. In addition, molecular mass used were 24.3 and 65.4 g·mol^{-1} for Mg and Zn respectively and solid densities used were 1.74 and 7.13 for Mg and Zn respectively.

It was first decided to mix 22 wt% of Zn with Mg powder, using a Turbula 3D shaker mixer (Willy A. Bachofen AG, Munttenz, Switzerland). This powder mixture should give rise to 28 vol% liquid at 380 °C. According to Salehi *et al.* this should be more than enough to break the oxide layer and should even lead to a shape loss [SAL 19c]. But this blend can

always be mixed with a known volume fraction of pure Mg to adapt the proportion. An ink composed of the EC13 binder loaded with 60 vol% of this powder blend was printed with a 840 µm needle size. In view of the considered sintering temperature, debinding and sintering were carried out in a single step. A heating rate of $1\,°C{\cdot}min^{-1}$ was applied up to 350 °C, followed by 30 minutes of holding at this temperature to debind. Then the temperature was increased up to 380 °C and held for 60 h. This treatment has been first performed in steel tube under a slight overpressure of Argon. However as the resulting sample was not sintered at all, a second test was carried out using the same treatment but in a vacuum-sealed quartz bulb. As the latter was no more conclusive, a third test was carried out with a sample made from a 27 wt% Zn powder blend supposed to lead to more than 38 vol% liquid phase at 380 degrees. Once again the sample was not sintered. So a Differential Scanning Calorimetry (DSC) was conducted on the powder blend to check whether the diffusion between the two powders to obtain the MgZn compound (and therefore a liquid phase at 380 °C) took place. Results obtained are shown on Fig. 4.15.

DSC measurements were performed using a Labsys evo equipement (SETARAM, Caluire, France). A first heat treatment was applied to check whether a liquid phase is formed at 380 °C, as shown on Fig 4.15 (a) (heating and cooling rate of $5\,°C{\cdot}min^{-1}$ and holding time of 2 h). Then a second ramp is applied up to 660 °C to be sure to achieve complete melting (Fig 4.15 (b)). All measurements were carried out under nitrogen after three purges of the system.

The change in heating rate between the heating ramp and the isothermal holding leads to thermal instability, which disturbs the measured heat flow. However, despite this instability, the presence of an exothermic peak followed by an endothermic peak at the beginning of the plateau seems to be assertable. The melting event highlighted by the endothermic peak is confirmed by the presence of a crystallisation peak during cooling. The exothermic pre-melting peak can then be attributed to the bond formation between the magnesium and zinc atoms. Indeed, these bonds must necessarily be formed for fusion to take place below 419 °C, temperature at which Zn melts. The formation of a covalent bond is accompanied by a reduction in potential energy and thus a release of heat.

During the second ramp, as the defined compound Mg-Zn was already formed, the beginning of melting corresponds to the melting temperature of the eutectic and extends over the entire temperature range between liquidus and solidus. The area ratio of the peaks indicates the formation of 28 wt% liquid phase during the first rise in temperature, corresponding to 22 vol%. This value is lower than the 40 vol% expected according to thermocalc calculation. However, it should be mentioned that enthalpy of fusion is varying as the composition of the liquid phase formed evolves with the temperature. In addition, it is not sure that the first ramp allowed a complete interdiffusion between Mg and Zn, as diffusion can be slowed down by the presence of an oxide layer. However, diffusion is sufficient to effectively allow the formation of a liquid phase in these conditions. But at the time of writing this manuscript, additional characterisations are still needed to

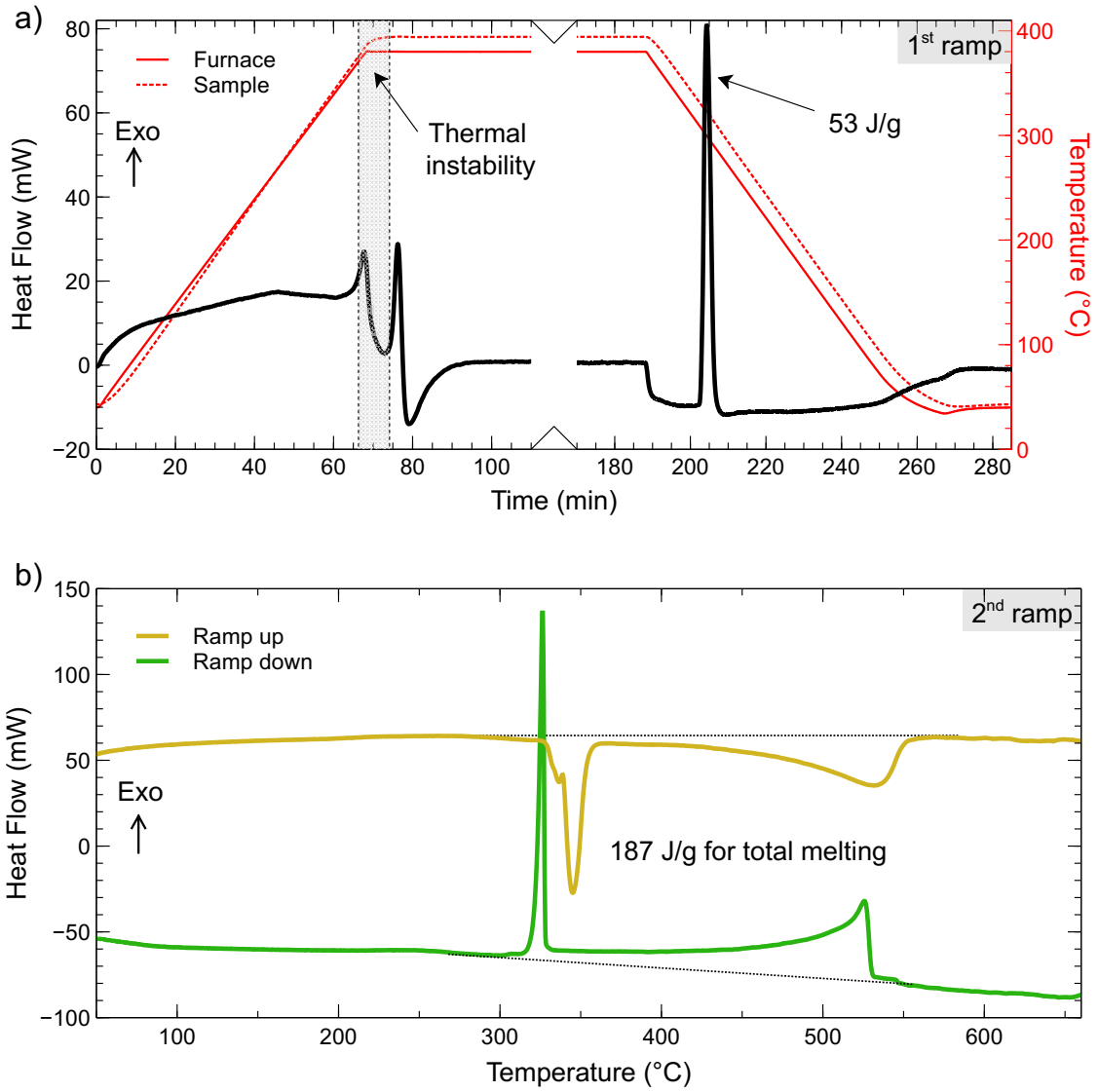

Figure 4.15: Differential Scanning Calorimetry performed on the powder blend containing 27 wt% of Zn

understand why sintering does not take place. Indeed it should be interesting to performed XRD measurement on scaffolds used for sintering attempts to check whether the defined compound MgZn has been formed or not. And DSC should also be performed on dried ink instead of powder blend to see if the presence of the binder has an influence on the formation of the liquid phase. Indeed, the liquid can be formed but remain trapped by the oxide layer, or this layer can actually prevent the formation of the liquid by limiting diffusion.

Additional characterisations would therefore be necessary to understand the real limitations of the use of liquid sintering within the framework of the robocasting process, keeping in mind that this kind of sintering might be facilitate by the use of a prealloyed

powder and can be assisted by microwave [SAL 19a]. However, as cracking of the oxide layer can also be achieved by mechanical pressure, another alternative was investigated in parallel.

4.3.2 Spark Plasma Sintering

Spark Plasma Sintering (SPS) is a technique that relies on the Joule effect to heat the sample. During the treatment a pressure is applied to the sample to ensure good electrical contact. Pure magnesium has already been successfully sintered thanks to this technique [MUH 10, CHE 17]. This might be due to the applied pressure during sintering that can crack the oxide layer and thus facilitate sintering [BUR 09]. However, in the context of this PhD work, high pressures cannot be applied since it is desired to keep the shape given by the robocasting process. Nevertheless, some strategies can be considered to limit the pressure seen by the scaffold.

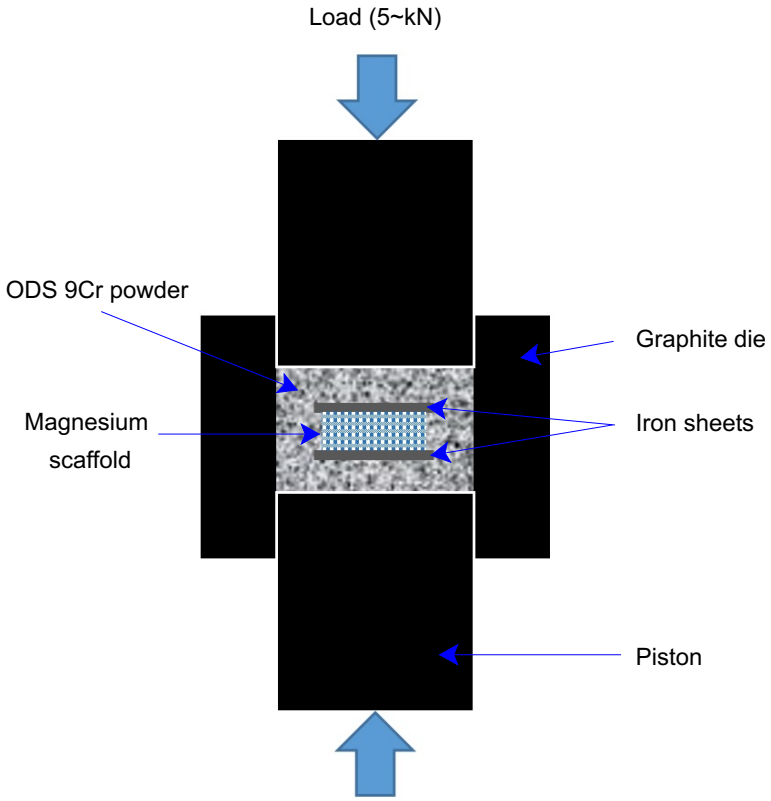

Figure 4.16: Scheme of the set-up used to sinter a magnesium scaffold by SPS.

To obtained sintered parts with SPS, powders are usually pourred in a graphite die. Variable die diameters can be used. To reduce the pressure seen by the scaffold, the latter can be placed in a die of a much larger diameter than its size, which would be filled with a

powder that is inert with the Mg and not sinterable at temperatures suitable for the Mg. Steel sheets can be used to prevent the powder to fill the scaffold and get trapped inside, as schemed on Fig. 4.16. In addition, a powder presenting a high hardness is preferable to limit compaction during the process.

To test the feasibility of such a method, a die with a diameter of 40 mm was first partially filled with an Oxide Dispersion Strengthened (ODS) 9Cr steel powder. Then a scaffold printed with a 610 µm needle size (8 mm side), protected with two steel sheets was placed on the powder, and the filling of the die was completed with ODS 9Cr powder. The assembly was then subjected to the following treatment: heating rate at 50 °C·min^{-1} up to 450 °C, followed by a second ramp at 25 °C·min^{-1} up to 500 °C and then a 10 min plateau at 500 °C to end with a return to room temperature at 50 °C·min^{-1}. During the whole process, the die was subjected to a force of 5 kN corresponding to a pressure of approximately 4 MPa.

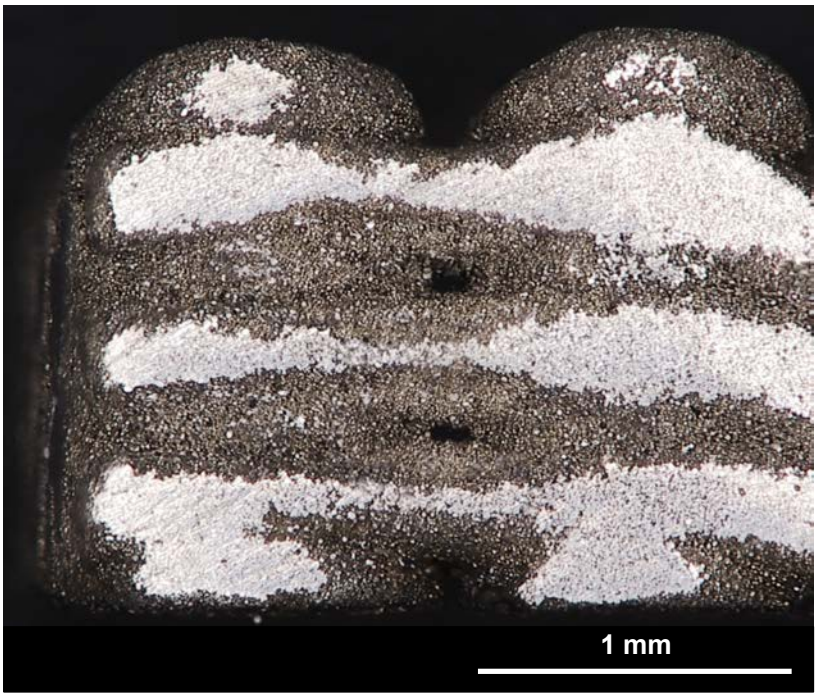

Figure 4.17: Photo taken with a binocular magnifying glass after lightly polishing one side of the SPS-sintered scaffold. White areas correspond to the areas in cross-section, which were in the polishing plane.

Once the treatment was completed, the sample was taken out of the partially compacted steel powder. This step was made easier by the presence of the stainless steel sheets but a better packaging of the sample using a complete cube of stainless steel sheets should be considered for the future. A quick polishing test on one side of the scaffold highlighted the success of sintering with this method, as shown on Fig. 4.17. However, a full monitoring should be carried out to ensure that this method does not damage the structure: X-Ray

tomography scan can be performed before and after this sintering treatment to follow the structure evolution. Note that crushing in the direction of compaction can be limited by using a steel ring of slightly lower height than the initial sample (if necessary).

This method therefore appears to be a promising solution for sintering magnesium (or magnesium alloy) parts that have previously been structured by robocasting.

4.4 Conclusion and perspectives

The main findings to be retained at the conclusion of this chapter are presented in the figure 4.18. First, printable inks were obtained raising the ethyl cellulose content in ethanol up to 13 - 17 wt% and the magnesium content in the binder up to 60 vol%. In addition, to help preserve the shape, a fast drying of the structure being printed were obtained through a temperature of 35 °C within the printing chamber. Drying has the effect of increasing the yield stress of the ink as it takes place and also allows the ink to switch from shear-thinning to shear-thickening behaviour. It therefore ensures the success of shape preservation. In these conditions, EC13-Mg60 ink was printable down to a needle size of 410 µm.

Then, structures were successfully debinded under a primary dynamic vacuum, using a heating rate of 1 °C·min^{-1} followed by a holding time of 2 h at 400 °C. Sintering, on the other hand, is more difficult to achieve due to magnesium reactivity. It was shown that a partial sintering through evaporation-condensation can be obtained by confining the sample within pure iron powder, in a quartz tube sealed under vacuum. However this sintering type prevents shrinkage from occurring, leaving between 28 and 30% of remaining porosity. In addition, using a cleaner atmosphere (Argon overpressure), but without confining the magnesium vapour near the structure to sinter was not sufficient to consolidate the structure.

Two alternatives for sintering magnesium-based structures were then investigated. While additional analysis are still required to conclude on the compatibility of liquid phase sintering with robocasting process, the use of SPS but with lowered pressure seems to be a promising route to be explored further. A follow-up of the scaffold structure evolution with this sintering method should be performed to decide whether it is necessary to use an additional piece to limit crushing in the direction of compaction. It must then be possible to vary the density of the filaments by adjusting the sintering parameters (time, temperature).

However, it should be noted that, contrary to what has been done for titanium, no optimisation of debinding has been carried out here. But, as a holding time is added after the heating ramp, the debinding temperature might probably be lowered to 350 or even to 330 °C. This might maybe help to decrease the thickness of the oxide layer formed around particles, that further prevents sintering to occur.

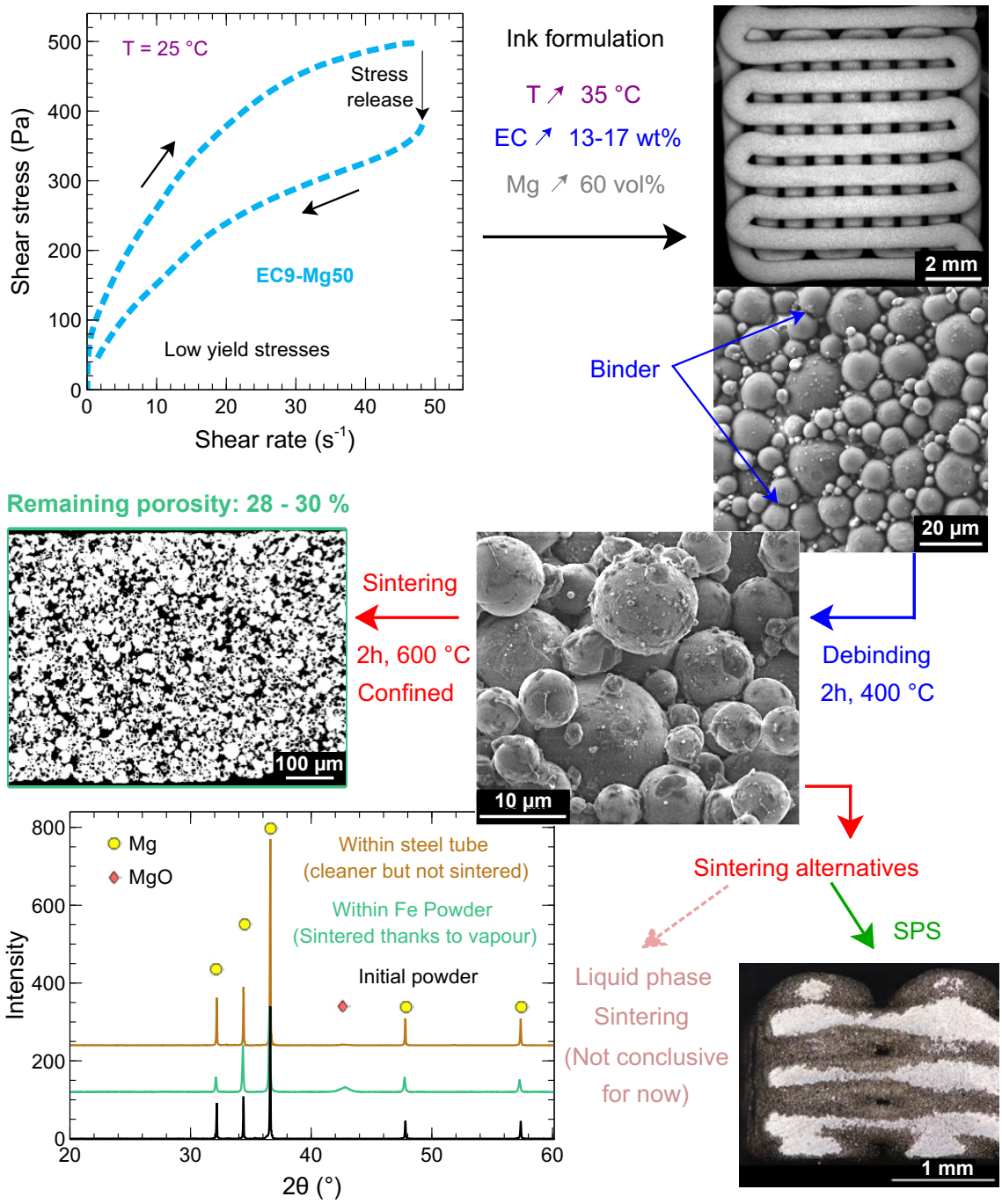

Figure 4.18: Graphical summary containing main results presented in this chapter.

In addition, only one set of conditions has been tried for vapour sintering. It would therefore be interesting to check what densification could be brought by a higher temperature and a longer sintering time.

Conclusion and Perspectives

Robocasting of metals: promising process or curiosity for science?

The present PhD-work investigated robocasting as a process to design metallic parts for orthopaedic implant applications. The study was conducted on two different materials: titanium, which is currently a reference for permanent implants, and magnesium, whose alloys are promising for applications as resorbable implants.

As micropores have been identified as beneficial for osseointegration by various authors, a parametric study was carried out on Ti64 to vary the residual microporosity and evaluate its consequences on the final properties of the part (both from a dimensional and structural point of view, as well as from a point of view of usage properties). In addition, as the final chemical composition and phase assemblage can greatly impact the mechanical properties of the parts obtained, the influence of the debinding parameters was also studied in terms of interstitial enrichment and induced embrittlement.

Concerning magnesium, as its reactivity makes its processability more complicated, the aim of the study was to assess whether the robocasting process could be applied to magnesium-based alloys. The problem was therefore, above all, to find solutions compatible with this material for each stage of the process.

Robocasting of Ti64

Printing

The first step of the robocasting process consists in the ink formulation. An easy way to fulfill the ink requirements (extrudable through a fine nozzle under pressure but capable to retain its shape once deposited) is to disperse the powder in a thixotropic gel. Under the effect of shearing, the gel is destroyed allowing it to flow, but once deposited, it rebuilds itself allowing the shape to be maintained. The choice fell on pluronic F-127 hydrogels, already in use in the laboratory.

Inks were thus containing only three ingredients: water, pluronic F-127 and Ti64 particles. Varying the proportion of these three ingredients made it possible to vary the rheological properties of the inks. It has been found that, using a printing temperature of 25 °C, inks made by adding between 45 and 50 vol% of Ti64 in pluronic hydrogels con-

taining between 25 and 30 wt% of Pluronic F-127 (P25T45, P25T50 and P30T50) allow layers to be stacked while maintaining the required macropores, down to a nozzle size of 250 µm. This successful stacking of layers was correlated to a sufficient dynamic yield stress (between 250 and 300 Pa for these inks). However, finer characterisation, based on comparison of the X-ray tomography scans of the dried samples with the original Computer Aid Design (CAD), revealed that the inks at 50 vol% powder were more faithful to the input CAD. Printing with these inks lead to dimensional deviations from the CAD file of less than 10 % of the strut diameter.

However, it has been observed that the largest deviations from the CAD were located at the corners and layer changes (which were also done while turning). But it is worth noting that CAD files used in this study were asking for two closely spaced right angles, where a circle arc would have been easier to draw. Thus it would be interesting to see by how much this deviation can be reduced by using a CAD requiring circular arcs. In addition, the same printing speed was used for all printed segments. However, it might be relevant for the future to verify if slowing down when cornering enhances the precision.

Debinding

Once the shaping step is done, the parts have to be dried, debinded and sintered to reach their final structures and properties. To reduce the number of variables for these steps, only one ink was kept to study the influence of both debinding and sintering conditions. It has thus been chosen to use the P25T50 ink to minimise the amount of binder and thus facilitate the debinding stage. Contrary to what is observed with ceramics, drying was not seen here as a limiting step.

The debinding conditions are often chosen using a large margin to make sure that the binder has been properly removed. However, as shown during this thesis work, this strategy must be absolutely avoided when debinding parts made of titanium alloys. Indeed, the higher the debinding temperature, the more titanium is enriched with interstitial elements present in the binder and becomes brittle. A too high carbon intake can even lead to a further carbide precipitation in the beta phase during the sintering or the cooling from sintering, depending on both the sintering temperature and the cooling rate used. Thus, for titanium alloys, the lowest possible debinding temperature should always be used to prevent embrittlement. This was demonstrated by both experimental evidences (XRD, SEM) and precipitation modelling.

The lowest temperature at which the pluronic F-127 can be degraded has been determined by TGA as being 350 °C. A debinding treatment of 30 min at 350 °C under primary dynamic vacuum (heating rate of 1 °C·min^{-1}), followed by a sintering of 2 h at 1200 °C under dynamic secondary vacuum (5×10^{-4} mBar) gives the best compromise of final interstitials contents measured in this study. All of them were below the acceptable limit given by the ASTM F1108 standard for Ti64 surgical implants except the oxygen content

that was slightly too high (0.219 wt% for 0.2 wt% required). *It should be pointed out here that these values have been obtained by optimising debinding treatment only and that the other stages of the process could also be improved (ink formulation with less binder, sintering on less reactive support...). In particular, sintering could be improved by using a dedicated furnace (Mo chamber with very clean atmosphere like secondary vacuum).*

Sintering

With a process such as robocasting, the final structure of the part is strongly driven by the sintering process. Both sintering temperature and initial powder size enable to vary the final density. Increasing the sintering temperature of the coarse powder (mean diameter of 23 µm) from 1000 to 1200 °C has led to increase the densification of the filaments from 73 to 87.5% (and so the associated shrinkage), while keeping an interconnection of these residual micropores. The characteristic sizes of this microporous network remained similar in the different cases, with interconnection necks ranking from 1 µm diameter to 7 - 8 µm and presenting a mean diameter around 4 - 5 µm, and a mean pore size about 15 µm. Further filament densifications were obtained by keeping the sintering temperature at 1200 °C but adding fine powder in the ink (mean diameter of 4.3 µm), with the highest densification observed for 100% of fine powder (0.025 % of remaining porosity within filaments). Lowering the diameter of the powder used also led to a reduction in roughness (R_a measured along a filament decreased from about 10 to 2 µm), which was already initially lower than that obtained by powder bed fusion technologies.

Properties

The observed densification was accompanied by an increase in the Young's modulus of the filaments but also by an increase in the micro-hardness and yield strength of the scaffolds. A slight increase in scaffolds Young's modulus was also observed according to the curves obtained using the strain measured by Digital Image Correlation (DIC). However, the use of the fine powder induced again the embrittlement of the constitutive filaments due to higher oxygen intake. This loss of ductility was also observed on scaffold structures even though a strain between 5 and 10% was still reachable. Globally, scaffolds developed in this study show yield strengths superior to that of bones (except for samples sintered at 1000 °C) and Young's moduli close enough to that of bone to avoid the phenomenon of stress shielding.

From a biological point of view, the only conclusions that can be drawn for now are that MG-63 cells are able to grow on the scaffolds and can actually settle inside the pores left by partial sintering. In addition, the roughness of the scaffolds gives them a better adhesion than the Ti64-Ref, that can be visualised by a better spreading of the individual cells.

A final interesting point to note about the structures that can be achieved is the

possibility to produce samples with graded intra-filamentary porosity, by using different powder sizes within the same sample. In this study, samples containing three different inks (made from different powder batches) were printed to illustrate this opportunity. Resulting samples, containing stepped gradient, have their behaviour governed by the weakest characteristics of each layer, as highlighted by Digital Volume Correlation (DVC) performed during compression.

Robocasting of magnesium

Printing

Due to its reactivity, magnesium cannot be printed using aqueous binders. However, satisfying structures were obtained using an ethanol-based carrier solutions containing 13 to 17 wt% of ethyl cellulose and loaded with 56.5 to 60 vol% of magnesium powder. This high solid loading is comparable or higher than conventional feedstocks for metal injection moulding or equivalent processes. The structures were printed at a temperature of 35 °C to accelerate the drying of the ethanol, which helped to maintain the shape by initiating the transition of the ink from shear-thinning to dilatant behaviour. These inks presenting a high solid loadings were extrudable down to a nozzle size of 400 µm. It should be noted, however, that this parameter is dependent on the force that the machine can apply to the piston and can therefore vary from one robocaster to another. Following the same idea as for Ti64, the printable ink containing the lowest polymer content with the highest magnesium loading was kept for the further steps.

Debinding

Thermogravimetric analysis performed on the EC17 binder highlights that the main degradation of ethyl cellulose occurs between 260 and 330 °C. However, at 330 °C the degradation is not fully completed and a continuous mass loss is observed up to 500 °C. But, magnesium cannot be treated under dynamic vacuum at 500 °C as it vaporises. An intermediate debinding temperature of 400 °C was thus chosen, with a holding time of 2 h to be sure to reach the complete ethyl cellulose degradation. The treatment was performed under primary dynamic vacuum. According to both SEM and XRD analysis, this debinding treatment was successful without inducing microstructural changes.

Sintering

The sintering step was finally the most complicated to achieve. Due to the volatility of magnesium, it was not conceivable to carry out this treatment under secondary dynamic vacuum. In addition, magnesium is an extremely reducing metal, which therefore easily forms a very stable oxide layer on its surface and also easily reacts with every material containing oxygen. But as magnesium diffusion within its own oxide is extremely low, this MgO layer formed at particles surface tends to prevent sintering. The first solution found

to overcome these difficulties was to obtain sintering through the evaporation condensation phenomenon, by trying to keep the magnesium vapour emitted by the sample confined around it. To do so, the sample was completely immersed in pure iron powder, and the crucible containing both the sample and the iron powder was encapsulated under secondary vacuum. A sintering of 2 h at 600 °C in these conditions leads to a successful partial sintering that leaves around 28 - 30 % of remaining porosity.

This low densification might be due to the preponderance of the evaporation-condensation phenomenon, which is a non-densifying process. However, only one set of conditions has been tested here (2 h at 600 °C*) and it would be interesting to investigate the effect of an increase in sintering time and temperature on the obtained densification. Indeed, Wolff* et al. *suggest that a higher densification might be reachable in the presence of magnesium vapour as in their study, 64 h at* 630 °C *lead to a remaining porosity of 15 %. However, to increase the chance to enhance the sintering densification, an optimisation of the debinding treatment should be performed first, to be sure to limit the oxide layer thickness as much as possible. Thermogravimetric analyses up to different temperatures, with an additional holding time of 30 min, should therefore first be carried out to assist in the selection of the debinding temperature.*

As sealing the quartz tubes to encapsulate the samples under vacuum was not so easy and limited the size of the sinterable samples, other alternatives were explored to sinter the scaffolds obtained by robocasting. A first trial involving liquid phase sintering was performed but without being conclusive. Additional characterisations are still required to understand the reason of this failure. On the other hand, a SPS sintering test carried out by limiting the load seen by the sample appeared to be promising and therefore proves to be a track to be dug.

Toward controlled geometry?

Although robocasting was originally developed for ceramic shaping, it is possible to formulate inks for any type of material [LEW 06a, JAK 15, TRU 16]. Indeed it is not the shaping stage that represents the difficulty when transferring to metallic materials, but rather the heat treatments, as shown in this PhD work. This is particularly the case for metals exhibiting a high affinity with interstitial elements or those forming a stable oxide layer in which their own diffusion is slowed down. It can therefore be considered that all sinterable metals can be robocast.

However, it must be recalled that the resolution obtained is dependent on the ink used and, in particular, on the powder size and the loading content. A filament diameter of 2 µm has been reached by printing silver nano-particles presenting a mean diameter of 20 nm [AHN 09]. It is nevertheless not possible to find such fine powders for all types of materials.

The dimensional control of the parts obtained by robocasting is strongly linked to the rheology of the inks. This study has shown that ink rheology can impact the accuracy of the deposit but also the further shrinkage, if the stiffness of the ink modifies the interpenetration of the layers. It therefore becomes a real necessity to define a common methodology for rheological characterisation of inks and to link these properties with the fidelity to the CAD. Such approach should make it possible to subsequently adapt the ink with the design (and *vice versa*) to maximise printing accuracy (particularly in terms of interlayer spacing and rod spacing to prevent sagging).

Considering this, it would therefore be interesting to perform complementary rheological measurement on the inks used in this study. In particular, it would be necessary to characterise the properties of the ink containing the fine powder and perform a comparison of the scaffolds made from this ink with the input CAD. Complementary moduli measurement should also be performed on each ink and be related to the interlayer space that it is possible to respect.

In addition, the method presented in this thesis work for assessing dimensional compliance would also deserve to be taken further. The analysis applied to dried scaffolds could also be applied to sintered scaffolds but allowing the calculation (and the use) of a shrinkage correction that minimises the measured deviation from CAD. The result should then consist in both: the shrinkage value used to minimise the difference between the two volumes (related to drying and sintering), and the measured discrepancy (related to ink sagging and other distortions) using this shrinkage correction.

If the rheology of the ink is well mastered, robocasting is a process that can be easy to handle, especially as there are more and more improvements being made to the machine, that make printing easier. One example is the production of temperature-controlled nozzles, which can be extremely convenient when the inks used have a temperature-dependent rheology. It should be noted that this type of system can at the same time further increase the versatility of the process. In the same way, some machines are also able to detect the zero position of each of their syringes by themselves, thus avoiding the need to manually adjust the distance to the print substrate and enabling printing on non-planar substrates.

A number of devices developed to complement the possibilities offered by the process aim to exploit its versatility for the production of multi-material parts. A mixer feeding two different inks can for example be added above the nozzle [SMA 08, ORT 19]. This device can allow the manufacturing of gradual gradient that would make it possible, among other things, to overcome the excessive residual stresses observed here due to too great a difference in shrinkage between the different layers. Following the same goal of multi-material parts, Lewis' team developed a multi-material multi-nozzle head that enables to print several materials at the same time but also to quickly switch between two of them [SKY 19]. Robocasting of multi-materials has until now mainly been considered for soft (non-sintered) materials because it eliminates the problem of co-sintering [G.R 20].

However, a gradient from one steel grade to another steel grade could for example be considered. In addition, the densification of two materials with different sinterability temperature ranges can even be considered by adjusting the size of the powders. But this, of course, remains within the limit of having two materials that are relatively inert with each other (which is the most critical point).

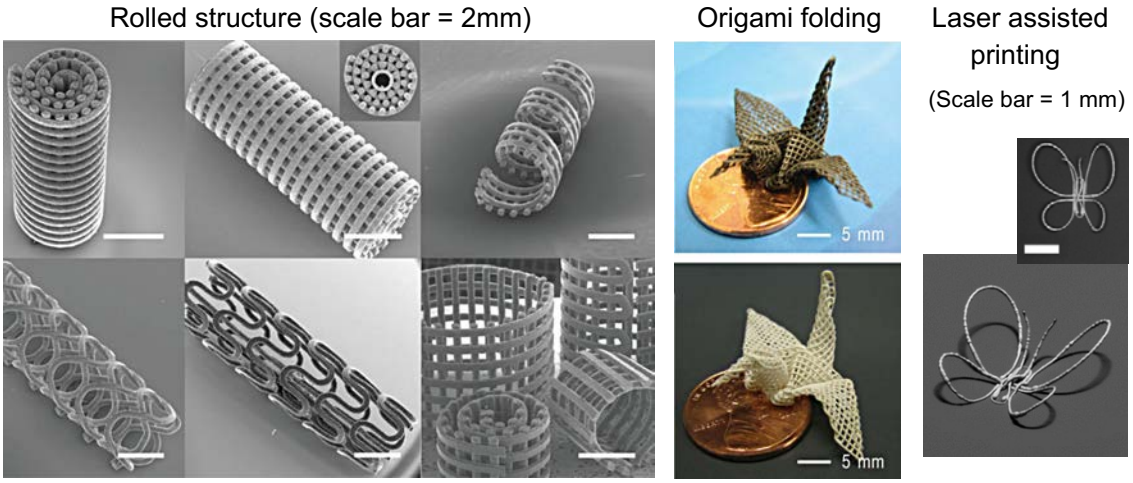

Figure 4.19: Complex structures: SEM images of TiH_2 structures obtained by rolling procedure (left); Optical image of printed origami TiH_2 crane further transformed into TiO_2 by annealing at $1050\,^{\circ}C$ under air (middle); Butterflies silver structures printed without any support using laser assisted DIW. Adapted from [AHN 10] and [SKY 16]

The point often considered to be the major drawback of robocasting is the limit in terms of complexity of shape that can be reached. However different studies have shown that this limitation can be partly circumvented by using the right rheology and specific practical tricks, such as rolling or origami approach as presented on Fig.4.19 [AHN 10, JAK 15]. In addition, J. Lewis' team also achieved complete freedom of shaping, but with the help of a laser that sintered the just extruded ink, resulting in a significant increase in system complexity [SKY 16]. As the ink is sintered almost immediately after printing, the stiffness of the part being printed is sufficient to print in any direction of space without the help of any support. An example of an obtainable structure is also shown on Fig. 4.19. However, it should be noted that to use such a process on Ti64 ink, the whole system should then be kept in an inert atmosphere, probably synonym of high cost and complexity.

Perspectives

Coming back to the overall framework of this thesis, certain perspectives opened up by this work deserve to be deepened.

Toward titanium implants with required properties?

Concerning what has been achieved on titanium, the search for a compromise of properties could be further refined. Indeed, the acceptable limit of 0.2 wt% of oxygen is not so far and might be reachable by adjusting other parameters (initial powder or even ink formulation, sintering support and environment).

In addition, microstructural changes that can be induced by varying the cooling rate applied on Ti64 are known to lead to mechanical properties variation. It would therefore be interesting to check whether an increase in the cooling rate can actually induce an increase in the yield strength of the scaffolds. Indeed, an important difference in microstructure can be obtained by moving the oven away from the quartz tube at the end of the sintering holding time, as shown on Fig 4.20. A difference in scaffold behaviour is thus expected. However, refining the microstructure is also known to decrease the ductility of titanium. So this finer microstructure might help to find a better strength ductility compromise for scaffolds presenting interconnected micropores, as they present an important ductility, but might not be adapted for scaffolds containing fine powder.

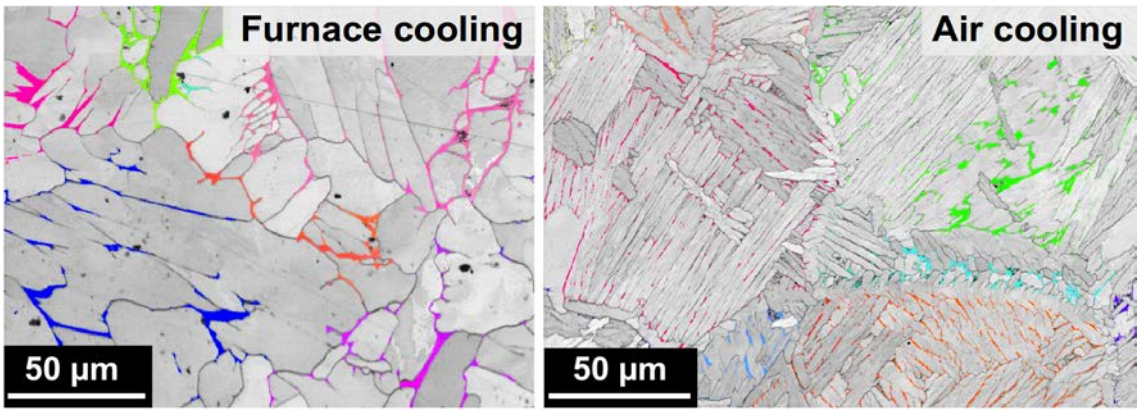

Figure 4.20: IPF maps of the β phase overlaid on the band contrast obtained by EBSD showing the impact of cooling rate on the microstructure obtained. Air cooling of the quartz tube containing sample lead to acicular α grains.

But in any case, knowing the impact of the cooling rate remains interesting and important to understand the behaviour observed when the diameter of the constitutive filaments is reduced. Indeed, Ti64 scaffolds produced by Elsayed *et al.* showed dispersed yield strengths, in particular for the smaller nozzle diameters used (250 and 400 µm) [ELS 20]. But as the microstructures observed on these samples are both finer and richer in TiC than for larger diameters, additional data are needed to separate the different contributions.

This study should, of course, be completed by the biological study initially planned to be carried out during this PhD work (including cytotoxicity, morphological evaluation, cellular adhesion and calcium deposition assessment). However, an additional type of sample should be added to the study to eliminate the problem of the great difference in roughness by adding a comparable case. It might be either a sample made from fine powder but using a lower sintering temperature to keep interconnected micropores, or a

sample made from coarse powder but sintered at 1400 °C to close pores.

This additional sample would, moreover, enable to discriminate the contributions of C and O in the weakening of parts. Indeed, parts made from fine powder are richer in oxygen but contain the same carbon level as part made from large powder. So having samples with the same porosity level but with various oxygen contents would be a way to complete the first data on embrittlement obtained during the debinding optimisation. The contribution of TiC could besides also be assessed since a faster cooling ramp should prevent their formation.

In addition, to better understand the microstructural evolution during sintering, the influence of powder size, chemical composition and debinding parameters on the evolution of porosity and phase transformation (α, β, TiC) has been investigated through an *in situ* synchrotron study combining XRD and X-Ray tomography acquisitions during sintering. The analysis of these data acquired a few days ago (November 2020) should provide access to sintering and phase transformation kinetics.

A complete evaluation of achievable properties would then make it possible to produce an Ashby's map of the biological properties (cell adhesion, matrix synthesis) as a function of the mechanical properties (E/ρ ; σ_E/ρ). This would then give an overview of the best possible compromises obtainable with these scaffolds.

Toward robocasting of bio-resorbable structures?

As the magnesium study was more exploratory, it leaves a number of tracks barely walked on. Both liquid phase sintering and SPS should be explored as means of densifying the scaffolds obtained by robocasting. If liquid sintering is to be explored to check whether or not it is compatible with the robocasting process on magnesium alloys, the success of SPS is beyond doubt. However, it should be carefully studied to assess the structural evolution it induces.

This study should besides be applied to an alloy more representative of what can be used as an implant. Indeed, pure magnesium (that does not present a ultra high purity) has a too high degradation rate in the human body. Alloying elements are known to strengthen the magnesium matrix and reduce its corrosion rate, leading to more appropriate properties for orthopaedic applications [STA 06, CHE 14]. When one wants to avoid the use of rare earth elements, whose effects can be controversial, Mg-Zn alloys represent the second strongest alloying system according to Chen *et al.*. In addition, an increase up to 3 wt% of Zn has been shown to decrease the corrosion rate of magnesium [JIN 16]. Zirconium is also known to refine magnesium grains and thus enhance its strength, but also to reduce its corrosion rate when added in small amount [SON 02]. In parallel, ZK30 alloy (Mg-3Zn-0.6Zr) has shown promising degradation rate, even lower than the WE43 alloy already in use for bone fixation through the Magnezix screws. This alloy could therefore be a good basis for continuing the tests started with this thesis.

In addition, as Zn is also a resorbable and well accepted compound in the human body [BOW 13, LI 19], and as its diffusivity within its own oxide is not decreased compared to its self-diffusivity [MUN 79], another idea would be to try the robocasting of Zn based alloy to obtain resorbable implants. This would enable to avoid the difficulties regarding the sintering step. However an alloy design study will still be necessary to find a compromise of properties as the degradation rate and mechanical properties of Zn can once again be tailored by alloying elements [LI 19]. This perspective has been the topic of a Carnot subject proposal which has been awarded funding for a thesis that will start in 2021.

Appendix A

Robocaster used in this study

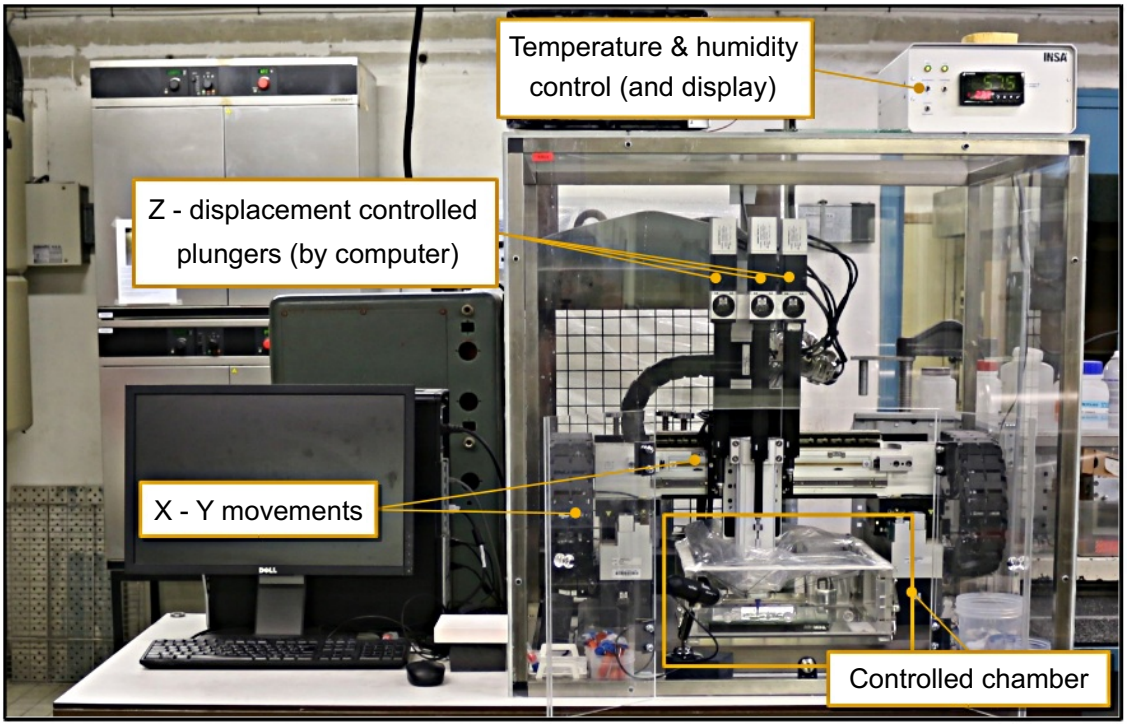

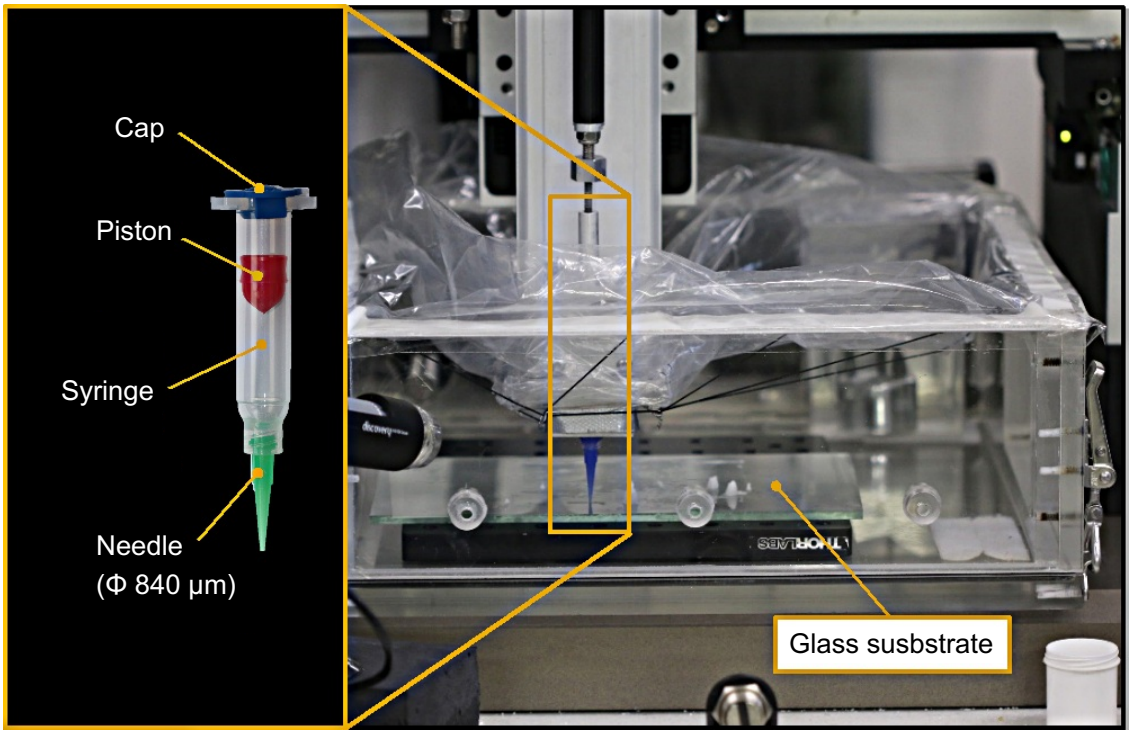

Appendix B

Datasheets of the two standard reference materials used in this study

Approved by AQSIQ

Administration of Quality Supervision
Inspection and Quarantine

Certificate Of Reference Materials

P/N:	58A SY13001-1
Category:	Titanium Alloy
Certified date:	October 2014
Verified date:	
Form:	Chips
size:	50g

HRT Labortechnik GmbH
Brauerstr. 36 a · DE-21244 Buchholz
Telefon +49 (0) 4181 201 87-30 · Fax +49 (0) 4181 201 87-50
info@hrt-labortechnik.de · www.hrt-labortechnik.de

Provided By Well Group Scientific (USA) Ltd

Preparation

Collect materials --- Smelt materials in a frequency induction ---- Cast it into ingots of DIA 120mm ---- Demould it --- Carry out initial test --- Carry out homogeneity processing --- Peal it --- Carry out chipping process -- Carry out mixing and sieving process -- Carry out homogeneity test --- Carry out data analysis --- Get certifying process done

Certified Values

(Analysis listed as percentage by weight)

P/N		Al	C	Fe	Mo	Nb	Si	Zr
58A SY13001-1	Cert.Value	4.62	0.124	0.347	0.103	3.94	0.007	2.94
	Std.Dev	0.02	0.005	0.006	0.005	0.03	0.002	0.03

Note: Above values are from 9 sets of data
Std.Dev. means Standard Deviation

Analysis Method used

Al	ICP-AES ;EDTA titration method（Ethylene Diamine Tetraacetic Acid titration method）;
C	Combustion-gas volumetric method ;Combustion IR ;
Fe	ICP-AES ;Phenanthroline photometric method ;
Mo	ICP-AES ;Thiocyanate photometry ;
Nb	ICP-AES ;5-Br-PADAP photometric method; ;
Si	ICP-AES ;Silicon molybdenum blue photometric method ;
Zr	ICP-AES;Complexometric titration

Homogeneity and Stability

1. This Reference Material has been proved good at homogeneity by Range method.
2. The homogeneity of this Reference Material has been proved good by investigating 20 bottles chose randomly. No evidence of in homogeneity was observed for all these elements. The statistical result by F method is at the 95% level of probability.
3. The stability of this Reference Material was evaluated with the use of ICP-AES and other chemical methods and was found good.

Traceability

All original data came from 10 labs.
All measurement units use International System Unit
All Reference Materials used in the certified process are traceable CRM.

Expiration

This Reference Material is to be stable at least for 10 years if it is stored in dry and clean places at a room temperature
This material is nullified if it is contaminated or otherwise altered.

Package, usage and storage

This Reference Material should be stored in dry, ventilated and clean places at a room temperature.

National Institute of Standards & Technology

Certificate of Analysis

Standard Reference Material® 173c

Titanium Alloy UNS R56400 (chip form)

This Standard Reference Material (SRM) is intended primarily for use in evaluating chemical and instrumental methods of analysis of titanium and its alloys. A unit of SRM 173c consists of a single bottle containing approximately 50 g of chips.

Certified Mass Fraction Values: Certified values for elements of SRM 173c are reported in Table 1 as mass fractions on an as-received basis [1]. A NIST certified value is a value for which NIST has the highest confidence in its accuracy in that all known or suspected sources of bias have been investigated or taken into account [2]. A certified value is the present best estimate of the true value based on the results of analyses performed at NIST and collaborating laboratories.

Reference Mass Fraction Values: Reference values for elements are reported in Table 2. Reference values are non-certified values that are the present best estimates of the true values; however, the values do not meet the NIST criteria for certification and are provided with associated uncertainties that may not include all components of uncertainty [2]. The uncertainty listed with the value is calculated according to the method in the ISO/JCGM Guide [3] and is an expanded uncertainty (95 % confidence interval [4]).

Information Mass Fraction Values: Information values for elements of SRM 173c are reported in Table 3. An information value is considered to be a value that will be of interest and use to the SRM user, but insufficient information is available to assess the uncertainty associated with the value.

Expiration of Certification: The certification of **SRM 173c** is valid indefinitely, within the uncertainty specified, provided the SRM is handled and stored in accordance with the instructions given in this certificate (see "Instructions for Use"). Periodic recertification of this SRM is not required. The certification will be nullified if the SRM is damaged, contaminated, or otherwise modified.

Maintenance of SRM Certification: NIST will monitor this SRM over the period of its certification. If substantive technical changes occur that affect the certification, NIST will notify the purchaser. Registration (see attached sheet or register online) will facilitate notification.

Coordination of the technical measurements for the certification of this SRM was performed by J.R. Sieber of the NIST Chemical Sciences Division.

Analytical measurements for certification of this SRM, including homogeneity testing, were performed by J.R. Sieber, A.F. Marlow, and R.L. Paul of the NIST Chemical Sciences Division; S. Bissell-Seymour and S. Cooper, Allegheny Ludlum (Brackenridge, PA); P. Cole, ATI Allvac, Monroe, NC; L. Trecani, CEZUS (Ugine, France); M. Chamberlain-Webber, TIMET UK, Ltd. (Witton, Birmingham, UK); L. Creasy, J. Kiely, and G. Boesenecker, Titanium Metals Corp. (Henderson, NV and Morgantown, PA); and G. Beck, ATI Wah Chang (Albany, OR).

Statistical consultation was provided by S.D. Leigh, A.N. Heckert, and H.-K. Liu of the NIST Statistical Engineering Division.

Support aspects involved in the issuance of this SRM were coordinated through the NIST Office of Reference Materials.

Carlos A. Gonzalez, Chief
Chemical Sciences Division

Gaithersburg, MD 20899
Certificate Issue Date: 16 November 2016
Certificate Revision History on Last Page

Stephen J. Choquette., Director
Office of Reference Materials

INSTRUCTIONS FOR USE

To relate analytical determinations to the values on this Certificate of Analysis, a minimum sample quantity of 250 mg should be used. The material may be used directly from the original container. Sampling and sample preparation procedures should be designed to avoid material segregation on the basis of chip size. It is recommended to thoroughly mix the contents of the bottle prior to sampling by turning the bottle end over end for one minute.

PREPARATION AND ANALYSIS[1]

The material for SRM 173c is an alloy fitting the description of Universal Numbering System (UNS) R56400 and was obtained from ATI Allvac (Monroe, NC). The material was chipped, blended and bottled at NIST under the supervision of M.P. Cronise of the NIST Office of Reference Materials. Analytical methods employed for quantitative analyses and homogeneity testing at NIST and collaborating laboratories are reported in Table 4.

Certified Mass Fraction Values: The measureands for aluminum, chromium, copper, iron, nickel, and vanadium are listed in Table 1. The certified values are metrologically traceable to the SI unit for mass fraction (expressed as a percent). The values for all elements, except copper, are weighted means of the results from two to seven analytical methods [5]. The uncertainty listed with each value is an expanded uncertainty about the mean, with a coverage factor 2 (approximately 95 % confidence), calculated by combining a between-source variance incorporating between-method bias with a pooled within-source variance following the ISO/JCGM Guide [3]. The assigned value for copper is the unweighted mean of the results from four analytical methods. The uncertainty listed with the value is an expanded uncertainty about the mean, with coverage factor 2, calculated by combining a between-method variance [6] with a pooled, within-method variance following the ISO/JCGM Guide [3].

Table 1. Certified Mass Fraction Values for SRM 173c Titanium Alloy (6Al-4V)

Element	Mass Fraction (%)
Aluminum (Al)	6.245 ± 0.036
Chromium (Cr)	0.0165 ± 0.0005
Copper (Cu)	0.0040 ± 0.0004
Iron (Fe)	0.2130 ± 0.0040
Nickel (Ni)	0.0203 ± 0.0009
Vanadium (V)	4.154 ± 0.016

Reference Mass Fraction Values: The measureands for carbon, molybdenum, nitrogen, oxygen, silicon, tin, titanium, zirconium, and boron are listed in Table 2. The reference values are metrologically traceable to the SI unit for mass fraction (expressed as percent, or for boron, in milligrams/kilogram). The values for carbon, molybdenum, and zirconium are weighted means of the results from two to seven analytical methods [5]. The uncertainty listed with each value is an expanded uncertainty about the mean, with a coverage factor 2 (approximately 95 % confidence), calculated by combining a between-source variance incorporating between-method bias with a pooled within-source variance following the ISO/JCGM Guide [3]. The assigned values for nitrogen, oxygen, silicon, and tin are the unweighted means of the results from two to five analytical methods. The uncertainty listed with each value is an expanded uncertainty about the mean, with coverage factor 2, calculated by combining a between-method variance [6] with a pooled, within-method variance following the ISO/JCGM Guide [3]. The values for boron and titanium are the means of the results from a single analytical method performed at NIST. The uncertainty listed with each value is an expanded uncertainty about the mean, with coverage factor 2, calculated by combining all known sources of uncertainty for the method, following the ISO/JCGM Guide [3].

[1] Certain commercial equipment, instruments, or materials are identified in this report to adequately specify the experimental procedure. Such identification does not imply recommendation or endorsement by the National Institute of Standards and Technology, nor does it imply that the materials or equipment identified are necessarily the best available for the purpose.

Table 2. Reference Mass Fraction Values for SRM 173c Titanium Alloy (6Al-4V)

Element	Mass Fraction (%)
Carbon (C)	0.027 ± 0.002
Molybdenum (Mo)	0.0068 ± 0.0004
Nitrogen (N)	0.028 ± 0.005
Oxygen (O)	0.164 ± 0.003
Silicon (Si)	0.019 ± 0.005
Tin (Sn)	0.010 ± 0.002
Titanium (Ti)	89.15 ± 0.49
Zirconium (Zr)	0.0053 ± 0.0004

Element	Mass Fraction (mg/kg)
Boron (B)	0.45 ± 0.12

Information Mass Fraction Values: The values in Table 3 are intended to provide additional information on the composition of SRM 173c. Due to insufficient information, uncertainties are not assigned to these values. Information values cannot be used to establish metrological traceability.

Table 3. Information Mass Fraction Values for SRM 173c Titanium Alloy (6Al-4V)

Element	Mass Fraction (%)
Cobalt (Co)	0.002
Hydrogen (H)	0.006
Manganese (Mn)	0.002
Ruthenium (Ru)	0.0006
Tungsten (W)	0.002

Table 4. Analytical Methods

Method	Elements Determined
Wavelength Dispersive X-Ray Fluorescence Spectrometry (WDXRF) at NIST	Al, Cr, Cu, Fe, Ni, Ti, V
WDXRF at Collaborating Laboratories	Al, Cr, Cu, Fe, Ni, V, Zr
Inductively-Coupled Plasma Optical Emission Spectrometry (ICP-OES) at Collaborating Laboratories	Al, B, Co, Cr, Cu, Fe, Mn, Mo, Ni, Ru, Si, Sn, V, W, Zr
Direct Current Plasma Optical Emission Spectrometry (DCP-OES) at Collaborating Laboratories	Al, Cr, Cu, Fe, Mo, Ni, Si, V, Zr
Combustion with Infrared Detection at Collaborating Laboratories	C, N, O
Inert Gas Fusion at Collaborating Laboratories	H, N, O
Prompt Gamma-Ray Activation Analysis at NIST	B

REFERENCES

[1] Thompson, A.; Taylor, B.N.; *Guide for the Use of the International System of Units (SI);* NIST Special Publication 811; U.S. Government Printing Office: Washington, DC (2008); available at http://physics.nist.gov/cuu/pdf/sp811.pdf (accessed Nov 2016).

[2] May, W.; Parris, R.; Beck, C.; Fassett, J.; Greenberg, R.; Guenther, F.; Kramer, G.; Wise, S.; Gills, T.; Colbert, J.; Gettings, R.; MacDonald, B.; *Definitions of Terms and Modes Used at NIST for Value-Assignment of Reference Materials for Chemical Measurements;* NIST Special Publication 260-136; U.S. Government Printing Office: Washington, DC (2000); available at http://www.nist.gov/srm/upload/SP260-136.PDF (accessed Nov 2016).

[3] JCGM 100:2008; *Evaluation of Measurement Data — Guide to the Expression of Uncertainty in Measurement* (GUM 1995 with Minor Corrections); Joint Committee for Guides in Metrology (JCGM) *(2008); available at* http://www.bipm.org/utils/common/documents/jcgm/JCGM_100_2008_E.pdf (accessed Nov 2016); see also Taylor, B.N.; Kuyatt, C.E.; *Guidelines for Evaluating and Expressing the Uncertainty of NIST Measurement Results*; NIST Technical Note 1297; U.S. Government Printing Office: Washington, DC (1994); avail*able at* http://www.nist.gov/pml/pubs/tn1297/index.cfm (accessed Nov 2016).

[4] Hahn, G.J.; Meeker, W.Q.; *Statistical Intervals*: *A Guide for Practitioners*; John Wiley & Sons, Inc., New York (1991).

[5] Ruhkin, A.L.; Vangel, M.G.; *Estimation of a Common Mean and Weighted Mean Statistics*; J. Am. Statist. Assoc.; Vol. 93, pp. 303–308 (1998).

[6] Levenson, M.S.; Banks, D.L.; Eberhardt, K.R.; Gill, L.M.; Guthrie, W.F.; Liu, H.-K.; Vangel, M.G.; Yen, J.H.; Zang, N.F.; *An Approach to Combining Results from Multiple Methods Motivated by the ISO GUM*; J. Res. Natl. Inst. Stand. Technol.; Vol. 105, pp. 571–579 (2000).

Certificate Revision History: 16 November 2016 (Editorial changes); 24 June 2013 (Removed expiration of certification date; added reference value for boron; editorial changes.); 30 July 2004 (Editorial changes); 22 June 2004 (Original certificate date).

Users of this SRM should ensure that the Certificate of Analysis in their possession is current. This can be accomplished by contacting the SRM Program at: telephone (301) 975-2200; fax (301) 948-3730; e-mail srminfo@nist.gov; or via the Internet at http://www.nist.gov/srm.

References

[ADA 67] Adamson A. W.
Physical Chemistry of Surfaces. , 1967, Page 12.

[AHN 09] Ahn B. Y., Duoss E. B., Motala M. J., Guo X., Park S.-I., Xiong Y., Yoon J., Nuzzo R. G., Rogers J. A., Lewis J. A.
Omnidirectional Printing of Flexible, Stretchable, and Spanning Silver Microelectrodes. *Science*, vol. 323, n° 5921, 2009, p. 1590–1593.

[AHN 10] Ahn B. Y., Shoji D., Hansen C. J., Hong E., Dunand D. C., Lewis J. A.
Printed Origami Structures. *Advanced Materials*, vol. 22, n° 20, 2010, p. 2251–2254.

[AND 17] Andreau O., Peyre P., Penot J. D., Koutiri I., Dupuy C., Pessard E., Saintier N.
Deterministic Defect Generation in Selective Laser Melting: Parametric Optimization and Control. , 2017, Page 11.

[ANS 06] Anselme K., Bigerelle M.
Statistical Demonstration of the Relative Effect of Surface Chemistry and Roughness on Human Osteoblast Short-Term Adhesion. *Journal of Materials Science: Materials in Medicine*, vol. 17, n° 5, 2006, p. 471–479.

[ARM 14] Armillotta A., Baraggi R., Fasoli S.
SLM Tooling for Die Casting with Conformal Cooling Channels. *The International Journal of Advanced Manufacturing Technology*, vol. 71, n° 1-4, 2014, p. 573–583.

[ASH 00] Ashby M. F., Evans A. G., Fleck N. A., Gibson L. J., Hutchinson J. W., Wadley H. N. G.
Metal Foams: A Design Guide. , 2000, Page 263.

[ATZ 20] Atzeni E., Balestrucci A., Catalano A. R., Iuliano L., Priarone P. C., Salmi A., Settineri L.
Performance Assessment of a Vibro-Finishing Technology for Additively Manufactured Components. *Procedia CIRP*, vol. 88, 2020, p. 427–432.

[BAD 00] Badini C., Ubertalli G., Puppo D., Fino P.
High Temperature Behaviour of a Ti-6Al-4V/TiCp Composite Processed by BE-CIP-HIP Method. , 2000, Page 10.

[BAI 15] Bai Y., Williams C. B.
An Exploration of Binder Jetting of Copper. *Rapid Prototyping Journal*, vol. 21, n° 2, 2015, p. 177–185.

[BAL 16] Balart M., Patel J., Gao F., Fan Z.
Grain Refinement of Deoxidized Copper. *Metallurgical and Materials Transactions A*, vol. 47A, 2016.

[BAL 20] Ballard D. H., Mills P., Duszak R., Weisman J. A., Rybicki F. J., Woodard P. K.
Medical 3D Printing Cost-Savings in Orthopedic and Maxillofacial Surgery: Cost Analysis of Operating Room Time Saved with 3D Printed Anatomic Models and Surgical Guides. *Academic Radiology*, vol. 27, n° 8, 2020, p. 1103–1113.

[BAR 10] Baril E.
Titanium and Titanium Alloy Powder Injection Moulding: Matching Application Requirements. *PIM International*, vol. 4, n° 4, 2010, p. 22–32.

[BAR 16] Bardel D., Fontaine M., Chaise T., Perez M., Nelias D., Bourlier F., Garnier J.
Integrated Modelling of a 6061-T6 Weld Joint: From Microstructure to Mechanical Properties. vol. 117, 2016, p. 81–90.

[BEC 75] Beck
Effect of Hydrogen on Mechanical Properties of Titanium and Its Alloys. rapport n° CR - 134796, 1975, NASA.

[BHA 17] Bhavar V., Kattire P., Patil V., Khot S., Gujar K., Singh R.
A Review on Powder Bed Fusion Technology of Metal Additive Manufacturing. 2017.

[BIA 19] Biasetto L., Bertolini R., Elsayed H., Ghiotti A., Bruschi S.
Use of Cryogenic Machining to Improve the Adhesion of Sphene Bioceramic Coatings on Titanium Substrates for Dental and Orthopaedic Applications. *Ceramics International*, vol. 45, n° 5, 2019, p. 5941–5951.

[BLA 17] Bland L. G., Gusieva K., Scully J.
Effect of Crystallographic Orientation on the Corrosion of Magnesium: Comparison of Film Forming and Bare Crystal Facets Using Electrochemical Impedance and Raman Spectroscopy. *Electrochimica Acta*, vol. 227, 2017, p. 136–151.

[BOH 17] Bohner M., Baroud G., Bernstein A., Döbelin N., Galea L., Hesse B., Heuberger R., Meille S., Michel P., von Rechenberg B., Sague J., Seeherman H.
Characterization and distribution of mechanically competent mineralized tissue in micropores of β-tricalcium phosphate bone substitutes. *Materials Today*, vol. 20, n° 3, 2017, p. 106-115.

[BOW 13] Bowen P., Drelich J., Goldman J.
Zinc Exhibits Ideal Physiological Corrosion Behavior for Bioabsorbable Stents. *Advanced Materials*, , 2013.

[BRA 79] Bradley J. N., Capey W. D., Shere J. F.
Kinetics of Reaction of Magnesium Vapour with Silica. *Journal of the Chemical Society, Faraday Transactions 1: Physical Chemistry in Condensed Phases*, vol. 75, n° 0, 1979, Page 2807.

[BUR 09] Burke P., Kipouros G. J., Fancelli D., Laverdiere V.
Sintering Fundamentals of Magnesium Powders. *CANADIAN METALLURGICAL QUARTERLY*, vol. 48, n° 2, 2009, Page 10.

[CES 97] Cesarano J. I., Baer T., Calvert P.
Recent Developments in Freeform Fabrication of Dense Ceramics from Slurry Deposition. rapport n° SAND–97-2857C, CONF-970888–, 554831, 1997.

[CES 98] Cesarano III J. C., King B. H., Denham H. B.
Recent Developments in Robocasting of Ceramics and Multimaterial Deposition. , 1998, Page 8.

[CHA 12] Chan O., Coathup M. J., Nesbitt A., Ho C. Y., Hing K. A., Buckland T., Campion C., Blunn G. W.
The Effects of Microporosity on Osteoinduction of Calcium Phosphate Bone Graft Substitute Biomaterials. *Acta Biomaterialia*, vol. 8, n° 7, 2012, p. 2788–2794.

[CHÁ 17] Chávez J., Olmos L., Jiménez O., Bouvard D., Rodríguez E., Flores M.
Sintering Behaviour and Mechanical Characterisation of Ti64/xTiN Composites and Bilayer Components. *Powder Metallurgy*, vol. 60, n° 4, 2017, p. 257–266.

[CHE 14] Chen Y., Xu Z., Smith C., Sankar J.
Recent Advances on the Development of Magnesium Alloys for Biodegradable Implants. *Acta Biomaterialia*, vol. 10, n° 11, 2014, p. 4561–4573.

[CHE 15] Chen Q., Thouas G. A.
Metallic Implant Biomaterials. *Materials Science and Engineering: R: Reports*, vol. 87, 2015, p. 1–57.

[CHE 17] Cheng Y., Cui Z., Cheng L., Gong D., Wang W.
Effect of Particle Size on Densification of Pure Magnesium during Spark Plasma Sintering. *Advanced Powder Technology*, vol. 28, n° 4, 2017, p. 1129–1135.

[CHE 19] Chen Y., Han P., Vandi L.-J., Dehghan-Manshadi A., Humphry J., Kent D., Stefani I., Lee P., Heitzmann M., Cooper-White J., Dargusch M.
A Biocompatible Thermoset Polymer Binder for Direct Ink Writing of Porous Titanium Scaffolds for Bone Tissue Engineering. *Materials Science and Engineering: C*, vol. 95, 2019, p. 160–165.

[COM 14] Compton B. G., Lewis J. A.
3D-Printing of Lightweight Cellular Composites. *Advanced Materials*, vol. 26, n° 34, 2014, p. 5930–5935.

[CON 08] Conrad J. C., Lewis J. A.
Structure of Colloidal Gels during Microchannel Flow. *Langmuir*, vol. 24, n° 15, 2008, p. 7628–7634.

[COO 88] Cook S. D., Thomas K. A., Kay J. F., Jarcho M.
Hydroxyapatite-Coated Titanium for Orthopedic Implant Applications:. *Clinical Orthopaedics and Related Research*, vol. &NA;, n° 232, 1988, Page 225???243.

[COS 16] Costakis W. J., Rueschhoff L. M., Diaz-Cano A. I., Youngblood J. P., Trice R. W.
Additive Manufacturing of Boron Carbide via Continuous Filament Direct Ink Writing of Aqueous Ceramic Suspensions. *Journal of the European Ceramic Society*, vol. 36, n° 14, 2016, p. 3249–3256.

[CUM 12] Cummins G., Desmulliez M. P.
Inkjet Printing of Conductive Materials: A Review. *Circuit World*, vol. 38, n° 4, 2012, p. 193–213.

[CUN 14] Cundy T., Reid I. R., Grey A.
CHAPTER 31 - Metabolic Bone Disease. Marshall W. J., Lapsley M., Day A. P., Ayling R. M., Eds., *Clinical Biochemistry: Metabolic and Clinical Aspects (Third Edition)*, p. 604–635 Churchill Livingstone, 2014.

[da 05] da Silva A. A., dos Santos J. F., Strohaecker T. R.
Microstructural and Mechanical Characterisation of a Ti6Al4V/TiC/10p Composite Processed by the BE-CHIP Method. *Composites Science and Technology*, vol. 65, n° 11-12, 2005, p. 1749–1755.

[DĄB 11a] Dąbrowski R.
The Kinetics of Phase Transformations During Continuous Cooling of the Ti6Al4V Alloy from the Single-Phase β Range. *Archives of Metallurgy and Materials*, vol. 56, n° 3, 2011, p. 703–707.

[DAB 11b] Dabrowski R.
The Kinetics of Phase Transofmations during Continuous Colling of the Ti6Al4V Alloy from the Single-Phase β Range. vol. 56, n° 3, 2011, p. 703–707.

[DAS 07] Das K., Bose S., Bandyopadhyay A.
Surface Modifications and Cell–Materials Interactions with Anodized Ti. *Acta Biomaterialia*, vol. 3, n° 4, 2007, p. 573–585.

[DEB 99] De Barros M., Rats D., Vandenbulcke L., Farges G.
Influence of Internal Diffusion Barriers on Carbon Diffusion in Pure Titanium and Ti–6Al–4V during Diamond Deposition. *Diamond and Related Materials*, vol. 8, n° 6, 1999, p. 1022–1032.

[DEF 18] Deffrennes G.
Étude expérimentale et évaluation thermodynamique du système Al-C-Mg. , 2018, Page 315.

[DEL 12] Deliormanli A. M., Rahaman M. N.
Direct-Write Assembly of Silicate and Borate Bioactive Glass Scaffolds for Bone Repair. *Journal of the European Ceramic Society*, vol. 32, n° 14, 2012, p. 3637–3646.

[DER 10] Derby B.
Inkjet Printing of Functional and Structural Materials: Fluid Property Requirements, Feature Stability, and Resolution. *Annual Review of Materials Research*, vol. 40, n° 1, 2010, p. 395–414.

[DEW 16] De Wild M., Zimmermann S., Rüegg J., Schumacher R., Fleischmann T., Ghayor C., Weber F. E.
Influence of Microarchitecture on Osteoconduction and Mechanics of Porous Titanium Scaffolds Generated by Selective Laser Melting. *3D Printing and Additive Manufacturing*, vol. 3, n° 3, 2016, p. 142–151.

[DOC 08] Docheva D., Padula D., Popov C., Mutschler W., Clausen-Schaumann H., Schieker M.
Researching into the Cellular Shape, Volume and Elasticity of Mesenchymal Stem Cells, Osteoblasts and Osteosarcoma Cells by Atomic Force Microscopy. *Journal of Cellular and Molecular Medicine*, vol. 12, n° 2, 2008, p. 537–552.

[DOL 19] Dolimont A., Demarbaix A., Ducobu F., Rivière-Lorphèvre E.
Chemical Etching as a Finishing Process for Electron Beam Melting (EBM) Parts. *AIP Conference Proceedings*, vol. 2113, n° 1, 2019, Page 150020, American Institute of Physics.

[DOU 07] Dougherty R., Kunzelmann K.-H.
Computing Local Thickness of 3D Structures with ImageJ. *Microscopy and Microanalysis*, vol. 13, n° S02, 2007.

[DU 12] Du Q., Perez M., Poole W. J., Wells M.
Numerical Integration of the Gibbs–Thomson Equation for Multicomponent Systems. vol. 66, n° 419-422, 2012.

[EBE 17] Ebel T., Beissig T., Ebner S., Luo X., Nagaram A. B., Zhao D.
Reduction of the Embrittlement Effect of Binder Contamination in MIM Processing of Ti Alloys. *Powder Metallurgy*, vol. 60, n° 3, 2017, p. 157–166.

[EDW 14] Edwards P., Ramulu M.
Fatigue Performance Evaluation of Selective Laser Melted Ti–6Al–4V. *Materials Science and Engineering: A*, vol. 598, 2014, p. 327–337.

[ELD 17] Eldesouky I., Harrysson O., West H., Elhofy H.
Electron Beam Melted Scaffolds for Orthopedic Applications. *Additive Manufacturing*, vol. 17, 2017, p. 169–175.

[ELK 20] Elkaseer A., Schneider S., Scholz S. G.
Experiment-Based Process Modeling and Optimization for High-Quality and Resource-Efficient FFF 3D Printing. *Applied Sciences*, vol. 10, n° 8, 2020, Page 2899, Multidisciplinary Digital Publishing Institute.

[ELS 19] Elsayed H., Rebesan P., Giacomello G., Pasetto M., Gardin C., Ferroni L., Zavan B., Biasetto L.
Direct Ink Writing of Porous Titanium (Ti6Al4V) Lattice Structures. *Materials Science and Engineering: C*, vol. 103, 2019, Page 109794.

[ELS 20] Elsayed H., Novak N., Vesenjak M., Zanini F., Carmignato S., Biasetto L.
The Effect of Strut Size on Microstructure and Compressive Strength of Porous Ti6Al4V Lattices Printed via Direct Ink Writing. *Materials Science and Engineering: A*, vol. 787, 2020, Page 139484.

[EQT 13] Eqtesadi S., Motealleh A., Miranda P., Lemos A., Rebelo A., Ferreira J. M.
A Simple Recipe for Direct Writing Complex 45S5 Bioglass® 3D Scaffolds. *Materials Letters*, vol. 93, 2013, p. 68–71.

[EQT 14] Eqtesadi S., Motealleh A., Miranda P., Pajares A., Lemos A., Ferreira J. M.
Robocasting of 45S5 Bioactive Glass Scaffolds for Bone Tissue Engineering. *Journal of the European Ceramic Society*, vol. 34, n° 1, 2014, p. 107–118.

[FAL 08] Fall A.
RHEOPHYSIQUE DES FLUIDES COMPLEXES: ECOULEMENT ET BLOCAGE DE SUSPENSIONS. , 2008, Page 188.

[FEI 16a] Feilden E., Blanca E. G.-T., Giuliani F., Saiz E., Vandeperre L.
Robocasting of Structural Ceramic Parts with Hydrogel Inks. *Journal of the European Ceramic Society*, vol. 36, n° 10, 2016, p. 2525–2533.

[FEI 16b] Feilden E., Blanca E. G.-T., Giuliani F., Saiz E., Vandeperre L.
Robocasting of Structural Ceramic Parts with Hydrogel Inks. *Journal of the European Ceramic Society*, vol. 36, n° 10, 2016, p. 2525–2533.

[FEI 17a] Feilden E.
Additive Manufacturing of Ceramics and Ceramic Composites via Robocasting. , 2017, Imperial College London.

[FEI 17b] Feilden E., Ferraro C., Zhang Q., García-Tuñón E., D'Elia E., Giuliani F., Vandeperre L., Saiz E.
3D Printing Bioinspired Ceramic Composites. *Scientific Reports*, vol. 7, n° 1, 2017.

[FEN 13] Feng Q., Zhang D., Xin C., Liu X., Lin W., Zhang W., Chen S., Sun K.
Characterization and in Vivo Evaluation of a Bio-Corrodible Nitrided Iron Stent. *J Mater Sci*, , 2013, Page 12.

[FRA 10] Franco J., Hunger P., Launey M., Tomsia A., Saiz E.
Direct Write Assembly of Calcium Phosphate Scaffolds Using a Water-Based Hydrogel. *Acta Biomaterialia*, vol. 6, n° 1, 2010, p. 218–228.

[FU 11] Fu Q., Saiz E., Tomsia A. P.
Direct Ink Writing of Highly Porous and Strong Glass Scaffolds for Load-Bearing Bone Defects Repair and Regeneration. *Acta Biomaterialia*, vol. 7, n° 10, 2011, p. 3547–3554.

[GAL 17] Galarraga H., Warren R. J., Lados D. A., Dehoff R. R., Kirka M. M., Nandwana P.
Effects of Heat Treatments on Microstructure and Properties of Ti-6Al-4V ELI Alloy Fabricated by Electron Beam Melting (EBM). *Materials Science and Engineering: A*, vol. 685, 2017, p. 417–428.

[GAN 19] Gangireddy S., Gwalani B., Liu K., Faierson E. J., Mishra R. S.
Microstructure and Mechanical Behavior of an Additive Manufactured (AM) WE43-Mg Alloy. *Additive Manufacturing*, vol. 26, 2019, p. 53–64.

[GAR 06] García C., Ceré S., Durán A.
Bioactive Coatings Deposited on Titanium Alloys. *Journal of Non-Crystalline Solids*, vol. 352, n° 32-35, 2006, p. 3488–3495.

[GEL 17] Gella D., Maza D., Zuriguel I., Ashour A., Arévalo R., Stannarius R.
Linking Bottleneck Clogging with Flow Kinematics in Granular Materials: The Role of Silo Width. *Physical Review Fluids*, vol. 2, n° 8, 2017, Page 084304.

[GER 92] German R. M.
Prediction of Sintered Density for Bimodal Powder Mixtures. *Metallurgical Transactions A*, vol. 23, n° 5, 1992, p. 1455–1465.

[GER 97] German R. M.
Supersolidus Liquid-Phase Sintering of Prealloyed Powders. *METALLURGICAL AND MATERIALS TRANSACTIONS A*, , 1997, Page 15.

[GER 16] German R. M.
Particulate Composites. Springer édition, 2016.

[GIB 99] Gibson L. J., Ashby M. F.
Cellular Solids: Structure and Properties. Cambridge University Press, 1999.

[GIB 10] Gibson I., Rosen D. W., Stucker B.
Additive Manufacturing Technologies. Springer US, Boston, MA, 2010.

[GIL 04] Gilbert S. G.
A Small Dose of Toxicology: The Health Effects of Common Chemicals. CRC Press, 2004.

[GIO 16] Gioffredi E., Boffito M., Calzone S., Giannitelli S. M., Rainer A., Trombetta M., Mozetic P., Chiono V.
Pluronic F127 Hydrogel Characterization and Biofabrication in Cellularized Constructs for Tissue Engineering Applications. *Procedia CIRP*, vol. 49, 2016, p. 125–132.

[GLA 06] Glassman A. H., Bobyn J. D., Tanzer M.
New Femoral Designs: Do They Influence Stress Shielding? *A Publication of The Association of Bone and Joint Surgeons® / CORR®*, vol. 453, 2006, p. 64–74.

[GOL 07] Golub E. E., Boesze-Battaglia K.
The Role of Alkaline Phosphatase in Mineralization:. *Current Opinion in Orthopaedics*, vol. 18, n° 5, 2007, p. 444–448.

[Gon 18] Gonzalez-Gutierrez J., Cano S., Schuschnigg S., Kukla C., Sapkota J., Holzer C.
Additive Manufacturing of Metallic and Ceramic Components by the Material Extrusion of Highly-Filled Polymers: A Review and Future Perspectives. *Materials*, vol. 11, n° 5, 2018, Page 840.

[G.R 20] G. Rocha V., Saiz E., S. Tirichenko I., García-Tuñón E.
Direct Ink Writing Advances in Multi-Material Structures for a Sustainable Future. *Journal of Materials Chemistry A*, vol. 8, n° 31, 2020, p. 15646–15657, Royal Society of Chemistry.

[GRA 72] Gray D. E.
American Institute of Physics Handbook. 1972.

[GUI 04] Guizzardi S., Galli C., Martini D., Belletti S., Tinti A., Raspanti M., Taddei P., Ruggeri A., Scandroglio R.
Different Titanium Surface Treatment Influences Human Mandibular Osteoblast Response. *Journal of Periodontology*, vol. 75, n° 2, 2004, p. 273–282.

[GUI 05] Guillemot F.
Recent Advances in the Design of Titanium Alloys for Orthopedic Applications. *Expert Review of Medical Devices*, vol. 2, n° 6, 2005, p. 741–748.

[HER 26] Herschel W. H., Bulkley R.
Konsistenzmessungen von Gummi-Benzollösungen. *Kolloid-Zeitschrift*, vol. 39, n° 4, 1926, p. 291–300.

[HIN 05] Hing K. A., Annaz B., Saeed S., Revell P. A., Buckland T.
Microporosity Enhances Bioactivity of Synthetic Bone Graft Substitutes. *Journal of Materials Science. Materials in Medicine*, vol. 16, n° 5, 2005, p. 467–475.

[HIR 17] Hirt L., Reiser A., Spolenak R., Zambelli T.
Additive Manufacturing of Metal Structures at the Micrometer Scale. *Advanced Materials*, vol. 29, n° 17, 2017, Page 1604211.

[HUM 07] Humphries J. D., Wang P., Streuli C., Geiger B., Humphries M. J., Ballestrem C.
Vinculin Controls Focal Adhesion Formation by Direct Interactions with Talin and Actin. *Journal of Cell Biology*, vol. 179, n° 5, 2007, p. 1043–1057.

[JAC 09] Jacob K. T., Gupta S.
Calciothermic Reduction of TiO2: A Diagrammatic Assessment of the Thermodynamic Limit of Deoxidation. *JOM*, vol. 61, n° 5, 2009, p. 56–59.

[Jah 12] Jahnen-Dechent W., Ketteler M.
Magnesium Basics. *Clinical Kidney Journal*, vol. 5, n° Suppl_1, 2012, p. i3-i14, Oxford Academic.

[JAK 15] Jakus A. E., Taylor S. L., Geisendorfer N. R., Dunand D. C., Shah R. N.
Metallic Architectures from 3D-Printed Powder-Based Liquid Inks. *Advanced Functional Materials*, vol. 25, n° 45, 2015, p. 6985–6995.

[JAN 15] Janda A., Zuriguel I., Garcimartín A., Maza D.
Clogging of Granular Materials in Narrow Vertical Pipes Discharged at Constant Velocity. *Granular Matter*, vol. 17, n° 5, 2015, p. 545–551.

[JAN 20] Janna W. S.
Introduction to Fluid Mechanics, Sixth Edition. CRC Press, 2020.

[JIN 16] Jingyuan Y., Jianzhong W., Qiang L., Jian S., Jianming C., Xudong S.
Effect of Zn on Microstructures and Properties of Mg-Zn Alloys Prepared by Powder Metallurgy Method. *Rare Metal Materials and Engineering*, vol. 45, n° 11, 2016, p. 2757–2762.

[JOH 14] Johanne S., Guillaume C., Jean-Philippe C., Catherine F., Gilles M.
Stents coronaires. vol. 30, 2014, Page 8.

[JOO 20] Joo S.-H., Yubuta K., Kato H.
Ordering Kinetics of Nanoporous FeCo during Liquid Metal Dealloying and the Development of Nanofacets. *Scripta Materialia*, vol. 177, 2020, p. 38–43.

[JOS 15] Joshi S. C., Sheikh A. A.
3D Printing in Aerospace and Its Long-Term Sustainability. *Virtual and Physical Prototyping*, vol. 10, n° 4, 2015, p. 175–185.

[KAI 03] Kainer K. U., für Materialkunde D. G.
Magnesium Alloys and Technology. John Wiley & Sons, 2003.

[KAN 04] Kang S.-J. L.
Sintering: Densification, Grain Growth and Microstructure. Elsevier, 2004.

[KAR 05] Karageorgiou V., Kaplan D.
Porosity of 3D Biomaterial Scaffolds and Osteogenesis. *Biomaterials*, vol. 26, n° 27, 2005, p. 5474–5491.

[KIM 02] Kim Y.-J., Chung H., Kang S.-J. L.
Processing and Mechanical Properties of Ti–6Al–4V/TiC in Situ Composite Fabricated by Gas–Solid Reaction. *Materials Science and Engineering: A*, vol. 333, n° 1-2, 2002, p. 343–350.

[KIR 12] Kirkland N., Birbilis N., Staiger M.
Assessing the Corrosion of Biodegradable Magnesium Implants: A Critical Review of Current Methodologies and Their Limitations. *Acta Biomaterialia*, vol. 8, n° 3, 2012, p. 925–936.

[KOP 19] Kopp A., Derra T., Müther M., Jauer L., Schleifenbaum J. H., Voshage M., Jung O., Smeets R., Kröger N.
Influence of Design and Postprocessing Parameters on the Degradation Behavior and Mechanical Properties of Additively Manufactured Magnesium Scaffolds. *Acta Biomaterialia*, vol. 98, 2019, p. 23–35.

[KRI 07] Krishna B. V., Bose S., Bandyopadhyay A.
Low Stiffness Porous Ti Structures for Load-Bearing Implants. *Acta Biomaterialia*, vol. 3, n° 6, 2007, p. 997–1006.

[KRU 05] Kruth J.-P., Mercelis P., Van Vaerenbergh J., Froyen L., Rombouts M.
Binding Mechanisms in Selective Laser Sintering and Selective Laser Melting. *Rapid Prototyping Journal*, vol. 11, n° 1, 2005, p. 26–36.

[KRU 07] Krupa D., Baszkiewicz J., Rajchel B., Barcz A., Sobczak J., Biliński A., Borowski T.
Effect of Calcium-Ion Implantation on the Corrosion Resistance and Bioactivity of the Ti6Al4V Alloy. *Vacuum*, vol. 81, n° 10, 2007, p. 1310–1313.

[KUR 12] Kuroda K., Okido M.
Hydroxyapatite Coating of Titanium Implants Using Hydroprocessing and Evaluation of Their Osteoconductivity. *Bioinorganic Chemistry and Applications*, vol. 2012, 2012, p. 1–7.

[LAC 14] Lachambre J.
Développement d'une Méthode de Caractérisation 3D des Fissures de Fatigue à l'aide de la Corrélation d'Images Numériques obtenues par Tomographie X. , 2014, Page 166.

[LAH 10] Laheurte P., Prima F., Eberhardt A., Gloriant T., Wary M., Patoor E.
Mechanical Properties of Low Modulus $B\beta$ Titanium Alloys Designed from the Electronic Approach. *Journal of the Mechanical Behavior of Biomedical Materials*, vol. 3, n° 8, 2010, p. 565–573.

[LAN 02] Landers R., Hübner U., Schmelzeisen R., Mülhaupt R.
Rapid Prototyping of Scaffolds Derived from Thermoreversible Hydrogels and Tailored

for Applications in Tissue Engineering. *Biomaterials*, vol. 23, n° 23, 2002, p. 4437–4447.

[LAN 10] Lan Levengood S. K., Polak S. J., Wheeler M. B., Maki A. J., Clark S. G., Jamison R. D., Wagoner Johnson A. J.
Multiscale Osteointegration as a New Paradigm for the Design of Calcium Phosphate Scaffolds for Bone Regeneration. *Biomaterials*, vol. 31, n° 13, 2010, p. 3552–3563.

[LEE 88] Lee G. M., Huard T. K., Palsson B. O.
Effect of Anchorage Dependency on Growth Rate and Monoclonal Antibody Production of Hybridoma Cells. *Biotechnology Letters*, vol. 10, n° 5, 1988, p. 307–312.

[LEJ 09] Lejeune M., Chartier T., Dossou-Yovo C., Noguera R.
Ink-Jet Printing of Ceramic Micro-Pillar Arrays. *Journal of the European Ceramic Society*, vol. 29, n° 5, 2009, p. 905–911.

[LEN 87] Lenaerts V., Triqueneaux C., Quartern M., Rieg-Falson F., Couvreur P.
Temperature-Dependent Rheological Behavior of Pluronic F-127 Aqueous Solutions. *International Journal of Pharmaceutics*, vol. 39, n° 1-2, 1987, p. 121–127.

[LEW 06a] Lewis J. A.
Direct Ink Writing of 3D Functional Materials. *Advanced Functional Materials*, vol. 16, n° 17, 2006, p. 2193–2204.

[LEW 06b] Lewis J. A., Smay J. E., Stuecker J., Cesarano J.
Direct Ink Writing of Three-Dimensional Ceramic Structures. *Journal of the American Ceramic Society*, vol. 89, n° 12, 2006, p. 3599–3609.

[LEY 03] Leyens C., Peters M.
Titanium and Titanium Alloys: Fundamentals and Applications. John Wiley & Sons, 2003.

[LEY 15] Leyens C., Beyer E.
Innovations in Laser Cladding and Direct Laser Metal Deposition. *Laser Surface Engineering*, p. 181–192 Elsevier, 2015.

[LI 05] Li J. P., de Wijn J. R., van Blitterswijk C. A., de. Groot K.
Porous Ti6Al4V Scaffolds Directly Fabricated by 3D Fibre Deposition Technique: Effect of Nozzle Diameter. *Journal of Materials Science: Materials in Medicine*, vol. 16, n° 12, 2005, p. 1159–1163.

[LI 06] Li J. P., de Wijn J. R., Van Blitterswijk C. A., de Groot K.
Porous Ti6Al4V Scaffold Directly Fabricating by Rapid Prototyping: Preparation and in Vitro Experiment. *Biomaterials*, vol. 27, n° 8, 2006, p. 1223–1235.

[LI 13] Li N., Zheng Y.
Novel Magnesium Alloys Developed for Biomedical Application: A Review. *Journal of Materials Science & Technology*, vol. 29, n° 6, 2013, p. 489–502.

[LI 16] Li X., Liu X., Wu S., Yeung K., Zheng Y., Chu P. K.
Design of Magnesium Alloys with Controllable Degradation for Biomedical Implants: From Bulk to Surface. *Acta Biomaterialia*, vol. 45, 2016, p. 2–30.

[LI 19] Li G., Yang H., Zheng Y., Chen X.-H., Yang J.-A., Zhu D., Ruan L., Takashima K.
Challenges in the Use of Zinc and Its Alloys as Biodegradable Metals: Perspective from Biomechanical Compatibility, 2019.

[LID 04] Lide D. R.
CRC Handbook of Chemistry and Physics, 85th Edition. CRC Press, 2004.

[LIN 13] Lin W.-S., Starr T. L., Harris B. T., Zandinejad A., Morton D.
Additive Manufacturing Technology (Direct Metal Laser Sintering) as a Novel Approach to Fabricate Functionally Graded Titanium Implants: Preliminary Investigation of Fabrication Parameters. *The International Journal of Oral & Maxillofacial Implants*, vol. 28, n° 6, 2013, p. 1490–1495.

[LIN 14] Lindner R., Parfitt G. D.
Diffusion of Radioactive Magnesium in Magnesium Oxide Crystals. , 2014, Page 5.

[LIU 02] Liu X., Tao S., Ding C.
Bioactivity of Plasma Sprayed Dicalcium Silicate Coatings. *Biomaterials*, vol. 23, n° 3, 2002, p. 963–968.

[LIU 19] Liu Z., Lei Q., Xing S.
Mechanical Characteristics of Wood, Ceramic, Metal and Carbon Fiber-Based PLA Composites Fabricated by FDM. *Journal of Materials Research and Technology*, vol. 8, n° 5, 2019, p. 3741–3751.

[LÜT 98] Lütjering G.
Influence of Processing on Microstructure and Mechanical Properties of (α+β) Titanium Alloys. *Materials science & engineering A*, , 1998.

[LÜT 05] Lüthen F., Lange R., Becker P., Rychly J., Beck U., Nebe J. B.
The influence of surface roughness of titanium on β1- and β3-integrin adhesion and the organization of fibronectin in human osteoblastic cells. *Biomaterials*, vol. 26, n° 15, 2005, p. 2423-2440.

[MAL 02] Malinov S., Sha W., Guo Z., Tang C., Long A.
Synchrotron X-Ray Diffraction Study of the Phase Transformations in Titanium Alloys. *Materials Characterization*, vol. 48, n° 4, 2002, p. 279–295.

[MAN 16] Manakari V., Parande G., Gupta M.
Selective Laser Melting of Magnesium and Magnesium Alloy Powders: A Review. *Metals*, vol. 7, n° 1, 2016, Page 2.

[MAR 06] Marquardt B., Shetty R.
Beta Titanium Alloy Processed for High Strength Orthopedic Applications. *Titanium, Niobium, Zirconium, and Tantalum for Medical and Surgical Applications*, , 2006.

[MAS 05] Masood S., Song W.
Thermal Characteristics of a New Metal/Polymer Material for FDM Rapid Prototyping Process. *Assembly Automation*, vol. 25, n° 4, 2005, p. 309–315.

[M'B 17] M'Barki A., Bocquet L., Stevenson A.
Linking Rheology and Printability for Dense and Strong Ceramics by Direct Ink Writing. *Scientific Reports*, vol. 7, n° 1, 2017.

[MCG 62] McGonigal P. J., Kirshenbaum A. D., Grosse A. V.
THE LIQUID TEMPERATURE RANGE, DENSITY, AND CRITICAL CONSTANTS OF MAGNESIUM [1]. *The Journal of Physical Chemistry*, vol. 66, n° 4, 1962, p. 737–740.

[MIL 16] Milton S., Morandeau A., Chalon F., Leroy R.
Influence of Finish Machining on the Surface Integrity of Ti6Al4V Produced by Selective Laser Melting. *Procedia CIRP*, vol. 45, 2016, p. 127–130.

[MIN 13] Mingareev I., Bonhoff T., El-Sherif A. F., Richardson M.
Femtosecond Laser Post-Processing of Metal Parts Produced by Laser Additive Manufacturing. *MATEC Web of Conferences*, vol. 8, 2013, Page 02010.

[MON 08] Montanari R., Costanza G., Tata M., Testani C.
Lattice Expansion of Ti–6Al–4V by Nitrogen and Oxygen Absorption. *Materials Characterization*, vol. 59, n° 3, 2008, p. 334–337.

[MUH 10] Muhammad W. N. A. W., Mutoh Y., Miyashita Y.
Microstructure and Mechanical Properties of Magnesium Prepared by Spark Plasma Sintering. *Advanced Materials Research*, vol. 129-131, 2010, p. 764–768.

[MUN 79] Munir Z. A.
Analytical Treatment of the Role of Surface Oxide Layers in the Sintering of Metals. *Journal of Materials Science*, vol. 14, n° 11, 1979, p. 2733–2740.

[NAJ 19] Najmon J. C., Raeisi S., Tovar A.
2 - Review of Additive Manufacturing Technologies and Applications in the Aerospace Industry. Froes F., Boyer R., Eds., *Additive Manufacturing for the Aerospace Industry*, p. 7–31 Elsevier, 2019.

[NAY 05] Nayab S. N., Jones F. H., Olsen I.
Effects of Calcium Ion Implantation on Human Bone Cell Interaction with Titanium. *Biomaterials*, vol. 26, n° 23, 2005, p. 4717–4727.

[NEB 04] Nebe B., Lüthen F., Lange R., Becker P., Beck U., Rychly J.
Topography-Induced Alterations in Adhesion Structures Affect Mineralization in Human Osteoblasts on Titanium. *Materials Science and Engineering: C*, vol. 24, n° 5, 2004, p. 619–624.

[NG 10] Ng C. C., Savalani M. M., Man H. C., Gibson I.
Layer Manufacturing of Magnesium and Its Alloy Structures for Future Applications. *Virtual and Physical Prototyping*, vol. 5, n° 1, 2010, p. 13–19.

[NII 98] Niinomi M.
Mechanical Properties of Biomedical Titanium Alloys. *Materials Science and Engineering: A*, vol. 243, n° 1-2, 1998, p. 231–236.

[Nom 18] Nommeots-Nomm A., Lee P. D., Jones J. R.
Direct Ink Writing of Highly Bioactive Glasses. *Journal of the European Ceramic Society*, vol. 38, n° 3, 2018, p. 837–844.

[O'B 05] O'Brien F., Harley B., Yannas I., Gibson L.
The Effect of Pore Size on Cell Adhesion in Collagen-GAG Scaffolds. *Biomaterials*, vol. 26, n° 4, 2005, p. 433–441.

[OGD 55] Ogden H., Jaffee R.
THE EFFECTS OF CARBON, OXYGEN, AND NITROGEN ON THE MECHANICAL PROPERTIES OF TITANIUM AND TITANIUM ALLOYS. rapport n° TML-20, 4370612, 1955.

[OH 03] Oh I.-H., Nomura N., Masahashi N., Hanada S.
Mechanical Properties of Porous Titanium Compacts Prepared by Powder Sintering. *Scripta Materialia*, vol. 49, n° 12, 2003, p. 1197–1202.

[OH 13] Oh J.-M., Heo K.-H., Kim W.-B., Choi G.-S., Lim J.-W.
Sintering Properties of Ti-6Al-4V Alloys Prepared Using Ti/TiH_2 Powders. *MATERIALS TRANSACTIONS*, vol. 54, n° 1, 2013, p. 119-121.

[OLY] Olympus
. "Surface Roughness Measurement - Parameters''.

[ONA 01] Onagoruwa S., Bose S., Bandyopadhyay A.
Fused Deposition of Ceramics (FDC) and Composites. , 2001, Page 8.

[ORT 19] Ortega J. M., Golobic M., Sain J. D., Lenhardt J. M., Wu A. S., Fisher S. E., Perez Perez L. X., Jaycox A. W., Smay J. E., Duoss E. B., Wilson T. S.
Active Mixing of Disparate Inks for Multimaterial 3D Printing. *Advanced Materials Technologies*, vol. 4, n° 7, 2019, Page 1800717.

[PAR 10] Parthasarathy J., Starly B., Raman S., Christensen A.
Mechanical Evaluation of Porous Titanium (Ti6Al4V) Structures with Electron Beam Melting (EBM). *Journal of the Mechanical Behavior of Biomedical Materials*, vol. 3, n° 3, 2010, p. 249–259.

[PED 08] Peddi L., Brow R. K., Brown R. F.
Bioactive Borate Glass Coatings for Titanium Alloys. *Journal of Materials Science: Materials in Medicine*, vol. 19, n° 9, 2008, p. 3145–3152.

[PER 05] Perez M.
Gibbs-Thomson Effect in Phase Transformations. vol. 52, 2005, p. 709–712.

[PER 08a] Perez M., Dumont M., Acevedo D.
Corrigendum to "Implementation of the Classical Nucleation and Growth Theory for Precipitation". vol. 57, 2008, p. 1318–1318.

[PER 08b] Perez M., Dumont M., Acevedo D.
Implementation of the Classical Nucleation and Growth Theory for Precipitation. vol. 56, 2008, p. 2119–2132.

[PER 18] Persenot T.
Fatigue of Ti-6Al-4V thin parts made by Electron Beam Melting. , 2018, Page 218.

[PER 19] Persenot T., Burr A., Plancher E., Buffière J.-Y., Dendievel R., Martin G.
Effect of Ultrasonic Shot Peening on the Surface Defects of Thin Struts Built by Electron Beam Melting: Consequences on Fatigue Resistance. *Additive Manufacturing*, vol. 28, 2019, p. 821–830.

[PET 17] Petit C., Meille S., Maire E., Gremillard L., Adrien J., Lau G. Y., Tomsia A. P.
Fracture Behavior of Robocast HA/β-TCP Scaffolds Studied by X-Ray Tomography and Finite Element Modeling. *Journal of the European Ceramic Society*, vol. 37, n° 4, 2017, p. 1735–1745.

[PIN 20] Pini F., Morganti S., Airoldi L., Brucculeri R., Auricchio F., Anselmi-Tamburini U.
3D Printing of Bulk Copper and Copper Matrix Metal-Ceramic Composites Using Water Based Colloids and Reductive Sintering. *Young Ceramists Additive Manufacturing Forum*, , 2020.

[PIS 04] Piscanec S., Colombi Ciacchi L., Vesselli E., Comelli G., Sbaizero O., Meriani S., De Vita A.
Bioactivity of TiN-Coated Titanium Implants. *Acta Materialia*, vol. 52, n° 5, 2004, p. 1237–1245.

[POL 13] Polak S. J., Rustom L. E., Genin G. M., Talcott M., Wagoner Johnson A. J.
A Mechanism for Effective Cell-Seeding in Rigid, Microporous Substrates. *Acta Biomaterialia*, vol. 9, n° 8, 2013, p. 7977–7986.

[POP 16] Popovich A., Sufiiarov V., Polozov I., Borisov E., Masaylo D.
Producing Hip Implants of Titanium Alloys by Additive Manufacturing. *International Journal of Bioprinting*, vol. 2, n° 2, 2016.

[POQ 13] Poquillon D., Armand C., Huez J.
Oxidation and Oxygen Diffusion in Ti–6al–4V Alloy: Improving Measurements During Sims Analysis by Rotating the Sample. *Oxidation of Metals*, vol. 79, n° 3-4, 2013, p. 249–259.

[PUC 69] Puchtler H., Meloan S. N., Terry M. S.
ON THE HISTORY AND MECHANISM OF ALIZARIN AND ALIZARIN RED S STAINS FOR CALCIUM. *Journal of Histochemistry & Cytochemistry*, vol. 17, n° 2, 1969, p. 110–124.

[QIA 10] Qian M., Schaffer G., Bettles C.
Sintering of Titanium and Its Alloys. *Sintering of Advanced Materials*, p. 324–355 Elsevier, 2010.

[QIA 15] Qian M., Yang Y. F., Luo S. D., Tang H. P.
12 - Pressureless Sintering of Titanium and Titanium Alloys: Sintering Densification and Solute Homogenization. Qian M., (Sam) Froes F. H., Eds., *Titanium Powder Metallurgy*, p. 201–218 Butterworth-Heinemann, Boston, 2015.

[RAM 06] Rammelt S., Illert T., Bierbaum S., Scharnweber D., Zwipp H., Schneiders W.
Coating of Titanium Implants with Collagen, RGD Peptide and Chondroitin Sulfate. *Biomaterials*, vol. 27, n° 32, 2006, p. 5561–5571.

[RAT 13] Ratkovich N., Horn W., Helmus F., Rosenberger S., Naessens W., Nopens I., Bentzen T.
Activated Sludge Rheology: A Critical Review on Data Collection and Modelling. *Water Research*, vol. 47, n° 2, 2013, p. 463–482.

[RAY 78] Rayleigh L.
On The Instability Of Jets. *Proceedings of the London Mathematical Society*, vol. s1-10, n° 1, 1878, p. 4–13.

[REI 12] Reig L., Amigó V., Busquets D. J., Calero J. A.
Development of Porous Ti6Al4V Samples by Microsphere Sintering. *Journal of Materials Processing Technology*, vol. 212, n° 1, 2012, p. 3–7.

[RES 19a] Research G. V.
Healthcare Additive Manufacturing Market SIze - Industry Report, 2019. rapport, 2019.

[RES 19b] Research P. M.
Orthopedic Implants Market Size, Analysis - Industry Report, 2019-2026. rapport, 2019.

[ROU 18] Roussel M., Sauvage X., Perez M., Magné D., Hauet A., Steckmeyer A., Vermont M., Chaise T., Couvrat M.
Influence of Solidification Induced Composition Gradients on Carbide Precipitation in FeNiCr Heat Resistant Steels. vol. 4, 2018, p. 331–339.

[SAB 19] Saboori A., Aversa A., Marchese G., Biamino S., Lombardi M., Fino P.
Application of Directed Energy Deposition-Based Additive Manufacturing in Repair. *Applied Sciences*, vol. 9, n° 16, 2019, Page 3316, Multidisciplinary Digital Publishing Institute.

[ŠAF 19] Šafarič L.
Anaerobic Digester Fluid Rheology and Process Efficiency : Interactions of Substrate Composition, Trace Element Availability, and Microbial Activity, vol. 768 de *Linköping Studies in Arts and Sciences*. Linköping University Electronic Press, Linköping, 2019.

[SAH 15] Sahoo S. K., Sabat R. K., Panda S., Mishra S. C., Suwas S.
Mechanical Property of Pure Magnesium: From Orientation Perspective Pertaining to Deviation from Basal Orientation. *Journal of Materials Engineering and Performance*, vol. 24, nº 6, 2015, p. 2346–2353.

[Sal 13] Sallica-Leva E., Jardini A., Fogagnolo J.
Microstructure and Mechanical Behavior of Porous Ti–6Al–4V Parts Obtained by Selective Laser Melting. *Journal of the Mechanical Behavior of Biomedical Materials*, vol. 26, 2013, p. 98–108.

[SAL 19a] Salehi M., Maleksaeedi S., Nai M. L. S., Gupta M.
Towards Additive Manufacturing of Magnesium Alloys through Integration of Binderless 3D Printing and Rapid Microwave Sintering. *Additive Manufacturing*, vol. 29, 2019, Page 100790.

[SAL 19b] Salehi M., Maleksaeedi S., Nai S. M. L., Meenashisundaram G. K., Goh M. H., Gupta M.
A Paradigm Shift towards Compositionally Zero-Sum Binderless 3D Printing of Magnesium Alloys via Capillary-Mediated Bridging. *Acta Materialia*, vol. 165, 2019, p. 294–306.

[SAL 19c] Salehi M., Maleksaeedi S., Sapari M. A. B., Nai M. L. S., Meenashisundaram G. K., Gupta M.
Additive Manufacturing of Magnesium–Zinc–Zirconium (ZK) Alloys via Capillary-Mediated Binderless Three-Dimensional Printing. *Materials & Design*, vol. 169, 2019, Page 107683.

[SAN 07] Sandrini E., Giordano C., Busini V., Signorelli E., Cigada A.
Apatite Formation and Cellular Response of a Novel Bioactive Titanium. *Journal of Materials Science: Materials in Medicine*, vol. 18, nº 6, 2007, p. 1225–1237.

[SCH 00] Schramm G.
A Practical Approach to Rheology and Rheometry. , 2000, Page 291.

[SCH 10] Schinhammer M., Hänzi A. C., Löffler J. F., Uggowitzer P. J.
Design Strategy for Biodegradable Fe-Based Alloys for Medical Applications. *Acta Biomaterialia*, vol. 6, nº 5, 2010, p. 1705–1713.

[SCH 12] Schindelin J., Arganda-Carreras I., Frise E., Kaynig V., Longair M., Pietzsch T., Preibisch S., Rueden C., Saalfeld S., Schmid B., Tinevez J.-Y., White D. J., Hartenstein V., Eliceiri K., Tomancak P., Cardona A.
Fiji: An Open-Source Platform for Biological-Image Analysis. *Nature Methods*, vol. 9, nº 7, 2012, p. 676–682.

[SHA 03] Shaw B.
Corrosion Resistance of Magnesium Alloys, vol. 13A. Asm handbook édition, 2003.

[SHE 56] Shewmon P. G.
Self-Diffusion in Magnesium Single Crystals. *JOM*, vol. 8, n° 8, 1956, p. 918–922.

[SIM 14] Simonelli M., Tse Y., Tuck C.
Effect of the Build Orientation on the Mechanical Properties and Fracture Modes of SLM Ti–6Al–4V. *Materials Science and Engineering: A*, vol. 616, 2014, p. 1–11.

[SIN 16] Sing S. L., An J., Yeong W. Y., Wiria F. E.
Laser and Electron-Beam Powder-Bed Additive Manufacturing of Metallic Implants: A Review on Processes, Materials and Designs. *Journal of Orthopaedic Research*, vol. 34, n° 3, 2016, p. 369–385.

[SKY 16] Skylar-Scott M. A., Gunasekaran S., Lewis J. A.
Laser-Assisted Direct Ink Writing of Planar and 3D Metal Architectures. *Proceedings of the National Academy of Sciences*, , 2016, Page 6.

[SKY 19] Skylar-Scott M. A., Mueller J., Visser C. W., Lewis J. A.
Voxelated Soft Matter via Multimaterial Multinozzle 3D Printing. *Nature*, vol. 575, n° 7782, 2019, p. 330–335, Nature Publishing Group.

[SMA 02] Smay J. E., Cesarano J., Lewis J. A.
Colloidal Inks for Directed Assembly of 3-D Periodic Structures. *Langmuir*, vol. 18, n° 14, 2002, p. 5429–5437.

[SMA 08] Smay J. E., Tuttle B., III J. C.
Robocasting of Three-Dimensional Piezoelectric Structures. Safari A., Akdoğan E. K., Eds., *Piezoelectric and Acoustic Materials for Transducer Applications*, p. 305–318 Springer US, Boston, MA, 2008.

[SON 02] Song G., StJohn D.
The Effect of Zirconium Grain Refinement on the Corrosion Behaviour of Magnesium-Rare Earth Alloy MEZ. *Journal of Light Metals*, vol. 2, n° 1, 2002, p. 1–16.

[SON 12] Song B., Dong S., Liao H., Coddet C.
Process Parameter Selection for Selective Laser Melting of Ti6Al4V Based on Temperature Distribution Simulation and Experimental Sintering. *The International Journal of Advanced Manufacturing Technology*, vol. 61, n° 9-12, 2012, p. 967–974.

[STA 06] Staiger M. P., Pietak A. M., Huadmai J., Dias G.
Magnesium and Its Alloys as Orthopedic Biomaterials: A Review. *Biomaterials*, vol. 27, n° 9, 2006, p. 1728–1734.

[TAC 17] Tack P.
Cost-Effectiveness of Medical Innovations. *Materialise World Summit*, 2017.

[TAY 17] Taylor S. L., Jakus A. E., Shah R. N., Dunand D. C.
Iron and Nickel Cellular Structures by Sintering of 3D-Printed Oxide or Metallic Par-

ticle Inks: Iron and Nickel Cellular Structures by Sintering.... *Advanced Engineering Materials*, vol. 19, n° 11, 2017, Page 1600365.

[THE 18] ThermoTech
TTTI3 Database, 2018.

[THI 13] Thievessen I., Thompson P. M., Berlemont S., Plevock K. M., Plotnikov S. V., Zemljic-Harpf A., Ross R. S., Davidson M. W., Danuser G., Campbell S. L., Waterman C. M.
Vinculin–Actin Interaction Couples Actin Retrograde Flow to Focal Adhesions, but Is Dispensable for Focal Adhesion Growth. *Journal of Cell Biology*, vol. 202, n° 1, 2013, p. 163–177.

[TOF 20] Toffolon-Masclet C., Perron A., Mazères B., Dépinoy S., Desgranges C., Martinelli L., Monceau D., Boulnat X., Mathevon A., Perez M.
Computational Kinetics: Application to Nuclear Materials. *Comprehensive Nuclear Materials*, p. 850–880 Elsevier, 2020.

[TRU 16] Truby R. L., Lewis J. A.
Printing Soft Matter in Three Dimensions. *Nature*, vol. 540, n° 7633, 2016, p. 371–378, Nature Publishing Group.

[VIL 15] Vila P. B.
Phase Transformation Kinetics during Continuous Heating of $\alpha + \beta$ and Metastable β Titanium Alloys. Thèse de doctorat, 2015.

[WAG 05] Wagner R., Kampmann R., Voorhees P. W.
Homogeneous Second-Phase Precipitation. *Phase Transformations in Materials*, p. 309–407 John Wiley & Sons, Ltd, 2005.

[WAN 03] Wang L., Xian A., Shao H.
Density Measurement of Liquid Indium and Zinc by the γ-Ray Attenuation Method. *High Temperatures-High Pressures*, vol. 35/36, n° 6, 2003, p. 659–665.

[WEI 15] Wei K., Wang Z., Zeng X.
Influence of Element Vaporization on Formability, Composition, Microstructure, and Mechanical Performance of the Selective Laser Melted Mg–Zn–Zr Components. *Materials Letters*, vol. 156, 2015, p. 187–190.

[WEL 93] Welsch G., Boyer R., Collings E.
Materials Properties Handbook: Titanium Alloys. ASM international, 1993.

[WIT 06] Witte F., Fischer J., Nellesen J., Crostack H.-A., Kaese V., Pisch A., Beckmann F., Windhagen H.
In Vitro and in Vivo Corrosion Measurements of Magnesium Alloys. *Biomaterials*, vol. 27, n° 7, 2006, p. 1013–1018.

[WOL 10] Wolff M., Ebel T., Dahms M.
Sintering of Magnesium. *Advanced Engineering Materials*, vol. 12, n° 9, 2010, p. 829–836.

[WOO 12] Woodcock L. V.
Percolation Transitions in the Hard-Sphere Fluid. *AIChE Journal*, vol. 58, n° 5, 2012, p. 1610–1618.

[XAV 03] Xavier S. P., Carvalho P. S., Beloti M. M., Rosa A. L.
Response of Rat Bone Marrow Cells to Commercially Pure Titanium Submitted to Different Surface Treatments. *Journal of Dentistry*, vol. 31, n° 3, 2003, p. 173–180.

[XU 14] Xu X., Nash P.
Sintering Mechanisms of Armstrong Prealloyed Ti–6Al–4V Powders. *Materials Science and Engineering: A*, vol. 607, 2014, p. 409–416.

[YAN 14] Yan M., Xu W., Dargusch M. S., Tang H. P., Brandt M., Qian M.
Review of Effect of Oxygen on Room Temperature Ductility of Titanium and Titanium Alloys. *Powder Metallurgy*, vol. 57, n° 4, 2014, p. 251–257, Taylor & Francis.

[YET 17] Yetna N'Jock M., Camposilvan E., Gremillard L., Maire E., Fabrègue D., Chicot D., Tabalaiev K., Adrien J.
Characterization of 100Cr6 Lattice Structures Produced by Robocasting. *Materials & Design*, vol. 121, 2017, p. 345–354.

[ZAH 18] Zaharin H. A., Abdul Rani A. M., Azam F. I., Ginta T. L., Sallih N., Ahmad A., Yunus N. A., Zulkifli T. Z. A.
Effect of Unit Cell Type and Pore Size on Porosity and Mechanical Behavior of Additively Manufactured Ti6Al4V Scaffolds. *Materials*, vol. 11, n° 12, 2018, Page 2402.

[ZEI 02] Zein I., Hutmacher D. W., Tan K. C., Teoh S. H.
Fused Deposition Modeling of Novel Scaffold Architectures for Tissue Engineering Applications. *Biomaterials*, vol. 23, n° 4, 2002, p. 1169–1185.

[ZEN 08] Zeng R., Dietzel W., Witte F., Hort N., Blawert C.
Progress and Challenge for Magnesium Alloys as Biomaterials. *Advanced Engineering Materials*, vol. 10, n° 8, 2008, p. B3-B14.

[ZHA 06] Zhao G., Zinger O., Schwartz Z., Wieland M., Landolt D., Boyan B. D.
Osteoblast-like Cells Are Sensitive to Submicron-Scale Surface Structure. *Clinical Oral Implants Research*, vol. 17, n° 3, 2006, p. 258–264.

[ZHA 15] Zhao X., Wei Q., Song B., Liu Y., Luo X., Wen S., Shi Y.
Fabrication and Characterization of AISI 420 Stainless Steel Using Selective Laser Melting. *Materials and Manufacturing Processes*, , 2015, p. 1283–1289.

[ZHA 16] Zhao X., Li S., Zhang M., Liu Y., Sercombe T. B., Wang S., Hao Y., Yang R., Murr L. E.

Comparison of the Microstructures and Mechanical Properties of Ti–6Al–4V Fabricated by Selective Laser Melting and Electron Beam Melting. *Materials & Design*, vol. 95, 2016, p. 21–31.

[ZHO 05] Zhong Y.
Investigation in Mg-Al-Ca-Sr-Zn System by Computational Thermodynamics Approach Coupled With First-Principled Energetics Ans Experiments. , 2005, Page 360.

[ZHO 17] Zhou N., Liu C., Lewis J. A., Ham D.
Gigahertz Electromagnetic Structures via Direct Ink Writing for Radio-Frequency Oscillator and Transmitter Applications. *Advanced Materials*, vol. 29, n° 15, 2017, Page 1605198.

[ZUM 19] Zumdick N. A., Jauer L., Kersting L. C., Kutz T. N., Schleifenbaum J. H., Zander D.
Additive Manufactured WE43 Magnesium: A Comparative Study of the Microstructure and Mechanical Properties with Those of Powder Extruded and as-Cast WE43. *Materials Characterization*, vol. 147, 2019, p. 384–397.

[ZUR 14] Zuriguel I.
Invited Review: Clogging of Granular Materials in Bottlenecks. *Papers in Physics*, vol. 6, n° 0, 2014, Page 060014.

FOLIO ADMINISTRATIF

THESE DE L'UNIVERSITE DE LYON OPEREE AU SEIN DE L'INSA LYON

NOM : COFFIGNIEZ

DATE de SOUTENANCE : 15/01/2021

Prénoms : Marion

TITRE : Additive manufacturing of 3D architectured metallic biomaterials by robocasting

NATURE : Doctorat

Numéro d'ordre : 2021LYSEI007

Ecole doctorale : ED 34 : Matériaux de Lyon

Spécialité : Science des Matériaux

RESUME :

In addition to the customisation aspect that it can bring to the medical field, additive manufacturing also gives access to the development of cellular structures. These structures, with controlled porosity, allow the mechanical properties of the object to be modulated, but also promote the cellular invasion necessary for tissue engineering.

Among the metals commonly used in orthopaedic surgery, titanium alloys are the ones with the lowest stiffness compared to bone. This study therefore focuses on the development of structures made of Ti-6Al-4V, but also of magnesium since it has the advantage of being resorbable in the body. The scaffolds are obtained by robocasting, a process consisting of extruding, layer by layer, a pasty ink made up of powder and binder. The structures are then debinded and sintered at high temperature to achieve their final properties.

For the Ti-6Al-4V structures, a parametric study is carried out to evaluate the possibilities and limits of the process in terms of structures (and microstructures), chemical compositions and mechanical properties obtained.
After optimisation of debinding and sintering steps, it is possible to obtain parts with two levels of interconnected porosities (intra-filament microporosity, beneficial for cell attachment according to the literature, and designed macropores), keeping a specific yield strength higher than that of bone (105 MPa.cm³/g) and a Young's modulus close to that of bone (28-30 GPa). A gradient of intra-filament porosity can also be obtained by varying the powder size within a single piece.

For magnesium, a binder compatible with the reactivity of the powder (ethanol based) has been identified and the first steps of the process (printing, debinding) are therefore quite feasible for this material. However, conventional sintering of (pure) magnesium is complicated by its reactivity. Alternative sintering methods are therefore being studied (liquid phase sintering, SPS).

MOTS-CLÉS : Additive manufacturing, robocasting, biomaterials, titanium, magnesium, debinding, sintering, powder

Laboratoire (s) de recherche : MATEIS, UMR CNRS 5510

Directeurs de thèse:
Laurent Gremillard, INSA Lyon
Xavier Boulnat, INSA Lyon

Composition du jury :
Rapportrice : Dominique Poquillon, INP - ENSIACET
Rapporteur : Jean-Michel Missiaen, INP - Phelma
Président du jury : Thierry Gloriant, INSA Rennes
Invitée : Claire Rigollet, ECAM Lyon
Invité : Jérôme Andrieux, UCBL Lyon